SCUOLA DI DOTTORATO
UNIVERSITÀ DEGLI STUDI DI MILANO–BICOCCA

Department of Materials Science

PhD program in Materials Science and Nanotechnology, XXXVIII cycle

Light-driven Shaping of Free-electrons for Ultrafast Investigation of Quantum Materials

Beatrice Matilde Ferrari
Registration number: 820814

Tutor: Prof. Giovanni Maria Vanacore

Coordinator: Prof. Francesco Montalenti

Academic Year: 2024/25

Abstract

Advances in ultrafast pulsed–laser technology have made it possible to follow physical and chemical processes on their natural femtosecond timescales. To combine this temporal resolution with the atomic spatial resolution of electron microscopy, pulsed-laser illumination has been integrated into electron microscopes, giving rise to ultrafast transmission electron microscopy (UTEM). This work takes a further step inspired by optics: it introduces programmable control of the electron beam by shaping it with light inside the UTEM itself. While previous approaches achieved optical modulation only at the sample plane, this thesis demonstrates for the first time programmable, light-driven modulation of the electron wavefunction before the specimen, implemented through a Photonic-based free-ELectron Modulator (PELM) integrated into the TEM column at the University of Milano-Bicocca.

The PELM is a modified TEM column section that serves as the physical platform enabling the interaction between photoemitted electrons and a pre-shaped infrared laser field, and is designed for optical access and coherence control. The electron–light interaction is mediated by inverse transition radiation at a thin metallic film, which transfers to the electrons the transverse intensity pattern that a spatial light modulator previously imparts to the laser field. Spatiotemporal overlap between the laser and electron beams was verified through plasma–lensing measurements and momentum-streaking of the electron distribution induced by the optical field. Using this platform, we realized programmable, light-driven shaping of the transverse electron beam and demonstrated that the imposed modulation is preserved and can be demagnified onto the sample plane. The same setup enabled electron single-pixel imaging, in which nanostructured membranes were reconstructed from a sequence of programmed illumination patterns, extending optical imaging concepts into the nanometric regime of electron microscopy.

Further experiments were carried out at École Polytechnique Fédérale de Lausanne to explore beam shaping and ultrafast measurements on complex materials. Although an alternative version of the PELM based on a two-grid sample holder is still being commissioned, transverse beam shaping at the sample plane was reproduced using a standard holder and a thin silver film. This configuration allowed us to estimate the transverse coherence length of the electron beam under realistic UTEM conditions. We then investigated two representative materials—iAlPdMn quasicrystals and 30°-twisted bilayer graphene—to assess the practical limits of ultrafast electron diffraction and spectroscopy. In iAlPdMn, high-quality diffraction patterns were obtained and preliminary time-resolved electron diffraction was performed, although external issues-such as cumulative heating and sample fragility-need to be considered for a conclusive analysis. In 30°-TBLG, momentum-selected electron energy-loss spectroscopy revealed anisotropies

across Bragg conditions, and preliminary pump–probe data showed a transient suppression and recovery of the π plasmon, consistent with phonon-mediated relaxation on two distinct timescales.

Together, these results establish the feasibility of programmable, light-driven shaping of free-electron beams within an ultrafast transmission electron microscope for investigation of complex materials. Our findings outline both the novel possibilities as well as the current limitations of the method within the UTEM technique, defining the experimental conditions and technological requirements for improved efficiency, sensitivity, and temporal stability. By bridging instrumentation and application, this work outlines a pathway toward programmable ultrafast electron microscopy, where structured electron probes enable highly selective and energy/momentum-resolved investigations of complex and quantum materials.

List of Acronyms

AP Alternating Projection (algorithm)

CCD Charge-Coupled Device

CDEM Charge-Dynamics Electron Microscopy

CGD Conjugate Gradient Descent (algorithm)

CL Condenser Lens

CMOS Complementary Metal-Oxide-Semiconductor

CW Continuous Wave

DLA Dielectric Laser Acceleration

DP Diffraction Pattern

ECC Enhanced Correlation Coefficient

EDX Energy-Dispersive X-ray

EELS Electron Energy-Loss Spectroscopy

EFTEM Energy-Filtered Transmission Electron Microscopy

EPI Electron-Photon Interaction

ESF Edge Spread Function

ESPI Electron Single Pixel Imaging

FIB Focused Ion Beam

FWHM Full Width at Half Maximum

HDD High Dispersion Diffraction

HG Hermite-Gaussian (mode)

IR Infrared

ITR Inverse Transition Radiation

LCoS Liquid Crystal on Silicon

LSF Line Spread Function

LSTEM Light-Scanning Transmission Electron Microscopy

MTF Modulation Transfer Function

ND Neutral Density (filter)

OPA Optical Parametric Amplification

PELM Photonic-based free-ELectron Modulator

PINEM Photon-Induced Near-field Electron Microscopy

PSF Point Spread Function

PW Pulsed Wave

QC Quasicrystal

ROI Region of Interest

SEM Scanning Electron Microscopy

SLM Spatial Light Modulator

SPI Single Pixel Imaging

SPP Surface Plasmon Polariton

SR Sampling Ratio

SSIM Structural Similarity Index Measure

STEM Scanning Transmission Electron Microscopy

TBLG Twisted Bilayer Graphene

TEM Transmission Electron Microscopy

TR Transition Radiation

UED Ultrafast Electron Diffraction

UEM Ultrafast Electron Microscopy

UTEM Ultrafast Transmission Electron Microscopy

UV Ultraviolet

ZLP Zero-Loss Peak

Contents

Chapter 1

Introduction

The discovery of the electron and its wave-particle duality, first demonstrated in the diffraction experiments of Thomson [1] and of Davisson and Germer [2], and the subsequent construction of the first transmission electron microscope (TEM) by Knoll and Ruska [3], established electron microscopy as a fundamental tool for resolving the structure of condensed matter with atomic precision [4]. The field of electron microscopy has progressed significantly through instrumental breakthroughs. Early efforts focused on improving spatial resolution, leading to atomic-scale imaging through advancements such as aberration correction and new detectors [5, 6]. Subsequent developments introduced sophisticated techniques such as electron holography and scanning transmission electron microscopy by leveraging high-brightness electron sources [4, 7, 8].

While electron microscopy offers outstanding spatial resolution, its ability to capture dynamics was originally limited by detector frame rates. With modern direct electron detectors, temporal resolution has improved to the microsecond range [9], yet this remains orders of magnitude slower than the intrinsic femtosecond timescales of fundamental physical and chemical processes. Inspired by the groundbreaking progress in optical science, which achieved attosecond temporal resolution with ultrashort laser pulses [10], researchers began to integrate pulsed lasers with electron optics to achieve simultaneous nanometric spatial and femtosecond temporal resolution. This effort gave rise to new electron imaging techniques, such as single-shot dynamic TEM for irreversible events [11] and stroboscopic ultrafast TEM (UTEM) for reversible dynamics [12].

The continuous inspiration drawn from optics also extends to the realm of beam shaping, where the ability to manipulate light fields on demand is far more advanced than for electron beams. The field of electron-beam shaping has progressed from using static nanoscale masks to adopting programmable phase plates that leverage slowly varying electrostatic and magnetostatic fields [13]. A crucial step forward took place within the UTEM framework, which introduced a dynamic, femtosecond-scale dimension to beam shaping [14]. Early work in Photon-Induced Near-field Electron Microscopy demonstrated

the fundamental quantized, inelastic interaction between free electrons and nanoconfined light, laying the foundation for coherent control of free-electron states [15, 16]. This led to the development of methods that use light to modulate the longitudinal phase of the electron wavefunction, enabling the creation of attosecond electron pulse trains [17, 18, 19].

In parallel, researchers successfully generated pulsed electron vortex beams via chiral surface plasmon polaritons, which opened up new forms of chiral and phase-resolved imaging [20, 21]. The growing interest in light-mediated electron-beam shaping stems from its ability to introduce versatile and highly dynamic modulation, drawing upon the latest advancements in optical technology, such as spatial light modulators [22]. These developments have opened up exciting possibilities for implementing new imaging methods, including aberration correction, enhanced contrast in imaging weak scatterers, and phase-resolved techniques such as Ramsey holography [23, 24].

Building upon these advances, the *Photonic-based free-ELectron Modulator (PELM)* concept was proposed as an innovative platform for pre-sample control of the electron wavefunction. The initial demonstration of this concept at the sample plane showed that it was possible to use an externally controlled light field to effectively shape the electron beam [22]. However, to fully realize the potential of this approach, a technological platform enabling electron-beam shaping before the sample plane was needed.

This thesis presents the experimental realization of a new type of UTEM in which we integrate a PELM device to achieve this goal. A PELM leverages electron-photon interaction, specifically inverse transition radiation [25], mediated by a dedicated thin film placed within the microscope column prior to the sample. By shaping the electron wavefunction before the specimen, the PELM introduces photonics-inspired control into electron microscopy. While a standard Gaussian beam is s-symmetric and thus primarily excites states with no angular dependence, a structured beam with non-zero orbital angular momentum allows for the excitation of asymmetric modes (such as p and d states). This capability significantly expands the range of light-mediated interactions and opens new possibilities for selectively probing material dynamics with enhanced spatiotemporal resolution and sensitivity to specific degrees of freedom. For instance, structured electron beams could be used to access low-frequency excitations in materials [18, 26, 27], to enable low-dose imaging of sensitive scatterers [28], or to improve image resolution [29] and contrast [19] when detecting subtle changes, thereby expanding the capabilities of UTEM. In this perspective, the PELM establishes a technological foundation for future implementations of light-controlled electron imaging and spectroscopy, and for exploring electron-photon interactions as a new handle in electron microscopy.

As a final note, this research was conducted within the framework of the *SMART-electron* project, a *Horizon 2020 FET-Open* collaboration aimed at developing new paradigms for electron-beam shaping and quantum-inspired electron microscopy. Within this initiative, new UTEM platforms were realized by the *LUMiNaD* group at the University of Milano-Bicocca (Italy) and by the *AdQuanta* group at the Technion (Israel Institute of Technology, Haifa), enabling programmable light-driven modulation schemes based on

electron-photon interaction. École Polytechnique Fédérale de Lausanne (EPFL, Switzerland) was also part of the consortium, providing access to an existing UTEM infrastructure at the *LUMES* laboratory. Part of the experimental work presented in this thesis was carried out during a research stay at EPFL, where preliminary studies on two-dimensional materials and quasicrystals were performed.

This thesis is structured as follows: Chapter 2 introduces the principles of ultrafast transmission electron microscopy and the fundamental mechanisms of light-electron interaction that underpin beam shaping. Chapter 3 describes the hardware implementation of the UTEM developed at the University of Milano-Bicocca and the integration of the PELM device. Chapter 4 presents experiments demonstrating transverse and longitudinal beam shaping. Chapter 5 details the implementation of electron single pixel imaging using PELM-modulated beams. Chapter 6 reports ultrafast studies on materials, including twisted bilayer graphene and quasicrystals, followed by general conclusions and outlook in Chapter 7.

Chapter 2

General Background: Experiments and Theory

Realizing a photonic-based free-electron modulator (PELM) requires a deep understanding of how ultrafast electron microscopy (UEM) operates and how light-electron interaction can be harnessed to shape the electron wavefunction. This chapter provides the theoretical and conceptual background underlying these aspects and situates them within the broader context of recent developments in ultrafast TEM.

The first part introduces the operating principles of ultrafast TEM and reviews its main experimental implementations, highlighting how the combination of ultrashort laser pulses with electron probes enables femtosecond-resolved imaging, diffraction, and spectroscopy. The following sections discuss the mechanisms of electron-photon interaction that underpin beam modulation, with particular attention to the regimes relevant to photon-induced near-field electron microscopy (PINEM) and inverse transition radiation (ITR). Finally, the chapter examines how these interactions can be exploited for dynamic beam shaping, setting the theoretical foundation for the experimental realization of the PELM presented in Chapter 3.

2.1 Ultrafast Transmission Electron Microscopy

Ultrafast transmission electron microscopy (UTEM) extends the powerful spatial resolution of a TEM into the femtosecond time domain through optical excitation in a pump-probe scheme [24, 30, 31, 32, 33, 34]. In UTEM, the specimen is excited by an ultrashort optical pump and interrogated by a time-delayed electron probe, allowing the reconstruction of dynamics by scanning the delay and recording images, diffraction patterns, or energy-loss spectra at each time point. This capability enables the direct observation of

transient behaviors in matter, such as molecular motion [35], structural phase transitions [36, 37], and electronic processes [38], on their intrinsic femtosecond-picosecond timescales.

UTEM operates through a synchronization scheme combining pulsed lasers and electron beams (e-beams), generally referred to as the optical pump-electron probe technique. In this configuration, a femtosecond laser pulse is divided into two parts [39]. The first, frequency-converted into ultraviolet (UV) light, is directed toward the TEM cathode to generate ultrashort electron pulses (the probe) via photoemission. The resulting electron packets are accelerated (e.g., to 200 keV) and transmitted through the specimen. The second part of the laser pulse (the pump) excites the specimen, initiating the dynamic process under investigation (e.g., electronic excitation or thermal heating).

By controlling the time delay between the optical pump and electron probe pulses using an optical delay stage, the time evolution of the specimen can be measured stroboscopically. In this operation mode, the pump-probe sequence is repeated many times while the relative time delay is varied. For each selected delay, a large number of electron pulses probe the same excitation event, and the resulting scattering signals are integrated to form a single frame—an image, diffraction pattern, or electron energy-loss spectrum—corresponding to that delay. The sequence is then repeated for successive delay values, gradually building a time-resolved dataset as illustrated in Fig. 2.1. Such measurements require the process to be fully reversible and identical across repetitions, ensuring that each frame represents an equivalent excitation cycle of the specimen.

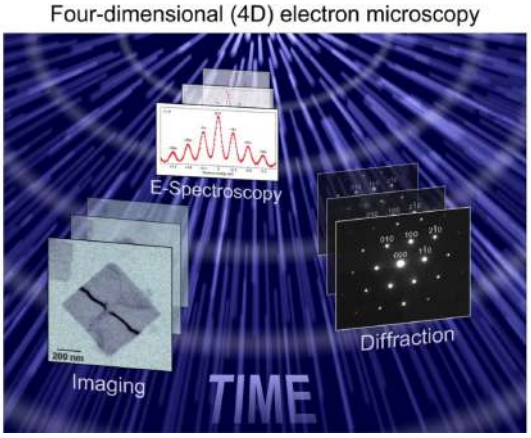

Figure 2.1: Schematic representation of the UTEM experiments concept. Ultrashort electron pulses are used to stroboscopically record time-resolved datasets in different acquisition modes: imaging, diffraction, and energy-loss spectroscopy.

The temporal resolution is governed by the convolution of the electron pulse duration Δt_e, the pump pulse duration Δt_L, and residual synchronization jitter Δt_{jitter} [12, 40]:

$$\Delta t_{\text{UTEM}} \simeq \sqrt{\Delta t_e^2 + \Delta t_L^2 + \Delta t_{\text{jitter}}^2}. \tag{2.1}$$

Operating in the single- or few-electron regime suppresses Coulomb repulsion within the pulse, which would otherwise stretch it in time and increase its energy spread [41]. At the

same time, high repetition rates (0.1-5 MHz) ensure sufficient signal accumulation while maintaining coherence. However, excessively high repetition rates may prevent complete thermalization of the specimen between consecutive pump-probe cycles, leading to cumulative heating and preventing a successful stroboscopic reconstruction of the dynamics. This balance between temporal resolution, coherence, and usable current defines the working space of UTEM.

Significant efforts have focused on enhancing electron-pulse coherence and shortening its duration, for instance by employing nanotip photoemission sources that offer reduced emittance for high-resolution nanoscale probing [42]. Furthermore, compression techniques based on terahertz radiation have been implemented to push the temporal resolution toward the femtosecond and attosecond regimes [43, 44].

Ultrafast electron diffraction (UED) and crystallography map transient structural dynamics in materials and molecules [35, 36, 37, 45]. These techniques capture changes in Bragg reflections and scattering vectors, revealing atomic motion during relaxation or phase transformation. A canonical demonstration is the femtosecond melting of aluminum, where Debye-Waller factors and Bragg-peak intensities quantify the onset of disorder and energy flow into phonons [40].

UED has been widely applied to benchmark systems and technologically relevant materials. In graphite, femtosecond diffraction revealed nonequilibrium chemical-bond dynamics and the subsequent electron-phonon relaxation pathways [38, 46]. Phase-change materials such as GeTe display ultrafast structural components distinct from slower thermal processes, pointing to carrier-driven pathways in structural transitions [36]. Correlated oxides like VO_2 have been examined to disentangle lattice and electronic contributions to the insulator-metal transition [37, 47], while studies on magnetic films have revealed the role of phonons in angular-momentum transfer during ultrafast demagnetization [43].

Beyond diffraction, UTEM also enables ultrafast electron energy-loss spectroscopy (EELS), which directly probes changes in the electronic structure and collective excitations. In graphite, time-resolved EELS revealed the redistribution of spectral weight between the π and $\pi + \sigma$ plasmons after optical excitation [38, 48]. This spectroscopic sensitivity complements diffraction by linking structural dynamics to electronic and vibrational degrees of freedom.

While ultrafast EELS provides energy-resolved information, its integration with energy-filtered TEM (EFTEM) extends these capabilities into real space. By selecting electrons within a narrow energy-loss window, ultrafast EFTEM produces images that isolate specific inelastic channels—such as plasmons, interband transitions, or excitons—as they evolve in time [15, 33, 35, 49, 50, 51, 52]. In this way, the method bridges spectroscopy and imaging, offering a spatially resolved view of transient excitations that cannot be obtained from diffraction alone. Complementary time-resolved cathodoluminescence in UTEM directly measures recombination and radiative pathways with sub-ns to ps lifetimes and can be synchronized to the pump-probe sequence [53].

Across these examples, a recurring theme is that the electron interacts not only with the atomic structure of matter but also with its optical response. The inelastic scattering events recorded in EELS or the transient contrast observed in energy-filtered imaging arise from the coupling between the electron's evanescent electromagnetic field and the sample's collective excitations—plasmons, phonons, or excitons. Understanding and exploiting this fundamental form of electron-photon interaction provides a natural bridge to the following section, which discusses photon-induced processes in electron microscopy from a broader theoretical perspective.

2.2 Electron-photon interactions

Historically, the coupling between free electrons and electromagnetic fields was first observed through radiation emitted by fast electrons interacting with their surrounding media. Examples include Cerenkov emission in dielectrics [54], transition radiation at material boundaries [55], and Smith-Purcell emission from metallic gratings [56]. The discovery of their inverse counterparts—inverse Cerenkov acceleration [57], inverse Smith-Purcell absorption [58], and stimulated inverse transition radiation [25]—demonstrated that electromagnetic fields can coherently transfer momentum and energy to free electrons. At relativistic energies, these principles underpin the operation of free-electron lasers and dielectric-laser accelerators [59, 60], forming the conceptual basis for modern light-electron coupling schemes.

At optical frequencies and at the electron energies relevant for transmission electron microscopy (100-300 kV), the direct absorption or emission of photons in free space is strongly suppressed by the mismatch between electron and photon dispersion relations [16, 61]. Efficient coupling requires the presence of a longitudinal field component or of an interface that breaks translational invariance, providing the additional momentum necessary for interaction. Under such conditions, electrons can exchange discrete energy quanta with the optical field, and the process must be described within a quantized framework. In our context, the electron-photon interaction (EPI) refers to the inelastic, quantized coupling regime that enables coherent energy-momentum transfer between light and free electrons. The most relevant examples at optical frequencies are photon-induced near-field electron microscopy and stimulated inverse transition radiation.

At lower electron energies, as in scanning electron microscopes (10-100 kV), the interaction can also occur in free space when a sufficiently strong optical field acts on the electrons. This process, known as ponderomotive scattering [29, 62], arises from the cycle-averaged potential of the optical field and can modulate the electron phase without requiring a nanostructure or an interface. Its elastic implementation has been successfully employed for e-beam shaping with light [63], while inelastic extensions of the same mechanism have also been explored [64, 65].

In summary, the interaction between light and free electrons relevant for this work

(i.e., for transverse e-beam shaping) occurs through three main mechanisms: the elastic ponderomotive coupling in free space, photon-induced near-field electron microscopy, and stimulated inverse transition radiation.

- **(i) Ponderomotive interaction (elastic limit).** A standing optical field exerts a cycle-averaged ponderomotive force on the electron, imprinting a spatially varying phase without net energy exchange [28, 62]. When the field symmetry is broken, for instance in travelling or bichromatic configurations, energy exchange becomes possible, bridging toward the inelastic regime described by quantized photon exchange [64].
- **(ii) Photon-induced near-field electron microscopy.** In this interaction, the electron couples to an evanescent near field possessing a longitudinal electric-field component, typically generated by light scattering at a nanostructure. This field enables the electron to absorb or emit integer multiples of the photon energy, leading to a ladder of sidebands separated by $\hbar\omega$ and weighted according to Bessel statistics [15, 16, 61]. PINEM constituted the first experimental demonstration of quantized energy-momentum exchange between free electrons and optical fields and underpins most present implementations of light-assisted beam shaping in UTEM.
- **(iii) Stimulated inverse transition radiation.** When an electron crosses a dielectric interface illuminated by a coherent optical field, the boundary conditions of the electromagnetic field give rise to transition radiation. In the stimulated inverse process, the optical field overlaps with the electron, enabling quantized transfer of both energy and phase [25, 44, 50]. In contrast to photon-induced near-field electron microscopy, where the near field is localized and geometry dependent, here the longitudinal field is defined by the macroscopic interface, allowing the optical phase to be directly and programmably mapped onto the electron wavefunction.

2.2.1 Ponderomotive Phase Modulation in Free Space

In the absence of interfaces or near fields, electrons can still interact with light through the cycle-averaged ponderomotive force [29], elastically [62, 63] or inelastically [64, 65]. This can happen, for example, in two-color fields (stimulated Compton scattering) [66] or travelling-wave configurations, as studied in Kapitza-Dirac scattering [59, 67]. In this regime, the electron experiences an effective potential given by:

$$U_p(\mathbf{r}, t) = \frac{e^2 |E(\mathbf{r}, t)|^2}{4m\omega^2}, \tag{2.2}$$

where e and m are the electron charge and mass, E is the optical field amplitude, and ω its angular frequency. Here $\mathbf{r} = (\mathbf{r}_\perp, z)$ denotes the electron trajectory, with $\mathbf{r}_\perp$ the transverse position relative to the laser focus and z the propagation coordinate. For a high-velocity, non-recoiling electron moving with constant velocity v along z, the accumulated phase

shift can be written as [65]:

$$\phi(\mathbf{r}_\perp) = \frac{1}{\hbar v} \int_{-\infty}^{+\infty} U_p(\mathbf{r}_\perp, z)\, \mathrm{d}z, \tag{2.3}$$

which modifies the electron wavefront without producing discrete energy sidebands. A monochromatic optical field therefore yields pure phase modulation, as illustrated schematically in Fig. 2.2.

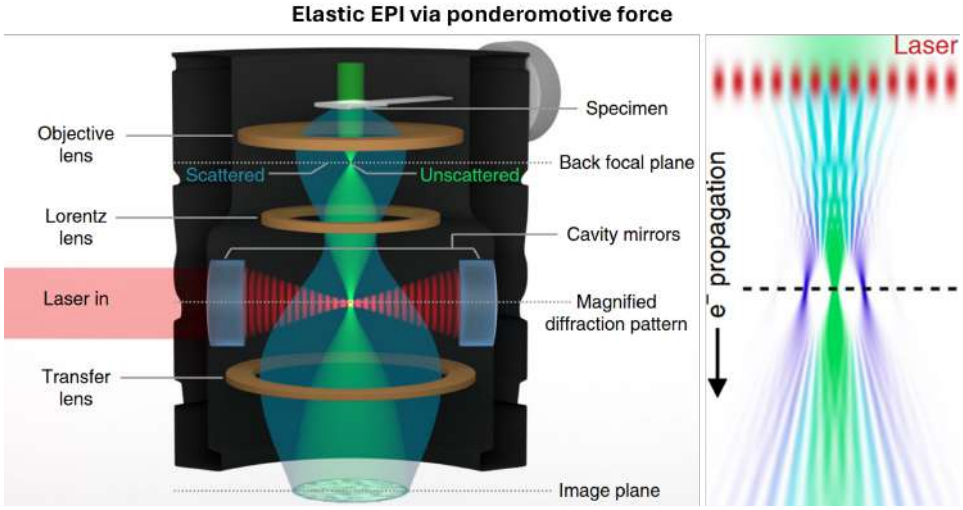

Figure 2.2: ***Elastic ponderomotive modulation.*** *An electron traversing a high-intensity optical travelling wave accumulates a cycle-averaged phase ϕ determined by the integrated ponderomotive potential. No discrete energy sidebands are generated and the effect manifests as pure phase modulation of the electron wavefront and as a spatial phase grating. Adapted from [62].*

In practice, the main limitation of ponderomotive modulation is the required optical intensity: since $\phi \propto E^2/\omega^2$, achieving phase shifts of order unity demands peak intensities in the terawatt/cm^2 range, far above those typically available in UTEM experiments [64]. For this reason, ponderomotive modulation has been explored primarily in dedicated high-field configurations, where measurable phase shifts could be obtained with tightly focused femtosecond pulses [62, 63, 65].

2.2.2 Inelastic Interaction via Optical Near Fields: PINEM

In photon-induced near-field electron microscopy (PINEM), a free electron interacts inelastically with the optical near field generated around an illuminated nanostructure. Unlike in free space, where the field has no longitudinal component, here the evanescent optical field possesses a nonzero E_z that can exchange both energy and momentum with the passing electron [15, 16, 61]. Physically, the process corresponds to the coherent absorption and emission of discrete photons from the optical mode: the electron wavefunction is split into

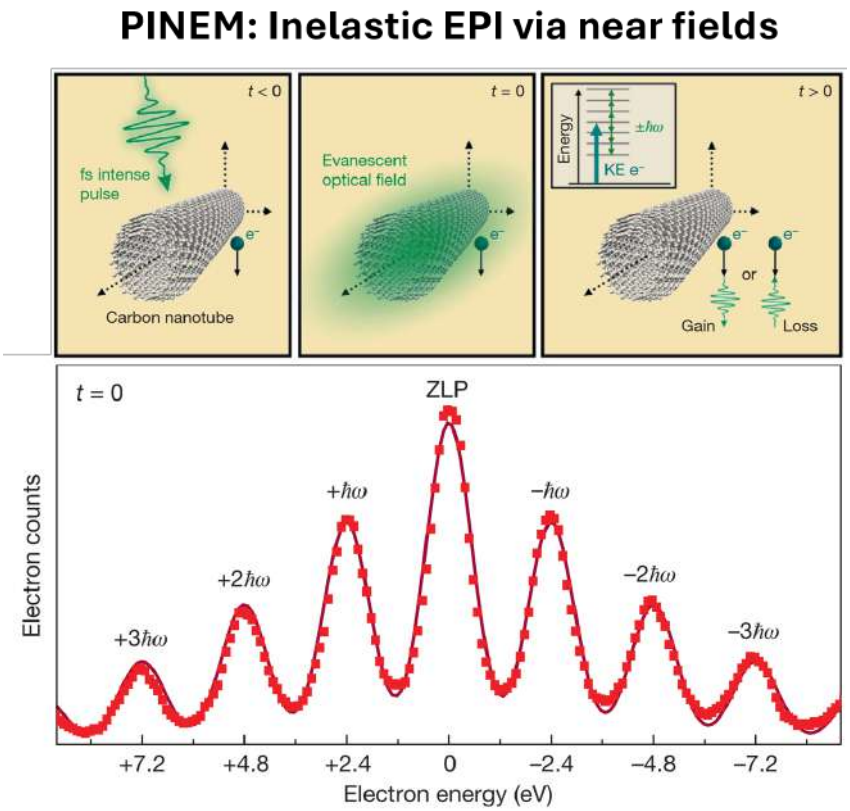

Figure 2.3: ***PINEM: near-field inelastic interaction.*** *The electron beam interacts with an evanescent optical field sustained by a nanostructure. The longitudinal component E_z enables quantized absorption and emission of photons, producing a spectrum with Bessel-distributed sidebands spaced by $\hbar\omega$ [15].*

multiple components separated in energy by integer multiples of the photon energy $\hbar\omega$, each accompanied by a corresponding change in longitudinal momentum $\Delta p_{\parallel} \approx \ell\hbar\omega/v$.

The interaction strength is described by the dimensionless coupling constant [61]:

$$g(\mathbf{r}_\perp) = \frac{e}{\hbar\omega}\int_{-\infty}^{+\infty} E_z(\mathbf{r}_\perp, z)\, e^{i\omega z/v}\, \mathrm{d}z, \tag{2.4}$$

which quantifies how efficiently the electron couples to the Fourier component of the optical field that travels synchronously with it ($k_z = \omega/v$). Here $\mathbf{r}_\perp$ denotes the transverse impact parameter relative to the nanostructure.

A few physical assumptions underlie this description. First, the non-recoil approximation ensures that the electron trajectory remains essentially straight, with the optical field acting only as a small perturbation. Second, the optical field is assumed to be monochromatic and coherent, so its time dependence is purely harmonic. Under these conditions, the electron wavefunction acquires a periodic phase factor that can be expanded using

the Jacobi–Anger identity. This expansion leads directly to a discrete ladder of sidebands separated by $\hbar\omega$, with amplitudes proportional to Bessel functions $J_\ell(2|g|)$ and probabilities:

$$P_\ell(\mathbf{r}_\perp) = |c_\ell|^2 = J_\ell^2\big(2|g(\mathbf{r}_\perp)|\big), \tag{2.5}$$

where ℓ denotes the net number of absorbed ($\ell > 0$) or emitted ($\ell < 0$) photons.

The resulting Bessel-law distribution of sidebands is the hallmark of PINEM. It directly reveals the quantized exchange of energy and momentum between the electron and the optical field and has been exploited to map plasmonic near fields, cavity excitations, and light-matter coherences with nanometer-femtosecond spatiotemporal resolution [15, 49, 52, 68]. An illustration of this process is shown in Fig. 2.3. While Eq. (2.4) relates the sideband populations directly to the longitudinal electric field, obtaining quantitative values for $E_z(\mathbf{r}_\perp)$ in a specific geometry usually requires full electromagnetic simulations [16, 61].

2.2.3 Inelastic Interaction at Interfaces via Stimulated Inverse transition Radiation

An alternative route for inelastic EPI exploits transition radiation (TR), the emission produced when an electron traverses a dielectric boundary, which enforces continuity of the electromagnetic fields [69]. In the inverse process, i.e. stimulated inverse transition radiation (ITR), a pre-existing coherent optical field impinging on the interface is scattered into the electron mode, enabling quantized energy–momentum exchange [25, 59, 67]. The resulting electron spectrum again follows a Bessel distribution, as in PINEM, but the origin of the longitudinal field is different: in ITR it is set by the macroscopic boundary conditions at the interface rather than by a confined plasmonic near field [22, 44, 50, 70, 71].

A key feature of stimulated ITR is that the phase of the incident optical field is directly imprinted on the electron wavefunction. This means that, unlike in PINEM where the near-field response of a specific nanostructure must be modeled, in ITR the final electron distribution can be predicted from the optical field at the interface. As a consequence, if the optical beam is shaped—for example with a spatial light modulator (SLM)— its transverse phase profile is faithfully transferred to the electron wavefunction. The far-field diffraction of the electrons then corresponds to the Fourier transform of the imposed optical pattern, a principle that underlies recent demonstrations of high-purity wavefunction modulation and single-pixel imaging with structured electron probes [28]. An illustration of this process is given in Fig. 2.4

Formally, both PINEM and ITR are described by the same coupling parameter [Eq. (2.4)]. In both phenomena, the exponential factor $e^{i\omega z/v}$ reflects the fact that the electron samples the optical field along its trajectory at velocity v. As a result, the interaction is sensitive only to the component of the optical field that is synchronous with the electron

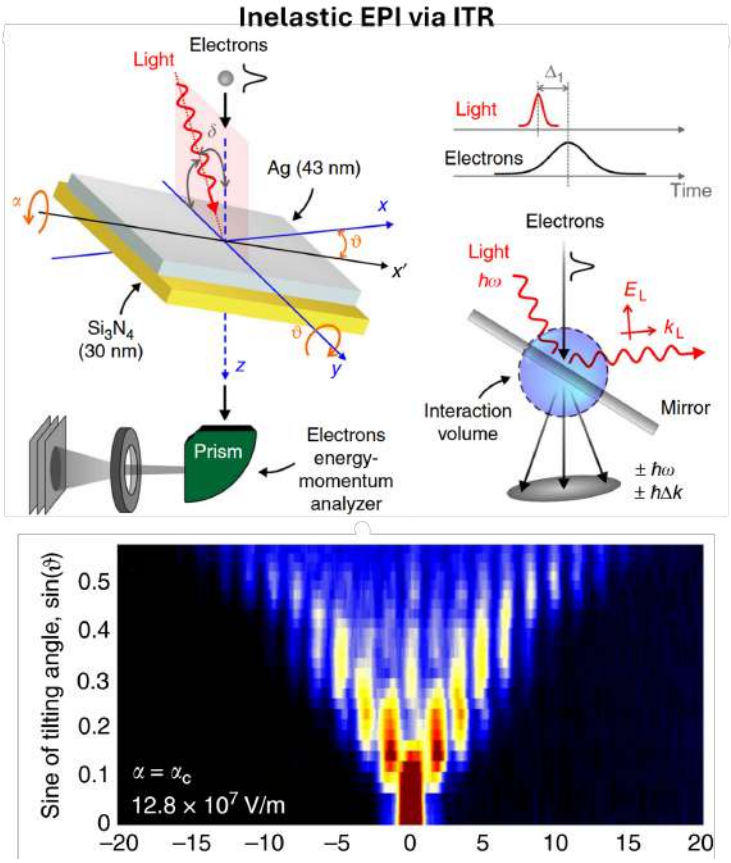

Figure 2.4: ***Stimulated ITR at a dielectric interface.*** *When an electron crosses a thin membrane illuminated by a coherent laser field, inverse transition radiation provides the longitudinal field component needed for coupling. Here, the phase of the incident optical field is directly imprinted on the electron wavefunction. Schematic adapted from Vanacore et al. [50].*

motion, i.e. the spatial Fourier component with longitudinal wavevector $k_z = \omega/v$. This component, provided by the surface or the nanostructure near field, is what enforces the discrete ladder of sidebands in both PINEM and ITR [16, 50, 72].

2.3 Charge-Dynamics Electron Microscopy

The interactions discussed so far describe the direct coupling of free electrons to optical near fields, where energy and momentum are exchanged coherently with the light field itself. At higher fluences and on longer timescales, however, the absorbed optical energy can drive the emission of a dense cloud of photoelectrons from a metallic surface. The resulting distribution of emitted and screening charges generates a transient field dominated by low-frequency electric components, which subsequently act back on the probing electrons. In this regime, the interaction is light-induced but collective: the probe no longer

couples to an optical near field, but to a space- and time-dependent field generated by the motion and screening of photoexcited carriers. This phenomenon underlies the so-called plasma-lensing effect [73] and forms the basis of Charge-Dynamics Electron Microscopy (CDEM) [74].

To describe this process quantitatively, one considers a metallic film irradiated by a femtosecond laser pulse at high fluence, where multiphoton photoemission releases electrons into vacuum and initiates an expanding electron gas above the surface [75].

The instantaneous charge distribution $\rho(\mathbf{r}, t)$ determines an electric potential $\Phi(\mathbf{r}, t)$ through Poisson's equation:

$$\nabla^2 \Phi(\mathbf{r}, t) = -\frac{\rho(\mathbf{r}, t)}{\varepsilon_0}, \tag{2.6}$$

whose associated field deflects nearby probe electrons. Under paraxial and thin-lens (impulsive) conditions commonly used to model ultrafast beam-field interactions in the TEM, the small-angle deflection at position x and delay t reads:

$$\theta(x, t) \simeq -\frac{e}{p_z} \int \frac{E_x(x, z, t)}{v_z}\, dz, \tag{2.7}$$

which connects the measured angular response to the path-integrated transverse field [73, 74].

The evolving charge distribution produces a time-dependent "plasma lens" for the probe. At early delays, repulsion from the dense negative charge sheet leads to defocusing. As the gas dilutes and positive surface charges (image charges) dominate the local field, the sign of the lens can invert, yielding transient focusing. This lensing picture and its realization inside a transmission electron microscope were established by Zandi *et al.* [73], who showed that the evolving electron gas acts as a tunable lens whose effective focal length changes with pump-probe delay and microscope optics. The relevant fields lie predominantly in the low-THz band and are quasi-electrostatic on the probe timescale, consistent with a collective, charge-generated origin [74].

Building on this concept, Madan *et al.* developed CDEM, a UTEM modality that extends the plasma-lensing approach by measuring both the angular broadening and the energy change of the probe as functions of delay and impact parameter [74]. By combining these two observables, the authors reconstructed the temporal evolution of charge emission, expansion, screening, and reabsorption near metallic nanostructures. Figure 2.5 illustrates this sequence: a femtosecond laser pulse excites a gold nanostructure, leading to the emission of electrons and the build-up of a transient field that expands, slows down, and is eventually reabsorbed. The lower panels show the spatial dependence of the measured probe energy shift at successive time delays, revealing alternating acceleration and deceleration regions that reflect the polarity and temporal evolution of the field. These results provide a direct visualization of the microscopic mechanisms governing charge motion on the picosecond scale, bridging ultrafast optics and electron microscopy. Earlier deflection-based measurements of quasi-static fields in laser-plasma and pump-probe electron experiments predate their implementation inside the TEM column [76, 77], but the

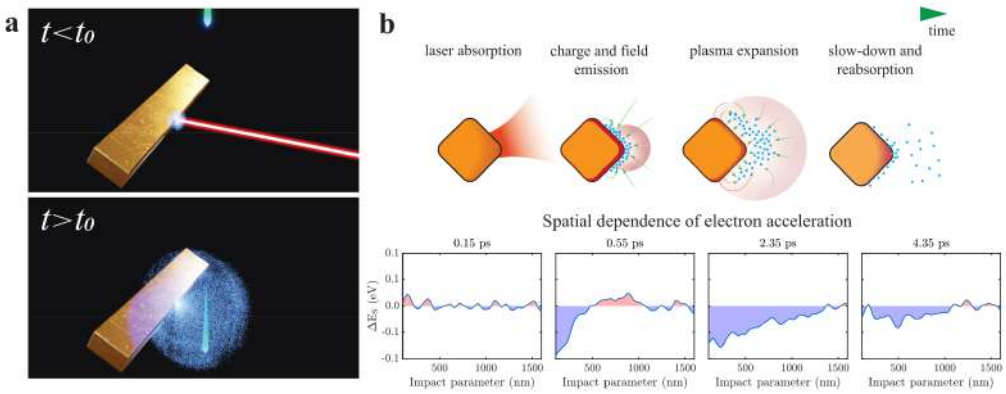

Figure 2.5: Charge-Dynamics Electron Microscopy (CDEM) and plasma-lensing dynamics. ***(a)*** *Illustration of the pump–probe geometry: a femtosecond laser pulse excites a metallic bar, releasing a cloud of electrons that expands into vacuum and generates a transient electric field. A delayed electron probe pulse traverses this evolving field, experiencing angular and energy modulation.* ***(b, top)*** *Schematic sequence of the process, from laser absorption to charge emission, plasma expansion, and reabsorption.* ***(b, bottom)*** *Measured spatial dependence of the probe energy shift at different delays, showing alternating acceleration and deceleration regions that reveal the polarity and temporal evolution of the field. Adapted from [74].*

TEM realization is what enables correlation with nanoscale imaging and spectroscopy [73, 74].

For ultrafast electron microscopy, the distinction from direct light-electron coupling (e.g., PINEM and ITR) is operational. In PINEM, the probe exchanges quantized energy with a laser-defined near field, producing a symmetric energy-sideband spectrum with zero net energy shift for monochromatic fields. In CDEM, the probe couples to a low-frequency field generated by nonequilibrium charges; the spectrum becomes asymmetric and exhibits a sizable net energy change alongside angle variations, reflecting the underlying charge transport and screening [74]. Practically, plasma lensing and CDEM are valuable for establishing spatiotemporal overlap, diagnosing pump-induced charging, and visualizing carrier dynamics relevant to UTEM beam shaping. In the point-projection configuration used later in this thesis, the spatial derivative $d\theta/dx$ provides a route to retrieve the charge density integrated along the probe path, thereby linking image contrast to the evolving electrodynamic environment at the specimen.

2.4 Light-Driven Electron Beam Shaping

This section builds upon and re-elaborates the overview of e-beam shaping presented in two of our works: Section 12 of Ref. [24] and the introduction of Ref. [78]. Together, these contributions trace the evolution from static, nanofabricated phase elements toward light-driven, reconfigurable control of the electron wavefunction within UTEM.

The field of e-beam shaping took off in 2010 with two pioneering demonstrations of e-beams carrying orbital angular momentum where helical phase fronts were generated using nanoscale holographic masks [79, 80]. These works inaugurated a new paradigm in transmission electron microscopy, showing that the wavefront of free electrons could be structured analogously to that of light. Subsequent advances extended this concept to a wide range of spatial modes and phase distributions, enabling the realization of tailored probes for magnetism, chirality, and beam-matter coupling studies [81]. To improve versatility, programmable phase plates employing slowly varying electrostatic and magnetostatic fields were later introduced, providing continuous tunability of the electron phase without physical mask replacement [13, 82]. These developments established the groundwork for dynamic electron-optical control, but the achievable complexity remained constrained by the number of controllable electrostatic elements and the static nature of the hardware.

Electron-photon interaction in UTEMs, discussed in Sec. 2.2, offered a radically different route for shaping. Here, coherent optical fields can imprint spatiotemporal modulations directly onto the electron wavefunction through quantized or ponderomotive coupling. Initially developed for probing photoexcited dynamics [12, 30, 32], EPI has evolved into an enabling mechanism for programmable beam shaping [23, 83]. In this picture, the optical field acts as an ultrafast phase plate whose structure can be dynamically reconfigured by shaping the laser wavefront, polarization, or temporal profile.

Several experimental strategies have been explored to realize such modulations, targeting either the longitudinal (energy-time) or transverse (momentum-space) degrees of freedom. Longitudinal modulation has been achieved through optical parametric amplification (OPA) [19], two-wave mixing [64], and dielectric laser acceleration (DLA) [84], each enabling the formation of attosecond electron pulse trains or energy-chirped beams. Conversely, SLMs [22, 63], nanoconfined near fields [20, 21], and resonant optical cavities [62] have enabled transverse shaping, controlling the phase and amplitude of the beam in reciprocal space. Together, these methods illustrate a growing unification between optical and electron optics: the former provides the field templates, the latter the high-resolution carrier of those modulations.

Focusing on *transverse* e-beam shaping, two regimes of electron-photon coupling can be exploited for e-beam shaping in UEM: elastic ponderomotive modulation (Sec. 2.2.1) and quantized inelastic scattering (Secs. 2.2.2 and 2.2.3). In the ponderomotive regime, the optical field, pre-shaped with an SLM, acts as a light-induced phase plate that can imprint transverse phase gradients without any material interface [29, 63, 85]. This approach offers a non-invasive control of the transverse wavefront through structured light fields. However, since the modulation arises from the optical intensity gradient, it modifies only the phase of the electron wavefunction, without affecting its amplitude distribution.

To achieve full amplitude-and-phase control of the transverse electron distribution, one must access the longitudinal-field-mediated regime, where electrons interact with optical fields possessing a component parallel to their propagation direction. This condition is realized near interfaces or structured optical modes, where Maxwell's equations allow

non-zero longitudinal fields. Such coupling, realized in PINEM and ITR, enables quantized energy-momentum exchange between light and electrons, permitting both amplitude and phase modulation of the transverse wavefunction.

In PINEM (see Sec. 2.2.2), the interaction is mediated by the optical near field of a nanostructure, often a plasmonic antenna, which locally satisfies the velocity-matching condition [15, 16, 20, 21, 61]. The near field maps its complex amplitude onto the transverse electron distribution, imprinting both phase and intensity modulations that mirror the spatial structure of the underlying optical mode. While this process allows detailed mapping of localized electromagnetic fields, it constrains flexibility: the resulting electron profile depends on the geometry and resonances of the nanostructure, making arbitrary shaping impractical. This limitation has motivated a transition toward regimes where the interaction field can be fully determined by the external optical setup.

Stimulated ITR (see Sec. 2.2.3) provides such a configuration, enabling deterministic and tunable transverse shaping [22, 26, 44, 50, 70, 71]. In ITR, the e-beam exchanges energy and momentum with the incident optical field to satisfy boundary continuity, such that the phase of the optical field is directly imprinted onto the electron wavefunction. As a result, the intensity distribution of the e-beam basically corresponds to the Fourier transform of the structured optical field [28]. Recently, Madan *et al.* [22] demonstrated electron modulation mediated via inelastic EPI based on ITR using light pre-shaped by an SLM. In that work, the interaction was still occurring at the sample plane, where the light-reflective and electron-transparent membrane used to mediate ITR was placed. Nevertheless, the authors foresaw a future technological implementation of a pre-sample PELM. This would be done by adding a new EPI interaction point in a pre-sample stage along the TEM column. Different types of modulation can be then achieved by exploiting the multiplicity of phase patterns that can be imprinted on the SLM. In this thesis, we present the first experimental implementation of this PELM device, integrated within the condenser system.

Beyond the demonstration of programmable control, transverse beam shaping enables practical gains for materials investigations. Mode-selective momentum probes prepared by optical phase modulation can increase sensitivity to targeted scattering vectors and symmetries, including chiral responses [26, 44]. Dose-efficient imaging and spectroscopy are enabled by single-pixel schemes that exploit programmable masks in the electron channel [28]. Moreover, optical modulation of free electrons acts as a reconfigurable phase plate within the TEM optics, providing routes to contrast tuning and spatial-resolution benefits [29]. Within this framework, placing the modulator upstream of the specimen allows alignment, filtering, and demagnification of structured probes prior to interaction, setting the stage for the experiments developed in Chap. 4 and 5.

Chapter 3

UTEM Implementation at UniMiB

This chapter presents the technical realization of the UTEM developed at the University of Milano-Bicocca. The main goal of this implementation was to integrate the Photonic-based free-Electron Modulator (PELM) within the microscope column, enabling programmable, light-induced modulation of the electron wavefunction before its interaction with the sample.

To achieve this, a commercial JEOL JEM-2100 microscope was extensively modified. A femtosecond laser source was coupled to the column through custom optical ports, and a dedicated PELM interaction stage was implemented upstream of the sample plane. A spatial light modulator (SLM) was introduced to enable programmable optical shaping, and specific attention was given to achieving and monitoring the spatiotemporal overlap between electron and laser pulses. High-resolution diffraction and imaging capabilities were ensured by a direct electron detector optimized for low-flux operation.

The following sections introduce the laser system and optical layout, describe the mechanical and vacuum integration of the optical access ports, the design and operation of the PELM stage and the procedures for calibrating and characterizing the performance of the direct detector. Finally, the alignment and optimization steps required to achieve stable and reproducible conditions are presented. Together, these developments constitute the experimental platform employed for the e-beam-shaping experiments discussed in Chapters 4 and 5.

3.1 Laser System and Light Shaping Module

A central component of the UTEM platform is the femtosecond laser system, which provides the optical pulses used both for photoemission and for the modulation of the free-electron wavefunction. This section describes the laser source, the branching and routing of the beam to each interaction plane and the programmable SLM.

3.1.1 Laser Source and Beam Path

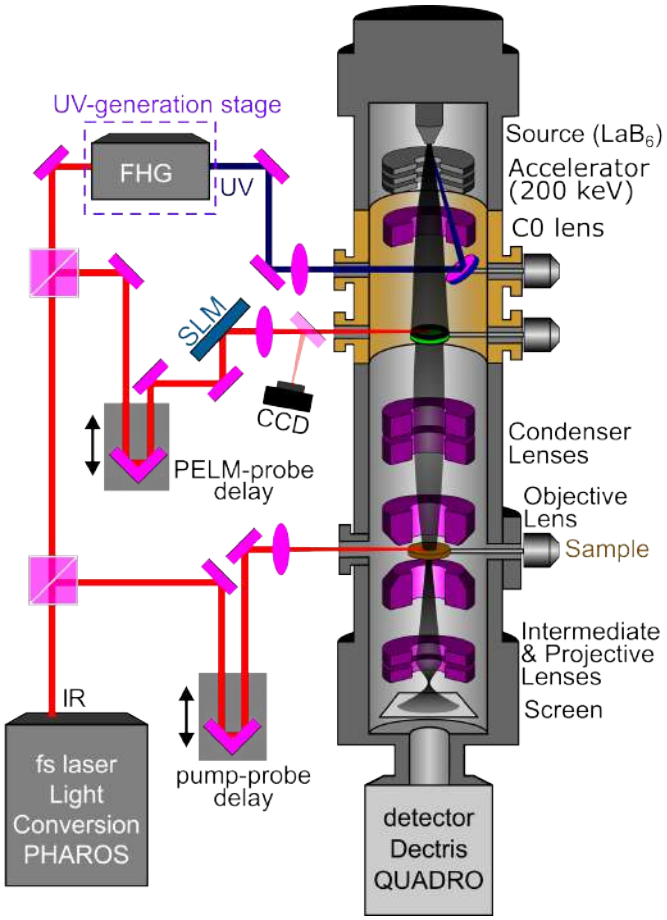

Figure 3.1: Schematic layout of the UTEM setup. A PHAROS femtosecond laser provides UV pulses for photoemission and IR pulses modulated by a spatial light modulator (SLM) for transverse e-beam shaping. A third IR branch, directed to the sample plane, is introduced via the EDX port to perform pump-probe experiments.

The optical source driving the UTEM setup is a Yb-based PHAROS femtosecond laser (Light Conversion), emitting 1030 nm pulses with 300 fs duration, a maximum power of 10 W, and a repetition rate tunable up to 1 MHz. The beam quality is rated as $M^2 = 1.2$.

The output laser pulse was initially split into two branches to realize the PELM pump-probe setup: a UV path generating photoelectrons at the photocathode and an IR path directed to the PELM stage for pre-sample modulation of the e-beam. This two-branch configuration enabled the first experimental demonstration of programmable electron shaping using an SLM, as reported in Chap. 4. Later, a third branch was implemented to enable pumping at the sample plane, allowing the shaped e-beam to probe specific photoinduced excitations. Temporal synchronization between the optical and electron pulses is achieved by a motorized delay line placed on the IR path. An overview of the complete optical routing system, including all three branches, is shown in Fig. 3.1.

The UV branch is generated by frequency quadrupling the 1030 nm output to 257 nm using two cascaded nonlinear crystals. The beam is then directed and focused with a 100 cm focal-length lens onto the LaB_6 photocathode to generate single-electron pulses via photoemission. Its power is tuned using a graded neutral-density (ND) filter.

The remaining IR beam forms the modulation branch. It is directed through a motorized delay stage equipped with a retroreflector, which adjusts the optical path length to synchronize the IR and UV pulses at the PELM plane. The IR beam fluence is then adjusted with a graded ND filter and the wavefront is shaped via the SLM (Sec. 3.1.2). The IR light is p-polarized with respect to the PELM film to maximize the photon-electron interaction [22], and it is focused using a 50 cm focal-length lens.

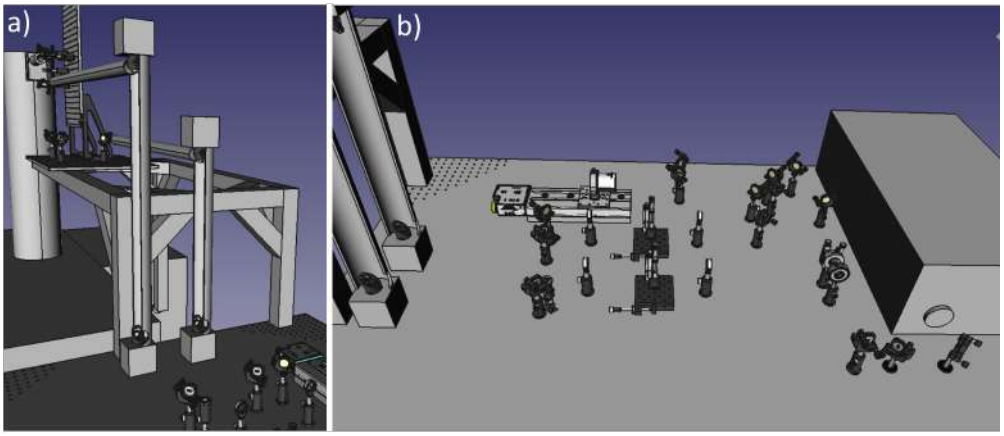

Figure 3.2: CAD drawings of the laser routing system implemented at UniMiB. a) Periscopes and upper breadboards guiding the UV and IR beams from their respective periscopes to the PELM injection window. Both designs were realized in FreeCAD by the author. b) Main optical table with the PHAROS laser, delay line and frequency conversion system.

Finally, the UV and IR beams are directed to separate custom-built periscopes that elevate them closer to the correct injection height (see fig. 3.2a). Final delivery into the microscope, shown in Fig. 3.3, is achieved via a vertical breadboard mounted on a horizontal breadboard on a custom support structure that bridges the optical table and the

TEM body. This breadboard hosts the final optical components, including the SLM, mirrors, waveplates, and focusing optics. The UV and IR beams enter the microscope after a second, smaller periscope enclosed in a leaded box. This is needed to avoid dangerous X-ray radiation to exit the microscope. To optimize design and alignment, the complete optical routing system was modeled in FreeCAD prior to implementation (Fig. 3.2).

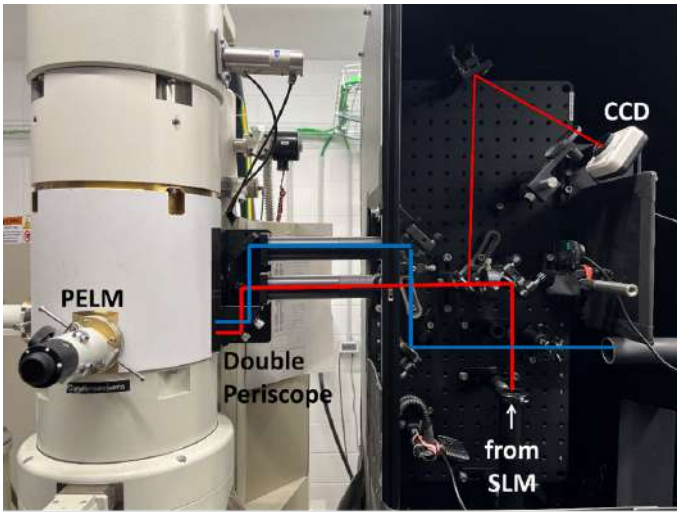

Figure 3.3: Photograph of the optical access to the UTEM column. The infrared (IR, red path) and ultraviolet (UV, blue path) beams are delivered to the PELM interaction stage through a custom double periscope system integrated into the microscope. The IR beam, shaped by the SLM, drives the electron-photon interaction at the PELM film. The UV beam is directed to the photocathode for electron generation. A CCD camera is positioned on the optical breadboard to monitor the incoming beam profiles and ensure stable alignment.

Figure 3.4: Photograph of the optical access implemented at the sample plane in the UTEM setup. The pump beam is injected through the EDX port using a periscope and beam-shaping optics.

While the interaction at the PELM plane imprints the desired wavefront modulation on the e-beam, it does not excite the specimen itself. Instead, this modulation stage prepares

the electron probe that will later interrogate photoexcited materials placed at the sample plane. To enable this pump-probe experiments with shaped electrons, a third IR branch was later added after the initial beam split. This new path is routed independently to the sample plane and includes its own motorized delay line, enabling control over the relative timing between the sample pump and the shaped electron probe. The pump beam can be used either at 1030 nm or after frequency doubling to 515 nm, with separate fluence and polarization control. Optical access to the sample is achieved through the energy-dispersive X-ray (EDX) port, equipped with a leaded glass viewport. The final routing into the sample region includes a periscope, a 1:3 beam expander, and a 20 cm focal length lens, as illustrated in Fig. 3.4.

Figure 3.5: ***a)*** *Laboratory room before the installation of the UTEM setup, at the start of my PhD.* ***b)*** *Large view of the complete UTEM setup at UniMiB. The femtosecond laser system (right) is optically coupled to the modified transmission electron microscope (left) via a custom-designed routing system including periscopes and breadboards.*

Figure 3.5 shows an overview of the laboratory evolution and the final implementation of the UTEM system. Panel (a) depicts the empty room at the start of the my PhD, before the installation of any optical or mechanical components. Panel (b) illustrates the completed setup, where the femtosecond laser system is coupled to the modified TEM column through a fully integrated routing assembly designed and built during this work. The image highlights the scale of the experimental platform and the extent of the modifications required to realize a fully operational PELM-equipped UTEM.

3.1.2 Spatial Light Modulator

The transverse profile of the modulation pulse is shaped using a phase-only SLM. The SLM is integrated in the laser line on the horizontal upper breadboard, as shown in Fig. 3.6 The device is a HOLOEYE Pluto-2.1 reflective panel based on liquid crystal on silicon (LCoS). It has 1920×1080 pixels with an $8\,\mu$m pitch. Each pixel acts as a tunable phase retarder that can impose a local phase shift between 0 and 2π depending on the applied gray level.

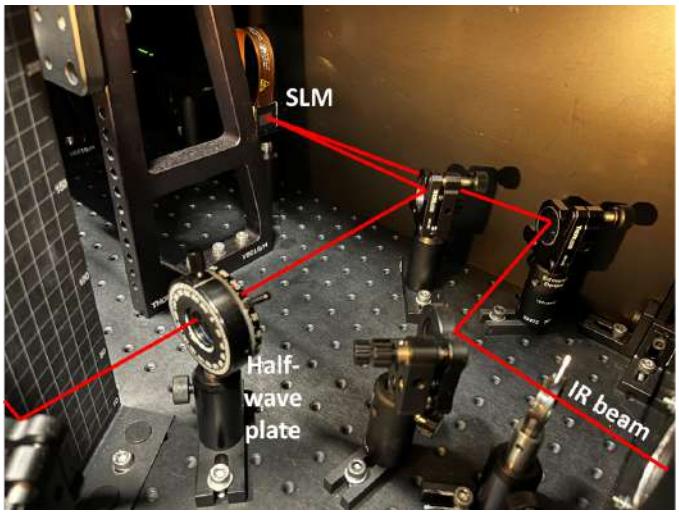

Figure 3.6: Photograph of the SLM integrated into the UTEM setup on the upper horizontal breadboard. The infrared beam is shaped by the SLM and then directed toward the the vertical breadbourd shown in Fig. 3.3. The compact geometry ensures mechanical stability and beam delivery within the TEM column.

The liquid crystals respond to the applied voltage by changing their tilt angle and effective refractive index. This modulates the phase of the reflected beam. The device is optimized for the 650-1100 nm range, and the 1030 nm beam is set to p-polarization and a 7° incidence angle to maximize efficiency.

In free space, the SLM-modulated phase pattern becomes an intensity pattern at the Fourier plane. This plane is optically conjugated to the PELM film. Examples of beam

shaping include lateral shifts (via blazed gratings), split beams, and Hermite-Gaussian modes. These profiles were used to control the momentum distribution of the e-beam via ITR (Sec. 2.2.3), transferring the maturity and flexibility of light modulation technologies to the electron domain.

3.2 TEM Column Modifications

To implement programmable pre-sample e-beam shaping, the TEM column was extensively modified. Two dedicated components, shown in Fig. 3.7, were added upstream of the standard condenser system: i) a custom column section hosting the PELM stage, which provides the interaction plane between the e-beam and the structured optical field, and ii) an auxiliary condenser lens (C_0), designed to control the beam coherence at the modulation plane.

In the following, we describe the design of the PELM section and the integration of the C_0 lens, highlighting their respective roles in establishing a stable and tunable platform for EPI.

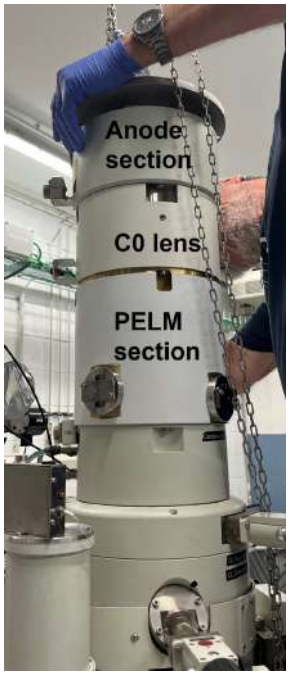

Figure 3.7: Modified TEM column at UniMiB. The additional modules installed upstream of the condenser system include the PELM section, which hosts the thin-film interaction stage and optical access ports, and the C_0 lens, which provides control over beam coherence at the modulation plane. Above them, the original anode section of the JEOL JEM-2100 microscope is visible. This assembly illustrates the physical integration of the new components into the commercial column.

3.2.1 PELM Section and Optical Access

The PELM is the core element enabling programmable shaping of the electron wavefunction before the sample plane. Its operation relies on the interaction of the e-beam with a structured optical field at a thin metallic film through the mechanism of ITR. A detailed discussion of the physical principles is provided in Sec. 2.2.3; here we focus on the device implementation.

To accommodate the PELM stage, a custom stainless-steel column section was designed and installed upstream of the JEOL JEM-2100 condenser system, illustrated in Figs. 3.8 and 3.9. This module integrates (i) a vacuum window for laser injection, (ii) an aluminum mirror at 45° to direct the UV beam toward the photocathode, and (iii) a holder for the thin film that mediates the ITR interaction. The lateral window provides optical access for both the UV beam, used for photoemission at the LaB_6 cathode, and the pre-shaped IR beam, used to modulate the e-beam at the PELM plane.

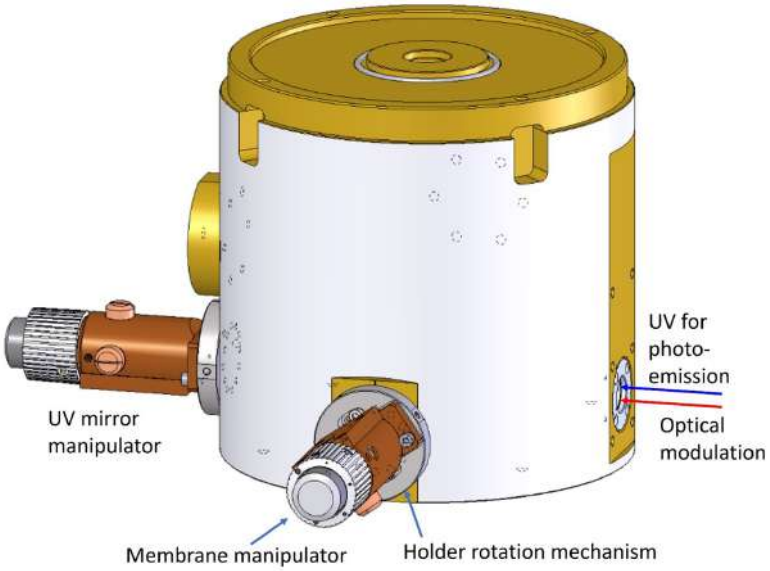

Figure 3.8: CAD model of the custom TEM column section housing the PELM platform at UniMiB. The module combines optical injection, UV redirection, and the micromanipulator stage for the thin-film interaction.

Both the mirror and the PELM stage are equipped with micromanipulators that allow precise positioning under vacuum. The PELM holder also includes a rotation mechanism for angular alignment, operable without breaking the vacuum. The design was optimized through multiple iterations to satisfy the space constraints of the JEM-2100 TEM column while preserving unobstructed beam paths. Magnetic shielding and custom mechanical mounts were added to ensure compatibility with TEM operation and optical stability once the column is closed.

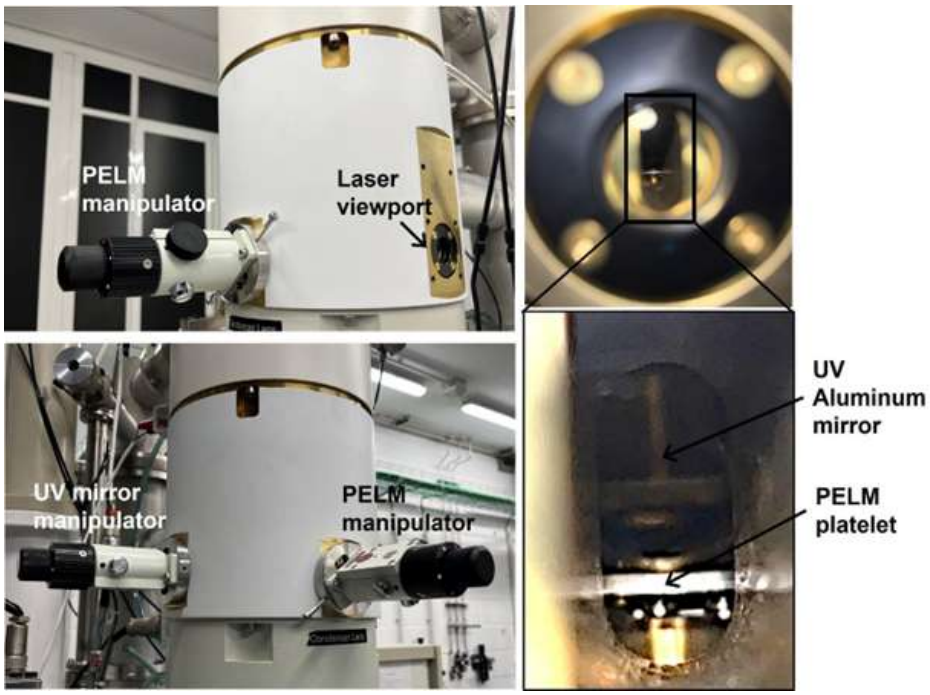

Figure 3.9: Photographs of the PELM section integrated into the UTEM column. ***Top left:*** *PELM manipulator and laser window (or viewport).* ***Bottom left:*** *PELM and UV mirror manipulators on the opposite side of the column.* ***Top right:*** *view of the laser injection window.* ***Bottom right:*** *close-up showing the UV aluminum mirror and the PELM-stage platelet inside the column.*

3.2.2 C_0 Condenser Lens: Source Imaging and Coherence Control

The introduction of the C_0 condenser lens in the modified TEM column is essential to restore conventional TEM operation after the physical extension of the column caused by the PELM section integration. The C_0 is a magnetostatic lens consisting of an electromagnetic coil as the other condenser lenses. During standard TEM operation—whether for imaging, diffraction, or alignment—this additional lens collects and collimates the divergent e-beam, which would otherwise be too spread to be captured by the regular condenser system due to the increased source-to-lens distance.

The lens is controlled by a dedicated power supply. For conventional operation, it is typically driven slightly offset from its optimal excitation current, experimentally determined by the peak in beam transmission shown in Fig. 3.10. This offset is a necessary compromise between maximizing the beam current at the sample plane and minimizing aberrations that would degrade image quality. The specific setting is determined for each experiment, depending on the required balance between signal intensity and resolution.

Beyond restoring standard TEM operation, the C_0 lens also provides a flexible control parameter for tuning the electron-beam convergence and, consequently, its transverse coherence. By operating the lens in a much weaker excitation regime, the e-beam remains

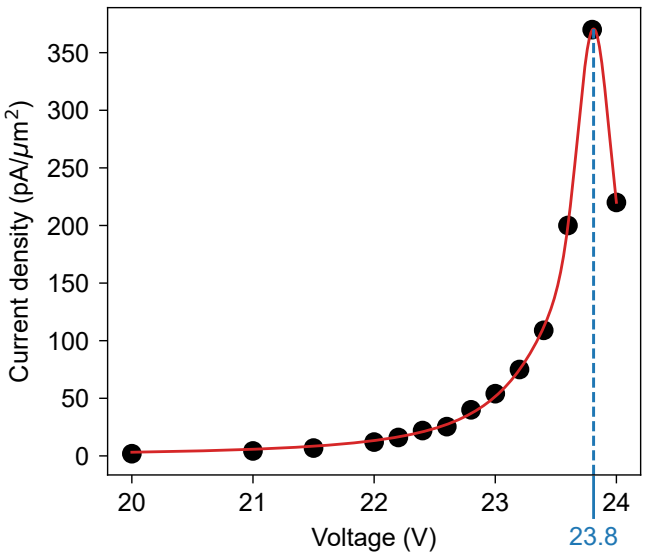

Figure 3.10: Calibration of the C_0 lens. The e-beam current density on the phosphor screen is shown as a function of C_0 lens excitation voltage, with the resonance voltage measured at 23.8 V. In standard TEM mode, we operate C_0 close to its resonance (typically 22.5 V). In e-beam shaping experiment, the operation voltage lies well below this resonance point (typically 15 V)

highly divergent at the 3 mm opening of the PELM stage. The opening then behaves as a condenser aperture and selects only electrons with nearly identical emission angles resulting in a high transverse coherence e-beam. This setup is used for e-beam shaping at the PELM plane (Chaps. 4 and 5), where maintaining a good transverse coherence becomes critical to enable quantized EPI, as detailed in Sec. 4.1. With this setting, only highly coherent electrons interact with light via ITR at electron-transparent film, which is mounted at the PELM plane.

3.3 Electron Detection and Characterization

The UTEM setup includes a Dectris QUADRO direct electron detector, a hybrid pixel device combining high sensitivity with single-electron counting capability. The detector exhibits zero dark noise and a high detective quantum efficiency even at very low electron flux, making it particularly suited for the low-dose conditions typical of ultrafast experiments. Such characteristics are essential not only to detect weak signals but also to preserve the spatial fidelity of individual electron events, which becomes critical in beam-shaping measurements.

Resolving the small angular deflections imparted by EPI requires that the detector preserves high spatial-frequency information. As shown in Chapter 4, these deflections correspond to weak intensity redistributions extending over only a few tens of pixels on

the detector plane. If a single-electron event spreads across too many pixels, the resulting overlap would smear the modulation and prevent the detection of the interaction. In practice, this means that the detector's point-spread function (PSF) must be narrow and its modulation transfer function (MTF) must remain high over the relevant spatial frequencies, so that signal-induced modulations spanning only a few pixels are not blurred or lost.

For this reason, a detailed characterization campaign was performed to quantify the detector's PSF and MTF under different illumination and acceleration-voltage conditions. These measurements assess the detector's ability to preserve fine spatial features and to capture weak modulations induced by the PELM. The following subsection presents the detector architecture and working principle, while the subsequent ones describe the methods used for MTF and PSF extraction and the results obtained under various operating conditions.

3.3.1 Overview of the Detector System

Hybrid pixel detectors have become the reference technology for electron detection in modern UTEMs. They are designated as "hybrid" because the sensor and the readout electronics are distinct components, fabricated on different wafers using different technologies. These two parts are subsequently connected via "bump-bonding" (typically using indium or tin microspheres), resulting in a detector structure where every pixel of the sensor is coupled one-to-one to a dedicated pixel of the readout chip. This hybridization is crucial as it allows for the independent optimization of both components: the sensor material can be selected to maximize energy sensitivity or efficiency without the constraints of standard CMOS manufacturing, while the application-specific integrated circuit can be designed with sophisticated per-pixel electronics for counting, time-over-threshold measurements, or noise suppression [86, 87].

This architecture, shown in Fig. 3.11, provides several advantages compared to scintillator-based charge-coupled device (CCD) and CMOS cameras: negligible dark current, absence of scintillator blur, single-electron sensitivity, and strong radiation hardness [88, 89]. These properties are crucial for UTEM applications, where electron counts per frame are intrinsically low, as detailed in Sec. 2.1. Direct detection also ensures a very high dynamic range, preventing saturation and radiation damage even under focused or thermionic illumination, and allowing safe switching between photoemitted weak-beam and thermionic bright-beam operation.

The working principle is schematically illustrated in Fig. 3.12. An incoming electron penetrating the semiconductor sensor produces a cascade of electron-hole pairs, which are collected by the bump-bond connections linking each pixel to its front-end electronics. The resulting charge pulse is amplified, compared with a preset threshold, and then digitally counted by the read-out integrated circuit. The hybridization between the sensor and the read-out chip allows independent optimization of their materials and geometries,

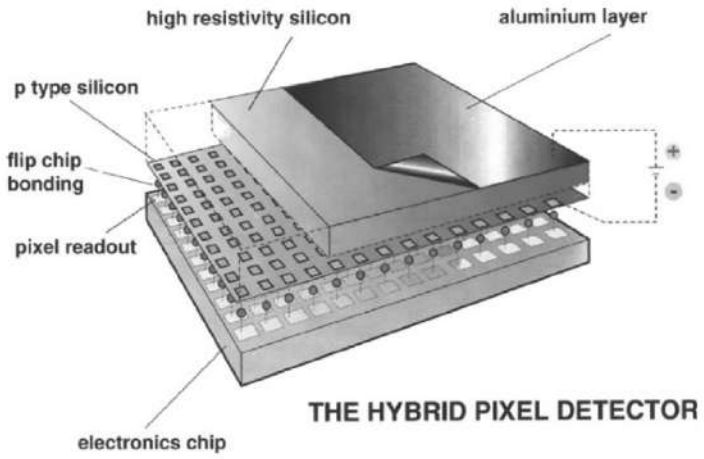

Figure 3.11: Schematic design of a hybrid pixel detector, showing the connection between the sensor layer and the front-end electronics via bump bonds. Image from Ref. [86]

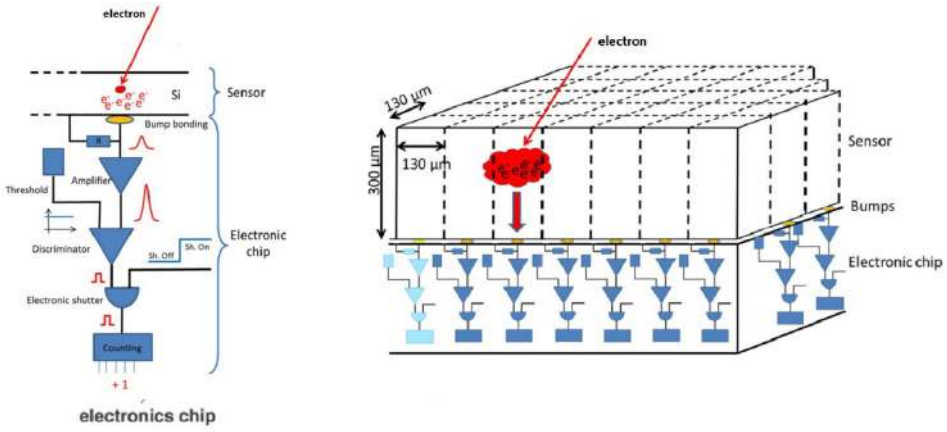

Figure 3.12: Schematic representation of the working principle of a hybrid pixel detector. Images form Ref. [87]

maximizing detection efficiency and speed.

3.3.2 Detector Characterization Methods

To quantitatively evaluate the spatial resolution and imaging performance of a direct electron detector, the MTF is the most commonly used figure of merit [88, 90]. The MTF quantifies how well the detector preserves the contrast of features at different spatial frequencies. In this work, we evaluated the MTF using two independent methods: the knife-edge technique and a low-dose cluster-based analysis.

MTF from Knife-Edge Method

In the knife-edge method straight-edged object is placed at the sample position and an image is acquired. Fig. 3.13 shows the typical image obtained in this configuration. From the image it is possible to extract the so-called edge spread function (ESF). The latter is the one-dimensional profile orthogonal to the edge. To avoid aliasing, the ESF must be oversampled [89]. This is achieved by slanting the knife edge a few degrees off with respect to the pixel rows and by following the procedure described below and schematically depicted in Fig. 3.13. Each row of Fig. 3.13 is considered as a single ESF(x), where the x-values are the discrete pixels.

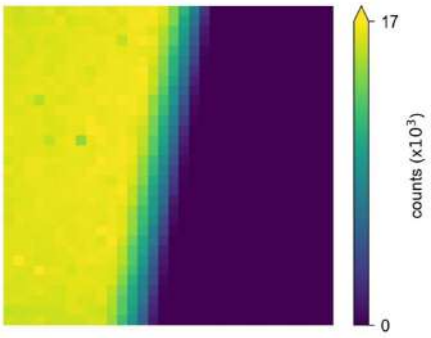

Figure 3.13: Typical knife-edge image recorded on the QUADRO detector

First, the location of the edge must be estimated with sub-pixel accuracy. For this purpose, the ESF of each column is fitted to an error function [91], defined as:

$$\mathrm{ESF}_{\mathrm{fit}}(x) = \frac{A}{2}\left[1 + \mathrm{erf}\left(\frac{\mu - x}{\sigma}\right)\right], \tag{3.1}$$

where A is the amplitude, μ is the inflection point, and σ is the standard deviation of the distribution.

The edge location is defined as the inflection point μ of the fitted curve. Each ESF is then shifted by its associated μ, and the oversampled ESF is obtained by merging all the shifted ESFs into a single dataset. This procedure is schematically represented in Fig. 3.14. The oversampled ESF obtained from this method is shown in Fig. 3.15.

The next step to obtain the MTF is to compute the first derivative of the ESF, also called the Line Spread Function (LSF).

$$\mathrm{LSF}(x) = \frac{d}{dx}\,\mathrm{ESF}(x). \tag{3.2}$$

Since standard differentiation algorithms require equally spaced datapoints, while the oversampled ESF does not satisfy this condition, the ESF is first fitted with Eq. 3.1 and then remapped on an equally spaced x-axis.

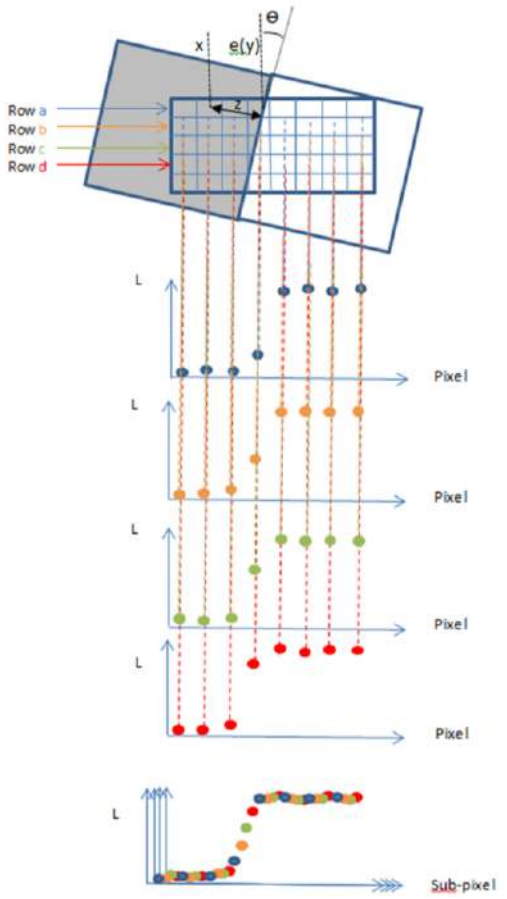

Figure 3.14: Schematic representation of the procedure used to determine the oversampled edge spread function from a slanted knife-edge image. Image from Ref. [90].

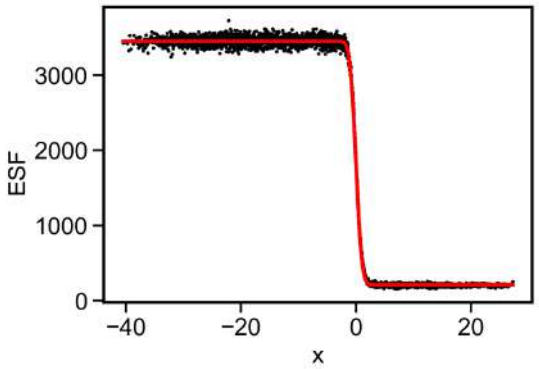

Figure 3.15: Oversampled edge spread function (ESF) obtained from the knife-edge image shown in Fig. 3.13. Red line is the fit with Eq. (3.1)

Finally, the MTF is computed as the normalized Fourier transform of the LSF), hence becoming a function of the spatial frequency ω:

$$\mathrm{MTF}(\omega) = \frac{|\mathcal{F}\{\mathrm{LSF}(x)\}(\omega)|}{|\mathcal{F}\{\mathrm{LSF}(x)\}(0)|} = \mathcal{F}\left\{\frac{d}{dx}\,\mathrm{ESF}_{\mathrm{os}}\right\}(\omega), \tag{3.3}$$

where $\mathcal{F}$ denotes the Fourier transform operator and $\mathrm{ESF}_{\mathrm{os}}$ the oversampled ESF. The results are shown later in Sec. 3.3.3.

Low-Dose Cluster Method & results

An alternative method to characterize the performance of the detector is based on the statistical analysis of individual electron events in the low-dose regime. In this approach, the spatial response of the detector is probed directly by acquiring a large number of frames under conditions where, on average, only a few electrons interact with the detector per frame. Each impinging electron generates a localized signal that may be confined to a single pixel or spread over adjacent pixels, forming a cluster. The spread is due to charge diffusion within the sensor and capacitive coupling between neighboring readout channels. By acquiring a sufficiently large number of frames, the distribution of cluster sizes and shapes can be extracted (see Fig. 3.16), providing insight into the detector's spatial resolution.

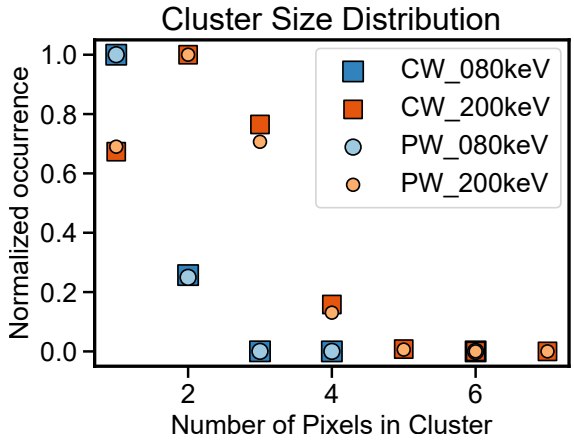

Figure 3.16: Cluster size distribution measured in low-dose conditions across different operating modes and beam energies. The plot reports the normalized occurrence of clusters containing 1 to 6 pixels, for continuous-wave (CW) and pulsed-wave (PW) operation, at 80 kV and 200 kV. At 80 kV, the reduced penetration depth of electrons in the silicon sensor leads to more localized energy deposition and a higher probability of single-pixel clusters. At 200 kV, the increased lateral charge diffusion results in larger cluster sizes. These measurements highlight the dependence of the spatial response on beam energy and confirm the improved resolution at lower accelerating voltages.

Here follows the mathematical expression of the previous concepts. Let $d_n(x, y)$ denote the counts at pixel (x, y) in frame n. The two-dimensional PSF is obtained by calculating the autocorrelation of the recorded signal (shown in Fig. 3.17) and taking the square root:

$$\mathrm{PSF}(x,y) \propto \sqrt{\langle d_n(x,y) * d_n(x,y) \rangle_n}, \tag{3.4}$$

where $*$ denotes convolution and $\langle \cdot \rangle_n$ indicates the average over all frames. The square root removes the broadening introduced by the autocorrelation process, yielding an estimate of the average charge distribution produced by a single electron. The LSF is then obtained by integrating the PSF along one axis, and the MTF is computed as its Fourier transform, following the same procedure as in the knife-edge method.

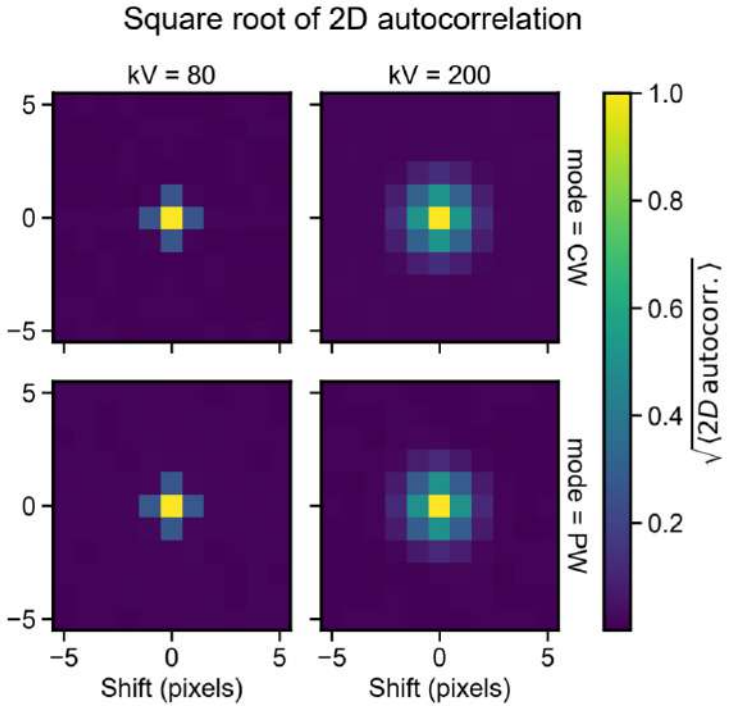

Figure 3.17: Reconstructed spatial response of the detector obtained by autocorrelating low-dose cluster data. Each panel shows the average charge distribution resulting from single-electron events, computed as the square root of the autocorrelation of individual frames and normalized across all pixels. The four panels correspond to continuous-wave (CW) and pulsed-wave (PW) operation at 80 kV and 200 kV. At lower beam energies, the clusters are more localized, resulting in sharper PSFs. These reconstructions confirm the dependence of charge spreading on acceleration voltage and validate the spatial resolution characterization in the single-electron regime.

The spatial response of the detector is obtained by averaging the signal over 10^4 frames with an average electron dose of 10^{-5} electrons/pixel/frame. The measurements are acquired at different electron acceleration voltages (200 keV and 80 keV) and under different e-beam conditions (thermionic, continuous beam (CW) and photoemitted, pulsed beam (PW)) Results are shown in Fig. 3.16.

At 80 kV, the charge cloud created by each electron is more localized due to the reduced penetration depth in the sensor, leading to a narrower PSF and therefore higher MTF

values. This behavior is consistent with previously reported results [9] and confirms the enhanced spatial resolution of the detector at lower beam energies.

The low-dose method is particularly useful in ultrafast or low-flux experiments, where traditional high-dose imaging techniques are impractical. It also allows MTF characterization in pulsed mode, where the electron statistics per frame are limited. This cluster-based low-dose method therefore provides a complementary detector characterization method, particularly suited for regimes where high-dose averaging is impractical due to low electron flux or where single-electron response is of primary interest, such as with our pulsed e-beam.

3.3.3 MTF Results

To benchmark the performance of the hybrid pixel detector under experimental conditions relevant to ultrafast TEM, we measured the MTF at two accelerating voltages (80 kV and 200 kV), and in both CW and PW e-beam operation modes. The MTF was evaluated using both the knife-edge and low-dose cluster methods described in the previous sections.

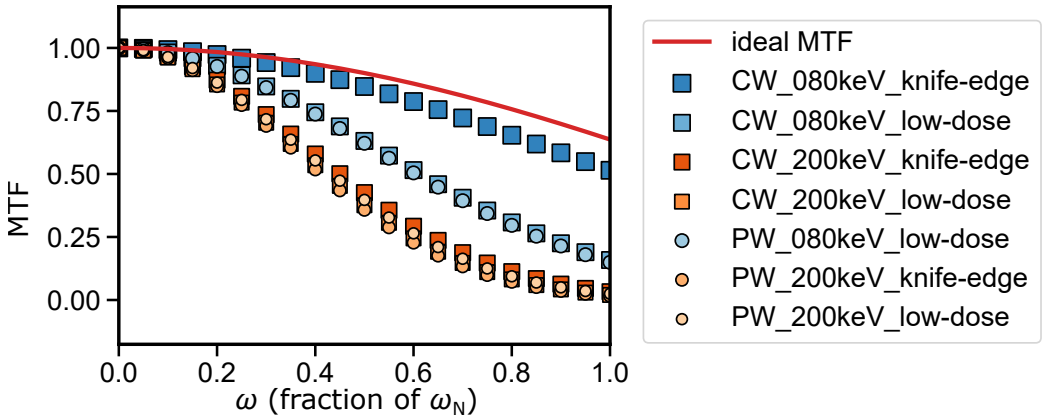

Figure 3.18: Modulation Transfer Function (MTF) curves measured under different conditions. The red solid line represents the theoretical ideal MTF for a detector with perfect pixel isolation. Blue symbols correspond to measurements at 80 kV, while orange symbols refer to 200 kV. Squares indicate continuous-wave (CW, thermionic e-beam) acquisition, and circles indicate pulsed-wave (PW, photoemitted e-beam) acquisition. Filled symbols denote the knife-edge method, and empty symbols denote the low-dose cluster method. PW mode data are available only from the low-dose method at 80 kV and from both methods at 200 kV. All curves are plotted as a function of normalized spatial frequency.

The MTF results presented in Fig. 3.18 reveal several key features:

- At 200 kV, the MTF curves obtained from the knife-edge and low-dose cluster methods are in excellent agreement across all spatial frequencies. This confirms the consistency and validity of the two methods under continuous-wave conditions.
- At 80 kV, a significant discrepancy emerges between the two approaches. The MTF extracted from the low-dose method is systematically lower than that obtained from the knife-edge method, particularly at high spatial frequencies. A hypothesis for this deviation lies in the geometric difference between the two techniques: while the knife-edge provides 1D oversampling, the low-dose method relies on a 2D autocorrelation. The process of extracting a 1D LSF from a 2D PSF may lead to an over-evaluation of the spatial spread, a dimensionality effect that becomes more pronounced at lower voltages where the charge spread is comparable to the pixel size. Further investigation is required to fully decouple these geometric reconstruction factors from the detector's intrinsic response.
- For a given voltage and method, the MTF curves measured in pulsed-wave mode are in excellent agreement with their continuous-wave counterparts. This demonstrates that the detector preserves its spatial resolution even under ultrafast operation conditions. However, in the specific case of knife-edge MTF at 80 kV in PW mode, the measurement could not be performed due to insufficient beam current to achieve adequate statistics.
- In all cases, the MTF falls below the theoretical limit, as expected due to physical processes such as charge diffusion and inter-pixel coupling. Nevertheless, the detector maintains substantial contrast up to intermediate spatial frequencies, confirming its suitability for both imaging and momentum-resolved experiments in ultrafast TEM.
- As observed in previous studies [9, 89] and in the previous subsection, the MTF performance improves at lower acceleration voltages. At 80 kV, the shorter penetration depth of electrons into the silicon sensor leads to reduced charge spreading, resulting in a sharper spatial response and higher MTF at all frequencies.

To provide a quantitative comparison of the detector performance across the different configurations, we report in Table3.1 the values of the MTF at the Nyquist frequency. The Nyquist frequency is defined as the highest spatial frequency that can be sampled without aliasing, corresponding to a spatial period of two pixels. It is given by:

$$\omega_{\mathrm{N}} = \frac{1}{2x_0}, \tag{3.5}$$

where x_0 is the pixel size. The MTF at Nyquist is a common benchmark to quantify the high-frequency performance of imaging detectors.

The values obtained in CW mode at 80 kV are comparable to those reported by Fernández-Pérez *et al.* [9] for a similar hybrid pixel detector, further validating our measurements. At 200 kV, the MTF measured at the Nyquist frequency is around 0.02–0.03.

Table 3.1: Measured MTF values at the Nyquist frequency for different operating conditions and methods.

Condition	Voltage	Method	MTF(ω_N)
CW	80 kV	Knife-edge	0.524
CW	80 kV	Low-dose	0.158
CW	200 kV	Knife-edge	0.033
CW	200 kV	Low-dose	0.020
PW	80 kV	Knife-edge	—
PW	80 kV	Low-dose	0.150
PW	200 kV	Knife-edge	0.016
PW	200 kV	Low-dose	0.025

Because the MTF represents the fraction of the input contrast that the detector reproduces at a given spatial frequency, these Nyquist values mean that the finest resolvable features—those with a period of two pixels—are recorded with only about 2-3 % of their original contrast. Such a loss of contrast at high spatial frequencies is expected, since 200 keV electrons penetrate more deeply into the silicon sensor, causing increased charge sharing between adjacent pixels [9, 89]. However, the EPI-induced momentum redistributions shown in Chapter 4 occur on broader scales, spanning roughly twenty pixels, where the MTF exceeds 0.5 and the transferred contrast remains above 50 %. Consequently, the detector readily preserves the few-percent intensity modulations observed in those measurements, confirming that its spatial response is sufficient for momentum-resolved EPI experiments at 200 kV.

3.4 Alignment and Calibration Procedures

The successful operation of a UTEM relies on precise alignment and calibration of both the laser system and the electron-optical column. In particular, spatial overlap of the laser and electron beams, their temporal synchronization at the femtosecond scale, and proper detector calibration are prerequisites for observing EPI, for shaping the electron wavefunction, and for detecting any laser-induced phenomena.

I personally participated in the first complete alignment of the laser-electron beam overlap at the PELM plane, while the procedures at the sample plane were later refined during my stay at the LUMES laboratory. Since the two alignment strategies follow analogous principles, the discussion below focuses primarily on the PELM plane, highlighting specific steps that are not transferable to the sample configuration.

This section provides a structured overview of the alignment and calibration procedures adopted in our laboratory, integrating both general strategies and practical tips refined during the laboratory setup. The goal is to offer a reproducible methodology for future

users, ensuring stable operation and consistent experimental outcomes.

3.4.1 Photoelectron Generation

Figure 3.19: Optical camera view of the PELM section through the last dielectric mirror of the UV injection path. The glow from the heated LaB_6 filament is visible as a reflection on the aluminum UV mirror (top), while the PELM platelet of the holder is seen below it. Because the last dielectric mirror of the UV injection path is transparent in the visible, the camera provides a direct view inside the TEM column, enabling coarse alignment of the UV beam with respect to the cathode.

The generation of femtosecond electron pulses from the LaB_6 cathode is the first step toward operating the UTEM in pump-probe mode. Photoemission is driven by the UV laser at 257 nm, obtained from the fourth harmonic of the fundamental 1030 nm output. Accurate coupling of the UV beam to the cathode surface is essential as the resulting electron pulses provide the basis for all subsequent electron-photon interaction experiments.

Camera-based coarse alignment

The initial coupling of the UV beam to the cathode is facilitated by a diagnostic camera placed behind the last steering mirror of the injection path. This mirror is dielectric: it reflects UV and IR light while being transparent in the visible. This allows the camera to image the inside of the PELM section through the laser viewport. In this camera, the PELM platelet and the glow of the heated LaB_6 cathode filament, reflected on the aluminum UV mirror, are visible (Fig. 3.19). The filament glow serves as a reference to steer the UV beam.

The alignment principle is illustrated in Fig. 3.20. The UV beam is iteratively adjusted with the external mirrors until it overlaps with the filament-glow reflection at two distinct points along the optical path (one closer to the camera, one closer to the viewport). When this condition is met, the UV can be considered collinear with the filament-glow path. This means that the UV hits filament within a reasonable error and photoelectrons are being produced. This procedure is typically required only the first time the UV-cathode overlap is established, or in case the photoelectron signal is completely lost.

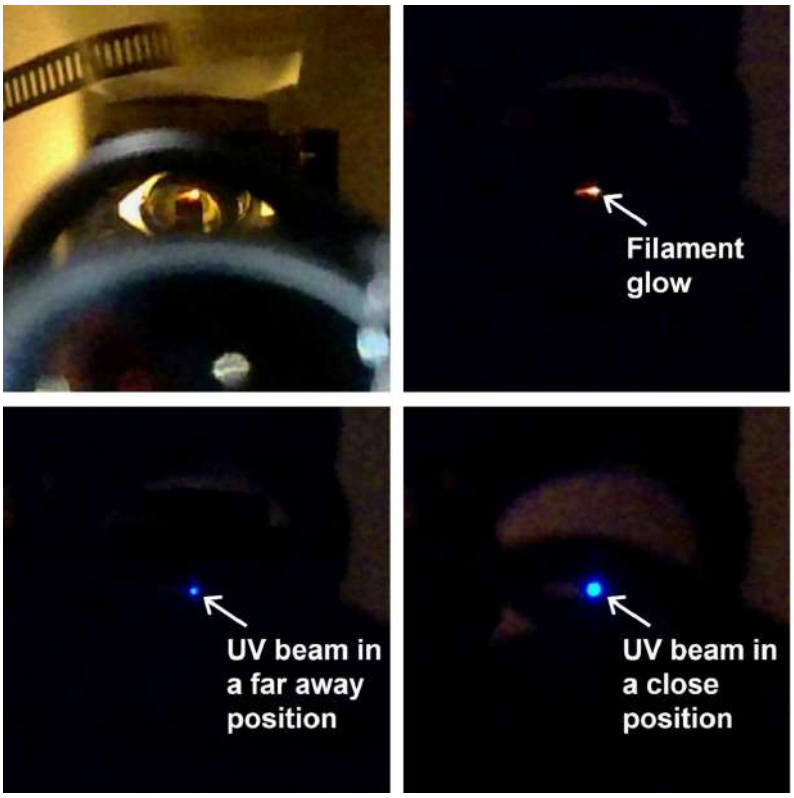

Figure 3.20: ***Coarse alignment procedure of the UV beam to the LaB_6 cathode, optical camera view. Top left:*** *view with laboratory light on. The last dielectric mirror and lenses as well as the TEM viewport are visible.* ***Top right:*** *laboratory light off. Filament glow clearly visible. Its position is marked on the computer screen.* ***bottom left:*** *UV card placed in front of the viewport. This reveals the UV position which is aligned to overlap the marked position of the filament glow.* ***bottom right:*** *UV card placed close to the camera. The UV position is aligned with a different, closer mirror to overlap the filament glow.*

Fine alignment with the detector.

After the coarse alignment procedure, the detector is turned on. This would show a photoelectron signal. Once the photoelectron signal is detected, the alignment is refined directly by monitoring the detector. Figure 3.21 shows the detector signal with the UV laser switched on (top) and off (bottom). During fine alignment, the translation knobs of the final focusing lens are adjusted until the integrated electron counts in a defined region of interest are maximized. This procedure is fast, reproducible, and sufficient for routine daily operation, since it directly optimizes the photoemission yield without requiring a camera view of the cathode region.

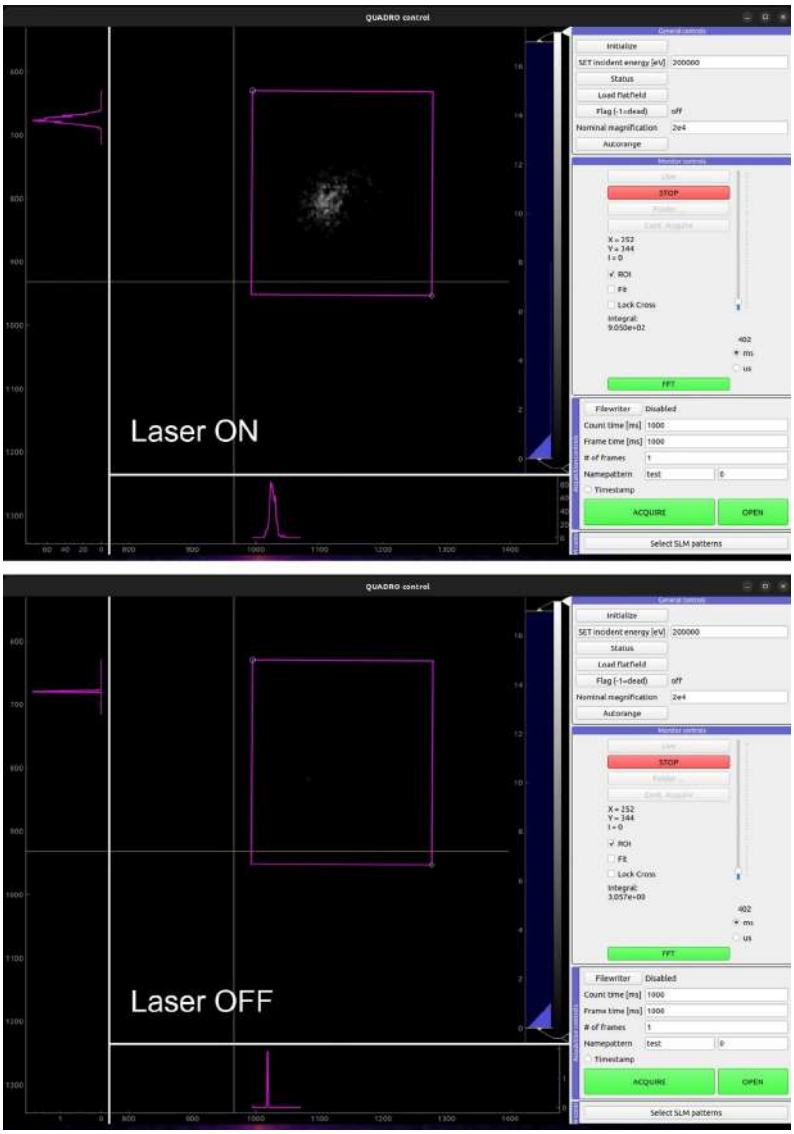

Figure 3.21: Historical image: first verification of photoelectron generation with the QUADRO direct detector. Top: UV laser ON, showing a clear photo-generated e-beam. Bottom: UV laser OFF, with no electrons detected. Fine alignment is performed by optimizing the signal on the detector using the translation knobs of the final focusing lens.

3.4.2 Spatial Overlap of Electrons and Laser

After establishing photoemission, the next step is to overlap the e-beam with the IR laser at the PELM film. This spatial overlap is required to obtain the EPI that would shape the e-beam. As in the case of the UV alignment on the cathode, the procedure combines a camera-based coarse alignment with a fine optimization performed directly on the detector.

Camera-based coarse alignment.

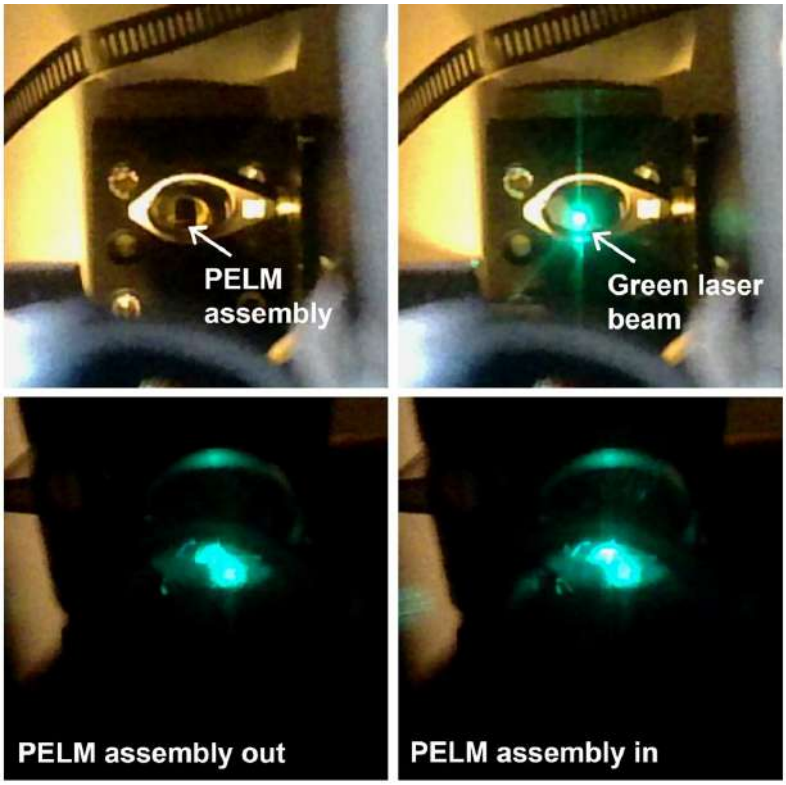

Figure 3.22: Camera view of the PELM section through the dielectric injection mirror. The PELM film platelet is visible, and the laser spot can be identified on its surface when it is inserted.

The same dielectric injection mirror and diagnostic camera used for UV coarse alignment are also employed for the IR beam, since both beams enter the TEM through the same viewport, as shown in Fig. 3.19. The initial alignment was performed with the IR laser frequency-doubled to generate green light, as visible wavelengths are easier to align and visualize on the camera. However, the same procedure was later successfully carried out using the fundamental IR wavelength, since the silicon-based camera retains sufficient sensitivity in the near-infrared range. In this configuration, the PELM film platelet can be directly imaged, and the green laser spot appears as scattered light from the film surface (Fig. 3.22). This coarse check is used to ensure that the optical beam is incident on the film region before proceeding to detector-based refinement.

Fine alignment using a sacrificial membrane

Once this coarse alignment procedure is accomplished, fine laser-e-beam alignment is performed by exploiting the destructive effect of a tightly focused laser spot and electron imaging. A thin sacrificial sample—typically a polymeric membrane or metallic

film—is mounted on the PELM stage and imaged using the TEM in diffraction or low-magnification imaging mode. The IR beam is then scanned across the field of view using the SLM, while the external steering mirrors are adjusted to center the spot.

When the laser hits the membrane in the imaged region, a visible rupture occurs in real time, allowing direct localization of the laser spot (see Fig. 3.23). This destructive interaction provides an unambiguous confirmation of spatial overlap between the IR and e-beams and allows sub-millimeter precision in their alignment.

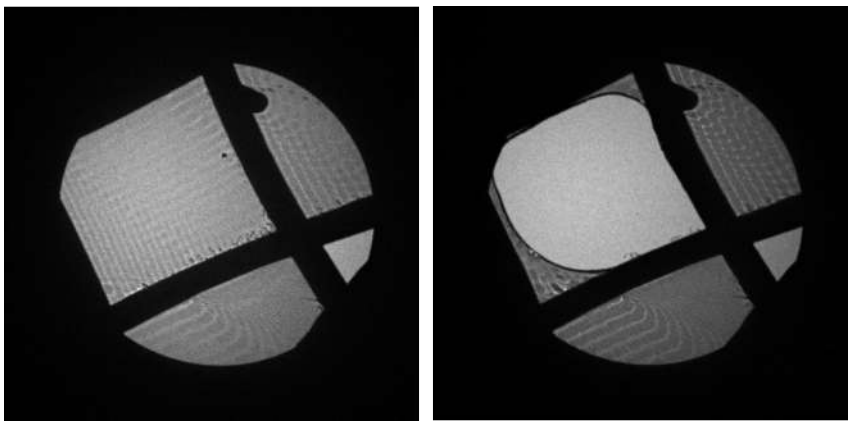

Figure 3.23: Fine spatial alignment of the IR beam using a sacrificial P3HT:PCBM membrane. Left: TEM image of the intact membrane. Right: same field of view after scanning the IR laser spot with the SLM and overlapping it with the e-beam, resulting in localized rupture of the membrane. This destructive test confirms spatial overlap at the PELM interaction plane with tens of micrometers precision.

The laser power used during this procedure is typically on the order of a few hundred milliwatts at a repetition rate of few hundreds of kHz. This combination is sufficient to damage the membrane via localized heating. At higher repetition rates and same laser power, the thermal energy deposited in each pulse may dissipate before the arrival of the next pulse, making membrane rupture less efficient unless higher power is used.

A similar procedure is adopted at the sample plane to verify overlap with the pump beam. In this case, a sacrificial sample is used, and the IR beam is scanned using a motorized mirror placed in the external laser delivery path, rather than the SLM.

3.4.3 Temporal Overlap and Interaction Signal Optimization

In addition to spatial alignment, the observation of EPI (or other laser-triggered phenomena) requires temporal synchronization between the pumping optical pulse and the probing electron pulse at the interaction plane (PELM and/or sample plane). Temporal overlap defines the condition in which both pulses arrive at the interaction region within their temporal duration. Establishing this condition involves again a coarse search,

followed by fine optimization based on the detected interaction signal.

Coarse Temporal Overlap via Plasma Lensing Signal

A robust method to establish temporal overlap between the electron and laser pulses is based on the transient plasma-lensing signal. When the IR pulse irradiates a metallic object, multiphoton photoemission launches an expanding electron cloud whose evolving charge distribution generates slowly varying, quasi-electrostatic fields that deflect the probe beam (see Sec. 2.3). This field, dominated by low-frequency space-charge components, acts as a transient lens on a timescale of tens to hundreds of picoseconds—well beyond the femtosecond EPI regime [73, 74].

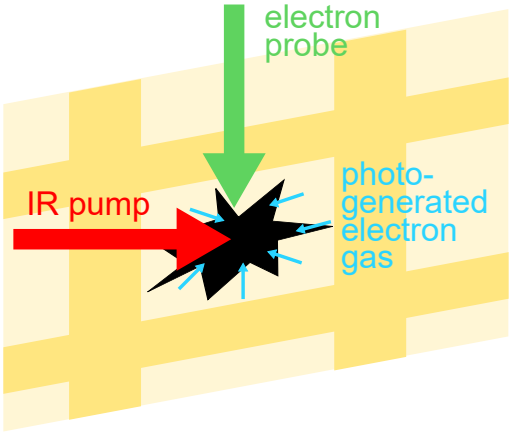

Figure 3.24: Experimental sketch of the plasma-lensing method. A gold-coated TEM grid placed at the PELM plane is broken to ensure spatial-overlap reference and consequently used as photoemission target. Upon IR irradiation, the expanding electron cloud produces a transient THz field that deflects the probing electron beam.

In our implementation, this method is realized by irradiating a broken gold-coated TEM grid placed at the PELM plane, which is the same specimen previously used to verify spatial overlap, as illustrated in Fig. 3.24. The photoemission from the partially fractured gold film produces a rapidly evolving near-surface charge distribution that deflects the electron probe, yielding a strong, easily detectable signal on the detector.

To access this signal, the column is operated in a point-projection regime. The intermediate lenses are tuned so that the detector records a magnified projection of the probe's angular distribution without forming a post-interaction crossover, as shown in Fig. 3.25. Within this geometry, specimen coordinates x are mapped to detector coordinates χ through effective propagation distances (L_0, L_1), while transient deflection angles $\vartheta(x,t)$ translate into spatial displacements on the detector. Consequently, the space- and time-dependent fields near the illuminated metal are converted into measurable, delay-dependent distortions of the beam profile, directly revealing the plasma-lensing response. Because the plasma-lensing signal is strong and persists for hundreds of picoseconds, it

enables efficient coarse scans with relatively large delay steps. This makes it particularly useful when the temporal-overlap position is unknown or has drifted since the previous alignment.

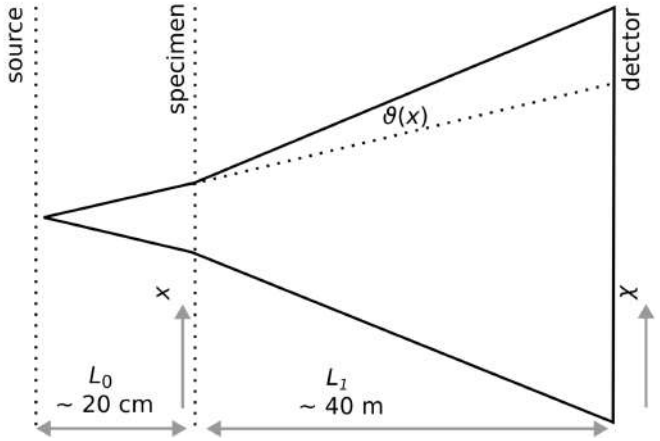

Figure 3.25: Point-projection imaging scheme. Parameters L_0 and L_1 describe the transport from virtual source to specimen plane, and from specimen to detector, respectively. The transverse coordinate x in the specimen plane is mapped to a detector coordinate χ via a time-dependent scattering angle ϑ.

Figure 3.26 shows a time-resolved sequence of point-projection images of the e-beam that crosses the interaction region. In the absence of the IR pump (left panel), the beam exhibits a symmetric profile. At temporal overlap (center), a transient distortion is clearly visible, corresponding to the presence of the space-charge field. After the pump (right), the beam relaxes toward its original shape. This sequence directly visualizes the temporal evolution of the electron-plasma interaction.

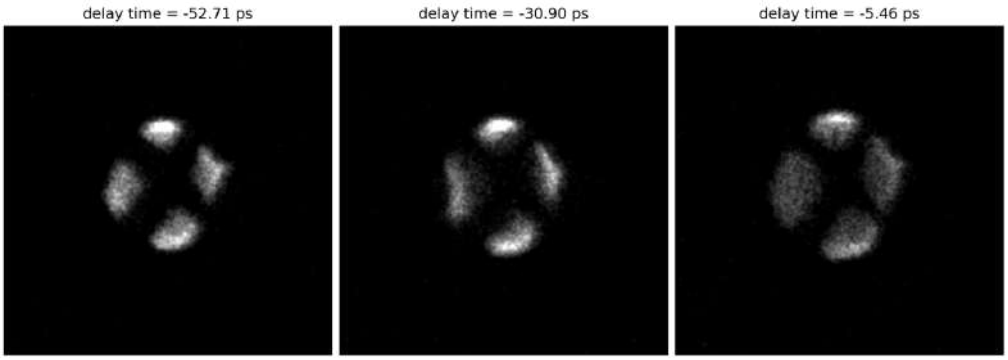

Figure 3.26: E-beam profiles recorded in point-projection imajing at different delay times. The cross is the TEM is that sustains the gold film. Left: before IR pulse arrival. Center: at temporal overlap, the beam is distorted by the plasma field. Right: after the interaction.

To quantitatively identify the moment of overlap, we track the evolution of the beam as a function of time delay using image similarity metrics or local intensity analysis. In

Fig. 3.27, we show two complementary methods: the Structural SImilarity Index (SSIM) [92], which compares each frame to a reference image, and the average intensity within a selected region of interest. Both quantities show a sharp temporal response at the onset of the interaction, which can be fitted to extract the temporal profile of the system. These metrics allow an objective and repeatable identification of time zero.

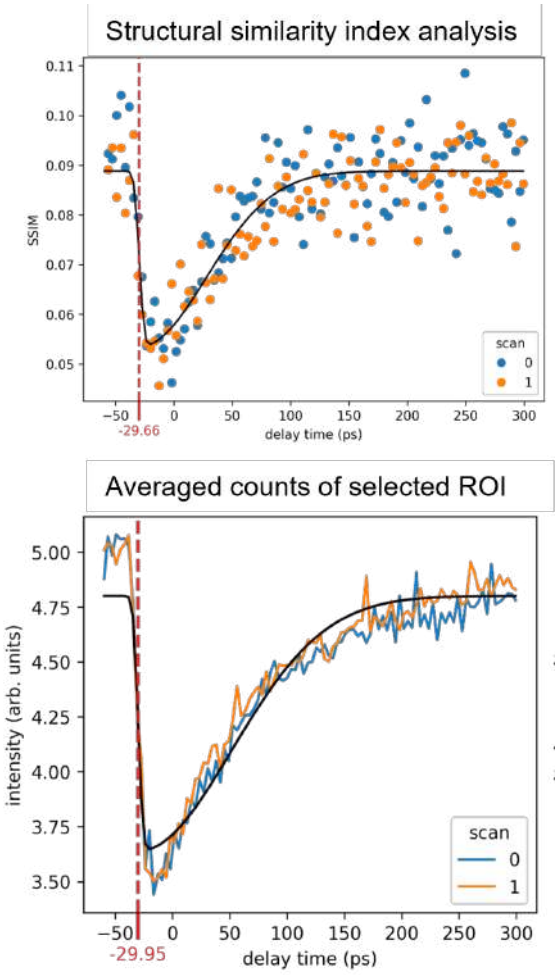

Figure 3.27: Quantitative evaluation of temporal overlap. Top: Structural SImilarity Index (SSIM) as a function of time delay. Bottom: averaged intensity in a selected ROI. In both cases, a clear step-like transition allows the identification of temporal overlap via fitting (black lines). Two consecutive scans (blue and orange data) were performed for robustness.

Because of its high signal-to-noise ratio, this method is routinely used in our system to determine the coarse temporal overlap (up to 1 ps precision). Although it does not probe coherent field-mediated interaction directly, the transient plasma lensing signal persists for several hundred picoseconds after excitation, allowing time-delay scans with relatively large step sizes (typically 5-10 ps) for a first coarse identification of temporal overlap. This makes it particularly valuable for initial delay-stage scans, especially when the position of temporal overlap is unknown or has drifted significantly.

Fine Temporal Overlap via Momentum Streaking

Once the temporal overlap region is coarsely localized using the plasma lensing signal (Sec. 3.4.3), the fine delay alignment is achieved by detecting EPI (see Sec. 2.2.3). This effect manifests as a streaking in the transverse momentum distribution of the e-beam when the optical and electron pulses overlap at a pristine metallic interface within a time window of a few tens of femtoseconds before the onset of plasma formation, as studied in Sec. 4.3. The interaction is probed using the high dispersion diffraction (HDD) mode, in which the focal plane of the condenser lens is projected to the detector, allowing access to the angular (momentum) profile of the e-beam at the PELM plane.

The HDD configuration is enabled by operating the microscope in free lens control and tuning the intermediate lenses to achieve an effective camera length[1] of approximately 100 m. The calibration of this lens configuration and of the resulting reciprocal space scale is discussed in detail in Sec. 3.4.4. This configuration enables the resolution of angular modulations in the microradian range, which are essential to detect interaction-induced streaking of the e-beam.

In this configuration, delay-dependent distortions of the e-beam are observed when the IR pulse overlaps temporally and spatially with the electron pulse at the PELM interaction region. An example is shown in Fig. 3.28, where the transverse momentum distribution of the beam is visualized for three different delay times. The central panel shows the maximal streaking signal, which corresponds to the optimal temporal overlap.

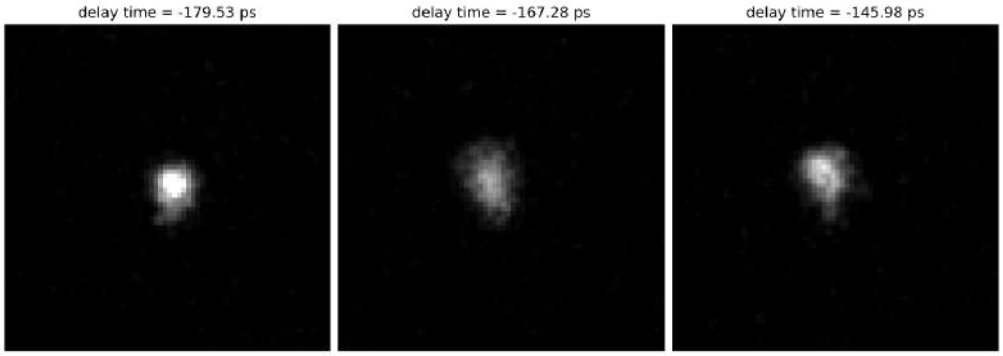

Figure 3.28: Transverse momentum distribution of a pulsed e-beam following IR laser irradiation measured for different delay times between electron and light. The center image corresponds to the maximal streaking effect at optimal temporal overlap.

To quantify the overlap and extract a time-zero reference, we analyze the evolution

[1] The camera length (L) is a functional parameter in electron diffraction that relates the radial distance (r) of a feature on the detector to the scattering angle (θ) according to the relationship $r = L\tan(2\theta) \approx 2L\theta$ for small angles [4].

of the beam profile across a delay scan. Figure 3.29 shows the spatio-temporal map extracted from the HDD streaking measurements, together with the temporal profile of the beam width. The latter reveals a sharp, sub-picosecond increase in beam extent, followed by a slower relaxation to the unperturbed shape. This response is used to determine the optimal delay for interaction-based experiments. This procedure is routinely used to check temporal overlap between the electron and the laser beam for e-beam shaping measurements.

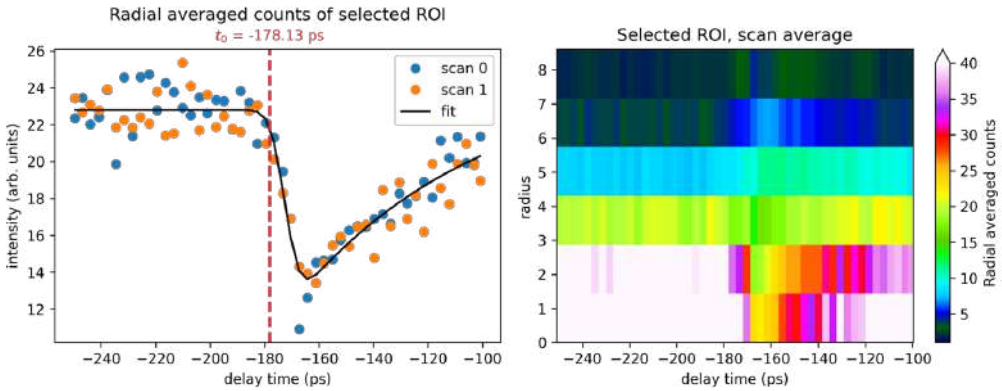

Figure 3.29: Spatio-temporal maps for the HDD measurements presented in Fig. 3.28, together with the extracted time profile of the electron spot height. The red dashed line indicates the identified time zero.

3.4.4 Detector and Lens Calibration

Accurate lens and detector calibration is essential for all type of measurements. This is especially important in our system, which is frequently operated in *free lens control* mode to allow custom tuning of beam size, convergence, and magnification at the PELM plane. In this mode, the lens currents are manually set, and standard microscope readouts (e.g., magnification and camera length) are no longer reliable. As a result, key calibration steps must be repeated before each experiment.

Additionally, due to the insertion of the C_0 lens and interaction region into the TEM column, the native microscope magnification values are no longer valid, even when operating in standard lens mode. To compensate for this, we use diffraction gratings and calibrated samples (such as latex spheres on grating replicas) to re-establish accurate spatial and angular scales in both imaging and diffraction configurations. This subsection details the procedures for both free-lens and standard-lens calibration.

Conventional Lens Control: Imaging and Diffraction Calibration

Due to structural modifications to the TEM column—most notably the integration of the PELM section and C_0 lens—the actual optical path of the e-beam differs from that of a factory-aligned microscope. As a result, the nominal magnification and camera length values reported by the microscope software are no longer quantitatively accurate. To enable reproducible and quantitative measurements, we established corrected calibration curves for both real-space and diffraction modes under conventional operating conditions, i.e., without activating free lens control.

For the calibration in imaging mode, we used a TED Pella test sample (Product No. 673) consisting of latex spheres with nominal diameter 0.262 µm deposited on a diffraction grating replica. The real-space calibration was performed by measuring either the latex sphere diameters or the known grating line spacing and comparing them to their known physical dimensions. The measured magnification was then plotted as a function of the nominal microscope setting. As shown in Fig. 3.30, both particle-based (blue) and grating-based (orange) measurements yield a consistent linear correction.

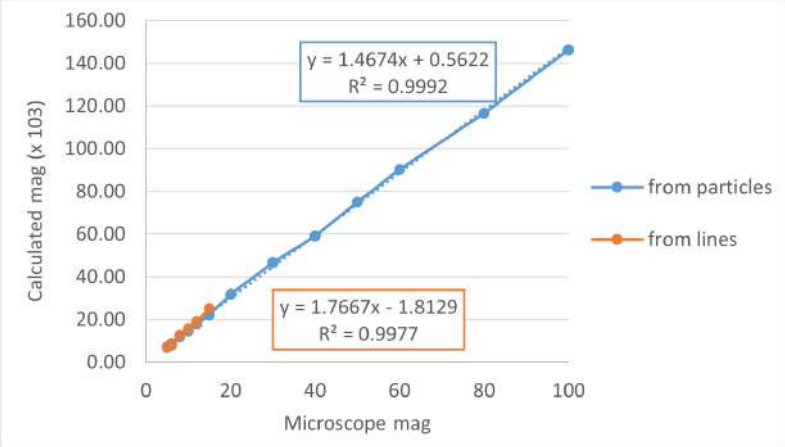

Figure 3.30: Real-space calibration of TEM magnification using a TED Pella sample (latex spheres and grating lines). Measured magnification values were plotted against microscope-reported values. The resulting calibration can be used to correct nominal settings when operating in conventional imaging mode.

For the diffraction calibration, a polycrystalline aluminum standard (Sample No. 619) was used. The diffraction ring pattern was recorded for multiple nominal camera length values. Each ring was assigned a known interplanar spacing d_{hkl}, and the corresponding ring radius R was measured on the detector in pixels. Using the standard formula:

$$\text{Camera Constant} = R \cdot d_{hkl} \tag{3.6}$$

we extracted the camera constant for each microscope setting. The resulting values were

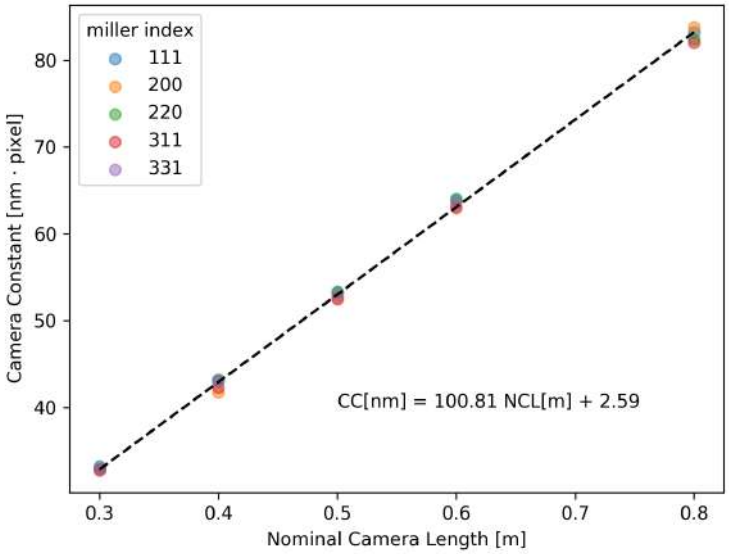

Figure 3.31: Diffraction calibration curve obtained using a polycrystalline aluminum standard TED Pella sample. The measured camera constant is plotted as a function of the nominal camera length. This correction must be applied for quantitative diffraction analysis.

plotted against the Nominal Camera Length (NCL) in Fig. 3.31. The linear fit provides a simple conversion rule:

$$\mathrm{CC}\,[\mathrm{nm}\cdot\mathrm{px}] = 100.81 \cdot \mathrm{NCL}\,[\mathrm{m}] + 2.59 \tag{3.7}$$

These calibration plots provide definitive references for converting nominal magnification and camera length values into physical units. They are intended to support future users of the modified LUMiNaD ultrafast TEM system who wish to operate the instrument in conventional (non-free-lens) mode for low-dose imaging, standard diffraction, or general alignment purposes.

Free Lens Control: High Dispersion Diffraction Calibration

In order to resolve the small momentum changes of the e-beam induced by ITR, the electron optics must be configured to project the transverse momentum distribution of the beam onto the detector. This requires operating the microscope in *free lens control* mode. The lens currents are manually tuned to access a long effective camera length to resolve the streaking signal. The calibration described below is valid for the beam shaping measurements discussed in Chapter 4 and must be repeated whenever the lens configuration is changed with respect to the one reported in Fig. 3.32.

Figure 3.32: Screenshot of the lens control panel during operation in free lens configuration. The condenser lenses CL1 and CL2, as well as multiple intermediate and projector lenses (e.g., IL3, PL2), are turned off to allow manual tuning of electron optics. Only a weak excitation of CL3 is used to maintain minimal beam demagnification. This configuration is employed to achieve high dispersion and resolve transverse momentum redistribution due to inverse transition radiation.

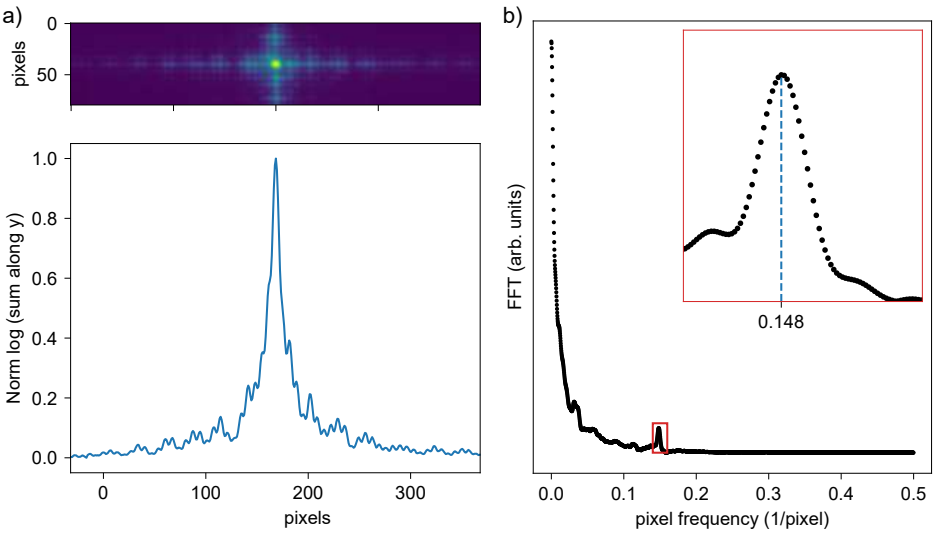

Figure 3.33: Calibration of the momentum scale for High Dispersion Diffraction (HDD) patterns. a) Diffraction pattern of the latex spheres on diffraction grating replica calibration sample placed at the PELM plane. The grating period is $2\,\mu\mathrm{m}^{-1}$*. b) Fourier transform of the diffraction pattern, used to extract the peak period in pixels. From the calibration, we determine that one pixel corresponds to a reciprocal-space value of* $0.296\,\mu\mathrm{m}^{-1}$*, and the effective camera length is calculated to be* $100\,\mathrm{m}$*.*

To achieve the large coherence needed to resolve EPI, the C_0 lens is excited at only 15 V, as detailed in Sec. 3.2.2. To directly correlate the electron profile between the sample plane and the PELM plane, we avoid forming crossovers between these two planes. This is achieved by turning off all lenses before the sample plane, except for a weakly excited C_3 lens, which results in a minimally demagnified e-beam. Operating the TEM in free lens control also allows us to reach the long camera length of 100 m through manual tuning of

the intermediate lenses. To establish a momentum scale for the HDD patterns, we place a calibration sample, *latex spheres on diffraction grating replica* (TED Pella product number 673), in the PELM plane. The calibration results are shown in Fig. 3.33.

The obtained reciprocal space sampling is:

$$\Delta k = \frac{\text{grating frequency } [\mu\text{m}^{-1}]}{\text{peak period [pixels]}} \times 2\pi[\text{rad}] = \frac{2\,\mu\text{m}^{-1}}{0.148} \times 2\pi\,\text{rad} \approx 1.862\,\text{rad}\,\mu\text{m}^{-1} \quad (3.8)$$

per pixel. The peak period, derived from the diffraction peaks in Fig. 3.33a, is obtained from the Fourier transform shown in Fig. 3.33b. Conventionally, the radians are dropped for simplicity.

Using these measurements, the camera length is calculated as:

$$L_C = \frac{\text{peak period [pixels]} \times \text{pixel length [m]}}{\lambda_e\ [\text{m}] \times \text{grating period } [\text{m}^{-1}]} = 100\,\text{m} \quad (3.9)$$

where $\lambda_e \approx 2.5\,\text{pm}$ is the de Broglie wavelength of relativistic electrons at 200 keV.

This configuration and calibration are used throughout the beam modulation experiments presented in Chaps. 4 and 5. Any variation in the lens settings—especially the intermediate and projector lenses—requires repeating this calibration procedure to maintain quantitative access to the momentum scale.

Chapter 4

Electron beam Shaping *via* Pre-Sample Photonic-based Free-Electron Modulation

Building on the theoretical and instrumental developments presented in Chaps. 2 and 3, this chapter reports the first light-enabled, programmable implementation of transverse e-beam shaping within a UTEM. In Chap. 2, we discussed how the coupling between free electrons and photons enables controlled modulation of the electron wavefunction via ITR. Chapter 3 detailed the integration of the PELM inside the TEM column, together with the custom optical injection path and the new C_0 lens assembly. Here, we experimentally realize the concepts introduced earlier, demonstrating that EPI can be harnessed to shape the transverse structure of free-electron wavefunctions on demand through purely optical means.

e-beam shaping enables the tailoring of the phase and amplitude of electron wavefunctions before their interaction with the specimen. This capability expands the toolbox of ultrafast electron microscopy by allowing the design of probes that emphasize specific spatial frequencies, enhance phase contrast or match the symmetry of a given material excitation. As discussed in Sec. 2.4, the ability to structure the e-beam in space and time extends the concept of contrast optimization from classical imaging to interaction-specific measurements, and it lays the foundation for quantum-inspired detection schemes in free-electron optics [24]. In this sense, the demonstration presented here marks a key step in linking optical wavefront engineering to the control of free-electron observables in the UTEM.

The PELM used for this purpose, described in detail in Sec. 3.2.1, employs ITR to mediate EPI between the e-beam and a transversely shaped laser beam. The laser beam, shaped by the phase-only SLM presented in Sec. 3.1.2, illuminates a thin gold film that

mediates ITR. This film is placed upstream of the condenser-lens (CL) system, which enables the modulated e-beam to be demagnified and projected onto the sample.

A key constraint of this pre-CL configuration is that the transverse coherence length of the e-beam must exceed the optical wavelength at the interaction plane, before any coherence enhancement can be introduced by the CL system. These coherence conditions and interaction regimes are analyzed in detail in Sec. 4.1. To relax these constraints, an alternative implementation was developed by other SMART-electron partners: the AdQuanta group at the Israel Institute of Technology (Technion). Their post-CL PELM placement facilitates access to the required e-beam coherence but does not allow manipulation of the shaped beam prior to the sample. This complementary approach enabled demonstrations of longitudinal shaping, as reported in Refs. [19, 78].

In this chapter, we first examine the coherence requirements that govern the visibility and efficiency of the modulation process. We then describe the experimental procedures adopted to align the laser and e-beams and to establish reliable interaction at the modulation plane. Once the interaction is characterized, we implement programmable transverse shaping using a set of test patterns and analyze the resulting electron momentum distributions at the detector. This work represents the first realization of a photonic-based, programmable free-electron modulator operating in the pre-sample region of a UTEM, as reported in Ref. [78], where the writer is first author.

4.1 Electron-Photon Interaction and Coherence

Our PELM exploits ITR to mediate EPI, as described in Chap. 2. In this process, electrons inelastically interact with a strong spectrally-coherent light source, absorbing and emitting an integer number of photons [16, 68]. This quantized interaction imprints distinct peaks in the electron distribution, corresponding to multiples of the photon's energy and momentum [44, 50, 59, 67, 71, 93].

To resolve these interaction peaks, and hence the quantized nature of EPI, the e-beam energy (or momentum) spread must be narrower than the photon's energy (or momentum). Such narrow spreads are achieved when the e-beam longitudinal (or transverse) coherence length exceeds the wavelength of the interacting photons [41]. This is because the longitudinal and transverse coherence lengths directly determine the e-beam spread in energy and momentum, respectively, when averaging over the electron ensemble of wave functions [94]. It is important to notice that, if the coherence length exceeds the photon wavelength but remains on the same order of magnitude, it is still possible to detect EPI; however, the interaction peaks will smear out and the quantum nature of EPI hidden. (note that this analysis covers only intrinsic coherence; extrinsic sources of broadening—such as mechanical or electrical instabilities—are separately discussed in App. A).

In the energy domain, EPI is detected if the temporal coherence of the e-beam is

longer than or on the order of an optical cycle. This condition is easily achieved thanks to the small energy spread that results from the photoemission process at the cathode, around $0.1-0.3\,\mathrm{eV}$ [41, 95]. As a consequence, the electron pulse has a temporal coherence $\xi_t \approx 5-10\,\mathrm{fs}$, which is greater than the optical cycle (in our case, $\tau = \lambda/c \approx 3.4\,\mathrm{fs}$) [41].

In contrast, detecting EPI in the momentum domain is more challenging. In this case, the electron transverse coherence must be greater than or on the order of the laser wavelength. Typical values of transverse coherence for thermionic electron sources, such as those used in our laboratories, are on the order of tens of nanometers [96, 97], which is not enough for experiments with visible and IR light. Therefore, particular microscope settings need to be used to increase the beam transverse coherence, as discussed in Sec. 3.4.4.

For e-beam shaping, it is crucial not only to achieve sufficient e-beam coherence but also to achieve coherent EPI, since preserving the phase information is critical for advanced imaging techniques. Coherent EPI occurs when the e-beam interacts with a homogeneous portion of the laser's electric field. For longitudinally coherent EPI, the laser pulse is stretched in time to exceed the duration of the electron pulse [44, 50]. For transversely coherent EPI, the e-beam spot size is reduced to be smaller than the laser spot size [44]. In this experiment, a portion of the e-beam, smaller than the laser spot size, is selected post interaction.

4.2 Experimental setup

The experimental demonstration of transverse e-beam shaping is performed on the custom UTEM described in Chap. 3. The microscope is operated at an accelerating voltage of 200 keV, and single-electron pulses were generated via UV photoemission at the cathode. The PELM was implemented in the pre-CL region of the column, as detailed in Sec. 3.2.1, enabling modulation of the electron wavefunction before beam focusing.

We implemented a pump-probe scheme extensively described in Sec. 3.1 and schematically shown in Fig. 4.1. Briefly, an IR laser pulse, produced by our femtosecond laser, is split in two branches. One pulse is up-converted to UV light by a 4th harmonic generation stage and is directed to the TEM cathode; its power is adjusted to generate single-electron pulses via photoemission. The other pulse is synchronized with the electron pulse and pre-shaped via the SLM. The two pulses interact via ITR on a light-reflective, electron-transparent metallic film at the PELM plane, where the SLM-shaped laser field imprints its modulation onto the electron wave function. To maximize EPI, the shaped laser pulse is p-polarized with respect to the PELM film [22]. We operate the laser at a repetition rate of 300 kHz and the power of the shaped IR beam is filtered down to 10 mW, to avoid breaking the gold film. With a $1/e^2$ beam diameter of $80\,\mu\mathrm{m}$, these parameters give an effective fluence at the sample $F_\perp \approx 9.7\,\mathrm{mJ/cm^2}$.

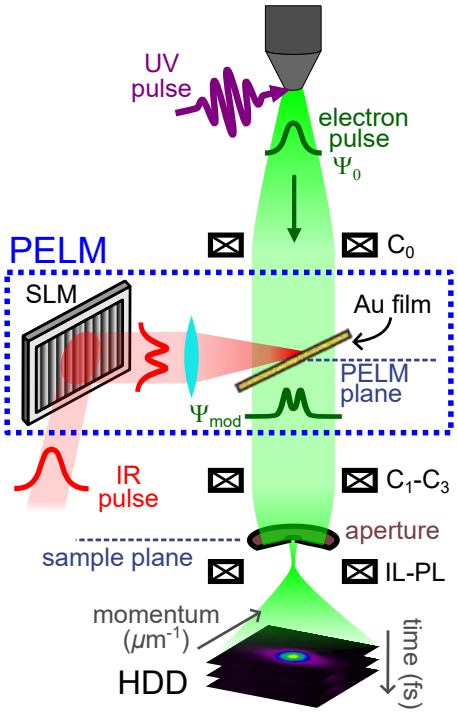

Figure 4.1: ***Schematics of experimental setups incorporating the PELM for transverse e-beam shaping.*** *A Spatial Light Modulator (SLM) is used to shape the transverse laser profile, which is then focused on a thin gold film positioned in a stage before the condenser lenses (C_1-C_3) inside the TEM. Femtosecond electron pulses generated by UV laser pulses interact with the modulated IR laser pulses at the PELM-film surface via stimulated ITR. A 20-µm aperture selectively samples a small portion of the modulated e-beam. high dispersion diffraction (HDD) patterns of the selected electrons are recorded. By scanning the aperture or laser, the entire transverse electron profile is reconstructed via the 4D-LSTEM method (see text for details).*

As explained above, a key experimental challenge lies in achieving sufficient transverse coherence at the PELM plane. Under typical imaging conditions, this is generally accomplished by demagnification with the CLs and transverse beam selection with the condenser aperture. Here, to reach the coherence required for resolving EPI at the pre-CL PELM plane, we substantially reduce the excitation voltage of the C_0 lens (see Sec. 3.2.2) and we use the PELM stage itself as an aperture. Consequently, the e-beam diameter significantly exceeds that of the laser, resulting in substantial loss of useful electron flux, as many electrons fall outside the laser interaction region and remain unmodulated.

In this experiment, ITR is mediated by a 5-nm-thick gold film at the PELM plane. Figure 4.2 illustrates the experimental geometry of the PELM film used in our setup, following the layout and labeling convention in Fig. 1 of Ref. [50] and Fig. S1 of Ref. [22] for consistency and ease of comparison. The supplementary materials in these references provide derivations for the film-parallel components of the incident light wavevector that are transferred to the electrons during interaction.

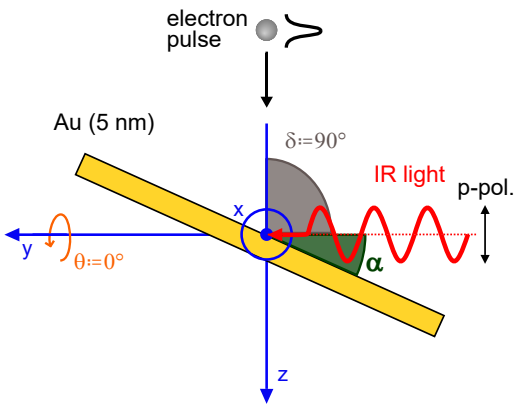

Figure 4.2: ***Experimental geometry of electron-photon interaction at the PELM-film.*** *The angles θ and α represent the film's rotation around the y-axis and x-axis, respectively, relative to the horizontal plane. The angle δ specifies the orientation between the e-beam and the light propagation direction. In our laboratory, $\theta = 0°$ and $\delta \approx 90°$ are fixed, while α is adjusted to optimize the interaction. The momentum transfer occurs predominantly along the y direction, aligned with the laser propagation.*

In our configuration, the angles $\theta = 0°$ and $\delta = 90°$ are fixed (as shown in Fig. 4.2), while α is varied to optimize interaction. Using the formula from the supplementary information in Ref. [22, 50], we calculate the coordinates of the light-wavevector transfer components as:

$$q_{L\parallel}(x, y, z) = \left(0,\ \cos^2\alpha, -\frac{\sin 2\alpha}{2}\right) \tag{4.1}$$

The momentum transferred to the electrons is then given by $p_L = \frac{\omega}{c} q_{L\parallel}(x, y, z)$, where $\frac{\omega}{c}$ is the light wavenumber. As described later, this momentum transfer occurs solely along the laser propagation direction y.

4.3 Experiment Preparation: Observation of EPI and Temporal Overlap

As introduced in Sec. 4.1, transverse modulation of the e-beam requires modifying both the spatial and momentum coordinates of the electron wave function. Before implementing programmable beam-shaping patterns, we first characterize the basic EPI at the PELM plane and establish the temporal overlap (t_0) between electron and laser pulses, as described in Sec. 3.4.3. This step ensures that the experimental conditions are optimized for efficient modulation and provides a benchmark for subsequent measurements.

As mentioned in Sec. 4.2, the PELM film used for this experiment is a 5-nm-thick gold film. This thickness is not sufficient to approximate the PELM film with a perfect mirror, given that the skin depth of gold is around $t = \lambda/(2\pi\sqrt{\varepsilon_2/2}) \approx 27\,\text{nm}$, where $\lambda = 1030\,\text{nm}$ is the wavelength of our laser. Using the approach outlined in the SI of Ref. [50], we simulated the EPI strength (β) as a function of the PELM-film tilt angle α, accounting for the non-ideal mirror conditions. Our results, displayed in Fig. 4.3a, indicate that an optimal interaction strength occurs at a tilt angle of $\alpha = -22°$, which was therefore used in all following experiments. The asymmetry of the distribution arises from the different phase shifts accumulated between the electrons and the reflected optical field in copropagating (positive α) and counterpropagating (negative α) configurations.

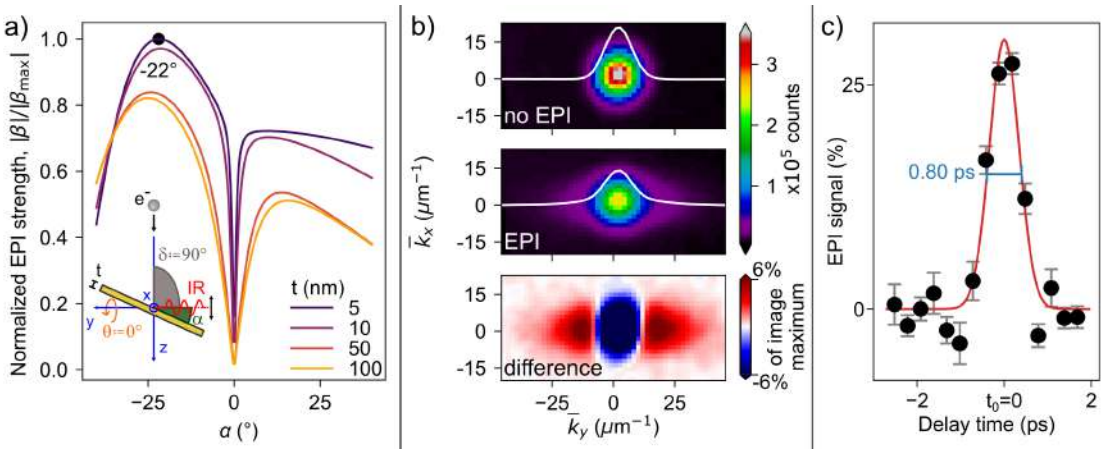

Figure 4.3: ***Analysis of EPI.*** ***a)*** *Simulated interaction strength as a function of the gold-film tilt angle α, accounting for non-perfect mirror conditions. The simulations are normalized to a maximum $\beta_{max} = 0.8$, extracted by comparing the simulated spectra with experimental measurements, as in the SI of Ref. [50]. The maximum EPI strength occurs at $\alpha = -22°$, which is used in all subsequent measurements. The inset illustrates the experimental geometry of EPI at the PELM film.* ***b)*** *high dispersion diffraction patterns of the e-beam under different conditions: without laser illumination (top panel), after interaction with IR photons (central panel), and their difference (lower panel). The interaction broadens the electron wave function along the k_y direction (laser propagation axis) and redistributes the intensity, reducing the signal near $k = 0$ and increasing it at higher k_y.* ***c)*** *Temporal evolution of the EPI signal (defined in the main text) as a function of the laser-electron pulse delay. Black dots are data, the error bars are derived from the covariance of the fit used to extract the EPI signal and red-solid line is a Gaussian fit. The extracted full width at half maximum (FWHM) is $800 \pm 30\,\text{fs}$. We define the temporal overlap t_0 between the two pulses as the center of the Gaussian.*

We measure EPI by imaging the transverse momentum distribution of the e-beam in high dispersion diffraction (HDD) mode using a 100-m camera length on a direct electron detector (see Sec. 3.4.4 for further information). The large camera length is crucial for detecting small momentum transfers. Indeed, the interaction imparts discrete multiples of the film-projected angular wave vector of light, $k_L = (2\pi/\lambda)\cos^2(\alpha) = \frac{2\pi}{1030\,\text{nm}}\cos^2(22°) \approx 5.2\,\mu\text{m}^{-1}$, which is equivalent to an angular deflection of $\theta \approx (k_\perp/k_\parallel) = k_L/(2\pi/\lambda_e) \approx 2.1\,\mu\text{rad}$, where $\lambda_e \approx 2.5\,\text{pm}$ is the relativistic de Broglie wavelength for 200-keV electrons.

Figure 4.3b presents HDD momentum patterns of the e-beam under different conditions. In the absence of EPI (no laser pulse), the e-beam has a Gaussian momentum distribution (top panel). In the central panel, following interaction with IR photons, the electron distribution broadens along the k_y-axis, corresponding to the laser propagation direction [50]. From the top panel of Fig. 4.3b, we extract the standard deviation $\sigma_k = 5.45(1)\,\mu\mathrm{m}^{-1}$ of the wave vector distribution, comparable to the expected sideband separation $k_L \approx 5.2\,\mu\mathrm{m}^{-1}$. As a result, the individual sidebands overlap, merging into the smooth profile presented in the central panel, despite the underlying quantized interaction. The lower panel in Fig. 4.3b displays the difference between the upper two panels, enhancing the contrast to clearly highlight the effect of EPI. The interaction reduces the electron signal around $k = 0$ while increasing it at higher k_y values.

We performed the experiment as a function of the delay time between laser and electron pulse to achieve a precise temporal overlap between the two (t_0: delay time = 0 ps). The results are shown in Fig. 4.3c. The EPI signal is represented by the depletion of the direct e-beam and we quantify it as $1 - A_{\mathrm{Voigt}}$, where A_{Voigt} is the amplitude of a Voigt function fitted to the normalized k_y-integrated pattern. The Voigt function was chosen to take into account both homogeneous (Lorentzian) and inhomogeneous (Gaussian) broadening. The temporal evolution of the EPI signal reveals a full width at half maximum (FWHM) of 800 ± 30 fs, consistent with previous studies [32].

4.4 Pre-sample, Transverse e-beam Shaping with Structured Light

Having demonstrated the ability to detect the effect of EPI on the electron wave function in momentum space, we performed 4D Light-Scanning TEM (4D-LSTEM) experiments to demonstrate transverse spatial modulation of the e-beam. In 4D-STEM, a focused e-beam is scanned across the sample while simultaneously capturing at each scan position a convergent-beam electron diffraction pattern, providing phase contrast analysis of the material under investigation [8]. Here, a focused light beam is scanned across the e-beam on the PELM film while simultaneously capturing at each scan position an HDD electron diffraction pattern (see also Fig. 4.3b), providing transverse phase contrast analysis of the shaped e-beam. Therefore, in our case of 4D-LSTEM, is the portion of light-modulated electrons to be scanned across the sample.

Figure 4.4 illustrates the experiments conducted with this 4D-LSTEM approach, with the electron and laser pulses in temporal overlap. A 20-μm aperture (as the ones commonly used in a TEM column) is placed in the sample holder, downstream of the PELM stage (see Fig. 4.1). This aperture, smaller than the laser spot size, selects the electrons that interacted with a homogeneous portion of the electromagnetic field, condition needed for coherent interaction [44]. Electrons passing through the most intense regions of the laser beam interact with more photons, resulting in a stronger EPI signal, and vice versa.

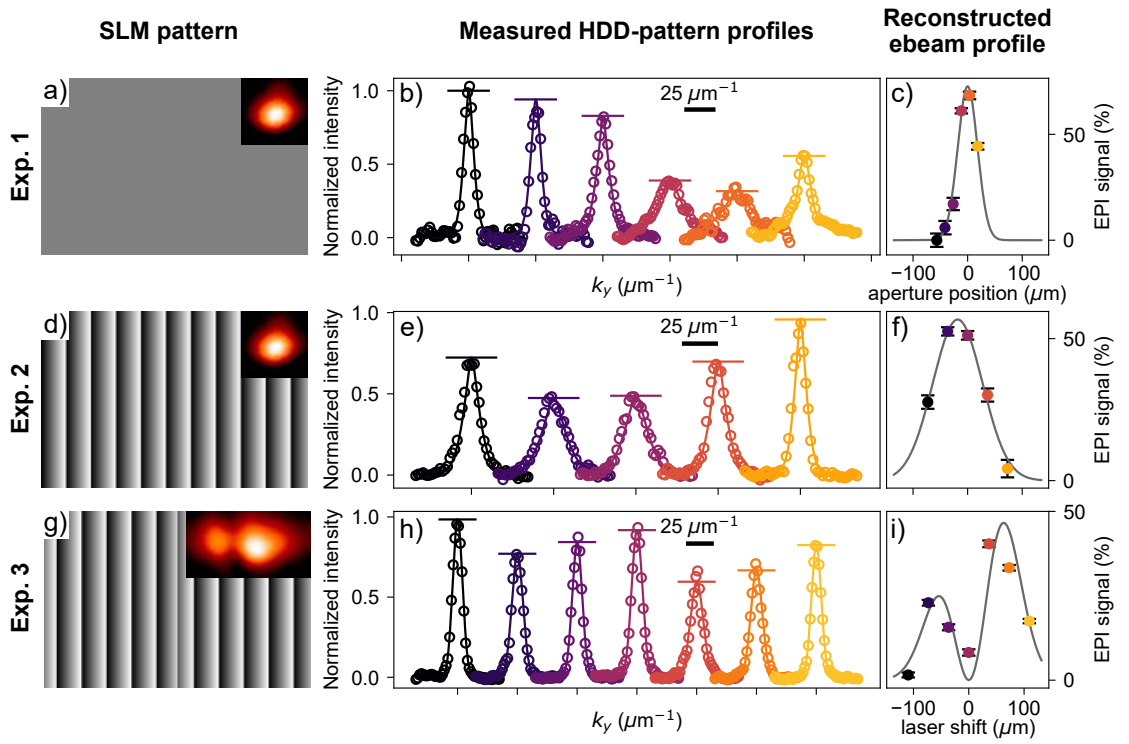

Figure 4.4: ***Reconstruction of e-beam transverse profiles at UniMiB. a,d,g)*** *patterns displayed by the SLM. The color scheme consist of a gray level of the pixels going from 0 to 255 to represent a laser phase shift from 0 to mod 2π. The insets show the modulated laser transverse profile recorded with a CCD camera in the conjugate plane (see Sec. 3.1.1 for further details on the experimental setup).* ***b,e,h)*** *k_x-integrated profiles (circles) of the HDD patterns acquired at maximum EPI. The colors represent different aperture positions (b) or laser shifts (e,h) coordinated with panels c,f,i). The curves are laterally shifted for clarity. Solid curves are Voigt function fits while horizontal lines represent the fitted amplitudes A_{Voigt}.* ***c,f,i)*** *Electron-photon interaction (EPI) signal, $1 - A_{\mathrm{Voigt}}$, as a function of the aperture position (c) or the laser shift (f,i). Dot colors in these panels match the corresponding profiles in panels b,e,h. The gray line is a gaussian fit (c,f) or a representative profile of the Hermite-Gaussian 01 mode (i).*

The first row of Fig. 4.4 depicts the initial experiment, in which the SLM serves as a simple mirror (pattern shown in panel a); the laser transverse profile is Gaussian, as shown in the inset. The aperture is scanned across this laser profile, and for each position, an HDD electron pattern is taken (as in Fig. 4.4b) before and at t_0 (see Fig. 4.4c). The pre-t_0 images serve as reference to normalize the k_x-integrated profiles measured at maximum interaction. The resulting profiles, shown as circles in panel b, are fitted with a Voigt function (solid curves in panel b) and the fitted amplitudes are displayed as horizontal lines. Panel c shows the EPI signal, $1 - A_{\mathrm{Voigt}}$, as a function of the aperture position, effectively reconstructing the e-beam profile at the aperture (sample) plane. We estimate the Gaussian-modulation diameter of the e-beam (at $1/e^2$ intensity) to be approximately $72 \pm 5\,\mu$m.

The second row of Fig. 4.4 presents a similar experiment where the aperture remains fixed while the laser beam is scanned across the PELM film using the SLM. In this case, a blazed grating (shown in panel d) is employed to shift the laser beam in a controlled manner, based on the diffraction condition for the first order: $\Delta\delta = \lambda\Delta n/H$. Here, $\Delta\delta$ is the laser tilt change, H is the SLM horizontal dimension and Δn is the difference in the number of grating periods, which is varied to scan the laser on the PELM stage. From these calculations, we can estimate the Gaussian modulation diameter at the PELM plane to have a $1/e^2$-diameter of $180 \pm 20\,\mu$m. By comparing panel f with panel c, we deduce that the e-beam has been de-magnified by a factor 2.5 between the PELM and the sample plane, consistent with the almost-parallel configuration of the e-beam post-PELM (see Sec. 3.4.4) and verifying that experiment 1 and experiment 2 give the same result.

To further validate the transverse shaping capability of our setup, we performed a two-dimensional scan of the laser beam across the PELM plane. This experiment complements the one-dimensional modulation shown in Fig. 4.4f by demonstrating control along both transverse directions. The resulting two-dimensional reconstuction of the e-beam modulation in Fig. 4.5.

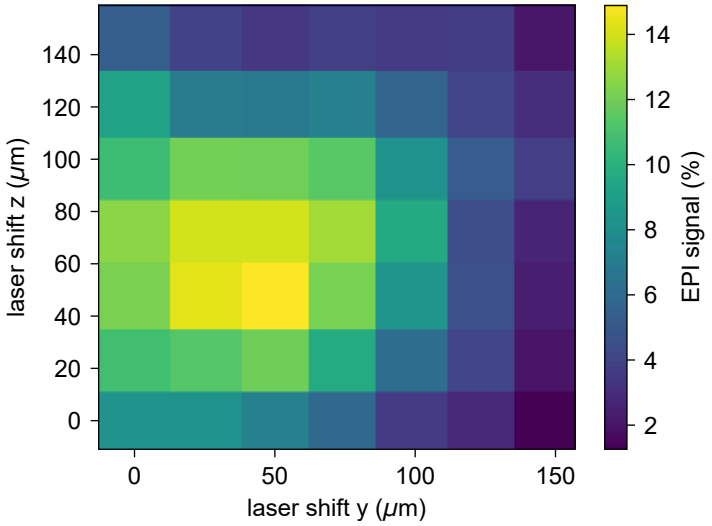

Figure 4.5: ***Two-dimensional laser scan.*** *EPI signal as a function of the laser shift along y and z, as defined for Fig. 4.2.*

The third row of Fig. 4.4 depicts a further variation of the experiment, using a different SLM pattern. Here, a horizontal phase shift is superimposed on the blazed grating pattern (panel g), producing a two-lobed Hermite-Gaussian profile HG_{01} in the far field, as shown in the inset of panel g. The integrated HDD patterns in panel h allow reconstruction of the e-beam profile (panel i), which mirrors the two-lobed shape imparted by the light beam.

4.5 Conclusions

Our results demonstrate the successful implementation of programmable transverse e-beam shaping using the PELM in a pre-sample geometry. By exploiting EPI with structured light shaped via an SLM, we have shown that transverse modulations can be imprinted on the e-beam and preserved during propagation through the microscope column down to the sample plane.

The experiments validate not only the shaping capability, but also the coherence conditions required for interaction, the ability to perform beam demagnification (here by a factor of 2.5), and the use of 4D-LSTEM to reconstruct the shaped beam profile. These findings establish the PELM as a ready-to-use platform for ultrafast measurements with shaped beams. In the following chapter, we will build on this capability to implement single-pixel imaging.

Chapter 5

Electron Single Pixel Imaging

The ability to coherently modulate the electron wavefunction, demonstrated in the previous chapter, opens the path to novel imaging modalities that go beyond conventional TEM. Among these, electron single pixel imaging (ESPI) represents a particularly promising approach, where structured illumination replaces the need for a pixelated detector. In this scheme, the sample is interrogated with a sequence of tailored e-beam patterns, while a bucket detector records only the integrated transmitted intensity. From this series of bucket measurements, the image of the sample can be computationally reconstructed using appropriate algorithms. While SPI has been widely explored in the context of optics and X-rays, its extension to electron microscopy remained purely theoretical until EPI showed the potential to shape e-beams fast and on demand. The use of optically modulated e-beams for single-pixel imaging was first proposed in [28], but no experimental realization had been demonstrated.

The concept originates from optical single-pixel imaging [98, 99] and ghost imaging [100, 101], where spatial information is recovered through shaped light fields and computational post-processing. Transferring this paradigm to electron microscopy is motivated by several advantages. First, by designing sparse, low-intensity electron patterns (i.e. patterns that are mostly 'empty' or with low local dose), one can distribute the exposure across many minimally damaging illuminations, mitigating per-shot damage. This is analogous to sparse-sampling strategies in STEM that reduce beam damage while maintaining structural information [102]. Second, it allows the reconstruction of images from scalar observables—such as the EPI signal—thereby decoupling image formation from the use of pixelated detectors and extending the range of measurable contrasts. Finally, the information content of each exposure can be tailored to the sample, allowing symmetry-guided acquisitions compatible with compressive-sensing strategies [98, 103].

In this chapter, we first outline the theoretical basis of single-pixel imaging and the reconstruction algorithms implemented in our work. We then present two experimental

realizations of the method. The first is a proof-of-concept ghost-imaging experiment performed using the plasma-lensing effect. The second employs optically shaped e-beams to perform programmable ESPI on nanostructured membranes. The chapter concludes with a discussion of the current limitations and perspectives of ESPI within our UTEM platform.

5.1 Theory of Single-Pixel Imaging

The SPI concept can be regarded as the deterministic evolution of ghost imaging, the first approach to demonstrate that spatial information about an object can be retrieved without a spatially resolving detector [100, 101]. In ghost imaging, the object is illuminated with a sequence of random, non-deterministic patterns (such as speckle fields), and a single-pixel (or "bucket") detector records only the integrated transmitted or reflected intensity for each pattern. An image of the object is then reconstructed by correlating these bucket signals with the illumination patterns. Because the illumination is random, each pattern must be acquired and stored individually — for example, by splitting the beam and recording it with a pixelated detector, which limits ghost imaging to experimental demonstrations rather than practical imaging.

Building upon this concept, SPI replaces the random illuminations with a set of known, deterministic structured patterns, such as Hadamard, Fourier, or other orthogonal bases [98]. Since the patterns are predetermined, the reconstruction can be formulated as a linear inverse problem and solved efficiently with algorithms that exploit orthogonality or sparsity. This makes SPI naturally compatible with the framework of compressive sensing [103].

Compressive sensing allows for the recovery of high-dimensional signals from a small number of measurements, provided that the signal is sparse or compressible in some basis. Many natural images exhibit such sparsity: they can be accurately represented by a limited number of coefficients in the Fourier or wavelet domain. In the context of SPI, this enables accurate image reconstruction even when the number of measured patterns is significantly smaller than the number of image pixels. Mathematically, the reconstruction is typically obtained by minimizing the ℓ_1 norm of the solution under the measurement constraints, which promotes sparsity while preserving fidelity to the data.

In the context of SPI, the imaging system is described by a linear measurement model:

$$\vec{I} = \hat{P}\vec{T}, \tag{5.1}$$

where $\vec{T}$ is the unknown object vector (the flattened image), $\vec{I}$ is the array of N recorded intensities (one per pattern), and $\hat{P}$ is the matrix whose rows contain the intensity distributions of the N structured illumination patterns.

To quantify measurement efficiency, it is customary to define the sampling ratio (SR):

$$\mathrm{SR} = \frac{N}{N_{\mathrm{pix}}}, \tag{5.2}$$

where N_{pix} is the number of pixels in the reconstructed image. Conventional imaging requires $\mathrm{SR} \geq 1$, but in SPI, acceptable reconstructions can often be achieved with $\mathrm{SR} \ll 1$, thanks to compressive sensing. This is particularly advantageous for imaging light-sensitive or fragile samples, or for achieving high-speed acquisitions, since fewer measurements reduce both acquisition time and total exposure [98, 99].

Several algorithms exist to reconstruct $\vec{T}$ from the measured data. In our implementation, we tested the following three:

- **The traditional algorithm** [101] is simple and fast, enabling real-time reconstruction during acquisition. It estimates the object as:

$$\vec{T} = \frac{1}{N} \sum_{i=1}^{N} (I_i - \bar{I})\, \vec{P}_i, \tag{5.3}$$

  where I_i is the measured intensity for the i-th pattern, $\vec{P}_i$ is the corresponding pattern, and $\bar{I}$ is the average intensity across all patterns. If the patterns vary in total power, a normalized version is used:

$$\vec{T} = \frac{1}{N} \sum_{i=1}^{N} I_i \vec{P}_i - \frac{\bar{I}}{\bar{S}} \cdot \frac{1}{N} \sum_{i=1}^{N} S_i \vec{P}_i, \tag{5.4}$$

  where S_i is the total intensity of the i-th pattern and $\bar{S}$ is the average across all S_i.

- **The Alternating Projection (AP) algorithm** [104] is an iterative method that updates the object estimate using the discrepancy between predicted and measured intensities. At each iteration, the object is updated as:

$$\vec{T}_{\mathrm{new}} = \vec{T}_{\mathrm{old}} - \frac{\vec{P}_i^T}{\max(\vec{P}_i)^2} \cdot \frac{\vec{P}_i \cdot \vec{T}_{\mathrm{old}} - I_i}{N_{\mathrm{pix}}}, \tag{5.5}$$

  where N_{pix} is the number of pixels in the image. This method can handle noise and undersampling better than the traditional approach, though convergence is not guaranteed.

- **The Conjugate Gradient Descent (CGD) algorithm** [105] is a robust iterative solver for linear systems. It is proven to converge in at most n steps, where n is the number of pixels. The object update at iteration k is computed as:

$$\Delta\vec{T}^{(k)} = \frac{\vec{r}^{(k-1)^T} \vec{r}^{(k-1)}}{\vec{g}^{(k)^T} (\hat{P}^T \hat{P}) \vec{g}^{(k)}}, \tag{5.6}$$

where the residual is:

$$\vec{r}^{(k)} = \hat{P}^T \vec{I} - \hat{P}^T \hat{P} \vec{T}^{(k)}, \tag{5.7}$$

and the gradient direction is given by:

$$\vec{g}^{(k)} = -\vec{r}^{(k-1)} - \frac{\vec{r}^{(k-1)^T} \vec{r}^{(k-1)}}{\vec{r}^{(k-2)^T} \vec{r}^{(k-2)}} \vec{g}^{(k-1)}. \tag{5.8}$$

5.2 Electron Ghost Imaging with Plasma Lensing Effect: First Proof-of-Concept Experiment

In this section, we present the first implementation of ESPI using femtosecond electron pulses modulated by SLM-controlled infrared laser pulses. At the time of this experiment, the setup was not yet capable of achieving controlled EPI as described in Chap. 4. Instead, e-beam modulation relied on the plasma lensing effect induced by femtosecond laser excitation of a gold TEM grid, as discussed in Secs. 3.4.3 and 2.3. As a consequence, the experiment was conducted in point-projection mode rather than in the configuration of Chap. 4, where the detector was placed in the far-field to record the angular distribution or Fourier transform of the scattered electron beam (Fraunhofer configuration). In contrast, the point-projection configuration operates in the Fresnel near-field regime: a divergent electron beam originating from a localized point source creates a magnified geometric shadow of the object onto the detector.

The plasma lensing effect imparts complex and non-deterministic deflections of the e-beam, which we are not able to map back to the optical excitation in a programmable way. As a result, the structured electron patterns cannot be predefined or engineered, and must be acquired individually before imaging. This configuration is therefore more closely related to ghost imaging than to standard single-pixel imaging: the patterns are unknown and must be recorded one by one, while the sample response is measured separately as an integrated bucket signal.

We acquired a total of 280 distinct patterns by varying the PELM stage position, the position of the laser spot on the gold grid, and the time delay between the electron and optical pulses. For each PELM stage position, we first recorded the modulated beam patterns without the sample, and then measured the total transmitted intensities with the sample inserted.

The test sample consisted of nanoparticles of $Ti_3Al_{0.4}Sn_{0.6}C_2$, belonging to the class of MAX phases. MAX phases are layered, hexagonal materials with the general stoichiometric formula $M_{n+1}AX_n$ (where M is a transition metal, A is a metalloid, X is C, N, or B, and $n = 1$–4). While the non-oxidized phases exhibit high conductivity, their controlled thermal oxidation is crucial for developing electrochemically active composites suitable as

anodes for alkaline-ion batteries. This potential for energy storage applications motivates their selection for the SMART-electron project. The sample was synthesized by Irene Ostroman as part of the project. The microscope was first operated in parallel imaging mode, with the Objective MiniLens used to bring the sample into focus. The condenser lens was then adjusted to achieve the Fresnel imaging condition.

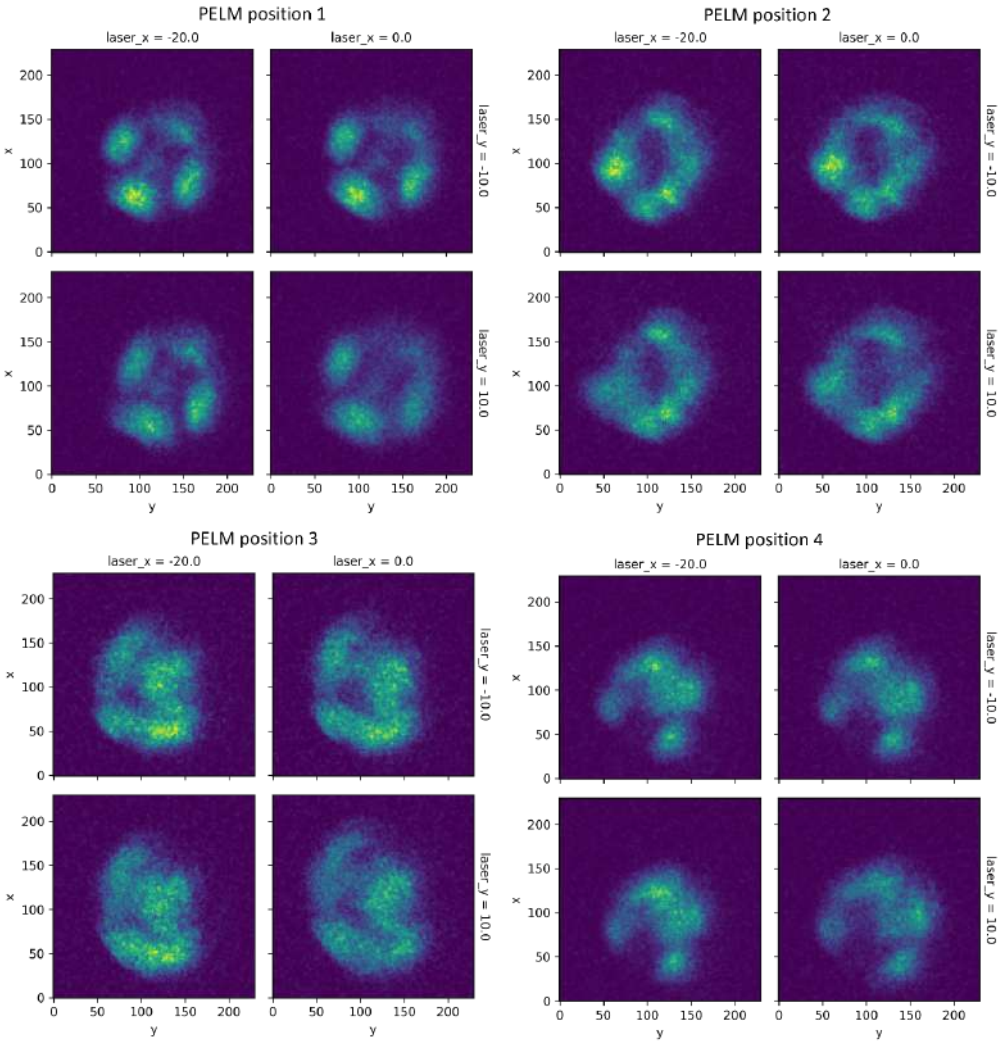

Figure 5.1: e-beam intensity patterns recorded at the detector without the sample for 16 representative patterns. Each pattern corresponds to a different combination of PELM stage position, laser spot position, and electron-photon delay.

Figure 5.1 shows a selection of recorded patterns. These were used as the measurement basis in the ESPI reconstruction. After recording the integrated intensity for each pattern with the sample inserted, we performed the image reconstruction using the traditional SPI algorithm described in Section 5.1. The data were 4x4 binned prior to reconstruction to improve the signal-to-noise ratio.

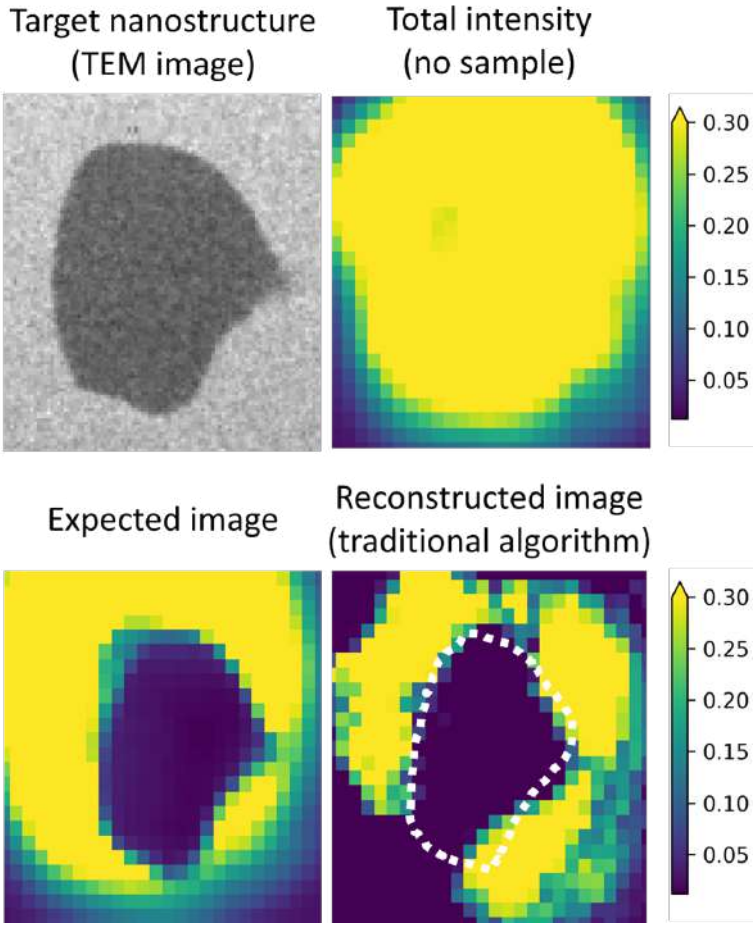

Figure 5.2: Experimental results of the first ultrafast ESPI reconstruction using the traditional algorithm. Top-left: reference TEM image of the MAX phase nanoparticle. Top-right: average of all patterns without sample. Bottom-left: average of all patterns with the sample, representing the expected image. Bottom-right: reconstructed image obtained from the single-pixel measurements using the traditional SPI algorithm.

The reconstructed image, shown in Fig. 5.2 (bottom right), reproduces the general shape and absorption contrast of the MAX nanoparticle. This constitutes the first demonstration of a SPI reconstruction using a light-modulated e-beam.

To further evaluate the reconstruction quality, the TEM group of CNR Nano in Modena (SE project partners) applied the AP and CGD algorithms to the same dataset. The results are presented in Fig. 5.3. The AP method produces results similar in quality to the traditional algorithm, whereas the CGD method performs more poorly. This outcome is likely due to the limited number of patterns (corresponding to a sampling ratio < 0.25) and the high noise level, consistent with previous studies on SPI algorithm performance under experimental conditions [106].

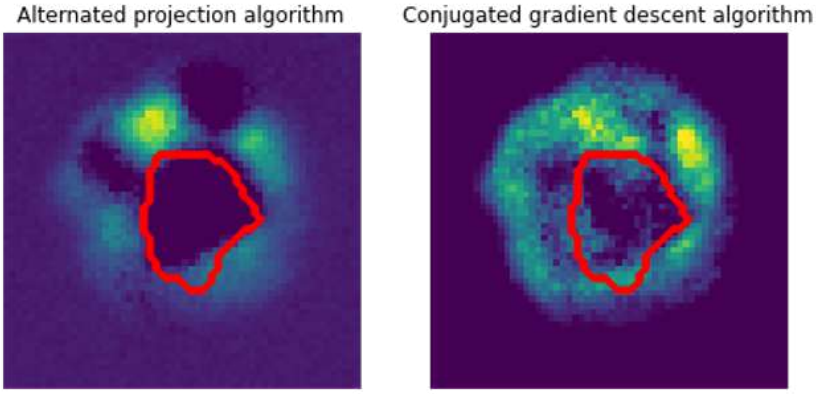

Figure 5.3: ESPI reconstructions of the MAX nanoparticle using: (left) the Alternating Projection algorithm and (right) the Conjugate Gradient Descent algorithm.

This proof-of-concept experiment demonstrates that the ESPI methodology is viable even in the absence of ideal beam shaping conditions. It also confirms the compatibility of our detector, sample holder, and acquisition protocol with ultrafast single-pixel imaging workflows. These results are a key step toward realizing fully programmable ESPI in our UTEM.

5.3 ESPI of Nanostructures via Electron-Photon Interaction Signal

Building on the proof-of-concept experiment presented in the previous section, we now demonstrate a realization of single-pixel imaging using programmable, deterministically shaped e-beams. In this configuration, shown in Fig. 5.4, the EPI signal is measured in HDD mode for a sequence of laser patterns imprinted by the SLM, exactly as described in Chap. 4. The only differences with respect to the experiments reported there are: (i) a nanostructured membrane is placed at the sample plane instead of a circular aperture,

and (ii) the C_3 lens is slightly more excited, resulting in a stronger demagnification (approximately $\times 6$) of the laser-imprinted pattern at the sample plane, in order to spatially resolve the structures. This leads to a pattern diameter of approximately $5\,\mu$m.

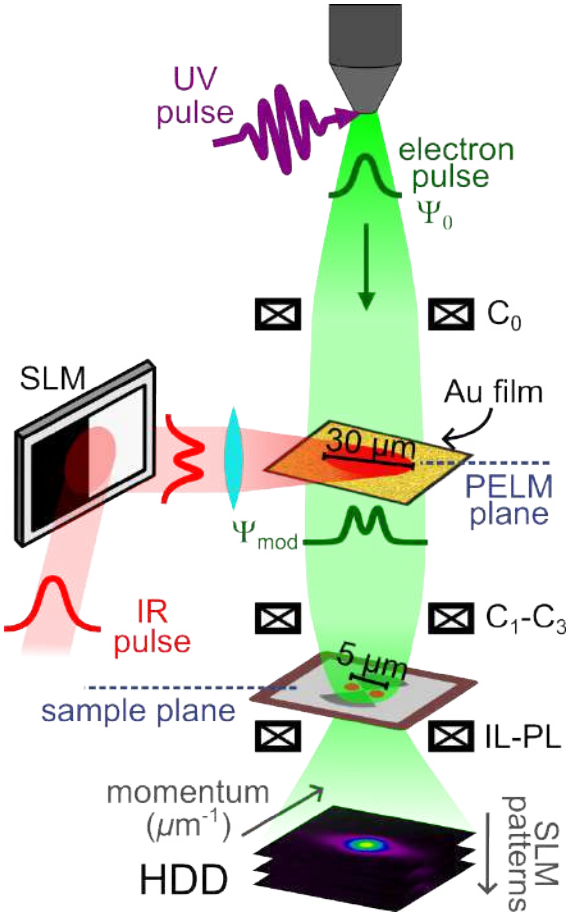

Figure 5.4: ***Schematic of the ESPI configuration with EPI detection.*** *The optical field shaped by the SLM interacts with the e-beam at the PELM plane via stimulated inverse transition radiation at a thin gold film. The modulated e-beam is focused by the condenser lenses onto the sample plane, where a nanostructured membrane is placed. The EPI signal is measured in high-dispersion diffraction (HDD) mode and used as a scalar input for single-pixel imaging reconstruction.*

The nanostructured samples consist of silicon nitride membranes coated on both sides with a thick silver layer, into which microcavities are milled by focused ion beam irradiation. They were fabricated by our CNR Nano partners. These patterned membranes act as effective spatial filters for the transmitted electrons: when the region of the e-beam that experienced EPI passes through the electron-transparent SiN area, the modulated component of the e-beam reaches the detector and contributes to the measured EPI signal; conversely, if it impinges on the Ag-coated region, the patterned electrons are blocked and the corresponding EPI signal is suppressed. As a result, the nanostructure spatially

modulates the measurable EPI signal for each illumination pattern. Thus, in these experiments, the EPI signal serves as the scalar value used for image reconstruction, replacing the total transmitted intensity introduced in Sec. 5.1.

5.3.1 Reconstruction of the SMART-electron Logo

We now demonstrate the reconstruction of a complex nanostructured pattern—the SMART-electron (SE) project logo shown in Fig. 5.5b—using the SPI method described above. A Gaussian laser spot is scanned laterally across the PELM plane by applying a blazed grating pattern to the SLM, as done in the experiments of Chap. 4. Each laser position modulates the e-beam at a different location, effectively raster-scanning the modulated beam across the SE logo. For each scan position, the EPI signal is extracted from the HDD pattern (as in Chap. 4) and used as a scalar measurement. By assembling these values according to the corresponding scan coordinates, we reconstruct the spatial structure of the sample.

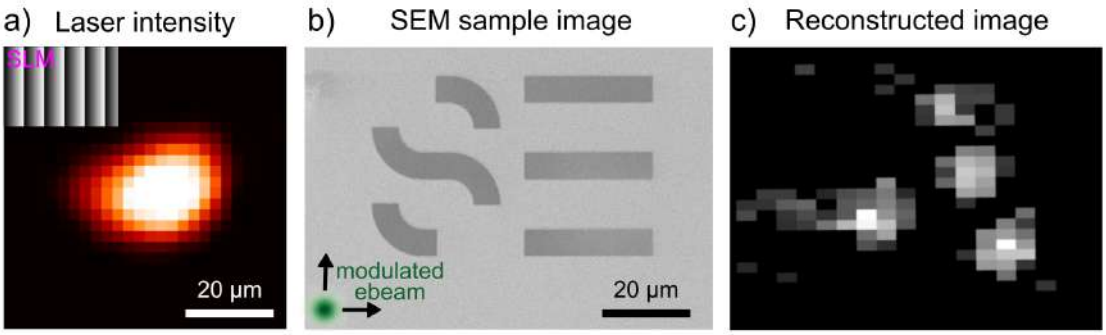

Figure 5.5: ***ESPI reconstruction of the SMART-electron logo using a scanning protocol.*** *(a) Laser intensity profile at the PELM plane corresponding to the blazed grating displayed on the SLM. (b) SEM image of the nanostructured membrane patterned with the SMART-electron logo. (c) Reconstructed image obtained from the EPI signal, showing the spatial features of the sample.*

5.3.2 Symmetry-Guided Reconstruction of Siemens Stars

In this experiment, we explore how prior knowledge of the sample's structure can be exploited to guide the single-pixel imaging protocol, an approach conceptually inspired by compressive sensing. Instead of scanning the shaped e-beam across the sample plane, we rotate it in discrete angular steps and measure how the EPI signal varies as a function of rotation angle. This allows us to probe the object's symmetry using a minimal number of measurements.

The first sample consists of a nanostructured membrane patterned with a Siemens star

exhibiting four-fold ($\pi/2$) rotational symmetry, shown in Fig. 5.6b. We use a Hermite-Gaussian beam with a matching four-lobed symmetry (HG_{11}), shaped by the SLM and demagnified by the CL system onto the sample plane. By changing the SLM pattern, we rotate the laser beam in steps, each time measuring the EPI signal in HDD mode (see Fig. 5.6).

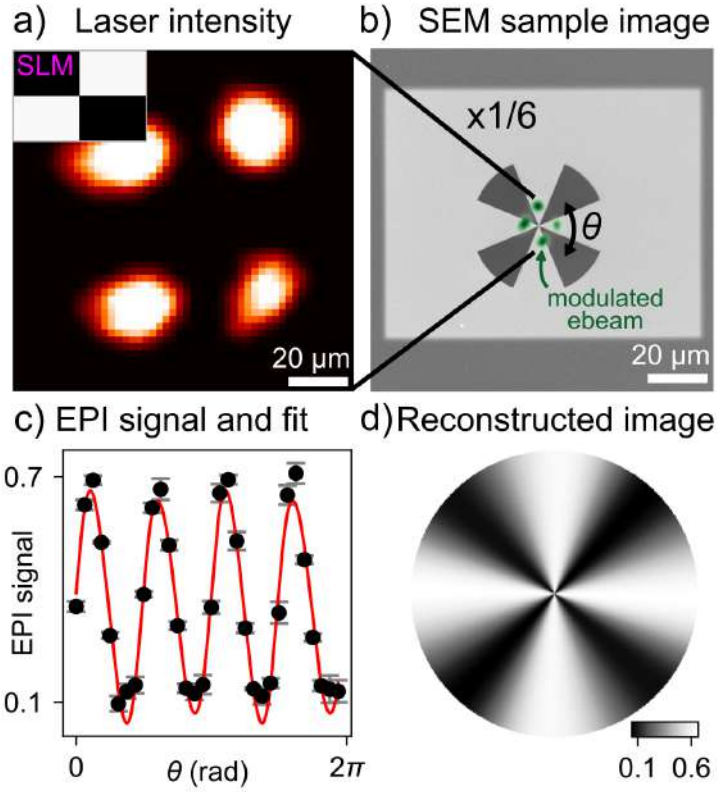

Figure 5.6: ***Symmetry-guided ESPI reconstruction of a four-spokes Siemens star.*** *(a) Four-lobed Hermite-Gaussian beam profile displayed on the SLM. (b) SEM image of the nanostructured membrane patterned with a four-spoke Siemens star. (c) EPI signal measured as a function of laser beam rotation angle, showing clear $\pi/2$ periodicity. (d) Reconstructed image highlighting the object's angular symmetry. The color bar represents the EPI signal.*

The measured scalar signal oscillates periodically as a function of rotation angle, with a dominant component at four times the base frequency, consistent with the object's symmetry. This angular response is well described by a low-order Fourier series, and the reconstructed image reflects the underlying $\pi/2$ periodicity of the structure (Fig. 5.6d). While this method does not retrieve absolute dimensions—since no lateral scan is performed—it demonstrates that structural information can be extracted from a low-dimensional measurement space when the symmetry is known.

This approach is conceptually similar to compressive sensing, where prior knowledge or sparsity assumptions reduce the number of measurements needed for reconstruction. Here, the symmetry of both beam and sample ensures that a small set of angularly rotated

patterns suffices to extract the dominant structural features.

We apply the same method to a second Siemens star patterned with two radial spokes, corresponding to a π rotational symmetry. In this case, we use a two-lobed Hermite-Gaussian laser beam (HG_{10}), rotated in discrete angular steps to match the symmetry of the structure. The EPI signal exhibits a clear π periodicity as a function of beam orientation, and the reconstructed image correctly reflects the two-fold symmetry of the object, as shown in Fig. 5.7. This result confirms the generality of the approach, highlighting how prior knowledge of symmetry can enable efficient single-pixel reconstructions with minimal measurements.

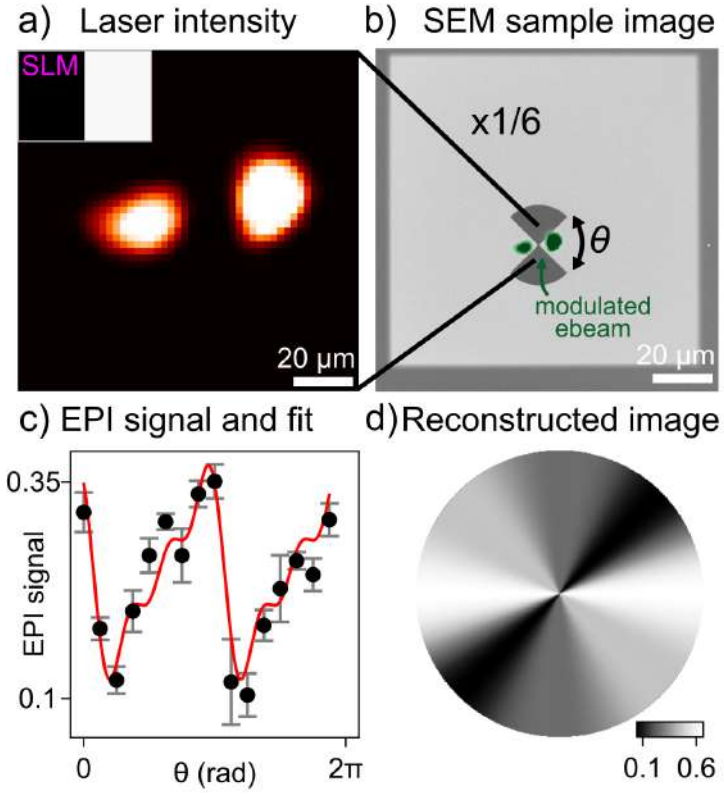

Figure 5.7: ***Symmetry-guided ESPI reconstruction of a two-spokes Siemens star.*** *(a) Two-lobed Hermite-Gaussian beam profile displayed on the SLM. (b) SEM image of the nanostructured membrane patterned with a two-spoke Siemens star. (c) EPI signal measured as a function of beam rotation angle, showing clear π periodicity. (d) Reconstructed image highlighting the object's two-fold angular symmetry. The color bar represents the EPI signal.*

5.4 Conclusions and Outlook

In this chapter, we have demonstrated the implementation of ESPI using optically modulated e-beams shaped via EPI through our PELM device. By selectively imprinting structured laser patterns onto the e-beam at the PELM plane, and measuring the EPI signal in HDD mode, we have reconstructed a variety of nanostructured objects using the single-pixel framework.

Two experimental regimes were explored. First, we demonstrated a proof-of-concept ghost imaging experiment using a laser-induced plasma lensing effect, validating the ESPI method in our UTEM. Second, we exploited programmable beam shaping to perform single-pixel reconstructions of nanostructured membranes, using either spatial scanning or symmetry-guided rotation protocols. The reconstruction signal was the EPI component, extracted as a scalar value from pixelated detector images and interpreted in the single-pixel imaging formalism. While no full SPI matrix inversion was performed, we showed that even minimal sets of measurements can retrieve meaningful structural information, particularly when guided by prior knowledge.

It is worth pointing out that, although the original modulation is defined on the laser field and thus limited in resolution by the optical wavelength of 1030 nm (Abbe criterion), once imprinted onto the e-beam, the pattern can be further demagnified by the TEM optics. In these experiments, we already approach this optical limit by reducing a 30 µm laser modulation to approximately 5 µm at the sample plane. Thus, the resolution of the modulated e-beam is ultimately determined not by the wavelength of the optical field, but by the electron optics themselves. In principle, the pattern could be further reduced to reach nanometric resolution.

In the present configuration, however, this was not pursued. The modulation was condensed using C_3, with the distance from the PELM to C_3 (p) being comparable to that from C_3 to the sample (q). According to the lens magnification relation $m = -\frac{q}{p}$, this geometry leads to $m \approx -1$, and therefore limits the achievable demagnification. Alternative schemes involving the objective lens could in principle overcome this constraint in future experiments.

Overall, while the present implementation remains inefficient and limited in resolution, it establishes a novel paradigm in electron microscopy: the reconstruction of real-space objects using programmable, light-mediated electron-sample interactions. This approach could become particularly valuable in dose-sensitive regimes, or when prior knowledge about the sample—such as symmetry or sparsity—can be used to minimize the number of required measurements. Moreover, the ability to reconstruct images using only electrons that underwent a controlled light-matter interaction suggests a path toward selective imaging strategies. In the long term, these results represent a first step toward shaped e-beam imaging protocols that exploit the unique combination of programmable optical modulation and electron optics, potentially enabling low-dose reconstructions, selective probing with nanometric resolution.

Chapter 6

Beam Shaping Experiments and Ultrafast Studies on Complex Materials at EPFL

As part of the SMART-electron European project, the LUMES laboratory at EPFL contributed to the development of advanced electron-light interaction schemes for UTEM. The objective was to implement a PELM via a mechanically compact solution integrated within the sample holder, enabling pre-sample e-beam shaping without the need for integrating a customized extra section of the TEM column. The goal, analogous to the implementation at UniMiB explained in Chap. 1, was to encode phase and amplitude modulation onto the e-beam immediately before it interacts with the sample, enabling phase resolved measurements of light-driven phenomena.

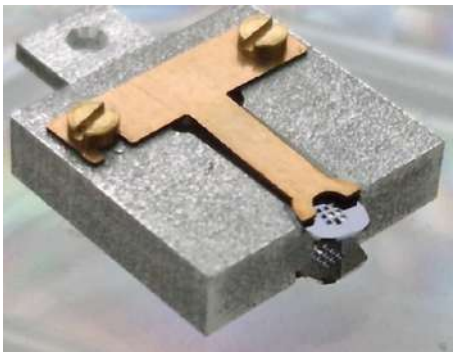

Figure 6.1: Sample-stage PELM implementation developed at EPFL. The image shows the fabricated sample holder, in which a TEM grid with a thin silver film is mounted under a copper support arm. A femtosecond laser pulse is focused onto the grid with Ag/Si_3N_4 to modulate the e-beam before it reaches the sample. The distance between the modulator and the sample plane is approximately 1.5 mm. Courtesy of Thomas Lagrange.

To realize this, a custom two-grid sample holder was designed and fabricated, as shown in Fig. 6.1. The holder allows two standard TEM grids to be mounted with a fixed separation of approximately 1.5 mm. The top grid contains a thin Ag-coated Si_3N_4 film that reflects the incoming femtosecond laser pulse and mediates EPI (see Sec. 2.2), shaping the transverse and longitudinal structure of the electron wavefunction. The bottom grid hosts the sample and is independently illuminated by a time-delayed pump pulse. This configuration enables pre-sample beam shaping without the need for optical access ports in the upper column or extensive modifications to the microscope. The short separation between the modulator and the sample makes the preservation of the imprinted spatial structure straightforward; in contrast to the UniMiB configuration where a complex lens setting was required to ensure that the e-beam coherence would be preserved along the larger PELM-to-sample distance.

The optical layout envisioned for this configuration is illustrated in Figure 6.2. A femtosecond laser pulse is split into three branches: one for photoemission, one for shaping the e-beam at the top grid, and one for exciting the sample at the bottom grid. Although the mechanical implementation of the holder was successfully completed, the full optical alignment and temporal synchronization required for electron-light interaction at the modulator grid were very challenging and thus were not achieved within the available timeframe of one year. Consequently, the experiments performed at EPFL relied on a standard UTEM configuration, using a single laser beam either to induce a specific transverse e-beam modulation or to excite the sample without any pre-sample modulation.

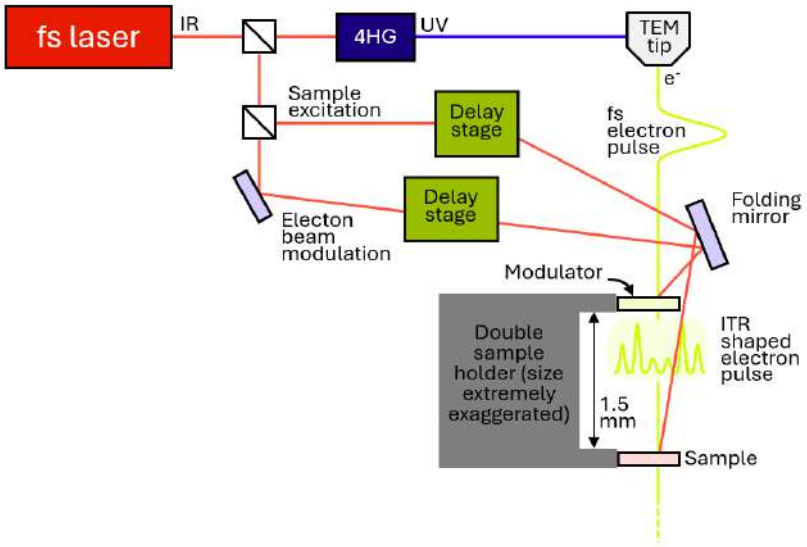

Figure 6.2: Conceptual optical layout for the EPFL sample-stage PELM configuration. The laser is split into three branches to independently control photoemission, e-beam modulation at the top grid, and sample excitation at the bottom grid. The compact geometry avoids the need for upstream optical access ports by integrating the modulator directly into the sample holder.

Nevertheless, this configuration remains relevant for future implementations and could enable novel experimental schemes, especially for time-resolved phase-sensitive imaging of

complex materials. One notable example is Cu_2OSeO_3, a multiferroic Mott insulator that hosts Bloch-type magnetic skyrmions coupled to electric polarization. Recent studies have demonstrated the optical creation of metastable skyrmion phases in this material using femtosecond near-IR pulses [107]. Phase-structured e-beams generated by a sample-stage PELM could be used to investigate skyrmion helicity, rotation, or other ultrafast dynamics beyond the capabilities of conventional Lorentz-TEM [108, 109]. Such approaches would benefit from the short propagation distance and high coherence of the modulated beam at the sample plane.

In this chapter, we first describe the experimental configuration of the EPFL UTEM, including the optical layout, beam routing, and detection scheme. We then present transverse e-beam shaping experiments performed at the sample stage, where Hermite-Gaussian optical modes are imprinted onto the e-beam via inverse transition radiation. The second part of the chapter reports ultrafast diffraction and spectroscopy studies on two representative systems: the icosahedral quasicrystal iAlPdMn and 30° twisted bilayer graphene. These experiments explore lattice and plasmon dynamics under femtosecond optical excitation.

6.1 Experimental Setup

The experiments presented in the following sections were performed on a JEOL JEM-2100Plus microscope located at EPFL and operated in standard UTEM configuration. As in the UniMiB implementation (see Sec. 3.1), the setup employs photoemission from a Schottky cathode triggered by a UV pulse derived from a femtosecond laser. Similarly, two additional TEM column sections are required for this standard UTEM operation: (i) the section with the aluminum mirror for UV injection and (ii) the C_0 lens module to refocus the beam upstream of the condenser system (see Section 3.2). A key distinction between the EPFL and UniMiB setups is the integration of an in-column electron energy-loss spectrometer (EELS): the Gatan Quantum SE with imaging filter. This spectrometer played a central role in several of the experiments presented in this chapter. The spectrometer is coupled to a Gatan UltraScan 1000 CCD camera.

Although LUMES has a long-standing track record in UTEM, the setup used for these measurements is effectively a new platform. In the years preceding my arrival, the laboratory underwent major changes: the TEM, the femtosecond laser, and the detector were all replaced, and the previous experimental infrastructure was dismantled. Together with the EPFL team, I contributed to rebuilding the UTEM platform, implementing beam routing, harmonic generation stages, delay lines, and diagnostics, and performing the alignment procedures needed to achieve spatiotemporal overlap. The configuration described below reflects the result of this integration phase and is used for the experiments presented in this chapter.

The laser source is a commercial Yb-based femtosecond system (Satsuma, Amplitude),

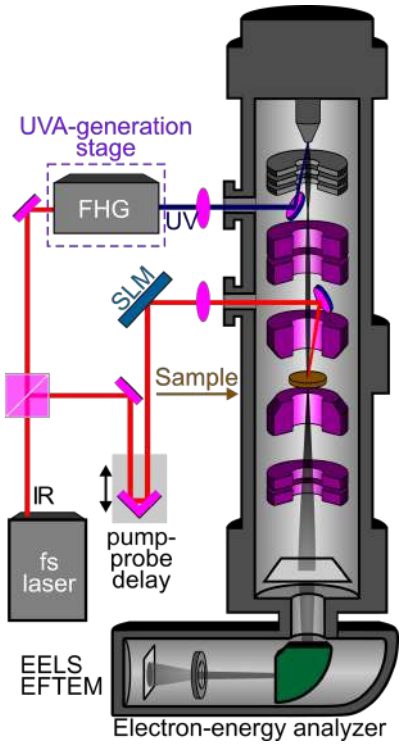

Figure 6.3: Schematic of the optical setup implemented at EPFL. A femtosecond Yb-based laser (1030 nm) is split into two branches: one for fourth-harmonic UV photoemission (blue) and one for sample excitation (red). A delay lines are inserted in the IR branch for temporal synchronization.

emitting 1030 nm pulses with tunable repetition rate and pulse duration. The beam is split into two arms: one for UV generation and photoemission, and one for sample excitation. The optical layout is shown in Figure 6.3, and a photograph of the beam routing and microscope coupling is presented in Figure 6.4.

In the UV branch, the IR light is frequency converted to 257.5 nm via fourth-harmonic generation (FHG) and coupled into the cathode region to generate ultrashort electron pulses. In the pump branch, the IR pulse is directed to the sample plane to drive optically induced dynamics in the specimen under investigation. This branch optionally includes the same SLM used at UniMiB (Holoeye PLUTO-2 NIR-2), enabling structured optical excitation or beam shaping at the sample stage.

As a final remark, the same UTEM configuration was also employed during my stay for the experiments reported in Ref. [110], which investigated the cumulative effects of femtosecond laser excitation on the magnetostructural phase transition in freestanding FeRh thin films. By combining in situ Lorentz TEM with controlled laser irradiation, the study revealed that repeated phase cycling leads to the formation of dislocation networks that switch the nucleation mechanism from homogeneous to heterogeneous. I contributed to the operation of the ultrafast TEM during these measurements, assisting in the optical alignment, synchronization, and stability control that ensured successful data acquisition.

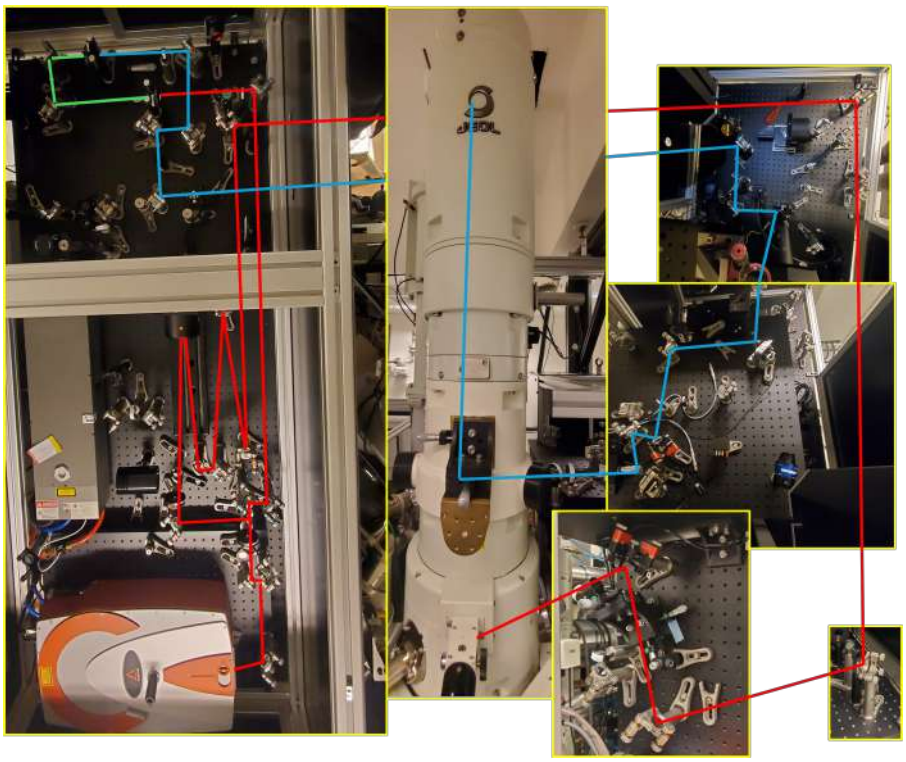

Figure 6.4: Photograph of the EPFL UTEM optical setup. The color-coded beam paths correspond to the sketch in Fig. 6.3. Insets show periscope modules, delay stages, and beam-routing optics used to deliver the UV and IR beams into the JEOL JEM-2100Plus microscope.

6.2 Transverse Beam Shaping at the Sample Stage

In this section, we present transverse e-beam shaping experiments in which the optical field interacts with the e-beam at the sample stage of the TEM. These experiments reproduce the configuration reported in previous EPFL experiments of Ref. [22], where an SLM-shaped optical field is used to imprint Hermite-Gaussian and vortex modes onto the e-beam via ITR and the PELM concept was proposed. While the interaction mechanism and geometry remained unchanged, we extended the analysis by acquiring a defocus series of the modulated beam.

The aim is to assess whether the observed transverse modulation includes a genuine phase component and to investigate how this phase structure evolves during propagation. In principle, a purely amplitude-modulated beam loses its structured profile rapidly under defocus, whereas a beam carrying transverse phase information—such as a Hermite-Gaussian mode—can preserve its nodal features over a finite defocus range, depending on the coherence properties of the e-beam. This behavior, compared against analytical models, provides an indirect probe of both phase imprinting and transverse coherence.

6.2.1 Experimental Geometry and Optical Modulation

The modulating structure used in these experiments consists of a 30 nm-thick silver layer deposited via sputtering at a rate of 5.8 Å/s onto a 20 nm-thick Si_3N_4 membrane supported on a silicon frame. The geometry is illustrated in Figure 6.5, adapted from [22]. The grid is mounted on a standard double-tilt TEM holder, enabling independent rotation around the transverse x and y axes. In particular, the plate is tilted by an angle ϑ around the y-axis (in-plane tilt) and by an angle α around the x-axis (out-of-plane tilt), allowing optimization of the interaction geometry.

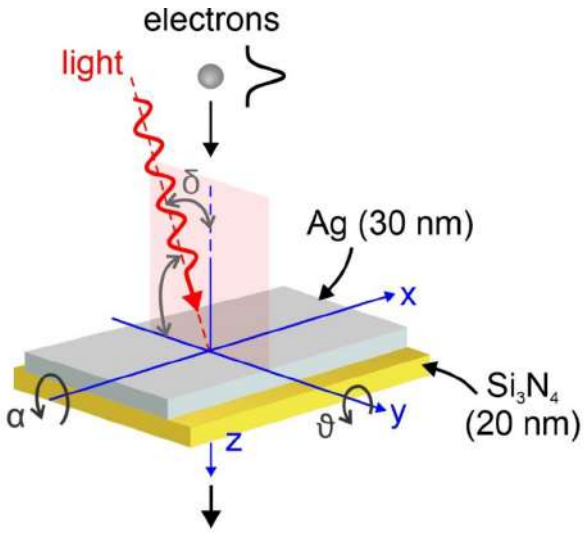

Figure 6.5: Schematic of the interaction geometry, adapted from [22]. The Ag-coated Si_3N_4 membrane is mounted on a double-tilt holder allowing independent rotation around the x and y axes. The incident laser pulse impinges at an angle δ, while the e-beam remains normal to the sample.

The sample is illuminated with 600 fs IR pulses at $\hbar\omega = 1.57$ eV and a repetition rate of 1 MHz. The peak electric field at the interaction plane is estimated to be on the order of 10^7 V/m. The optical beam is shaped using the SLM to generate the HG_{01} mode (a two lobed laser beam). The modulated laser beam is then focused onto the Ag/Si_3N_4 plate using a plano-convex lens with a focal length of 25 cm. This configuration places the SLM and the silver surface in conjugate optical planes.

A small fraction of the modulating laser beam is diverted by a beam sampler placed after the last focusing lens along the optical path. This fraction is directed onto an external beam profiler positioned at the same conjugate distance as the sample inside the microscope. In this way, the profiler provides a direct measurement of the optical intensity distribution at the interaction plane without perturbing the beam delivered to the TEM.

6.2.2 Defocus Series and Hermite-Gaussian Mode Evolution

To investigate the evolution of the shaped e-beam under propagation, we acquired a focal series by varying the objective lens defocus over a range from −4 mm to +4 mm. The transverse structure is generated by displaying a phase step on the SLM corresponding to an HG_{01} mode, as illustrated in Figure 6.6. The resulting optical field is focused onto the Ag-coated membrane, and the modulation imprinted onto the e-beam is probed by energy-filtered imaging. The images are acquired at zero delay to ensure temporal overlap between the laser and electron pulses, selecting only inelastically scattered electrons.

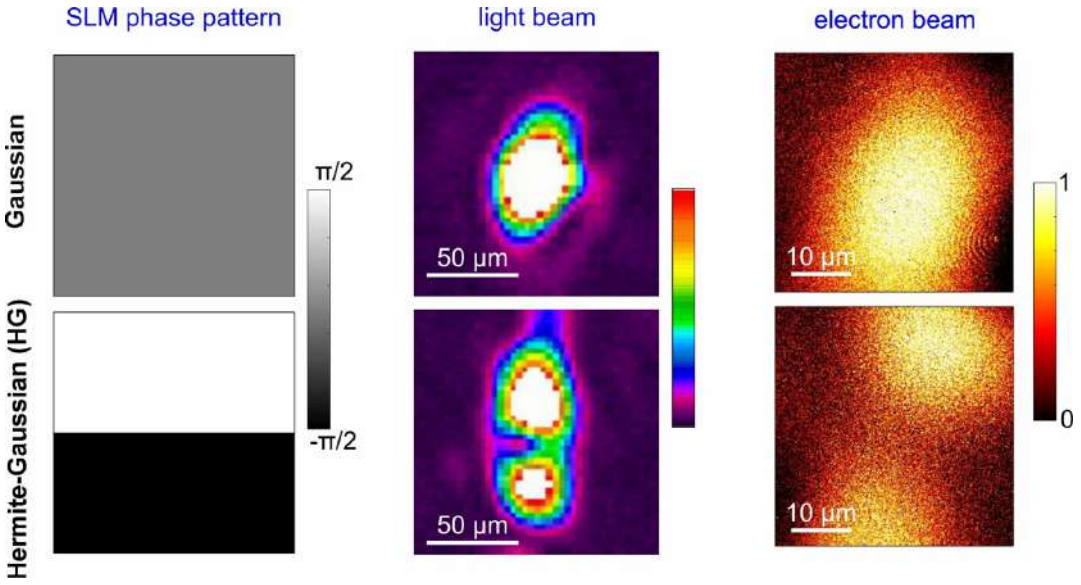

Figure 6.6: Generation and imprinting of a Hermite-Gaussian optical mode onto the e-beam. Left: SLM phase patterns for a Gaussian (top) and HG_{01} (bottom) modulation. Center: Corresponding transverse optical intensity profiles at the sample plane, measured with a beam profiler. Right: Energy-filtered images of the e-beam shaped via the ITR interaction, showing direct imprinting of the optical profile onto the electron wavefunction.

Images are recorded by selecting the +1 EPI sideband with the spectrometre, thus isolating only those electrons that underwent a single-photon interaction with the structured optical field. Figure 6.7 shows the resulting energy-filtered images acquired at different defocus values. This technique is analogous to phase contrast methods in Lorentz microscopy, where defocus reveals phase gradients through fringe visibility [111]. The central node remains clearly visible at all defocus values, while the intensity of the lobes progressively decreases. This behavior suggests that the phase structure of the HG_{01} mode is preserved upon propagation because the e-beam transverse coherence is high enough (see Sec. 6.2.3).

To analyze the evolution of the beam structure with defocus more quantitatively, we extracted one-dimensional line profiles from each energy-filtered image in the series. The profiles were obtained by averaging the intensity along the short axis of a fixed rectangular ROI, shown in red in Figure 6.7. This yields horizontal line profiles along the nodal

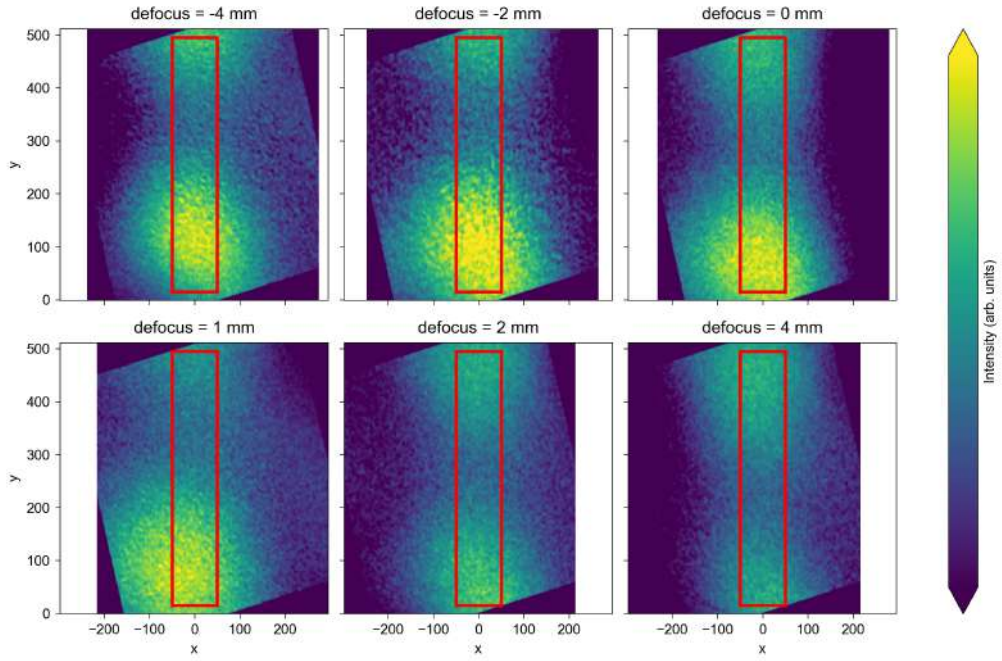

Figure 6.7: Energy-filtered images of the shaped e-beam at different objective lens defocus values, ranging from −4 mm to +4 mm. The red rectangle is the selected ROI for data integration (See next subsection).

direction of the HG_{01} mode. Before averaging, the profiles were spatially aligned to a common center, and a constant background —attributed to the residual zero-loss peak— was subtracted. Each profile was then normalized to the global maximum across the dataset to enable consistent contrast analysis.

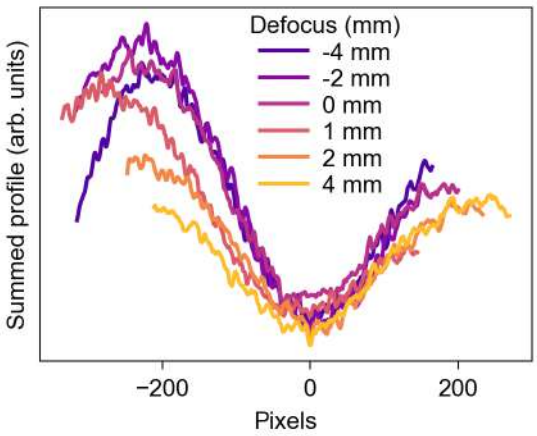

Figure 6.8: Normalized horizontal intensity profiles extracted from energy-filtered images at different defocus values between −4 mm to +4 mm.

Figure 6.8 shows the resulting profiles as a function of lateral position for defocus values ranging from −4 mm to +4 mm. As anticipated by the images, the central node remains clearly visible at all defocus values, while the intensity of the lobes progressively decreases. This behavior suggests that the transverse phase structure of the HG_{01} mode is preserved upon propagation, and that the loss of contrast is primarily due to limited spatial coherence. A more quantitative interpretation of this effect and an estimation of the coherence length are discussed in the following subsection through comparison with numerical simulations.

6.2.3 Simulation and Coherence Length Estimation

The degradation of the Hermite-Gaussian beam profile with defocus, observed in the previous section, is influenced by the finite transverse coherence length of the e-beam. To interpret this behavior quantitatively, our CNR Nano partner developed an analytical model of beam propagation in the TEM under partially coherent conditions. The goal is to evaluate how e-beam transverse coherence affects the visibility of structured beam features as the objective lens defocus is varied.

The idea behind the model is that the beam shaped by the light at the sample plane has a certain structure (in our case, a Hermite-Gaussian shape), but it is not fully coherent across its whole transverse extent. Instead, the beam can be thought of as made up of many small coherent patches, each about δ wide, the transverse coherence length. Each of these patches is focused by the TEM lenses, but since they are not phase-related to one another, they don't interfere globally. So the final image we see is not the coherent image of the entire beam, but rather the sum of all the individual sharp images from each patch. As defocus increases, these contributions begin to blur, and the structured features in the image, like the HG_{01} node, starts to fade. By simulating this effect for different coherence lengths δ, we can compare the results to the experimental images and extract an estimate for how coherent the beam actually was.

The analytical model is based on a simplified description of the microscope optics, illustrated schematically in Figure 6.9. The structured e-beam is assumed to enter the objective mini-lens in a parallel configuration, which is reasonable given the low magnification used during the experiment. The main contribution to image formation comes from the propagation through this lens, followed by free-space propagation to the image plane.

The beam entering the objective mini-lens is assumed to be a Hermite-Gaussian transverse mode:

$$\Psi_0(\mathbf{r}) = H_l\left(\frac{\sqrt{2}x}{w}\right) H_m\left(\frac{\sqrt{2}y}{w}\right) e^{-r^2/w^2} \tag{6.1}$$

where H_l and H_m are Hermite polynomials, w is the beam waist, and r is the transverse coordinate. We used $w = 20\,\mu$m to match experimental beam profiles.

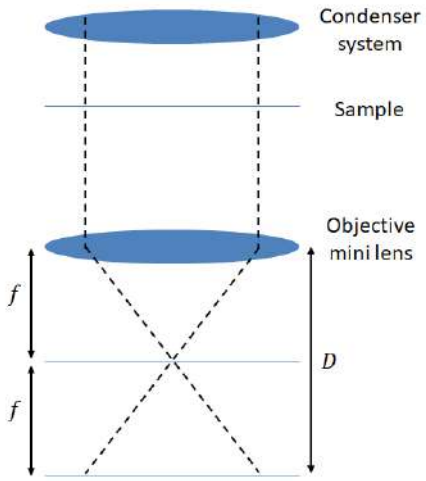

Figure 6.9: Simplified optical model used in the simulation. The shaped e-beam is focused by the objective mini-lens with focal length f, and observed at a defocus df. The image is formed at a distance D from the lens. The transverse coherence of the beam is modeled via local coherence patches of width δ.

The effect of the lens is described by a quadratic phase factor:

$$L(\mathbf{r}) = \exp\left(-i\frac{kr^2}{f+\Delta f}\right) \tag{6.2}$$

where k is the electron wave number (at 200 keV acceleration), f is the focal length of the lens, and Δf is the defocus.

Propagation from the lens to the image plane is described using the Fresnel impulse response:

$$h_D(\mathbf{r}) = \frac{e^{ikD}}{i\lambda D}\exp\left(i\frac{kr^2}{2D}\right) \tag{6.3}$$

To include partial coherence, we assume that only electrons within a transverse coherence patch of width δ interfere coherently. This is modeled using a Gaussian envelope:

$$P_\delta(\mathbf{r}) = \exp\left(-\frac{r^2}{2\delta^2}\right) \tag{6.4}$$

The image is obtained by incoherently summing the intensities from each coherence patch:

$$I(\mathbf{r}) = \int \left\|[\Psi_0(\mathbf{r})\cdot L(\mathbf{r})\cdot P_\delta(\mathbf{r}-\mathbf{r}_p)] * h_D(\mathbf{r})\right\|^2 d\mathbf{r}_p \tag{6.5}$$

Assuming δ is small compared to the variation scale of Ψ_0 and L, we can approximate:

$$\tilde{\Psi}_0(\mathbf{r}_p) = \int \Psi_0(\mathbf{r})P_\delta(\mathbf{r}-\mathbf{r}_p)d\mathbf{r} \tag{6.6}$$

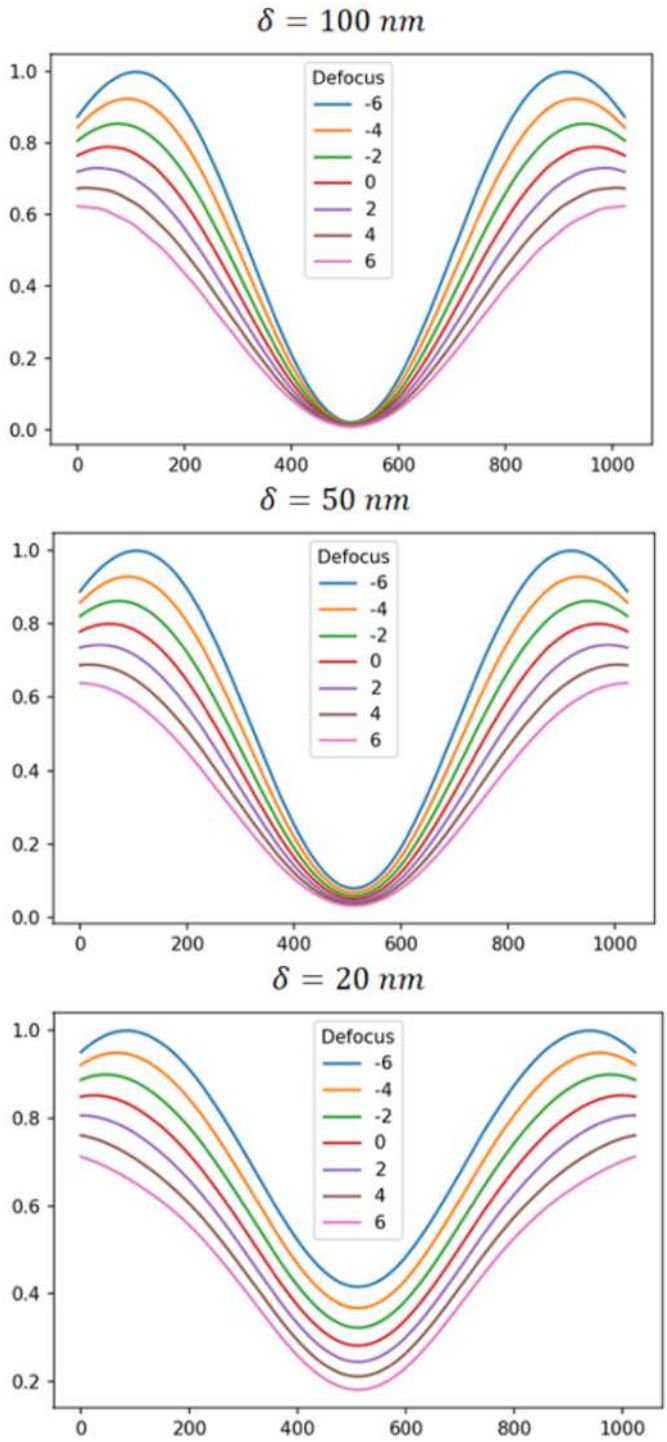

Figure 6.10: Simulated defocus series of the HG_{01} beam for different transverse coherence lengths: $\delta = 100\,\mathrm{nm}$ (top), $50\,\mathrm{nm}$ (middle), and $20\,\mathrm{nm}$ (bottom). Simulations were performed for a focal length $f = 100\,\mathrm{mm}$ and defocus range $\Delta f \in [-6, +6]$ mm. Smaller coherence lengths result in higher central intensity and blurring of the node, which is not compatible with the experimental profiles in Figure 6.8.

and expand the phase term $L(\mathbf{r})$ around $\mathbf{r}_p$ to obtain:

$$L_p(\mathbf{r}) = \exp\left(-i\frac{2k\mathbf{r}_p \cdot (\mathbf{r}-\mathbf{r}_p)}{f+\Delta f}\right)\exp\left(-i\frac{k(\mathbf{r}-\mathbf{r}_p)^2}{f+\Delta f}\right) \tag{6.7}$$

In this framework, the image can be expressed as:

$$I(\mathbf{r}) = \int \left\| \tilde{\Psi}_0(\mathbf{r}_p) \cdot \left[L_p(\mathbf{r}')P_\delta(\mathbf{r}'-\mathbf{r}_p) * h_D(\mathbf{r}-\mathbf{r}')\right]\right\|^2 d\mathbf{r}_p \tag{6.8}$$

This shows that the final image is the convolution of the coherent beam with the propagated coherence patch $I_P(\mathbf{r})$. As δ decreases, this kernel broadens, increasing image blur. However, at large negative defocus, lensing effects can compress I_P, partially recovering contrast.

The evolution of the propagated coherence patch I_P follows the Gaussian beam propagation law:

$$w(z) = w_0\sqrt{1+\left(\frac{z}{z_R}\right)^2} \tag{6.9}$$

where $z_R = \pi w_0^2/\lambda$ is the Rayleigh range and $w_0 = \delta$ is the initial coherence width. An effective propagation distance z_f through the lens system is given by:

$$z_f = \frac{4f(f+\Delta f)}{f+\Delta f} \tag{6.10}$$

By comparing the contrast degradation in the experimental profiles to this analytical model, we can extract the transverse coherence length δ as the parameter that best reproduces the observed visibility trend of Fig. 6.8. The key observable is the intensity at the center of the Hermite-Gaussian profile: in a perfectly coherent beam, the phase discontinuity at the node leads to zero intensity at the center. Partial coherence introduces additional intensity at this point, and the magnitude of this effect depends on both the coherence length and the defocus value, primarily due to the changing magnification of the coherence kernel.

Using the experimental parameters ($f = 100\,\text{mm}$ and defocus range $\Delta f \in [-6, +6]\,\text{mm}$), we simulated the HG_{01} beam evolution for different coherence lengths and compared it to the experimental profiles (Figure 6.8). A value of $\delta = 50\,\text{nm}$ yields a distribution that closely matches the experimental behavior. Smaller coherence lengths, such as $\delta = 20\,\text{nm}$, result in much greater central intensities and loss of nodal structure, which is not observed experimentally. Larger values (e.g., $\delta = 100\,\text{nm}$) yield flatter profiles, but the difference becomes too subtle to distinguish reliably due to experimental noise. We therefore conclude that the transverse coherence length of the e-beam is at least 50 nm under our conditions.

6.3 Ultrafast Electron Diffraction on iAlPdMn Quasicrystal

My interest in quasicrystals (QCs) was sparked by a talk given by Luca Bindi at the University of Milano-Bicocca, in which he presented the discovery of a natural quasicristalline phase in a meteorite from the Koryak Mountains [112]. The idea that long-range atomic order could exist without translational symmetry-violating the foundational rules of crystallography-was both counterintuitive and fascinating [113, 114, 115, 116]. Quasicrystals are precisely this kind of structure: ordered, but not periodic. They exhibit sharp diffraction patterns and forbidden crystal symmetries (such as fivefold or icosahedral), placing them between crystals and amorphous solids in a unique and still somewhat mysterious category. I was drawn to these systems not only for their conceptual beauty, but also because many fundamental questions about their stability and excitations remain open.

This interest evolved into an independent project during my research stay at EPFL, where I initiated an exploratory ultrafast diffraction study on the icosahedral phase of AlPdMn (iAlPdMn). This material, a stable ternary alloy, is a benchmark system in the QC literature as it can be grown as large, high-quality single grains [117]. We carried out the first UTEM experiments ever performed on iAlPdMn, using femtosecond laser excitation and time-resolved electron diffraction to probe its lattice dynamics. The goal was to explore whether one could access the phason degrees of freedom—collective rearrangements of atoms unique to quasiperiodic order—and gain insight into the thermodynamic stabilization mechanisms of the QC phase.

While the previous part of this chapter has focused on e-beam shaping, the measurements presented here shift the attention to the material itself. Using a standard UTEM configuration at EPFL, we investigated the structural response of a thin iAlPdMn lamella under ultrafast excitation. Although experimental challenges such as cumulative heating and lamella damage prevented the acquisition of conclusive time-resolved data, this work produced the highest-quality electron diffraction patterns of iAlPdMn ever obtained to our knowledge. It also defined important technical boundaries for future UTEM studies on quasicrystals, including the need for improved alignment, thermal control, and detector sensitivity.

6.3.1 Motivation

A fundamental question in quasicrystal research, still not fully clarified, concerns the thermodynamic stability of these structures [115, 118, 119]. Stability is generally discussed in terms of two competing influences on the material's free energy ($F = E - TS$, where E is internal energy and TS is the entropic contribution):

- **Energy Stabilization:** This scenario suggests the QC structure is the minimum energy state, potentially stable even at 0K [119]. In metallic systems like AlPdMn, the primary physical mechanism contributing to this stability is electronic stabilization [120, 121]. This stabilization occurs when a pronounced minimum (pseudo-gap) forms in the electronic density of states near the Fermi level, thereby lowering the overall electronic energy of the system [122].
- **Entropic Stabilization:** In this competing scenario the QC is only stable at elevated temperatures. This is because, the configurational entropy of QC is derived from the inherent structural fluctuations of quasiperiodic order, particularly the phason degrees of freedom (see Sec. 6.3.2), which become significant at high temperatures [118, 123, 124].

Direct evidence linking internal dynamics to stability in iAlPdMn is provided by high-temperature specific heat measurements. Above approximately 700 K, iAlPdMn exhibits a dramatic upward deviation of the specific heat at constant volume from the Dulong–Petit value ($3k_B$) [119, 123, 125]. This excessive heat capacity is a distinctive characteristic of QCs and is widely attributed to the thermal activation of phason degrees of freedom. This effect is systematically most pronounced in the QC compared to high-order approximants, suggesting it is tied directly to the unique quasiperiodic structural order.

Corroborating this picture, extensive X-ray and neutron diffuse-scattering studies have characterized the static distribution of structural fluctuations in iAlPdMn at high temperature [117, 118, 126, 127]. Diffuse scattering provides a unique signature of the phason degrees of freedom in aperiodic structures, as discussed in Sec. 6.3.2. These measurements revealed the counter-intuitive increase of diffuse intensity upon cooling, reflecting the softening of a phason elastic constant and signaling enhanced phason fluctuations at low temperature [118, 128]. This behavior marks a dynamical phase transition between activated and frozen phason states, rather than a structural transformation, kinematically forbidden in this material, and supports the view that entropic stabilization driven by phason motion governs the thermodynamic stability of iAlPdMn.

While these equilibrium studies identify the role of phasons, they do not capture their microscopic dynamics. Ultrafast electron diffraction (UED) provides a complementary, non-equilibrium approach: by exciting the quasicrystal with a femtosecond optical pulse and probing its response with ultrashort electron bunches, UED can directly resolve the lattice dynamics associated with both phonon and phason modes. Reaching the sensitivity required for diffuse scattering makes it possible to follow the transient population and relaxation of these modes in real time and to observe whether optical excitation can transiently drive the system across the activated-deactivated phason transition [46, 48, 129, 130].

At the same time, UED remains sensitive to electronically driven, reversible phase transitions, where photoexcitation modifies the electronic potential and transiently stabilizes a higher-symmetry phase [36, 37]. In the case of iAlPdMn, the laser pulse could unlock the kinetically hindered transformation that is inaccessible under equilibrium conditions,

providing a non-thermal pathway across the activated-deactivated phason transition. Our experiment is therefore designed to probe both regimes: the ultrafast phonon-phason dynamics characteristic of quasicrystals and the possible onset of a laser-induced dynamical phase transition in iAlPdMn.

6.3.2 Theoretical Framework: Lattice Dynamics in *i*-AlPdMn

To interpret the diffuse-scattering response of iAlPdMn and its connection to phason-mediated dynamics, it is necessary to recall the theoretical framework describing lattice excitations in quasicrystals. This section outlines the elastic and geometrical formalisms used to describe the atomic structure and collective modes of iAlPdMn, based on the six-dimensional (6D) hyperspace approach and generalized elasticity theory. These concepts provide the foundation for understanding how phonon-phason coupling governs the diffuse intensity distribution and guides the simulations presented in the following sections. The unique atomic dynamics of iAlPdMn are described using generalized elasticity theory and the hyperspace formalism.

Hyperspace Description and Cut-and-Projection Method [131]

The icosahedral quasicrystal can be described as the projection of a periodic lattice embedded in a six-dimensional (6D) hyperspace onto the three-dimensional (3D) physical space $E_{\parallel}$. The need for six dimensions arises from the fact that the icosahedron is defined by six independent vectors from its center to vertices, which cannot be accommodated within a 3D periodic lattice.

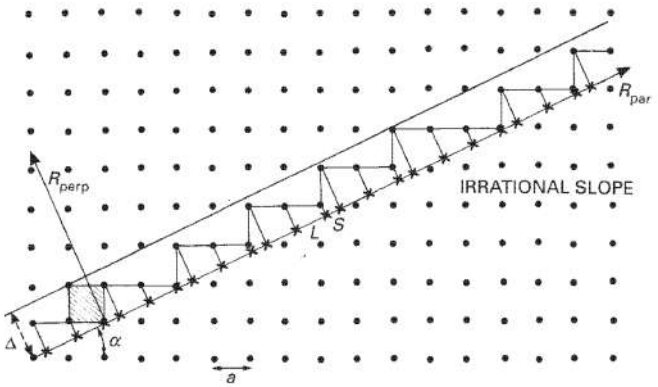

Figure 6.11: Illustration of the cut-and-projection method for generating the Fibonacci chain. A two-dimensional (2D) square lattice is considered, with the physical space $E_{\parallel}$ oriented at an irrational slope with respect to the lattice axes and the perpendicular space $E_{\perp}$ orthogonal to it. Lattice points lying within the acceptance strip Ω (highlighted region) are projected onto $E_{\parallel}$, producing a quasiperiodic sequence of long (L) and short (S) intervals that form the Fibonacci tiling.

In this formalism, the 6D hypercubic lattice $\mathbb{Z}^6$ is decomposed into two orthogonal subspaces: the parallel space $E_\parallel$, corresponding to the physical 3D space, and the perpendicular (internal) space $E_\perp$, also of dimension three. The projection operator maps lattice points $\mathbf{R}_6 \in \mathbb{Z}^6$ into a physical position $\mathbf{r}_\parallel$ and an internal coordinate $\mathbf{r}_\perp$, such that

$$\mathbf{R}_6 \mapsto \left(\mathbf{r}_\parallel, \mathbf{r}_\perp\right). \tag{6.11}$$

Atomic positions in the quasicrystal are obtained by accepting only those $\mathbf{R}_6$ for which $\mathbf{r}_\perp$ lies inside a bounded acceptance domain $\Omega \subset E_\perp$:

$$\mathbf{R}_6 \mapsto \mathbf{r}_\parallel \quad \text{iff} \quad \mathbf{r}_\perp \in \Omega. \tag{6.12}$$

This projection generates a quasiperiodic tiling in $E_\parallel$, reproducing the icosahedral symmetry observed in diffraction. A simple illustration is provided by the Fibonacci chain, obtained by projecting a square lattice $\mathbb{Z}^2$ onto a line of irrational slope $\tan\alpha = 1/\tau$, where τ is the golden ratio (Fig. 6.11). The resulting 1D sequence has long-range order without translational periodicity. In this construction, only lattice points whose perpendicular projection falls inside the acceptance strip Δ contribute to the physical tiling (Fig. 6.12).

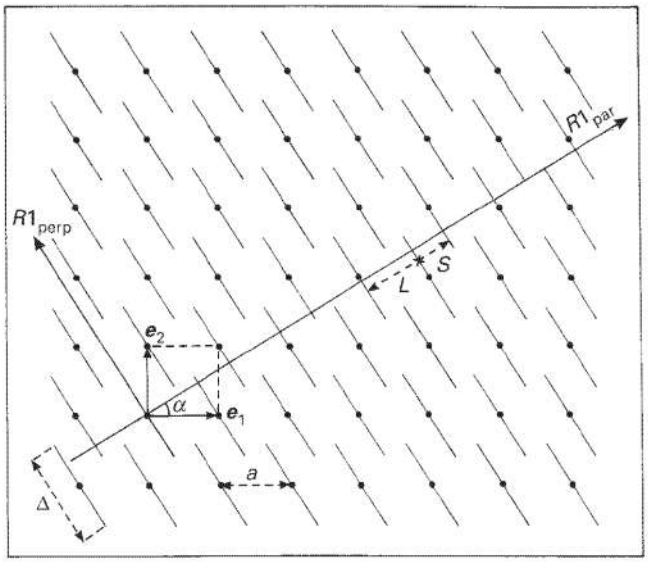

Figure 6.12: Cut-and-projection construction with acceptance window Δ (adapted from [131]). A 2D square lattice is decomposed into a parallel axis $R1^\parallel$ and a perpendicular axis $R1^\perp$. Only nodes whose perpendicular projection lies within the acceptance strip Δ are projected onto $R1^\parallel$, producing a quasiperiodic sequence of long (L) and short (S) intervals. In the general case, the Fourier transform of the acceptance domain in $E_\perp$, $G(\mathbf{Q}_\perp)$, modulates the diffraction intensities.

The mass density in physical space can then be written as a Fourier series indexed by 6D reciprocal vectors $\mathbf{G}$:

$$\rho(\mathbf{r}) = \sum_{\mathbf{G}} \rho(\mathbf{G})\, e^{i\mathbf{G}\cdot\mathbf{r}}, \tag{6.13}$$

where $\mathbf{G}$ belongs to the reciprocal lattice of $\mathbb{Z}^6$. In an ordinary crystal, the set of $\mathbf{G}$ is discrete and periodic. In a quasicrystal, the projection generates a *dense* set of allowed $\mathbf{G}$ values in reciprocal space. Bragg peaks appear at

$$\mathbf{G}_{\parallel} = \sum_{i=1}^{6} h_i \mathbf{a}_i^*, \qquad h_i \in \mathbb{Z}, \tag{6.14}$$

where $\mathbf{a}_i^*$ are the six reciprocal basis vectors oriented along the fivefold axes of the icosahedron.

The diffraction intensity of a given reflection depends on the Fourier transform of the acceptance window in perpendicular space:

$$F(\mathbf{Q}_{\parallel}) = \sum_{\mathbf{G}} \delta(\mathbf{Q}_{\parallel} - \mathbf{G}_{\parallel})\, G(\mathbf{G}_{\perp}), \tag{6.15}$$

where $G(\mathbf{G}_{\perp})$ acts as a modulation factor. Brightest reflections occur when indices correspond to consecutive Fibonacci numbers (in the 1D example), a general rule extending to higher dimensions. This explains why only a subset of the dense reciprocal lattice gives rise to strong Bragg peaks, while others remain weak.

Each Bragg peak of a diffraction pattern (DP) is indexed by a six-tuple $(h_1, ..., h_6)$ corresponding to a point in the 6D reciprocal lattice of the hyperspace construction. However, to simplify peak identification and visualization, it is often convenient to group reflections according to their norm G^2. This is commonly done using the so-called m/n indexing scheme introduced by Cahn and Gratias [116], where:

$$G^2 = \frac{m + n\tau}{\tau + 2} \tag{6.16}$$

with m and n being integers and τ the golden ratio. The value of G^2 uniquely identifies a quasi-spherical shell of Bragg reflections. The (m, n) labels serve as a compact and symmetry-aware way to characterize these shells and it is used along the rest of the chapter.

Generalized Elasticity Theory and Hydrodynamic Modes

The hyperspace description presented above not only explains the origin of noncrystallographic symmetries but also provides the natural framework for describing phason degrees of freedom. Phasons correspond to continuous shifts of the cut in the perpendicular space $E_{\perp}$, which change the set of lattice points projected into the physical space $E_{\parallel}$ and thus produce atomic rearrangements in the real structure. This follows from the invariance of the free energy under rigid translations of $E_{\parallel}$ within $E_{\perp}$ [119, 132].

The continuous nature of these phason degrees of freedom implies that they can propagate or relax collectively, giving rise to characteristic long-wavelength excitations. The

dynamic response of quasicrystals is described by the hydrodynamic limit of the generalized elasticity theory [132, 133, 134], which predicts two classes of such collective modes:

- **Phonons ($\mathbf{u}\parallel$):** Conventional elastic displacements within the physical space. In the long-wavelength limit ($q \to 0$), they behave as acoustic modes with linear dispersion ($\omega \propto q$) and are governed by the usual elastic constants describing the propagation of sound waves in solids.

- **Phasons ($\mathbf{u}\perp$):** Collective rearrangements associated with displacements in perpendicular space, which manifest in real space as correlated "tile flips" or local atomic rearrangements [135]. In the hydrodynamic limit, they are diffusive modes that decay exponentially with a characteristic time $\tau = 1/\Gamma \propto q^{-2}$.

This theoretical framework not only defines the fundamental lattice excitations of quasicrystals but also provides the quantitative basis for our measurements: it links the phason elastic constants to the diffuse-scattering intensity that we simulate in Sec. 6.3.3 and later aim to access experimentally through UED.

The generalized elasticity theory involves five independent elastic constants: two for phonon strain (λ, μ), two for phason strain (K_1, K_2), and one for phonon-phason coupling (K_3). Phason fluctuations produce observable diffuse scattering near Bragg reflections. This diffusive nature has been experimentally confirmed for iAlPdMn using coherent X-ray scattering [118]. The strong suppression of phonon-phason coupling in this material, leads to a diffusive term in the Bragg peak of the following form:

$$I_{\text{diff}}(\mathbf{Q}+\mathbf{q}) \propto \frac{\langle |u_\perp(\mathbf{q})|^2 \rangle}{q_\perp^2 + \frac{K_1}{K_2} q_\parallel^2}, \tag{6.17}$$

A key experimental observation in iAlPdMn is that the diffuse scattering intensity increases upon cooling [118]. This counter-intuitive trend is linked to a softening of the phason elastic constant K_2 [127], meaning that phason fluctuations become stronger at lower temperature. Within the framework of generalized elasticity, this behavior signals that the quasicrystal approaches a dynamical instability of the phason subsystem. Around 740-770 °C, iAlPdMn undergoes a transition between an *activated* and a *deactivated* phason state: above this temperature, phason flips are thermally activated and dynamically relax phasonic strain, whereas upon cooling, they become kinetically frozen. This transition from dynamic to frozen phason modes represents a purely dynamical phase transition rather than a structural transformation. In some related Al-Pd-Mn compositions, a reversible structural transformation between the icosahedral and approximant phases has been reported near this temperature [117], but in iAlPdMn the icosahedral order remains metastable.

6.3.3 Diffuse Scattering Simulations with `pyQCdiffuse`

To support the interpretation of our experimental data, we simulated the temperature dependence of the diffuse scattering in iAlPdMn using a custom Python code, `pyQCdiffuse`, based on the 6D formalism and developed by Tsunetomo Yamada. As explained in 6.3.2, each Bragg peak is labeled by six integers, corresponding to the coordinates of a reciprocal-lattice vector in 6D space. The parallel component $\mathbf{Q}_{\parallel}$ determines the position of the Bragg peaks in the DP, while the perpendicular component $\mathbf{Q}_{\perp}$ affects their intensity and contributes to diffuse scattering features. Symmetry operations are defined in the 6D hyperlattice, preserving the icosahedral symmetry upon projection.

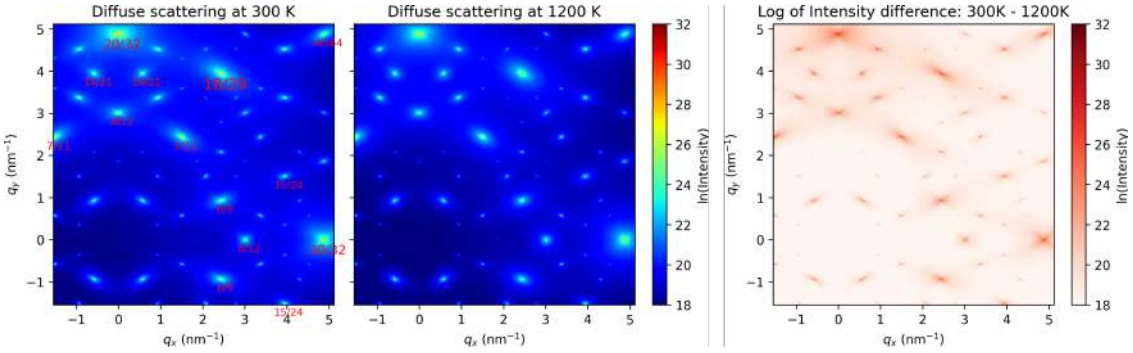

Figure 6.13: Simulated DPs from the 2-fold axis of iAlPdMn at different temperatures. The right panel (room temperature) shows stronger diffuse scattering compared to the left panel (1200 K), consistent with previous experimental reports [118]. The red numbers are the Cahn and Gratias index notation explaind in Sec. 6.3.2.c

Code functionality:

- Reads a list of reflections measured by Marc de Boissieu at the X3 beamline of the National Synchrotron Light Source (NSLS) in May 1993, on a single-grain iAlPdMn quasicrystal.
- Projects each 6D reflection into $\mathbf{Q}_{\parallel}$ and $\mathbf{Q}_{\perp}$ using linear mappings derived from the Cahn–Gratias formalism [116].
- Selects reflections within a thin slice around the 2-fold symmetry axis.
- Constructs elastic matrices (phonon, phason, and coupling terms) based on the theory of Jarić and Nelson [134], and computes the diffuse intensity using:

$$I_{\text{diffuse}} \propto \vec{Q}_6^{\top} \cdot \mathbf{C}^{-1} \cdot \vec{Q}_6 \tag{6.18}$$

- Generates 2D log-scaled intensity maps in reciprocal space and overlays Bragg peak indices (using the N/M labeling convention).
- Accepts temperature-dependent elastic constants, allowing the simulation of thermal disorder effects. The values used were taken from Ref. [127].

As expected, the simulations reproduce the counterintuitive increase in diffuse scattering intensity at lower temperatures. This trend, already observed in synchrotron experiments [118, 127], is interpreted as a consequence of phason mode softening. The simulated patterns serve as a reference to guide the interpretation of electron diffraction data.

6.3.4 Laser-Induced Heating Simulations with COMSOL Multiphysics

To estimate the thermal response of the iAlPdMn lamella under experimental excitation conditions, Jan Hajducek performed finite element simulations using COMSOL Multiphysics®. The goal was to verify whether cumulative heating could be avoided under different laser repetition rates and average powers.

The lamella geometry was modeled according to the actual FIB-prepared sample dimensions (see Figure 6.14), using literature values for the thermal parameters of iAlPdMn. A summary of the material constants used is reported in Table 6.1.

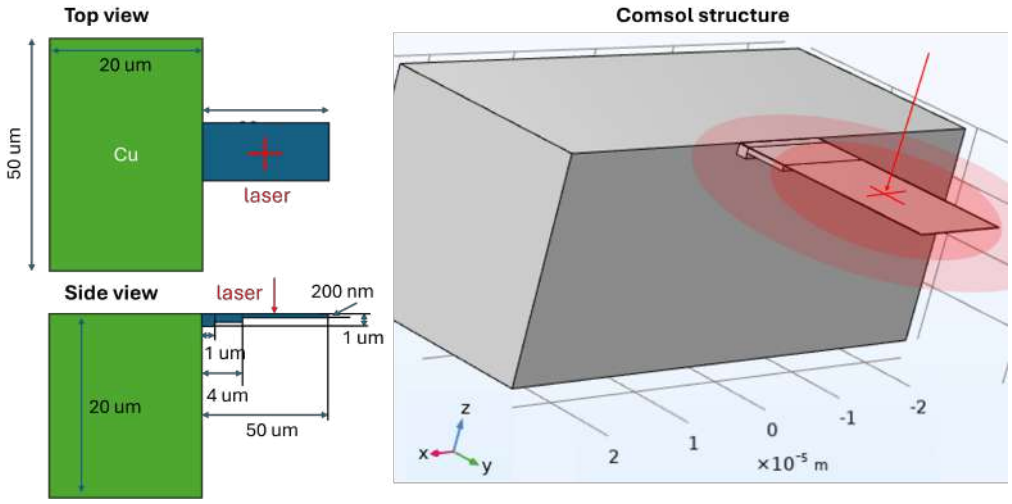

Figure 6.14: Geometrical model of the FIB-prepared lamella used in COMSOL simulations. The heat source was applied at the top surface, simulating laser absorption in the near-surface region.

Table 6.1: Thermal parameters used in the COMSOL model.

Parameter	Value	Reference
Density ρ [kg/m^3]	5150	[136]
Specific heat C_p [J/kg/K]	728 ($= 4\,k_B$/atom)[1]	[125]
Thermal conductivity κ [W/m/K]	1.5	[137]
Optical absorption coefficient α [m^{-1}]	10^8	Comparison with other semimetals

The laser excitation parameters were set to match the experimental conditions. Two regimes were simulated:

- **High rep. rate:** 1 MHz, 40 mW average power
- **Low rep. rate:** 10 kHz, 0.7 mW average power

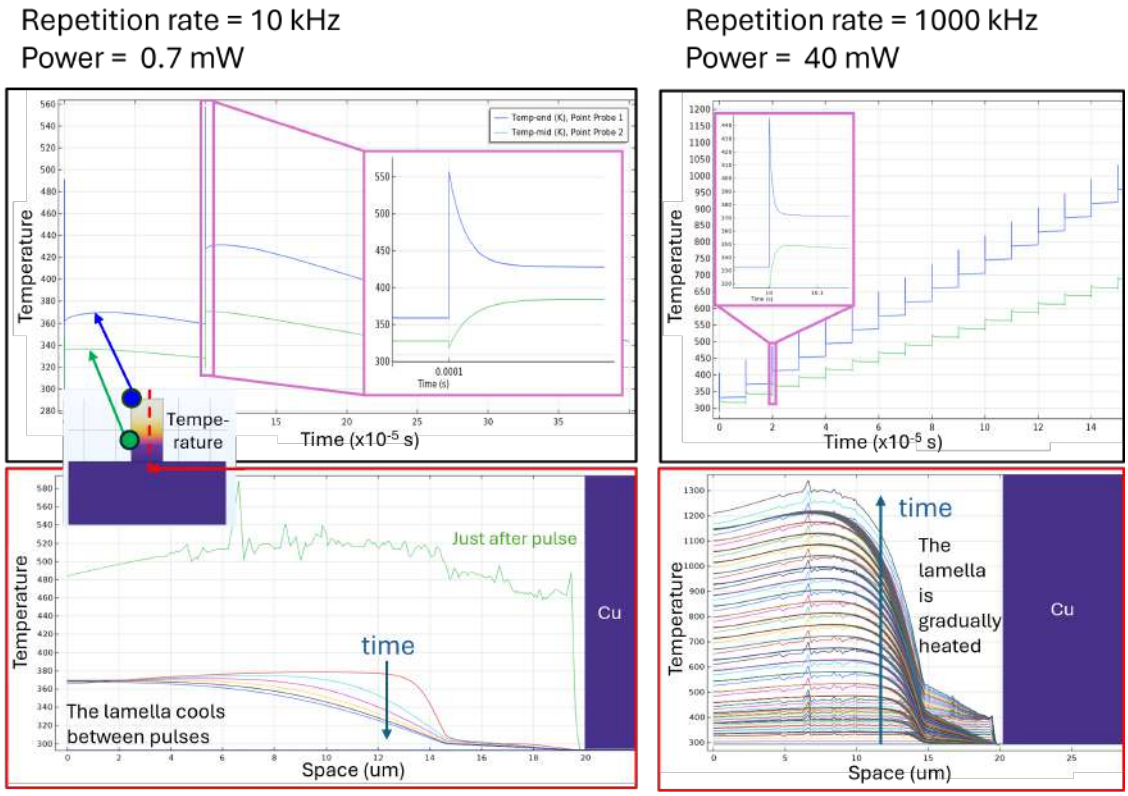

Figure 6.15: COMSOL simulation results. Left: temperature evolution under low rep-rate excitation (10 kHz, 0.7 mW). Right: cumulative heating under high rep-rate excitation (1 MHz, 40 mW).

The simulations show that at high repetition rate (1 MHz), the heat does not dissipate between pulses, resulting in cumulative heating and steady-state temperatures exceeding the melting point of iAlPdMn (approximately 1200 K). In contrast, under low rep-rate conditions (10 kHz), the lamella cools down to baseline temperature between pulses, avoiding thermal accumulation (see Figure 6.15).

[1]We used a constant value of C_p since this was the first implementation of the simulation. We did not investigate whether a temperature-dependent $C_p(T)$ function could be defined in `COMSOL`. However, iAlPdMn is known to depart from the classical Dulong-Petit limit above 700 K, with measured values increasing from 3.0 k_B/atom up to 5.0 k_B/atom at 1000 K [125].

These findings were critical to guide the design of the ultrafast diffraction experiments. In particular, they suggested that for time-resolved measurements, it is necessary to operate at low fluence and low repetition rate in order to avoid thermal smearing or irreversible structural changes. This condition is very difficult to achieve while maintaining a meaningful number of electron counts.

6.3.5 Measurements with Continuous Electron Beam

The experimental setup used for these measurements is the standard UTEM configuration described earlier in Sec. 6.1. The SLM was replaced with a simple mirror and no beam shaping was performed. The iAlPdMn sample used in this experiment is a single-grain quasicrystal provided by Marc de Boissieu, who I personally involved in the project. A thin lamella was extracted from this grain via Focused Ion Beam (FIB) milling and mounted on a standard FIB lift-out TEM grid. The sample was placed in a double-tilt TEM holder, allowing precise orientation along desired 2-fold symmetry zone axis.

Laser off

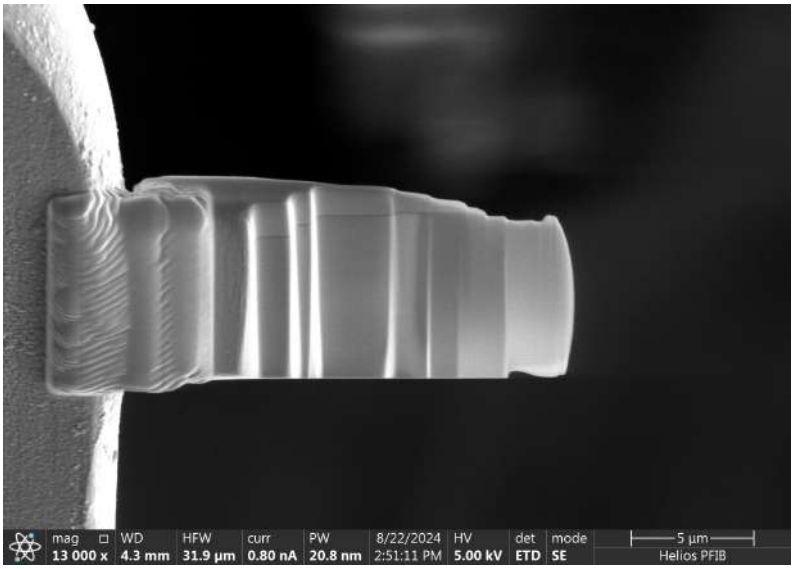

Figure 6.16: SEM image of the iAlPdMn lamella acquired after its preparation at the EPFL microscopy center.

We first inspected the FIB-prepared iAlPdMn lamella (SEM image shown in Fig. 6.16) using a continuous e-beam (i.e., thermal mode) to assess its crystalline quality and observe the expected diffraction and diffuse scattering features at room temperature. The high resolution TEM image is shown in Fig. 6.17.

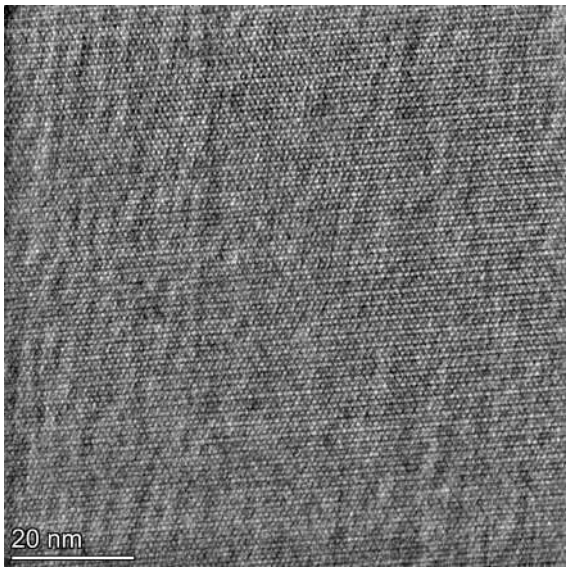

Figure 6.17: High-resolution TEM image showing atomic planes in the iAlPdMn lamella.

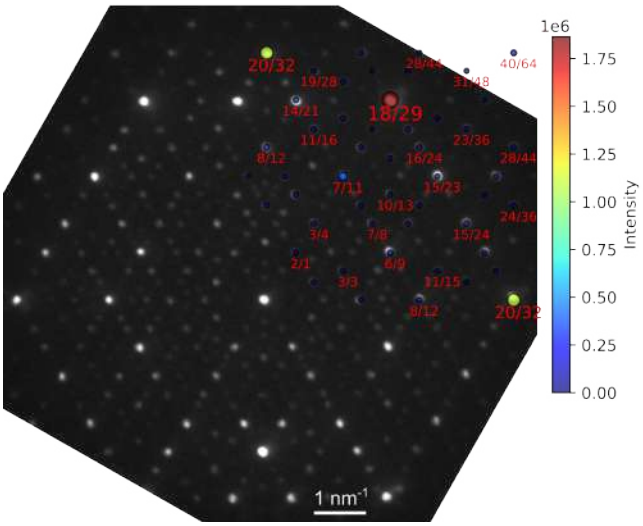

Figure 6.18: Electron diffraction pattern acquired along a 2-fold simmetry axis of iAlPdMn at room temperature. The positions and indices of the overlaid reflections (color scale) correspond to those reported by Marc de Boissieu from synchrotron X-ray experiments. To our knowledge, this is the first TEM measurement showing such a high density of indexed reflections in this system. The agreement with the expected pattern confirms both the alignment and the quality of the lamella.

The diffraction pattern (Fig. 6.18) displays a large number of clean, sharp Bragg peaks consistent with the expected structure of iAlPdMn. The visibility and density of the reflections match well with those previously reported in synchrotron X-ray experiments by Marc de Boissieu (overlaid), and their indexing confirms the successful alignment along the 2-fold axis.

These results represent one of the most successful outcomes of the experiment. To the best of our knowledge, such a detailed and well-indexed diffraction pattern from a quasicrystal lamella has not been previously obtained using TEM. This is likely due to the considerable experimental difficulty of preparing suitable specimens: quasicrystals such as iAlPdMn are brittle and prone to cracking, making particularly challenging the fabrication of a sample that is thin enough for TEM experiments. The presence of additional peaks in this DP, compared to de Boissieu's X-ray diffraction report, is still not fully understood and left for future work.

In situ laser experiments

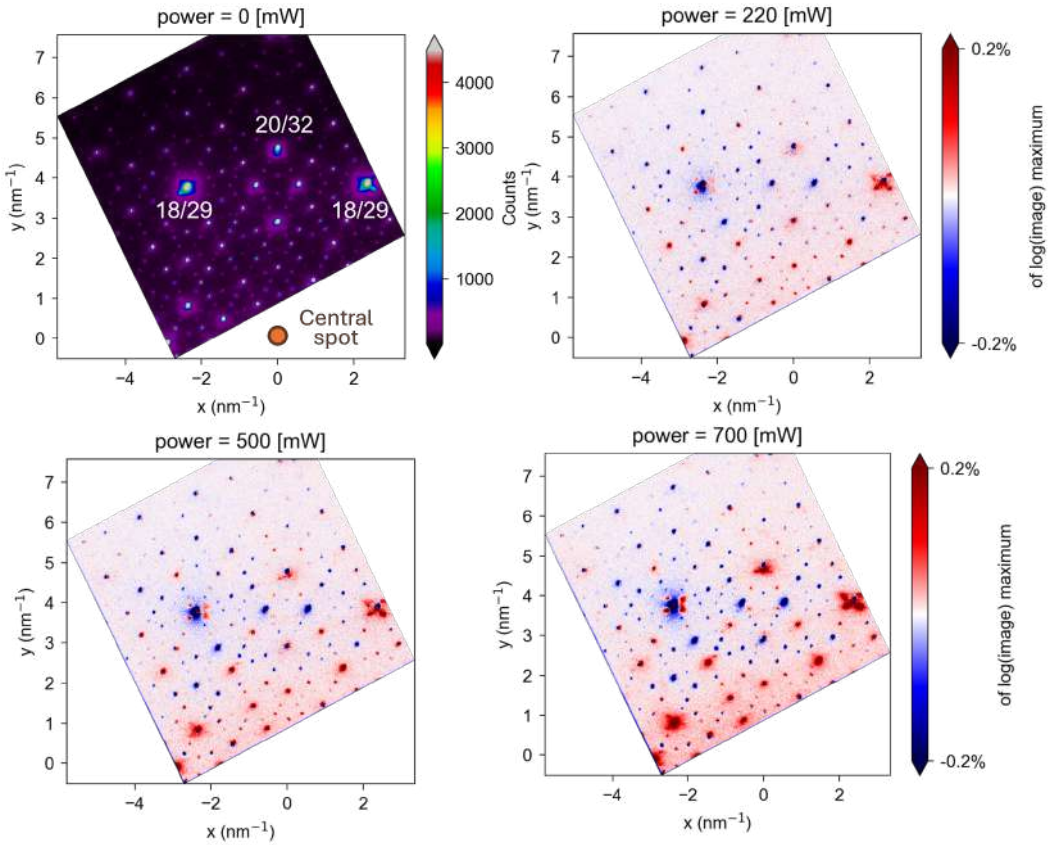

Figure 6.19: DPs along the 2-fold axis of the iAlPdMn lamella under different laser powers at 1 MHz repetition rate. First panel: no laser, the superimposed image shows the DP measured by Marc de Boissieu at NSLS in 1993. Other panels: difference between the DP acquired with the correspondent laser power and the first DP

We studied the effect of laser illumination on the iAlPdMn lamella as a function of laser power, with the goal of identifying signatures of cumulative heating, lattice expansion, or other laser-induced effects under continuous beam observation. The laser conditions were

the same as those listed in the previous table. At low repetition rates, no visible change in the DP was observed. On the other side, we observed changes in the DPs acquired at the high repetition rate of 1 MHz for increasing laser power, shown in Figure 6.19.

The results, exhibited if Fig. 6.19, show an increase in diffuse scattering with temperature, which is not expected in dodecagonal quasicrystals. Additionally, some peaks appear or disappear with heating. Further investigation in imaging mode revealed significant sample drift during illumination. Since, As shown in Fig. 6.20, the lamella is not uniform over hundreds of nanometers (the spatial scale selected by the SAD aperture) it is likely that slightly different phases were being probed [127].

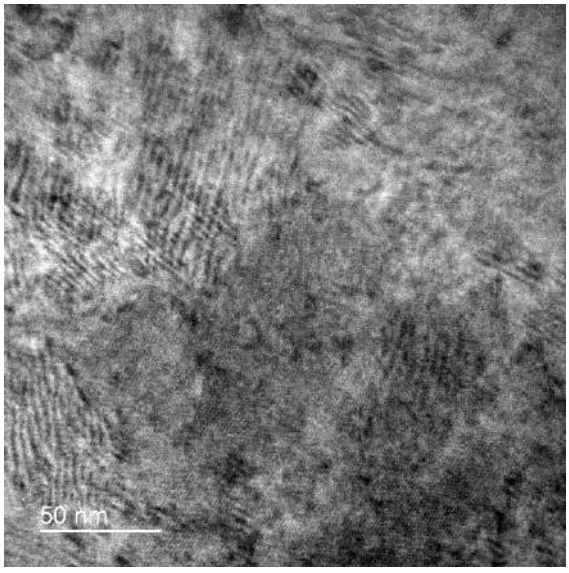

Figure 6.20: High-resolution TEM image showing non-uniformity of the iAlPdMn lamella at the sub-micron scale.

It should be noted that the used laser powers are much higher than those expected to induce heating based on simulations. We attribute this to: (1) a simplified lamella model, since the temperature rise is highly sensitive to the geometry, and (2) sub-optimal spatial overlap due to poor laser positioning.

6.3.6 Measurements with Pulsed Electron Beam

We investigated potential time-resolved structural dynamics in iAlPdMn using UED. An example of a time frame is shown in Fig. 6.24. In the first round of measurements, the e-beam was operated at 1 MHz repetition rate, even though simulations later revealed that such conditions would likely lead to cumulative heating. At the time of the experiment, however, these simulations had not yet been performed. The used laser power was 53 mW.

A comparative analysis of different diffraction spots was performed. The central spot

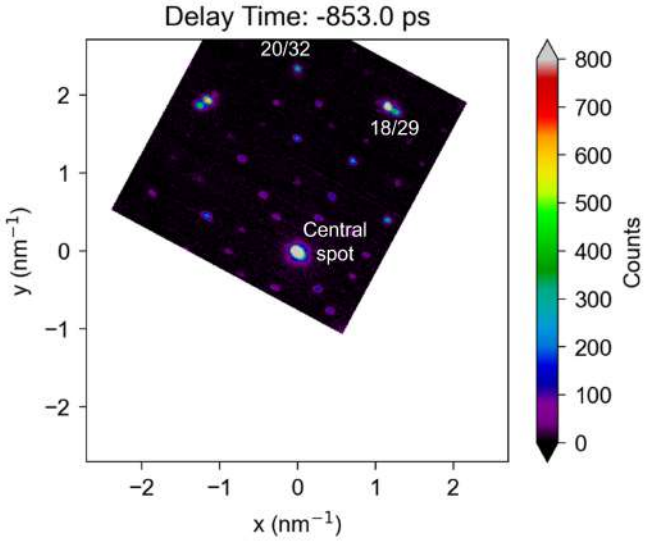

Figure 6.21: Example of a DP acquired during the first round of ultrafast measurements at 1 MHz and 53 mW.

and two higher-order reflections (labeled 20/32 and 18/29) were selected, and the intensity distribution was analyzed. A zoom-in on these spots on a representative frame is shown in Fig. 6.22. The intensity profiles were integrated along one axis and fitted with a Gaussian function. The evolution of the fit parameters (amplitude, centroid, width σ, and background) is shown in Figure 6.23.

As later confirmed by simulations, no ultrafast effect was observed within the timescales accessible in this configuration. However, since the delay axis also corresponds to real laboratory time, we observe a decrease in the σ parameter over the course of the scan. This trend is indicative of a possible reduction in diffuse scattering due to progressive heating of the sample. However, that this interpretation must be taken with caution. A gradual decrease in electron current is often observed in UTEM experiments due to cathod oxidation and contamination. This makes image normalization difficult and can introduce artefacts that resemble the trends observed in the σ parameter.

After this initial measurement run, several improvements were implemented:

- Acquisition of the full DP,
- Randomization of the delay points,
- Multiple scans for improved statistics,
- Reduction of repetition rate to 100 kHz.

It was not possible to further reduce the repetition rate to 10 kHz, as the resulting

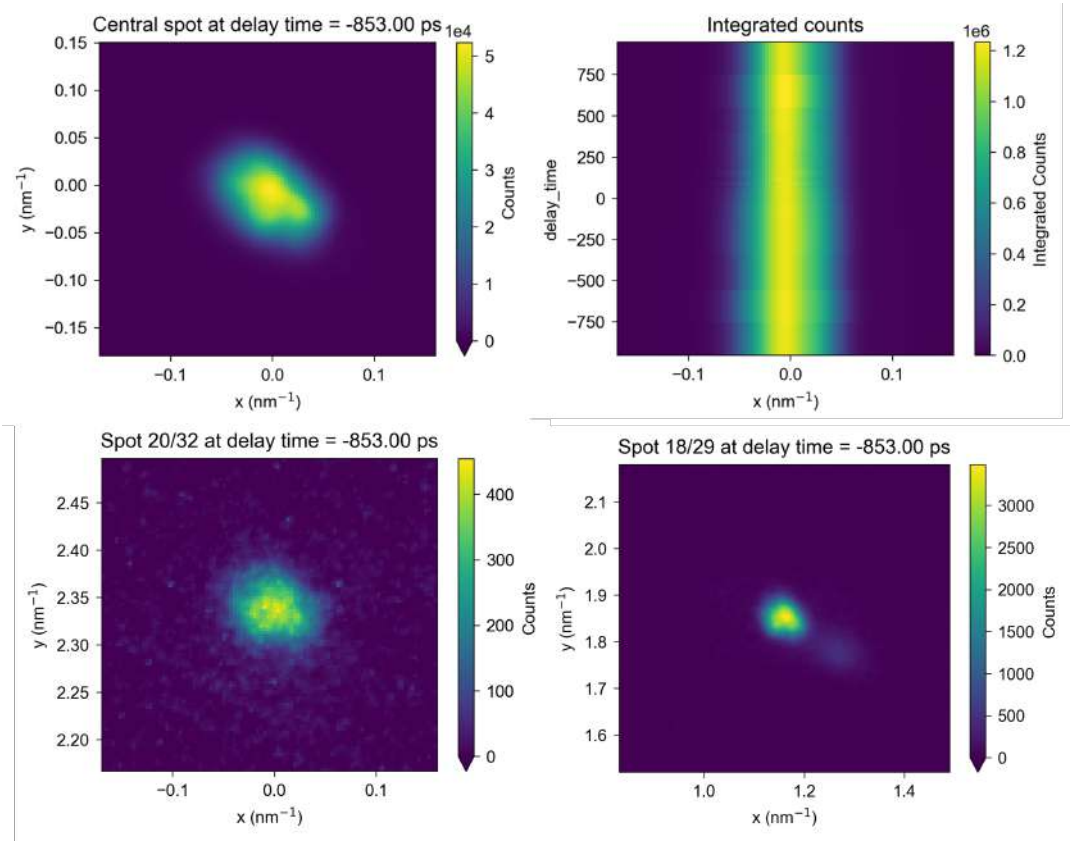

Figure 6.22: Diffraction spots selected for Gaussian fitting in the first round of ultrafast measurements. Zoomed-in views of individual diffraction spots at $t = -853$ ps. Top left: central spot. Top right: integrated intensity over time of the central spot. Bottom: spots 20/32 and 18/29. The central spot shows the highest fluence and is used to monitor normalization and intensity fluctuations.

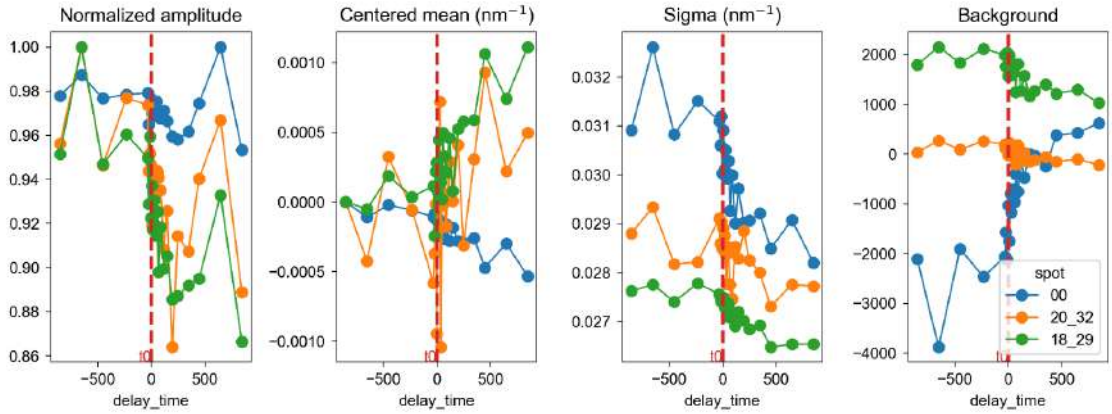

Figure 6.23: Fit parameters extracted from Gaussian fitting of selected diffraction spots as a function of delay time. The red dashed line marks the pump-probe overlap ($t = 0$).

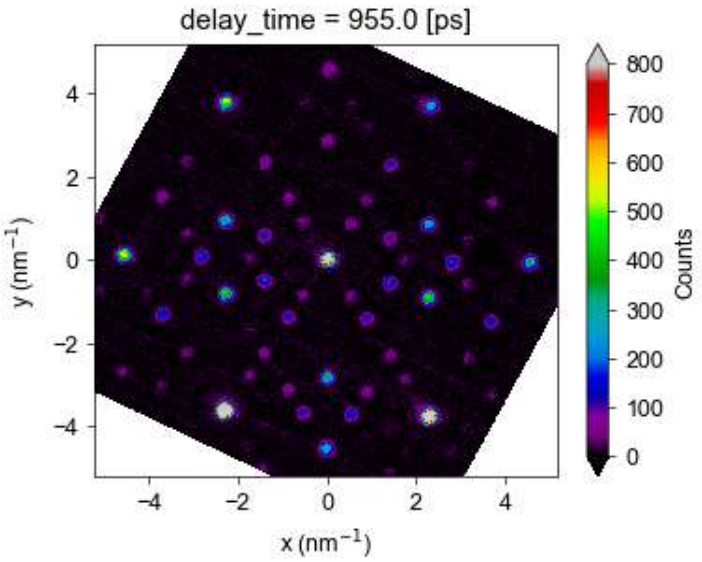

Figure 6.24: Example of a full DP acquired during the second round of ultrafast measurements (delay time = 955 ps), after implementing beam stopper and improved acquisition scheme.

electron fluence was too low to acquire meaningful data. Figure 6.24 shows one representative frame from this dataset. Furthermore, after the first measurement run, we realized that spatial overlap between the e-beam and the laser pulse had been lost for reasons that remained unclear. We then attempted to improve alignment by mounting both the FIB lamella and a sacrificial gold layered TEM grid on the same sample holder. This strategy was intended to facilitate real-time spatial overlap checks on the same sample holder. Unfortunately, during this procedure the iAlPdMn lamella was irreparably damaged. As a result, no conclusive time-resolved measurements could be performed.

6.3.7 Conclusions

This exploratory experiment marked the first attempt to study phason-related structural dynamics in iAlPdMn quasicrystals using UED. While conclusive time-resolved measurements could not be achieved—due to challenges in beam overlap, thermal effects, and mechanical damage to the lamella—the work provided useful insights into the experimental requirements and limitations of this approach and the first high quality DPs of this material obtained with a TEM.

A central limitation of the experiments was the inability to reach a laser repetition rate low enough to avoid cumulative heating effects. As shown by the COMSOL simulations presented Sec. 6.3.4, repetition rates above 10 kHz lead to significant thermal accumulation, effectively washing out any transient response. In UTEM experiments, the shared laser source used to trigger both the IR pump and the UV-driven electron emission

constrains the system to operate at a minimum of 100 kHz to obtain significant electron counts. Lowering the repetition rate further led to electron counts too low for reliable detection using the available CCD camera. It is possible that such measurements could become feasible using the direct electron detector available in the Milano-Bicocca setup, which offers significantly lower noise and higher sensitivity.

The room-temperature DPs obtained in this study confirmed the presence of Bragg peaks qualitatively consistent with earlier X-ray studies. Preliminary efforts to analyze diffuse scattering under laser excitation revealed both the potential and the sensitivity of such measurements to sample drift, alignment, and noise statistics. Despite its limitations, this initial campaign helped clarify the technical constraints involved in applying UTEM to complex aperiodic systems. It also defined critical conditions-such as repetition rate, spatial overlap, and sample stability-that must be satisfied for future time-resolved experiments on quasicrystals.

6.4 Ultrafast plasmon dynamics in 30°-twisted bilayer graphene

My interest in 30°-twisted bilayer graphene (TBLG) sparked during the Pisa 2D Quantum Matter Summer School, where Sergio Pezzini presented recent advances on this system [138]. When introduced as a 2D quasicrystal, it immediately resonated with the research direction I had just started on bulk quasicrystals. Indeed, at this twist angle, the system forms a dodecagonal moiré superlattice that lacks translational periodicity but preserves twelve-fold rotational symmetry, resulting in replicated Dirac cones and leads to unusual electronic properties [139, 140].

At 30°, TBLG departs from the conventional moiré physics observed at small twist angles: the quasicrystalline electronic structure leads to a decoupling of the Dirac cones near the Fermi level [141]. In contrast, higher-energy electronic states exhibit enhanced interlayer hybridization enabled by intervalley electron-phonon scattering [140, 142]. These features have made 30°-TBLG a platform of interest, not only for its exotic symmetry but also because large-area, high-quality samples can now be synthesized deterministically via chemical vapor deposition (CVD) [138, 139].

In 30°-TBLG, phonons are expected to mediate the relaxation of photoexcited carriers, as in most solids [130]. However, the bilayer geometry and large twist angle introduce new vibrational modes not present in monolayer graphene and low twist angles [143, 144]. Near the Dirac point the lattice dynamics may resemble those of monolayer graphene, while, at higher energies (e.g., > 1 eV), the coupling involves both interlayer acoustic modes—such as shear and breathing modes—and optical modes where the two layers oscillate out of phase. Their activation and coupling depend strongly on the twist angle and symmetry, and they are predicted to have high scattering cross-sections for hot carriers near high-symmetry points like K/K' [143]. The typical decay times are on the order of 0.1 to 1 ps

for optical phonons, and 1 to 10 ps for acoustic phonons [144]

These processes make phonons central to understanding the ultrafast response of 30°-TBLG. Their influence extends to the transient reshaping of energy-loss features, as previously demonstrated in graphite, where IR pumping led to renormalization of the π and $\pi+\sigma$ peaks via phonon-mediated scattering and thermal expansion [48]. Our objective is to investigate whether similar dynamics occur in 30°-TBLG and whether they are sensitive to interlayer coupling.

The π and $\pi+\sigma$ features dominate the low-loss EELS spectrum of graphene and its multilayers, typically appearing around 5 and 15-25 eV, respectively. Although often described as plasmons, their physical origin is not purely collective: in single-layer graphene they arise from interband transitions, while in multilayers or graphite they gain a more plasmonic character [145]. In 30°-TBLG, the situation could be more complex since near the Γ point the layers appear decoupled, but outside this region the electronic states are strongly hybridized.

To explore this regime, we performed pump-probe EELS experiments on 30°-TBLG using the EPFL UTEM in a standard configuration (see Sec. 6.1). Given the limited thickness of the sample, the number of inelastically scattered electrons is inherently low, leading to a poor signal-to-noise ratio and long acquisition times. Despite these challenges, we succeeded in acquiring delay- and fluence-dependent spectra across multiple runs. We used the undiffracted e-beam foreseeing possible future experiments using electrons satisfying different Bragg conditions. While the interpretation remains preliminary, these experiments represent, to our knowledge, the first time-resolved EELS measurements on a 2D graphene-based quasicrystal.

6.4.1 Static characterization and momentum-resolved EELS

Before performing time-resolved measurements, we characterized the sample through electron diffraction and momentum-resolved EELS. The 30°-TBLG flake was grown via chemical vapor deposition and transferred to a TEM grid by the group of Camilla Coletti. Optical inspection under a long working-distance objective was used to identify bilayer regions suitable for Raman spectroscopy and subsequent ultrafast measurements (see Fig. 6.25). This technique allowed spatial mapping of the sample quality and ensured that the e-beam probed well-defined 30°-TBLG domains, as reported in their article [138].

The high quality of the flake was confirmed by a high-resolution TEM image (Fig. 6.26a) that shows the presence of the moiré pattern. The selected area DP of the region is shown in Fig. 6.26b. The presence of sharp and well-separated Bragg spots confirms long-range order and a well-defined twist angle, in agreement with previous reports [138].

In monolayer graphene, electrons diffracted into different Bragg peaks sample equivalent regions in reciprocal space, essentially all probing the Γ point due to the linear

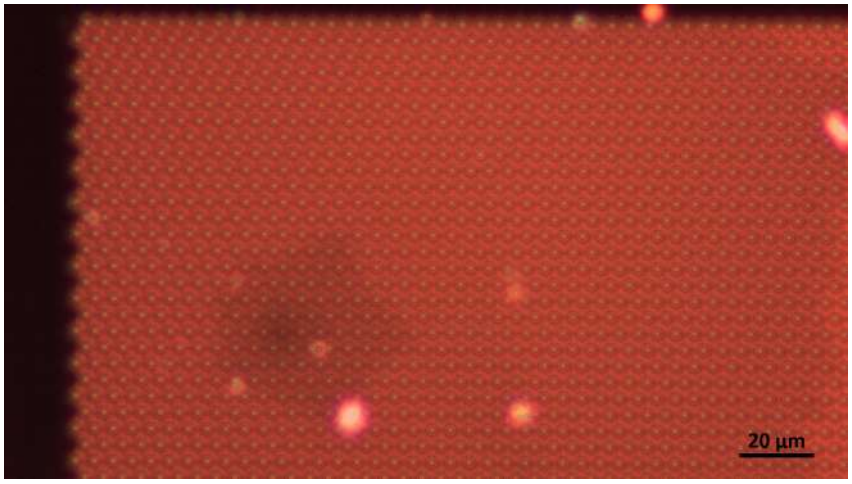

Figure 6.25: Optical image of the CVD-grown graphene flake prior to shipment. The flake is the barely visible hexagonal stucture. The periodic dot array corresponds to the PELCO Holey Silicon Nitride Support Films. Raman spectroscopy was performed at selected positions to identify regions with twisted bilayer graphene. The area later used for ultrafast EELS measurements lies near the center of the darker region.

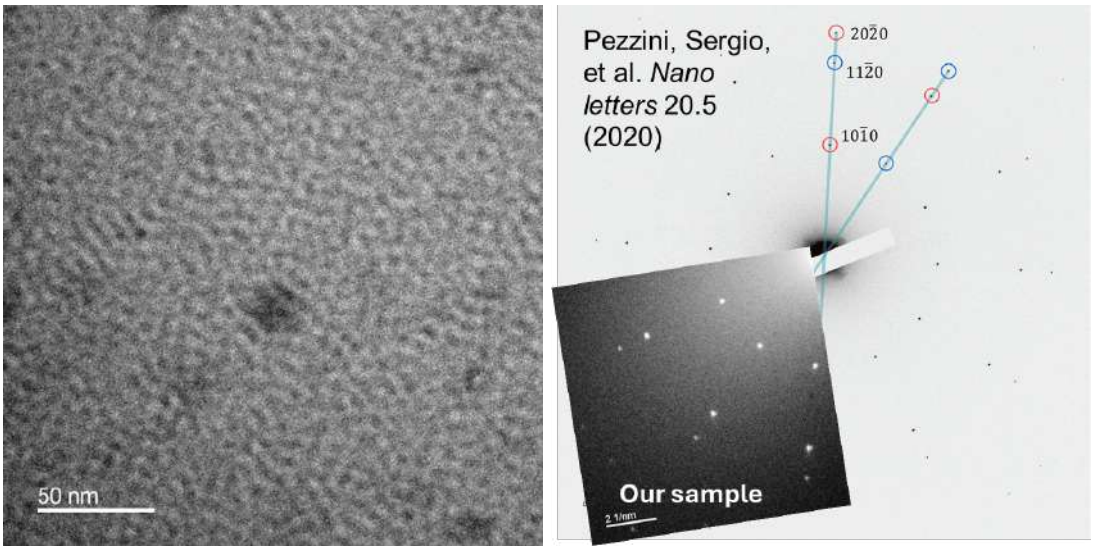

Figure 6.26: (a) High-resolution TEM image showing the moiré interference pattern characteristic of 30°-twisted bilayer graphene. (a) DP of the 30°-TBLG flake (bottom left) compared with Ref. [138]

dispersion and symmetry. However, in 30°-twisted bilayer graphene, this equivalence is broken: the reciprocal lattices of the two layers are rotated relative to each other. This results in a situation where electrons scattered into a given Bragg spot from one layer correspond to different high-symmetry points in the Brillouin zone of the other. In particular, the Γ point of one layer can align with a boundary point between K and M of the second layer. Figure 6.27 overlays the diffraction pattern with the reciprocal lattices of the two layers, highlighting the inequivalence of the scattering vectors.

To probe the momentum dependence of the plasmonic response, we performed EELS measurements by selecting individual Bragg spots using the objective aperture (see Fig. 6.28). The explained layer misalignment leads to momentum-dependent features in the EELS spectrum. Figure 6.29 shows representative spectra collected at different Bragg spots.

The EELS spectra acquired at different Bragg spots exhibit clear variations in the loss function of 30°-TBLG. Most notably, the $\pi+\sigma$ plasmon feature near 20 eV changes in intensity and spectral width depending on the selected diffraction order. The 10-10 spot, in particular, displays an unusually broad and asymmetric plasmon response, with a long high-energy tail extending beyond 80 eV.

This is not expected for monolayer graphene probed at the Γ point, where the π plasmon typically shows a symmetric peak dispersion [146] as in the other Bragg spots. Such spectral broadening likely reflects what explained earlier: the Γ point of one layer overlaps with a region between the K' and M points of the second layer. This overlap increases the available phase space for interband transitions and results in enhanced broadening of the loss function.

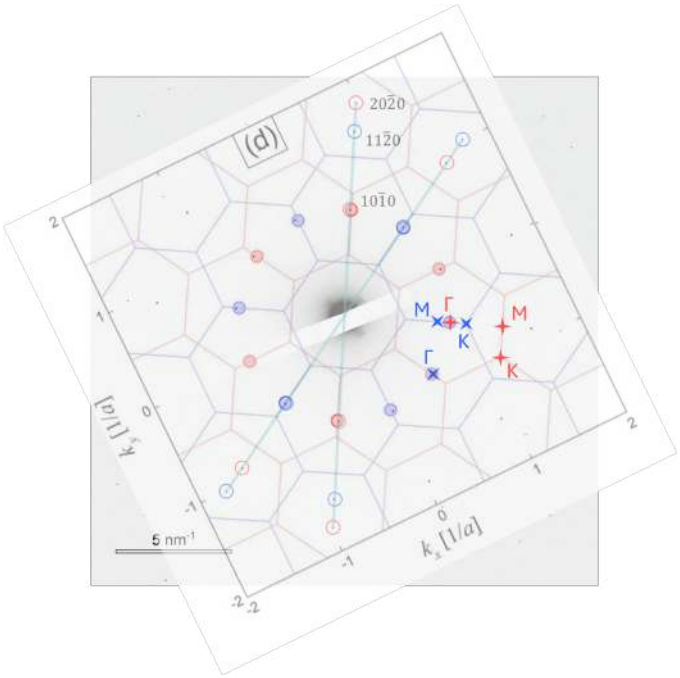

Figure 6.27: Reciprocal space map showing the overlapping Brillouin zones of the two graphene layers (blue and red) in 30°-TBLG, superimposed on the diffraction pattern of Ref. [138]. Adapted from [140].

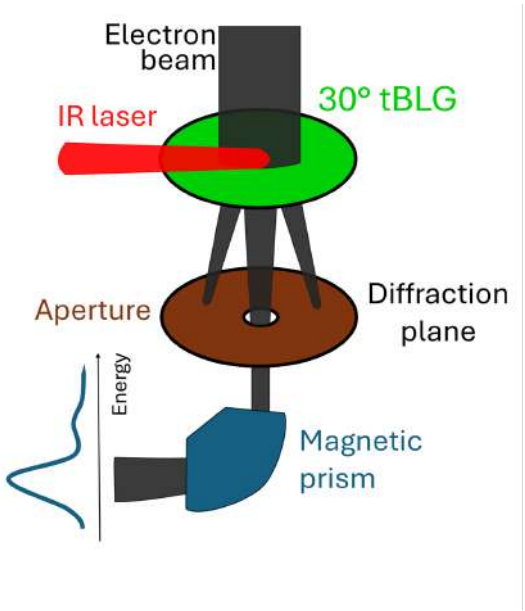

Figure 6.28: Schematic of the experimental setup for static momentum-resolved EELS. Different Bragg spots were selected using the objective aperture.

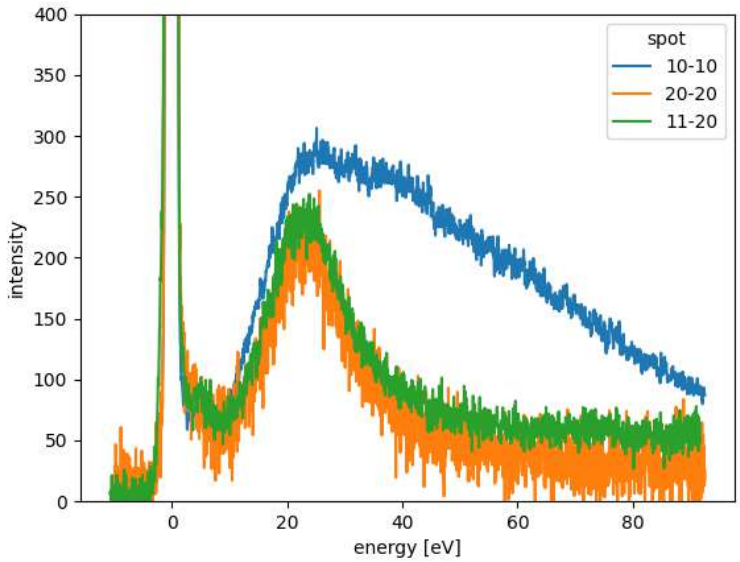

Figure 6.29: EELS spectra collected at different Bragg conditions, showing clear variation in the $\pi+\sigma$ loss peak around 20 eV as a function of reciprocal-space selection. Labels of bragg peaks are illustrated in Fig. 6.26

The anisotropic behavior across Bragg spots illustrates how the quasicrystalline superlattice and interlayer hybridization modify the dielectric response. Although our setup did not use a q-EELS slit, and thus lacks proper momentum resolution, the qualitative differences between spectra already reveal nontrivial features of the electronic structure. These findings motivate future momentum-resolved EELS studies using a q-EELS setup in continuous beam mode which were not the initial scope of this experiment. Such experiments could resolve the detailed dispersion of the π and $\pi+\sigma$ plasmons in twisted bilayers and reveal possible signatures of moiré-modulated collective modes.

6.4.2 Ultrafast plasmon dynamics

We performed pump-probe EELS experiments pumping with 1030 nm femtosecond laser with a pulse duration of 500 fs and a repetition rate of 1 MHz. Several delay scans were acquired at different laser fluences in the range of 0.5 to 3 $\mathrm{mJ/cm^2}$, guided by previous studies on graphite plasmon dynamics [48]. It is important to note that the original specimen was irreversibly damaged following the collapse of the carbon support film. Consequently, a backup sample was used, obtained by manually stacking two mechanically exfoliated single-layer graphene flakes at an estimated relative twist angle of approximately 30°. Over time, this backup sample likely underwent partial oxidation and surface contamination, which may have altered its electronic and dielectric properties.

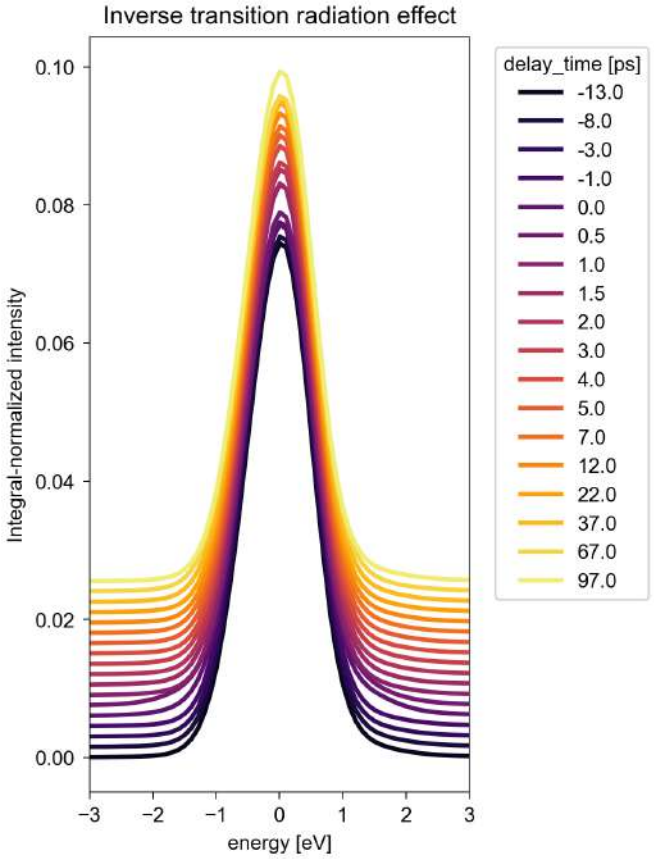

Figure 6.30: Temporal evolution of the ZLP during pump-probe delay scan. At $t = 0$, a clear broadening is observed, attributed to inverse transition radiation process. Spectra are normalized to their integral and aligned by recentering the ZLP.

Since the static characterization revealed differences in the EELS yield among various Bragg reflections, we first selected the undiffracted (direct) e-beam for the time-resolved measurements. This geometry places the experiment in the same optical and detection configuration that would be required for future measurements at individual Bragg conditions. Although such experiments would be more challenging due to the much lower intensity of the diffracted beams in these thin samples, this initial configuration allowed us to test the objective lens operation and alignment procedures needed to reach those conditions.

To enhance the quality of the data, we applied a spike removal filter, zero-loss peak (v) centering, and principal component analysis denoising. ZLP oscillations due to setup instabilities were corrected by recentring and normalizing each spectrum individually. We then performed deconvolution using the Richardson-Lucy algorithm [147, 148] with a point spread function estimated from the gain side of the ZLP. The original and deconvolved data are shown in Fig. 6.31.

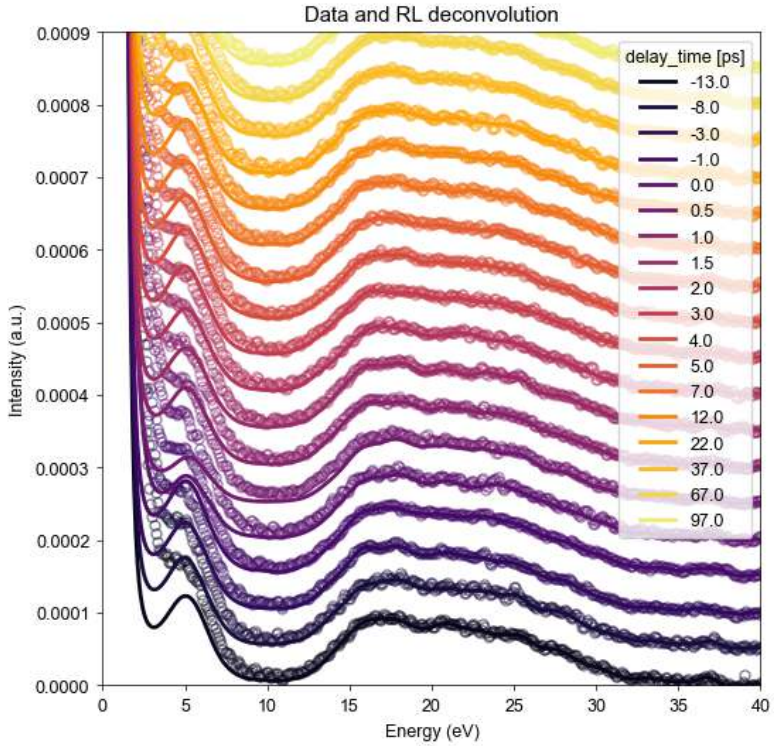

Figure 6.31: Richardson-Lucy deconvolution of the EELS spectra (solid lines) overlaid with the raw experimental data (circles), shown as a function of delay time. The plasmon features exhibit a clear transient intensity reduction followed by gradual recovery, consistent with ultrafast carrier-phonon coupling.

To isolate the transient response, the average spectrum at negative delays ($t < -5\,\mathrm{ps}$) was subtracted from each time step. The resulting difference spectra, shown in Fig. 6.32, reveal a suppression of the π-plasmon peak immediately after excitation, followed by partial recovery within a few picoseconds. Delay-time measurements were acquired in a randomized order to decouple pump–probe delay effects from real acquisition time effects, such as the gradual photocurrent decrease discussed in Sec. 6.3.6. To verify that this randomization effectively suppresses any residual correlation between electron yield and delay time effects, the black dots in Fig. 6.32 report the raw total electron counts per frame prior to normalization and therefore serve as an independent monitor of the photoemission yield. The absence of any systematic trend in the black-dot trace demonstrates that the observed π-plasmon suppression is not correlated with variations in electron yield.

The extracted amplitude of the π plasmon peak as a function of time delay is shown in Fig. 6.33. The dynamics exhibit a two-step behavior: a sub-picosecond suppression likely driven by fast optical phonons, followed by a slower recovery attributed to acoustic phonon thermalization. This observation is consistent with theoretical predictions and experimental results on related systems [143, 144].

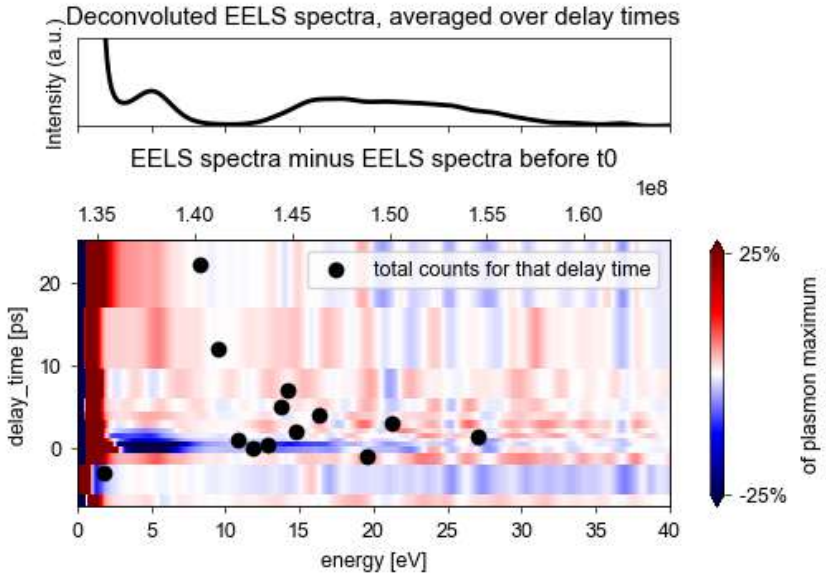

Figure 6.32: Top: Deconvolved EELS spectrum averaged over all delay times. Bottom: Delay-dependent difference spectra obtained by subtracting the average pre-time-zero spectrum ($t < -5$ ps). The colormap reflects the relative intensity changes in the loss function. Black dots indicate the total electron counts per delay time before normalization.

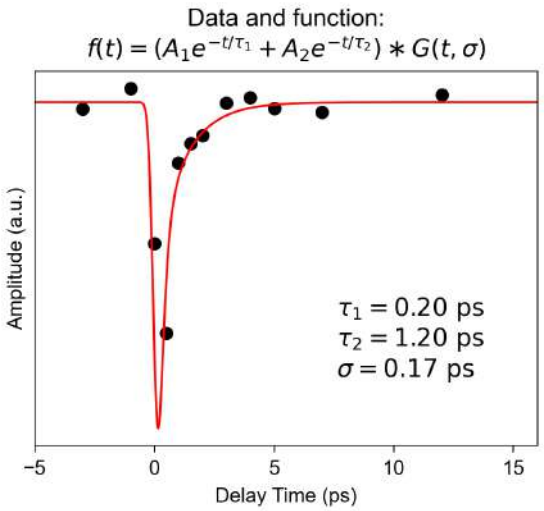

Figure 6.33: Time evolution of the π-plasmon peak amplitude extracted from the deconvolved spectra (black dots). The red line serves as a guide to the eye and corresponds to a double-exponential relaxation function. The function is defined in the title, and the term $* G(t, \sigma)$ indicates the convolution with a Gaussian of width σ, which accounts for temporal broadening. The corresponding parameter values are displayed in the plot.

Indeed, TBLG exhibits a strong interlayer coupling mediated by intervalley scattering

of electrons via phonons [149]. In particular, the K-phonon at 160 meV appears to have the highest scattering cross-section following electron excitation [143]. The typical decay times are on the order of 0.1–1 ps for optical phonons, and 1–10 ps for acoustic phonons [144]. The progressive excitation of acoustic phonons induces an increase of the lattice temperature, which directly influences the dielectric constant [150, 151].

These ultrafast results suggest that optical excitation of charge carriers in TBLG may lead to strong phonon excitation, modifying the dielectric function of the system. This, in turn, could affect the energy and intensity of the π and $\pi+\sigma$ features observed in the EELS spectrum. While our measurements are preliminary and the precise role of interlayer coupling, sample quality, and twist angle remains to be clarified, the observed dynamics are consistent with phonon-mediated renormalization processes reported in related materials. Further studies on cleaner and better-characterized samples, ideally with momentum-resolved detection, will be required to fully understand the plasmon-phonon interplay in twisted bilayer graphene.

6.4.3 Conclusions

This study represents an initial attempt to explore the ultrafast dielectric response of twisted bilayer graphene using time-resolved EELS. By focusing on a 30°-twisted geometry, we aimed to investigate how quasiperiodicity and interlayer coupling affect both the static and transient behavior of plasmonic excitations. The EELS measurements revealed clear anisotropies in the loss spectrum as a function of Bragg condition, consistent with the misalignment of high-symmetry points between the two layers.

Time-resolved measurements, though limited to the undiffracted e-beam and signal-to-noise ratio of the CCD detector, demonstrated the feasibility of ultrafast EELS on 2D heterostructures. With a direct electron detector it might be possible to perform these measurements on different Bragg conditions and unveil and eventual different response. The observed dynamics in the π-plasmon peak suggest a relaxation process occurring on two distinct timescales, potentially corresponding to optical and acoustic phonon scattering channels. While the precise mechanisms remain to be clarified, the results are qualitatively consistent with phonon-mediated dielectric renormalization observed in other carbon-based systems [48].

Nevertheless, this work provides a proof of principle for performing ultrafast EELS in twisted bilayer systems and outlines the conditions required to push such studies further. Future experiments using new samples, optimized optical alignment, and momentum-selective detection could shed light on the role of phonons and interlayer coupling in shaping the ultrafast dynamics of 2D quasicrystals.

6.5 Chapter Conclusions and Outlook

The experiments presented in this chapter extend the scope of ultrafast electron microscopy from the development of light-induced beam shaping methods to their application in complex materials. They highlight both the opportunities and the technical challenges associated with transferring concepts of photonic control to free electrons and employing them as selective probes of quantum matter.

At the methodological level, the Hermite–Gaussian beam experiments demonstrated that transverse shaping can be realized at the sample plane, enabling a quantitative estimate of the e-beam coherence under realistic UTEM conditions. This analysis could guide the design of a PELM device integrated within a sample holder.

Turning to materials investigations, two distinct systems were explored. In the case of iAlPdMn quasicrystals, UED provided the first high-quality diffraction patterns from such materials in a TEM. Although cumulative heating, alignment issues, and sample fragility prevented conclusive time-resolved measurements, the campaign clarified the experimental boundaries for addressing phason dynamics and established the requirements-low repetition rates, enhanced detector sensitivity, and robust sample preparation-that must be met in future studies.

In parallel, the investigation of 30°-twisted bilayer graphene illustrated how quasicrystalline order in two dimensions manifests in both static and ultrafast EELS spectra. The static measurements revealed anisotropies in the loss function linked to the misalignment of high-symmetry points between the layers, and preliminary pump-probe data suggested a relaxation pathway mediated by both optical and acoustic phonons. While limited by detector performance and the lack of momentum selectivity, this study represents a proof of principle for probing the ultrafast dielectric response of 2D quasicrystals.

Beyond the specific findings, these studies also motivate the adoption of structured electron probes for advancing materials investigations. Shaped beams can provide a higher degree of selectivity in reciprocal space, enhancing sensitivity to excitations localized at specific momenta, a feature particularly relevant for quasiperiodic systems where Brillouin-zone folding complicates the interpretation of diffraction and EELS spectra. Moreover, structured phase profiles such as vortex or Hermite-Gaussian modes naturally couple to anisotropic responses, offering a route to disentangle phononic and plasmonic channels in 2D quasicrystals like 30° TBLG. In this sense, the developments in beam shaping are not orthogonal to the materials case studies, but rather point toward a unified strategy in which tailored electron probes enable access to quantum excitations with improved contrast and selectivity [24]. Taken together, the results of this chapter close the loop between instrumentation and application, outlining a pathway where photonic-based e-beam shaping becomes a standard tool for ultrafast investigations of quantum materials.

Chapter 7

Conclusions and Outlook

This thesis presented the development and first experimental validation of a Photonic-based free-ELectron Modulator (PELM) integrated within a transmission electron microscope. The central goal was to establish a platform for programmable, light-driven control of the transverse electron wavefunction prior to its interaction with the specimen. By combining ultrafast electron microscopy with spatial light modulation, we demonstrated that structured optical fields can deterministically imprint phase patterns onto the transverse profile of a free-electron beam, enabling the first realization of programmable transverse e-beam shaping inside an ultrafast transmission electron microscope (UTEM).

The work began with the conceptual and theoretical foundations of electron-photon interaction (EPI), presented in Chap. 2. We identify inverse transition radiation as the most suitable mechanism for achieving deterministic, phase-preserving coupling between electrons and optical fields. This theoretical chapter explains how the optical phase of a structured light field can be directly transferred to the electron wavefunction when the interaction occurs at a laser-illuminated interface. This principle underpins the operation of the PELM and defines a route toward fully reconfigurable electron-beam control.

The implementation described in Chap. 3 constitutes the first integration of such a PELM device directly within a TEM column. A dedicated section was designed upstream of the condenser system to host the PELM interaction plane, providing optical access for both the ultraviolet beam that triggers photoemission and the spatial light modulator-shaped infrared beam. The optical system was complemented by a new condenser lens for e-beam collimation and coherence control as well as a direct hybrid-pixel detector optimized for low-flux, momentum-resolved detection (resolution of approximately $0.3\mathrm{m}^{-1}$). Through a combination of plasma-lensing and EPI momentum-streaking measurements, we established reproducible spatial and temporal overlap between electron and laser pulses, validating the functionality of the instrument. The EPI temporal cross-correlation extracted from the experiments has a FWHM of 800 fs in our measurements.

The experiments of Chaps. 4 and 5 demonstrate controlled transverse modulation of the electron wavefunction. Leveraging the interaction of the electrons with a laser field shaped by a spatial light modulator, we imprinted programmable transverse patterns on the e-beam. By reconstructing these patterns from the measured EPI signal, we confirmed that the imposed modulation is preserved during propagation to the sample plane on a scale of $10\,\mu m$. These experiments established the PELM as a ready-to-use instrument for ultrafast measurements with shaped e-beams.

Building on this capability, we used the same setup to implement electron single-pixel imaging. By inserting nanostructured membranes at the sample plane and measuring the EPI signal for a set of programmed illumination patterns, we reconstructed the objects within the single-pixel framework, exploiting prior knowledge about their symmetry to reduce the number of required measurements. Furthermore, we showed that the optical patterns imprinted on the electrons can be demagnified (by a factor six in our experiment) by the microscope optics beyond the diffraction limit of light, extending optical modulation techniques into the nanometric regime of electron microscopy. These experiments confirm that imaging techniques that leverage optically modulated electron beams are feasible in a TEM and enable the transfer of advanced optical imaging schemes into the electron domain.

While the present implementation of optical-inspired imaging schemes remains limited in efficiency and spatial resolution, it paves the way toward selective, low-dose, and symmetry-sensitive measurements using tailored electron probes. Further improvements in EPI coupling and pattern demagnification could extend the accessible spatial resolution and fully exploit the resolving power of the TEM. Together, these developments define a path toward programmable, light-driven electron microscopy, where the probe itself becomes an active element for tailored interaction with matter.

The EPFL campaign of Chap. 6 complemented the UniMiB work with material experiments performed in a standard UTEM configuration. The planned sample-stage-integrated PELM based on a two-grid holder is still under commissioning, yet transverse e-beam shaping at the sample plane was realized using a standard holder and an EPI mediating film, enabling a quantitative estimate of transverse coherence of $50\,nm$ under realistic conditions. The material studies probed the practical limits of UTEM, addressing systems at the edge of what can currently be investigated in a TEM. On an iAlPdMn quasicrystal, high-quality diffraction patterns were obtained in a TEM. On 30°-twisted bilayer graphene, static momentum-selected EELS revealed anisotropies across Bragg conditions, and preliminary pump-probe EELS on the undiffracted beam captured a transient suppression and recovery of the π plasmon, consistent with a relaxation process involving optical and acoustic phonon scattering channels

At the same time, the EPFL campaign exposed the main experimental challenges that currently limit ultrafast studies in transmission electron microscopes. Heat accumulation, sample fragility, limited detection sensitivity, and the difficulty of achieving precise spatio-temporal overlap are the main barriers that need to be overcome. In this sense, these experiments simultaneously provided preliminary results and served as a benchmark for

defining realistic operating conditions and future design priorities. By identifying both the possibilities and constraints of the present generation of UTEMs, this work establishes a solid foundation for the next phase of development, where improved detectors, optimized repetition rates, and robust sample geometries will enable conclusive studies of complex and aperiodic materials.

Taken together, the results of this thesis connect instrumentation and application, bridging the conceptual design of photonic electron control with its first experimental realizations. They demonstrate that programmable, light-based modulation of free-electron wavefunctions is both feasible and scientifically valuable, opening a route toward ultrafast measurements with tailored spatial and momentum sensitivity. In this broader perspective, the advances in beam shaping and material studies converge toward a unified strategy in which tailored electron probes enable access to coherent excitations with improved contrast and selectivity. This work thus outlines a realistic pathway where photonic-based e-beam shaping would evolve into a standard tool for ultrafast investigations of quantum materials.

Appendix A

Correcting Drift in EPI Data Using Short-Exposure Frame Alignment

As discussed in Chap. 3, the QUADRO detector enables single-pulse ultrafast operation with high detective quantum efficiency and stable response at long camera lengths, which is crucial for momentum-resolved measurements. The high efficiency of the QUADRO enables imaging with short exposure times (of the order of tens of seconds in pulsed mode). These short exposure images are sufficiently resolved to be compared to a reference frame and consequently aligned or discarded. This approach prevents the accumulation of drift and blur that would otherwise occur during long exposures, allowing us to post-align frames affected by slow mechanical or electrical instabilities (such as vibrations or TEM lens-current oscillations). This appendix documents the post-acquisition strategy we adopted to suppress such instabilities and preserve momentum resolution in the presence of residual drift and low-frequency noise.

A.1 Post-Acquisition Frame Alignment

The instabilities are addressed post-acquisition through a robust frame alignment procedure based on the enhanced correlation coefficient (ECC) algorithm implemented via the `cv2.findTransformECC()` function from the OpenCV Python library [152]. This post-acquisition drift correction preserves the resolution over the entire acquisition period. In practice, we (i) load short-exposure frames, (ii) select a region of interest (ROI), (iii) estimate the inter-frame transform with ECC, (iv) warp each frame to a common reference, (v) discard frames that exhibit intra-frame motion which cause them to fail convergence, and (vi) average the aligned stack to obtain the final momentum map.

A.2 Jupyter Notebook

All implementation details and output figures are reported in the following Jupyter notebook, which contains the most recent version of the alignment procedure. The notebook also includes the analysis used to reconstruct the nanostructured membrane patterned with a Siemens star exhibiting two-fold rotational symmetry, as discussed in Sec. 5.3.2. The complete code, intermediate results, and visual outputs are provided here to ensure full transparency and reproducibility of the data processing workflow.

In [1]:
```
#With importlib.reload(module) I can update my utils and do not restart the kernel
import importlib
# libraries in C:\Users\bea97\OneDrive\Documenti\my_utils_main or in your shared dr
# import my_utils.detector_v4 as ud
# import my_utils.data_analysis_v4 as uda
import my_utils.plt_style as ps

import h5py
import hdf5plugin

import numpy as np
import pandas as pd
import matplotlib.pyplot as plt
import xarray as xr
import os
import cv2

from tqdm import tqdm   #progressbar


from scipy.optimize import curve_fit
import matplotlib.ticker as mticker
from matplotlib.animation import FuncAnimation
from IPython.display import display, Image as IPImage

ps.article_style()
```

Doing ESPI with laser scanning

pinem scanning with SLM. The SLM grating determines the laser position. Reference delay times before t0 images taken at every laser position

In [2]:
```
day = '20240822'  #CHANGE ME
scan_name = r'pinem_rotate'  #CHANGE ME
f_name = r'G:\Shared drives\Data_2024_2\%s\%s' %(day,scan_name)
print(f_name)


im_names  = sorted(next(os.walk(f_name))[2])
file_names = [f_name+'/'+im_n for im_n in im_names]

#folder to save plots
plot_folder = r'plots\%s\%s_v2_thesis' %(day, scan_name)
if not os.path.exists(plot_folder):
    os.makedirs(plot_folder)

#folder to save datasets
ds_folder = r'%s\ds' %(f_name)
if not os.path.exists(ds_folder):
    os.makedirs(ds_folder)
```

```
G:\Shared drives\Data_2024_2\20240822\pinem_rotate
```

Sanity check, ROI selection and theshold set

In [3]:
```python
def hdf5_to_array(fileName, roi_L = 512, roi_x0 = 0, roi_y0 = 0):
    '''
    Read the hdf5 file and return the image as a numpy array of

    Params:
    fileName: str, path to the hdf5 file
    roi_L: int, length of the region of interest (ROI) in pixels
    roi_x0: int, x coordinate of the top left corner of the ROI
    roi_y0: int, y coordinate of the top left corner of the ROI
    Returns:
    im: numpy array, the image data in the ROI
    '''



    with h5py.File(fileName, 'r') as f:
        dset = f['entry']['data']['data']   #this is how the h5 file is structured

        im = np.array(dset[:, roi_y0:(roi_y0+roi_L), roi_x0:(roi_x0+roi_L)], dtype=

    return im
```

In [4]:
```python
import plotly.express as px

check_im = hdf5_to_array(file_names[0]).sum(0)
counts_ref_frame = check_im.sum()


fig = px.imshow(check_im, color_continuous_scale='Viridis', title="Use to set cente
fig.show()
```

In [5]:
```python
rough_xc, rough_yc = 195, 323
roi_L = 130
roi_x0, roi_y0 = rough_xc-roi_L//2, rough_yc-roi_L//2

#plot the image with the ROI and print tot sum count
#check different files and use this to set the threshold
check_frame = hdf5_to_array(fileName = file_names[-10], roi_L=roi_L, roi_x0=roi_x0,
plt.imshow(check_frame)
plt.title('Image with ROI')
plt.colorbar()

check_frame_sum = check_frame.sum()
print('Sum counts in the ROI: ', check_frame_sum)

########CHECK ME###############
threshold = check_frame_sum * 2
print('Assigned threshold: ', threshold)
```

```
Sum counts in the ROI:  2566
Assigned threshold:  5132
```

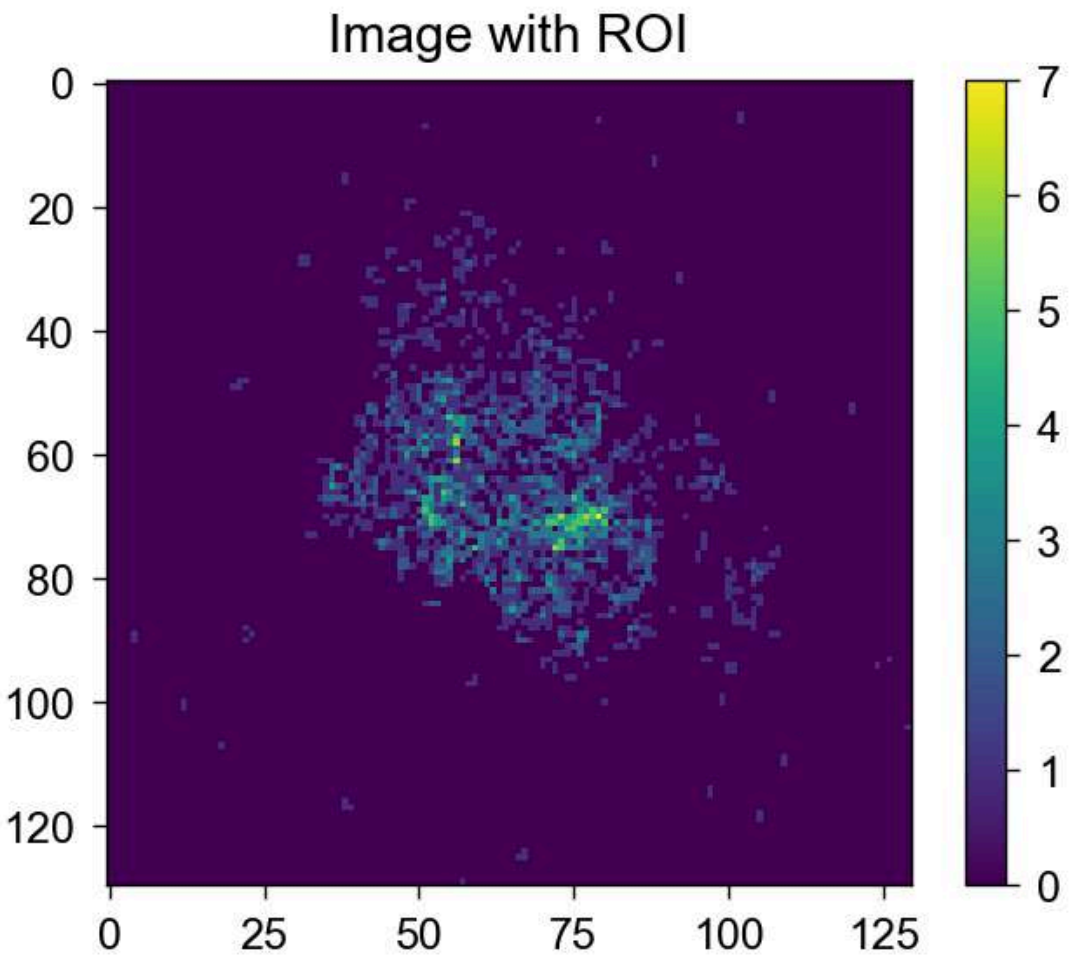

Frame alignement

Each file containes multiple images, that I call frames. These frames need to be aligned, summed and stored

In [23]:
```
def align_images(image, reference_image, min_cc=0.85, number_of_iterations=45, term
    '''
    Aligns image to reference_image using ECC. Raises error if ECC < min_cc.
    The ECC algorithm maximizes the correlation coefficient between the input image
    by estimating a transformation matrix iteratively. This method is robust and wi
    Reference:
    Evangelidis, G. D., & Psarakis, E. Z. (2008). https://doi.org/10.1109/TPAMI.200

    Params:
    - image: np.ndarray (grayscale)
    - reference_image: np.ndarray (grayscale)
    - min_cc: float, minimum acceptable correlation coefficient
    - number_of_iterations: int, ECC max iteration steps
    - termination_eps: float, convergence epsilon

    Returns:
```

```
    - aligned_image: np.ndarray
    - shift: (x, y) tuple

    Raises:
    - RuntimeError if ECC is too low (assumes non-convergence)
    '''

    warp_mode = cv2.MOTION_TRANSLATION
    criteria = (cv2.TERM_CRITERIA_EPS | cv2.TERM_CRITERIA_COUNT, number_of_iteratio

    warp_matrix = np.eye(2, 3, dtype=np.float32)
    ref = reference_image.astype(np.float32)
    img = image.astype(np.float32)

    try:
        cc, warp_matrix = cv2.findTransformECC(ref, img, warp_matrix, warp_mode, cr

        if cc < min_cc:
            raise RuntimeError(f"ECC too low: {cc:.4f}. Possible failure to converg

        aligned_image = cv2.warpAffine(img, warp_matrix,
                                       (ref.shape[1], ref.shape[0]),
                                       flags=cv2.INTER_LINEAR + cv2.WARP_INVERSE_MA
        shift = (warp_matrix[0, 2], warp_matrix[1, 2])
        return aligned_image, shift

    except cv2.error as e:
        raise RuntimeError(f"OpenCV error in ECC: {e}")
```

Test

In [44]:

```
ref_frame = check_frame.copy()
counts_ref_frame = ref_frame.sum()

to_be_aligned_frame = hdf5_to_array(file_names[165], roi_L, roi_x0, roi_y0)[6,:,:]
# # Normalize the image to the same number of counts as the reference frame
# to_be_aligned_frame = to_be_aligned_frame/to_be_aligned_frame.sum() * counts_ref_

test_aligned_frame, test_shift = align_images(to_be_aligned_frame, ref_frame)


#####Comparison plot
fig, axs = plt.subplots(2,2, dpi=300)
vmax = 7
val = 3

im = axs[0,0].imshow(ref_frame, vmax = vmax)
axs[0,0].set_title('Reference frame')
#colorbar
cbar = plt.colorbar(im, ax=axs[0,0])

axs[0,1].imshow(to_be_aligned_frame, vmax = vmax)
axs[0,1].set_title('Frame to be aligned')
```

```
#difference between the two images
im2 = axs[1,0].imshow(ref_frame - to_be_aligned_frame, cmap='seismic', vmin=-val, v
axs[1,0].set_title('Original difference')
#colorbar
cbar = plt.colorbar(im2, ax=axs[1,0])

axs[1,1].imshow(ref_frame - test_aligned_frame, cmap='seismic', vmin=-val, vmax=val
axs[1,1].set_title('Aligned difference')

plt.tight_layout()
test_shift
```

Out[44]: (np.float32(-6.002836), np.float32(3.8536456))

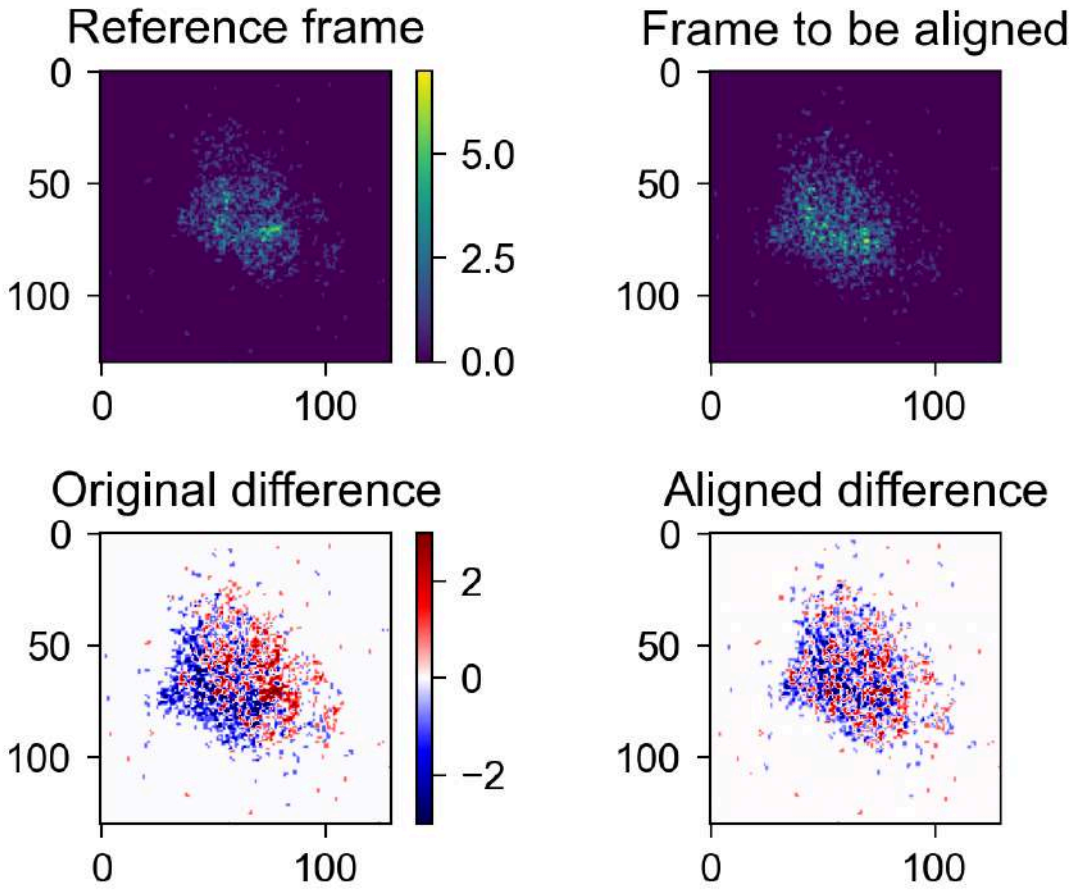

Aligning and discarding outliars (no normalization!)

In [28]:
```
import logging
# module-level logger; configure in your main script
logger = logging.getLogger(__name__)
```

In [82]:
```
def get_image(file_name, ref_frame, min_cc=0.8, number_of_iterations=40, terminatio
    '''
    Reads the hdf5 file, aligns all frames with total counts below the threshold, a
    Frames above the threshold or for which alignment fails (low ECC or convergence
```

```
    If more than 20% of the frames are discarded, returns an image full of NaNs.

    Params:
    file_name: str, path to the hdf5 file
    ref_frame: np.ndarray, the reference frame to align to
    min_cc: float, minimum ECC value to accept a frame
    number_of_iterations: int, max ECC iterations
    termination_eps: float, convergence epsilon for ECC
    plots: bool, if True, show discarded frames

    Returns:
    im: np.ndarray, the aligned image (or NaNs if too many discarded)
    counts: list of floats, total counts for each frame
    shifts: list of (x, y) shift tuples (or NaN if discarded)
    '''

    frames = hdf5_to_array(file_name, roi_L, roi_x0, roi_y0)
    N = len(frames)

    im = np.zeros_like(frames[0], dtype=np.float64)
    counts = []
    shifts = []
    n_discarded = 0

    for i, frame in enumerate(frames):
        total = frame.sum()
        if total < threshold:
            try:
                aligned, shift = align_images(
                    frame, ref_frame,
                    min_cc=min_cc,
                    number_of_iterations=number_of_iterations,
                    termination_eps=termination_eps
                )
                im += aligned
                counts.append(total)
                shifts.append(shift)

            # If ECC fails, discard the frame
            except RuntimeError as e:
                n_discarded += 1
                counts.append(0)
                shifts.append((np.nan, np.nan))
                logger.warning(f"Frame {i} discarded (ECC fail): {e}")
                if plots:
                    plt.figure(); plt.imshow(frame, vmax=val)
                    plt.title(f"Discarded {i}: ECC fail"); plt.show()

        # If the frame is too bright, discard it
        else:
            n_discarded += 1
            counts.append(0)
            shifts.append((np.nan, np.nan))
            logger.info(f"Frame {i} discarded (sum={total:.0f} ≥ threshold)")
            if plots:
                plt.figure(); plt.imshow(frame, vmax=val)
```

```
                plt.title(f"Discarded {i}: too bright"); plt.show()

    # If too many are bad, return NaN-image
    if n_discarded / N > 0.5:
        logger.error(f">20% frames discarded ({n_discarded}/{N}), returning NaN ima
        return np.full_like(im, np.nan), counts, shifts

    # Otherwise normalize by N / kept
    kept = N - n_discarded
    scale = N / kept
    im *= scale
    logger.info(f"Kept {kept}/{N} frames; applied scale factor {scale:.3f}")

    return im, counts, shifts
```

In [83]:
```
#check function
im, counts, shifts = get_image(file_names[91], ref_frame, plots=True)

fig, axs = plt.subplots(1, 3, figsize=(10, 2.7))

# Plot the aligned image
axs[0].imshow(im, cmap='viridis')
axs[0].set_title('Aligned Image')
axs[0].axis('off')

# Plot the counts
axs[1].plot(counts, marker='o', c='k')
axs[1].set_title('Count sum of Aligned Frames')
axs[1].set_xlabel('Frame Index')
axs[1].set_ylabel('Counts')
axs[1].set_aspect('auto')  # Keep default aspect ratio for line plot

# Plot the shifts
shifts = np.array(shifts)
axs[2].plot(shifts[:, 0], label='Shift X', marker='o', linestyle='-')
axs[2].plot(shifts[:, 1], label='Shift Y', marker='o', linestyle='-')
axs[2].set_title('Shifts (X and Y)')
axs[2].set_xlabel('Frame Index')
axs[2].set_ylabel('Shift')
axs[2].legend()

plt.tight_layout()
plt.show()
```

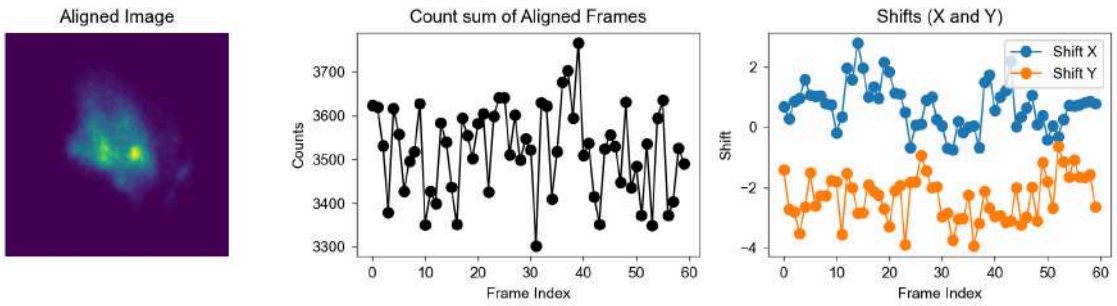

In [84]:
```
# loop over all files to store the aligned images in data

data = []
# counts are useful when I do normalization in get_image, because the counts inform
# Here I don't do normalization, so I don't need the counts, but I don't want to ch
counts = []
shifts = []

for fn in tqdm(file_names):
    im, count, shift = get_image(fn, ref_frame)
    data.append(im)
    counts.append(count)
    shifts.append(shift)

# Convert the lists to numpy arrays
data = np.array(data)
counts = np.array(counts)
shifts = np.array(shifts)

#Save the data as array
np.save(os.path.join(ds_folder, 'aligned_images_no_norm_v3.npy'), data)
np.save(os.path.join(ds_folder, 'counts_v3.npy'), counts)
np.save(os.path.join(ds_folder, 'shifts_v3.npy'), shifts)
```

```
  0%|          | 0/768 [00:00<?, ?it/s]
```

```
  2%|▏          | 19/768 [00:11<07:11,  1.73it/s]Frame 11 discarded (ECC fail): ECC
too low: 0.7823. Possible failure to converge within 40 iterations.
  5%|▍          | 39/768 [00:21<06:14,  1.95it/s]Frame 55 discarded (ECC fail): ECC t
oo low: 0.5515. Possible failure to converge within 40 iterations.
Frame 56 discarded (ECC fail): ECC too low: 0.7658. Possible failure to converge wit
hin 40 iterations.
 10%|▊          | 77/768 [00:49<08:56,  1.29it/s]Frame 30 discarded (ECC fail): ECC t
oo low: 0.7770. Possible failure to converge within 40 iterations.
 12%|▉          | 96/768 [01:02<06:49,  1.64it/s]Frame 26 discarded (ECC fail): ECC
too low: 0.7551. Possible failure to converge within 40 iterations.
Frame 27 discarded (ECC fail): ECC too low: 0.7326. Possible failure to converge wit
hin 40 iterations.
 14%|█          | 108/768 [01:10<09:05,  1.21it/s]Frame 10 discarded (ECC fail): ECC
too low: 0.7980. Possible failure to converge within 40 iterations.
 18%|█▍         | 135/768 [01:33<09:05,  1.16it/s]Frame 53 discarded (ECC fail): ECC
too low: 0.7448. Possible failure to converge within 40 iterations.
 21%|█▋         | 165/768 [01:58<06:37,  1.52it/s]Frame 7 discarded (ECC fail): ECC
too low: 0.7577. Possible failure to converge within 40 iterations.
Frame 8 discarded (ECC fail): ECC too low: 0.6159. Possible failure to converge with
in 40 iterations.
Frame 9 discarded (ECC fail): ECC too low: 0.7675. Possible failure to converge with
in 40 iterations.
 23%|█▊         | 173/768 [02:03<08:08,  1.22it/s]Frame 39 discarded (ECC fail): ECC
too low: 0.7817. Possible failure to converge within 40 iterations.
 28%|██▏        | 215/768 [02:51<09:34,  1.04s/it]Frame 19 discarded (ECC fail): ECC
too low: 0.7939. Possible failure to converge within 40 iterations.
 28%|██▏        | 218/768 [02:55<10:12,  1.11s/it]Frame 7 discarded (ECC fail): ECC
too low: 0.7966. Possible failure to converge within 40 iterations.
 29%|██▎        | 222/768 [02:59<09:51,  1.08s/it]Frame 46 discarded (ECC fail): ECC
too low: 0.7866. Possible failure to converge within 40 iterations.
Frame 47 discarded (ECC fail): ECC too low: 0.6387. Possible failure to converge wit
hin 40 iterations.
Frame 48 discarded (ECC fail): ECC too low: 0.7917. Possible failure to converge wit
hin 40 iterations.
 47%|███▋       | 364/768 [04:57<05:30,  1.22it/s]Frame 43 discarded (ECC fail): ECC
too low: 0.7826. Possible failure to converge within 40 iterations.
 57%|████▌      | 439/768 [05:56<04:10,  1.31it/s]Frame 25 discarded (ECC fail): ECC
too low: 0.7960. Possible failure to converge within 40 iterations.
 59%|████▋      | 453/768 [06:07<03:59,  1.31it/s]Frame 6 discarded (ECC fail): ECC
too low: 0.7986. Possible failure to converge within 40 iterations.
 63%|████▉      | 482/768 [06:31<05:24,  1.13s/it]Frame 2 discarded (ECC fail): ECC
too low: 0.7989. Possible failure to converge within 40 iterations.
 64%|█████      | 491/768 [06:41<05:22,  1.17s/it]Frame 50 discarded (ECC fail): ECC
too low: 0.7979. Possible failure to converge within 40 iterations.
 65%|█████      | 503/768 [06:56<05:26,  1.23s/it]Frame 59 discarded (ECC fail): ECC
too low: 0.7954. Possible failure to converge within 40 iterations.
 66%|█████      | 506/768 [07:01<06:15,  1.43s/it]Frame 11 discarded (ECC fail): ECC
too low: 0.5457. Possible failure to converge within 40 iterations.
Frame 44 discarded (ECC fail): ECC too low: 0.7724. Possible failure to converge wit
hin 40 iterations.
 66%|█████▏     | 509/768 [07:06<06:56,  1.61s/it]Frame 48 discarded (ECC fail): ECC
too low: 0.4812. Possible failure to converge within 40 iterations.
 67%|█████▏     | 518/768 [07:18<05:19,  1.28s/it]Frame 27 discarded (ECC fail): ECC
too low: 0.7567. Possible failure to converge within 40 iterations.
Frame 33 discarded (ECC fail): ECC too low: 0.7692. Possible failure to converge wit
hin 40 iterations.
```

```
Frame 55 discarded (ECC fail): ECC too low: 0.7943. Possible failure to converge wit
hin 40 iterations.
 69%|██████▉   | 527/768 [07:28<04:43,  1.18s/it]Frame 4 discarded (ECC fail): ECC
too low: 0.6924. Possible failure to converge within 40 iterations.
Frame 5 discarded (ECC fail): ECC too low: 0.6636. Possible failure to converge with
in 40 iterations.
Frame 6 discarded (ECC fail): ECC too low: 0.6866. Possible failure to converge with
in 40 iterations.
 69%|██████▉   | 530/768 [07:32<04:55,  1.24s/it]Frame 45 discarded (ECC fail): ECC
too low: 0.7921. Possible failure to converge within 40 iterations.
 69%|██████▉   | 533/768 [07:37<05:32,  1.42s/it]Frame 37 discarded (ECC fail): ECC
too low: 0.7806. Possible failure to converge within 40 iterations.
 70%|██████▉   | 539/768 [07:43<04:28,  1.17s/it]Frame 22 discarded (ECC fail): ECC
too low: 0.7304. Possible failure to converge within 40 iterations.
 72%|███████   | 554/768 [08:00<03:51,  1.08s/it]Frame 47 discarded (ECC fail): ECC
too low: 0.7998. Possible failure to converge within 40 iterations.
 72%|███████   | 555/768 [08:01<03:56,  1.11s/it]Frame 55 discarded (ECC fail): ECC
too low: 0.7887. Possible failure to converge within 40 iterations.
 73%|███████   | 563/768 [08:10<03:24,  1.00it/s]Frame 44 discarded (ECC fail): ECC
too low: 0.7965. Possible failure to converge within 40 iterations.
 74%|███████   | 572/768 [08:17<02:20,  1.40it/s]Frame 22 discarded (ECC fail): ECC
too low: 0.6229. Possible failure to converge within 40 iterations.
Frame 23 discarded (ECC fail): ECC too low: 0.6767. Possible failure to converge wit
hin 40 iterations.
 76%|███████▏  | 584/768 [08:26<02:00,  1.53it/s]Frame 57 discarded (ECC fail): Open
CV error in ECC: OpenCV(4.10.0) D:\a\opencv-python\opencv-python\opencv\modules\vide
o\src\ecc.cpp:589: error: (-7:Iterations do not converge) The algorithm stopped befo
re its convergence. The correlation is going to be minimized. Images may be uncorrel
ated or non-overlapped in function 'cv::findTransformECC'

Frame 58 discarded (ECC fail): ECC too low: 0.6429. Possible failure to converge wit
hin 40 iterations.
 77%|███████▏  | 593/768 [08:32<01:57,  1.49it/s]Frame 50 discarded (ECC fail): ECC
too low: 0.7948. Possible failure to converge within 40 iterations.
 78%|███████▏  | 600/768 [08:37<02:07,  1.32it/s]Frame 48 discarded (ECC fail): ECC
too low: 0.6487. Possible failure to converge within 40 iterations.
Frame 49 discarded (ECC fail): OpenCV error in ECC: OpenCV(4.10.0) D:\a\opencv-pytho
n\opencv-python\opencv\modules\video\src\ecc.cpp:589: error: (-7:Iterations do not c
onverge) The algorithm stopped before its convergence. The correlation is going to b
e minimized. Images may be uncorrelated or non-overlapped in function 'cv::findTrans
formECC'

Frame 50 discarded (ECC fail): ECC too low: 0.7768. Possible failure to converge wit
hin 40 iterations.
 80%|███████▎  | 616/768 [08:51<02:35,  1.02s/it]Frame 3 discarded (ECC fail): ECC t
oo low: 0.7884. Possible failure to converge within 40 iterations.
 82%|███████▍  | 632/768 [09:08<02:17,  1.01s/it]Frame 4 discarded (ECC fail): ECC
too low: 0.7503. Possible failure to converge within 40 iterations.
Frame 5 discarded (ECC fail): ECC too low: 0.5532. Possible failure to converge with
in 40 iterations.
 84%|███████▌  | 643/768 [09:20<02:23,  1.14s/it]Frame 20 discarded (ECC fail): ECC
too low: 0.7906. Possible failure to converge within 40 iterations.
Frame 21 discarded (ECC fail): ECC too low: 0.7180. Possible failure to converge wit
hin 40 iterations.
Frame 22 discarded (ECC fail): ECC too low: 0.6825. Possible failure to converge wit
hin 40 iterations.
```

```
Frame 23 discarded (ECC fail): ECC too low: 0.7878. Possible failure to converge wit
hin 40 iterations.
 85%|████████▌ | 655/768 [09:34<01:59,  1.06s/it]Frame 38 discarded (ECC fail): ECC
too low: 0.7990. Possible failure to converge within 40 iterations.
 86%|████████▌ | 659/768 [09:38<02:01,  1.11s/it]Frame 18 discarded (ECC fail): ECC
too low: 0.4448. Possible failure to converge within 40 iterations.
Frame 19 discarded (ECC fail): ECC too low: 0.6778. Possible failure to converge wit
hin 40 iterations.
 88%|████████▊ | 673/768 [09:53<01:35,  1.00s/it]Frame 23 discarded (ECC fail): ECC
too low: 0.7788. Possible failure to converge within 40 iterations.
 89%|████████▉ | 687/768 [10:11<01:43,  1.27s/it]Frame 33 discarded (ECC fail): ECC
too low: 0.6722. Possible failure to converge within 40 iterations.
Frame 34 discarded (ECC fail): ECC too low: 0.7455. Possible failure to converge wit
hin 40 iterations.
 90%|████████▉ | 688/768 [10:12<01:45,  1.32s/it]Frame 41 discarded (ECC fail): ECC
too low: 0.7957. Possible failure to converge within 40 iterations.
 92%|█████████▏| 703/768 [10:29<01:14,  1.14s/it]Frame 3 discarded (ECC fail): ECC
too low: 0.7790. Possible failure to converge within 40 iterations.
Frame 4 discarded (ECC fail): OpenCV error in ECC: OpenCV(4.10.0) D:\a\opencv-python
\opencv-python\opencv\modules\video\src\ecc.cpp:589: error: (-7:Iterations do not co
nverge) The algorithm stopped before its convergence. The correlation is going to be
minimized. Images may be uncorrelated or non-overlapped in function 'cv::findTransfo
rmECC'

Frame 5 discarded (ECC fail): ECC too low: 0.6145. Possible failure to converge with
in 40 iterations.
 93%|█████████▎| 718/768 [10:44<00:47,  1.05it/s]Frame 36 discarded (ECC fail): ECC
too low: 0.5705. Possible failure to converge within 40 iterations.
Frame 37 discarded (ECC fail): ECC too low: 0.6434. Possible failure to converge wit
hin 40 iterations.
 97%|█████████▋| 747/768 [11:13<00:18,  1.14it/s]Frame 38 discarded (ECC fail): ECC
too low: 0.7346. Possible failure to converge within 40 iterations.
Frame 39 discarded (ECC fail): ECC too low: 0.5793. Possible failure to converge wit
hin 40 iterations.
 98%|█████████▊| 751/768 [11:17<00:15,  1.12it/s]Frame 17 discarded (ECC fail): ECC
too low: 0.7552. Possible failure to converge within 40 iterations.
 99%|█████████▉| 762/768 [11:27<00:05,  1.13it/s]Frame 12 discarded (ECC fail): ECC
too low: 0.7680. Possible failure to converge within 40 iterations.
Frame 13 discarded (ECC fail): OpenCV error in ECC: OpenCV(4.10.0) D:\a\opencv-pytho
n\opencv-python\opencv\modules\video\src\ecc.cpp:589: error: (-7:Iterations do not c
onverge) The algorithm stopped before its convergence. The correlation is going to b
e minimized. Images may be uncorrelated or non-overlapped in function 'cv::findTrans
formECC'

Frame 14 discarded (ECC fail): ECC too low: 0.6659. Possible failure to converge wit
hin 40 iterations.
100%|██████████| 768/768 [11:32<00:00,  1.11it/s]
```

In [85]:

```python
# open the data
data = np.load(os.path.join(ds_folder, 'aligned_images_no_norm_v3.npy'))
counts_per_frame = np.load(os.path.join(ds_folder, 'counts_v3.npy'))  # it saved on
shifts = np.load(os.path.join(ds_folder, 'shifts_v3.npy'), allow_pickle=True)

data.shape
```

Out[85]: (768, 130, 130)

In [86]:
```
plt.plot(counts_per_frame.flatten())
plt.title('counts for all frames, sanity check')
```

Out[86]: Text(0.5, 1.0, 'counts for all frames, sanity check')

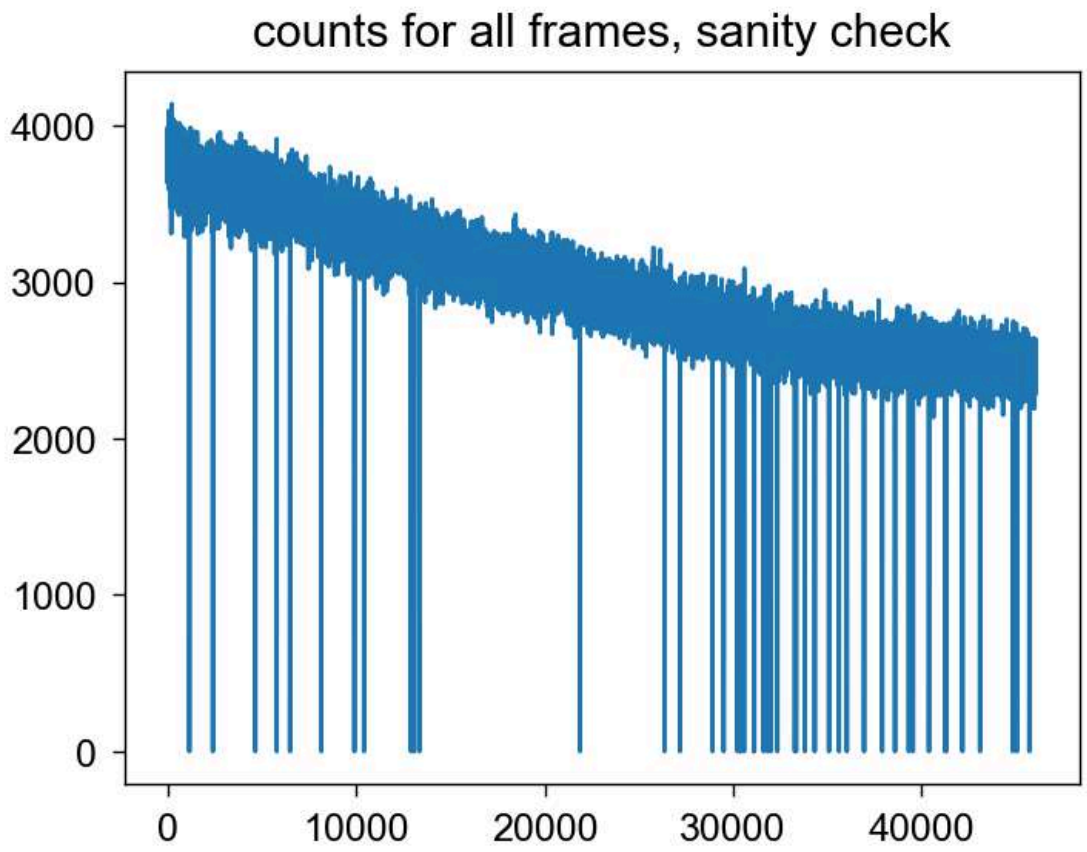

In [87]:
```
# Convert shifts to numpy arrays, replacing None with np.nan for plotting/statistic
shift_x = np.array([[s[0] if s[0] is not None else np.nan for s in row] for row in
shift_y = np.array([[s[1] if s[1] is not None else np.nan for s in row] for row in

plt.plot(shift_x.flatten(), marker='o', label='shift x')
plt.plot(shift_y.flatten(), marker='o', label='shift y')

plt.title('shifts for all frames, sanity check')

max_shift = np.nanmax([shift_x,shift_y])

print('Max shift: ', max_shift)
```

```
Max shift:  19.866701126098633
```

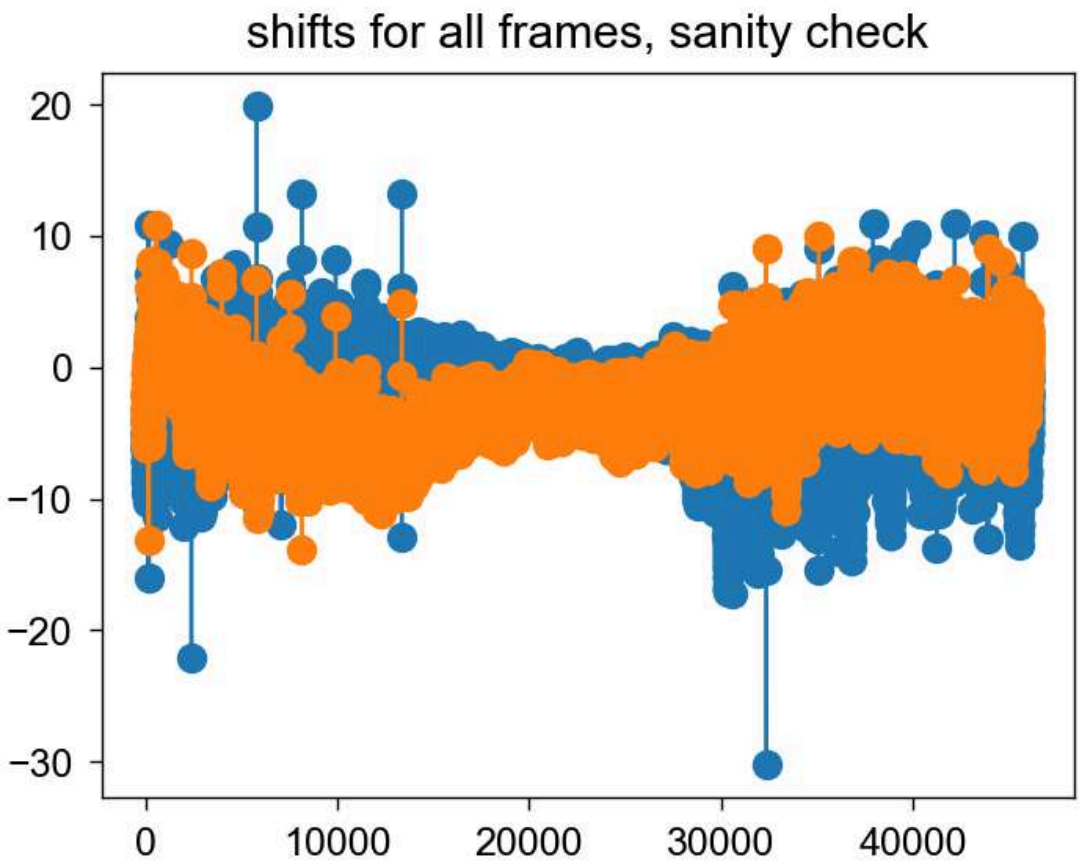

Dataset creation

In [88]:
```
def get_coordinates(im_names):

    from datetime import datetime

    lab_time = np.zeros(len(im_names), dtype='datetime64[us]')
    slow_scans = np.zeros(len(im_names))
    fast_scans = np.zeros(len(im_names))
    delay_time = np.zeros(len(im_names))
    theta = np.zeros(len(im_names))

    for i in range(len(im_names)):

        info = im_names[i].split('_')

        lab_time[i] = datetime(2024, *list(map(int, info[0:5])))
        slow_scans[i] = info[5]
        fast_scans[i] = info[6]
        delay_time[i] = np.round(float(info[7][:-1]),  -3)   #femtoseconds

        theta[i] = float(info[10][:-2])/10000  #radians

    return lab_time, slow_scans, fast_scans, delay_time, theta
```

In [89]:
```
lab_time, slow_scan, fast_scan, delay_time, theta = get_coordinates(im_names)
```

In [90]:
```
ds = xr.Dataset(
    data_vars=dict(
        im_old=(["lab_time", "x", "y"], data),
        counts=(["lab_time"], counts_per_frame.sum(1)),
        ),

    coords=dict(
        x=(["x"], np.arange(roi_L)),
        y=(["y"], np.arange(roi_L)),
        lab_time=(["lab_time"], lab_time),
        slow_scan=(["lab_time"], slow_scan),
        fast_scan=(["lab_time"], fast_scan),
        delay_time=(["lab_time"], delay_time),
        theta=(["lab_time"], theta),
        )
    )

ds['delay_time'] = ds.delay_time*1e-3 + 11 ## set t0 to 0

ds.to_netcdf(r"%s\ds_no_norm_v3.nc" %(ds_folder))
```

```
C:\Users\bea97\AppData\Local\Temp\ipykernel_28344\1855596810.py:1: UserWarning:

Converting non-nanosecond precision datetime values to nanosecond precision. This be
havior can eventually be relaxed in xarray, as it is an artifact from pandas which i
s now beginning to support non-nanosecond precision values. This warning is caused b
y passing non-nanosecond np.datetime64 or np.timedelta64 values to the DataArray or
Variable constructor; it can be silenced by converting the values to nanosecond prec
ision ahead of time.
```

In [91]:
```
with xr.open_dataset(r"%s\ds_no_norm_v3.nc" % (ds_folder)) as ds:
    ds = ds.load()

#delete counts variable
del ds['counts']

ds
```

Out[91]: xarray.Dataset

► Dimensions: (**lab_time**: 768, **x**: 130, **y**: 130)

▼ Coordinates:

x	(x)	int64	0 1 2 3 4 5 ... 125 126 127 ...
y	(y)	int64	0 1 2 3 4 5 ... 125 126 127 ...
lab_time	(lab_time)	datetime64[ns]	2024-08-22T21:19:59 ... 20...
slow_scan	(lab_time)	float64	0.0 0.0 0.0 0.0 ... 11.0 11.0 1...
fast_scan	(lab_time)	float64	0.0 0.0 1.0 1.0 ... 2.0 2.0 3.0 ...
delay_time	(lab_time)	float64	-3.0 0.0 -3.0 0.0 ... 0.0 -3.0 ...
theta	(lab_time)	float64	0.5 0.5 0.5 ... 1.375 1.375 1....

▼ Data variables:

im_old	(lab_time, x, y)	float64	0.0 0.0 0.0 0.0 ... 0.0 0.0 0.0 ...

► Indexes: (3)

► Attributes: (0)

NO Normalization

In [92]:
```
ds['tot_counts'] = ds.im_old.sum(('x','y'))

ds['im'] = ds.im_old   #/ ds.tot_counts * ds.tot_counts.mean()

# ds['im'].attrs['long_name'] = 'counts'

ds.tot_counts.plot()
ds.im.sum(('x','y')).plot()
```

Out[92]:
```
[<matplotlib.lines.Line2D at 0x2a920340130>]
```

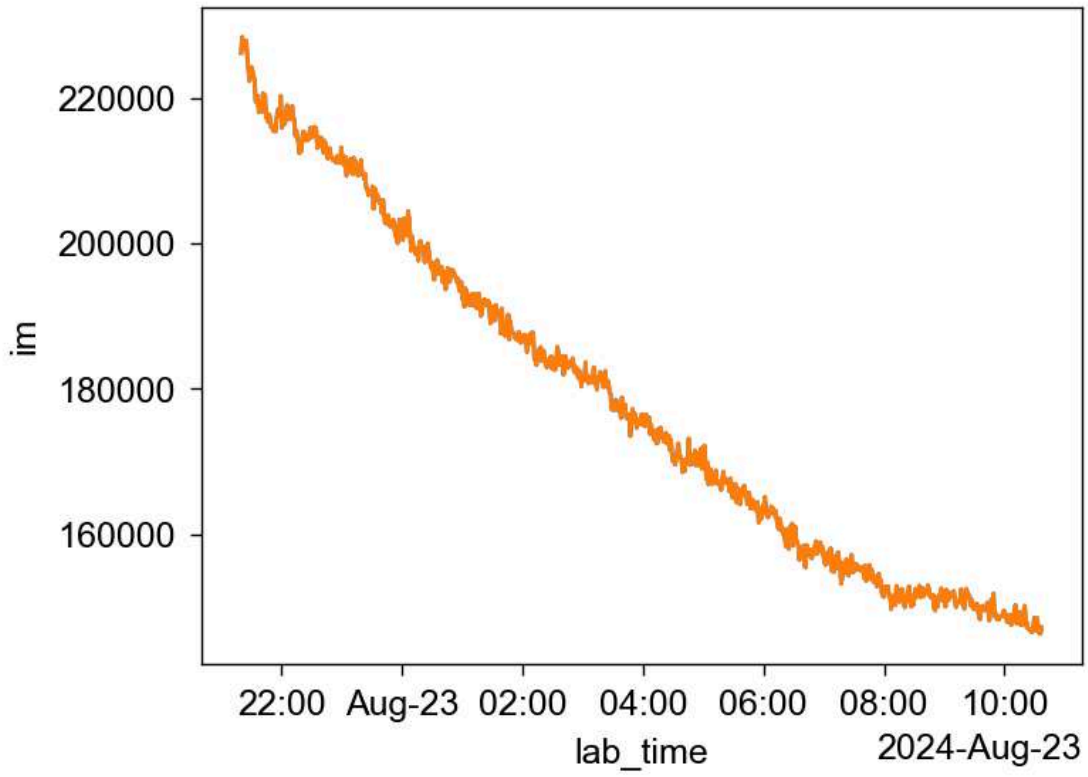

In [93]:
```
random_index = np.random.randint(0, len(ds.lab_time))
ds.isel(lab_time=random_index).im.plot()

plt.title('Random image for checking, index %s' % (random_index))
```

Out[93]:
```
Text(0.5, 1.0, 'Random image for checking, index 97')
```

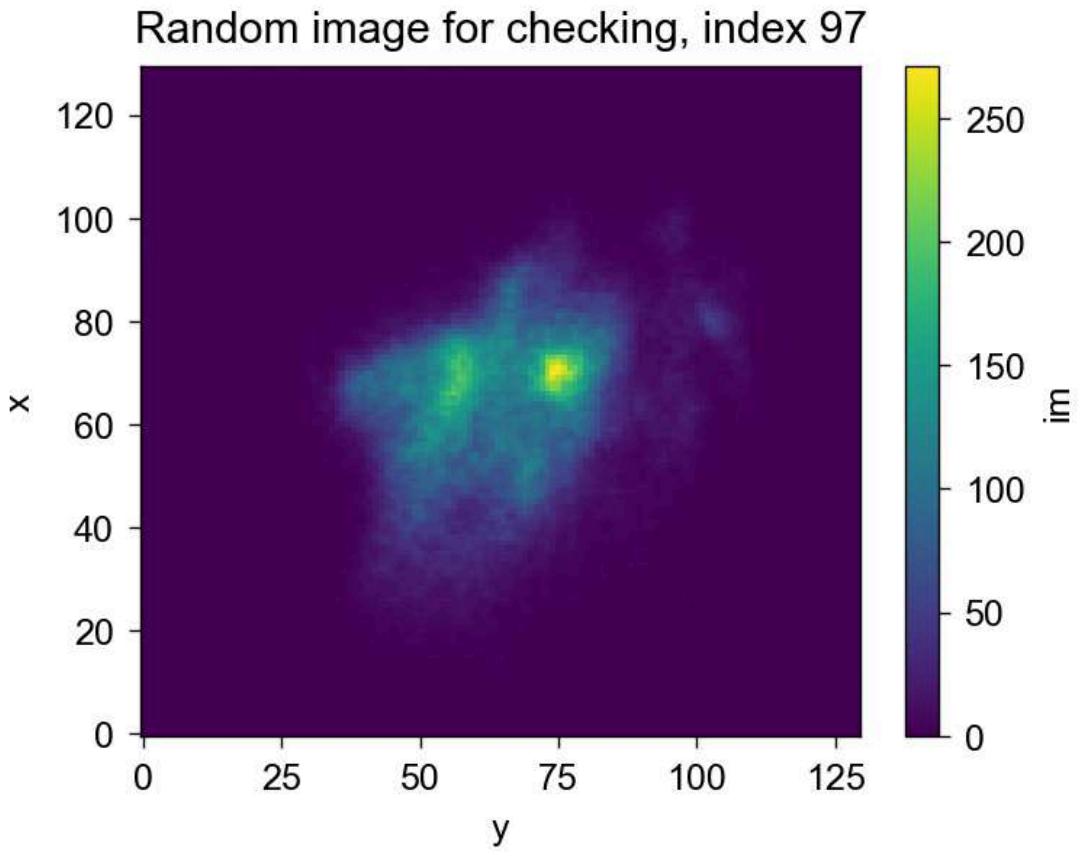

In [94]:
```
# ds.slow_scan.plot()
# ds.fast_scan.plot()
# (ds.theta).plot()
```

Animation, to chek everything is OK

In [95]:
```
#Check befure running the time consuming animation cell
vmax = 300

fig, ax = plt.subplots()
im_plot = ds.im.isel(lab_time=0).plot(vmax=vmax)
title = ax.set_title(f"Fast Scan: {int(ds.fast_scan.isel(lab_time=0).item())}, Slow
```

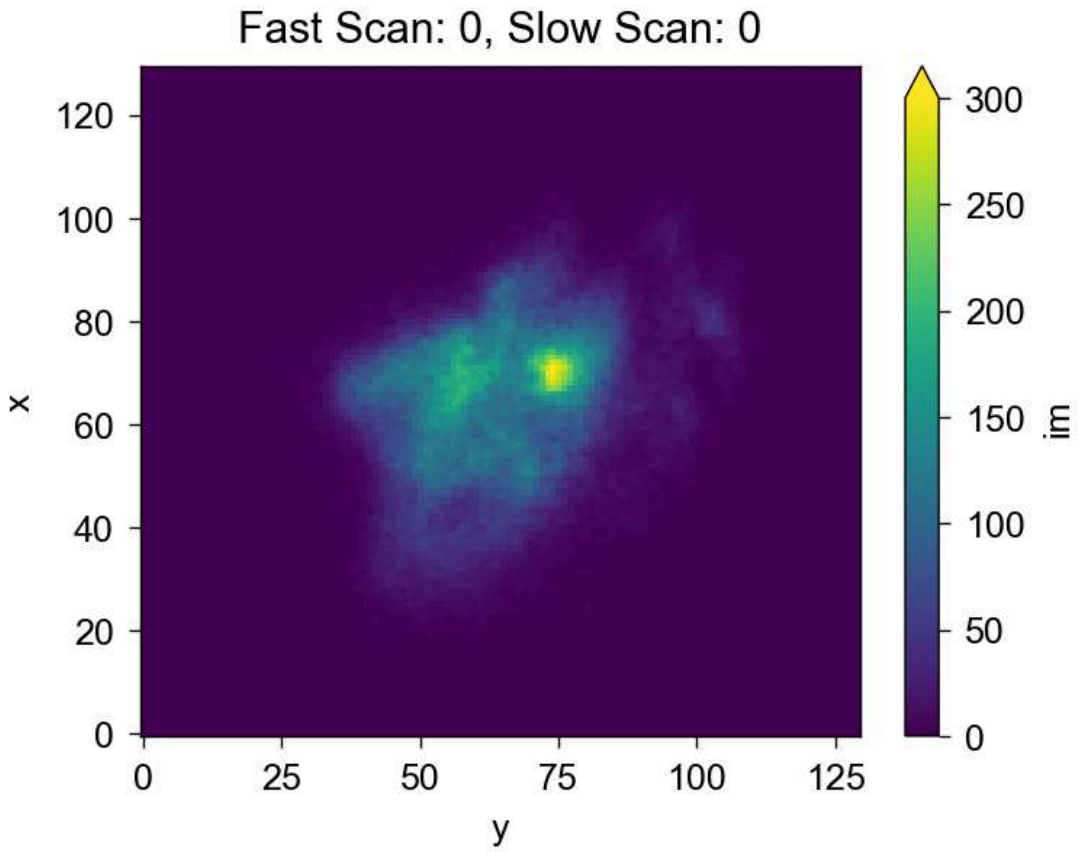

In [96]:
```
def update(frame):
    im_plot.set_array(ds.im.isel(lab_time=frame).values)
    title.set_text(f"Fast Scan: {int(ds.fast_scan.isel(lab_time=frame).item())}, Sl
    return im_plot, title
```

In [97]:
```
# from IPython.display import HTML

# fig, ax = plt.subplots()
# im_plot = ds.im.isel(lab_time=0).plot(vmax=vmax)
# title = ax.set_title(f"Fast Scan: {int(ds.fast_scan.isel(lab_time=0).item())}, Sl

# # Create the animation
# ani = FuncAnimation(fig, update, frames=len(ds.lab_time), interval=100, blit=True

# # Save the animation as a .mp4 file
# ani.save(os.path.join(plot_folder, 'aligned_images.mp4'), writer='ffmpeg', fps=10

# # Close the figure to avoid the static plot
# plt.close(fig)

# # Display the animation in the notebook
# HTML(ani.to_jshtml())
```

order by delay time

In [98]:
```
ds_us = ds.set_index(lab_time=('theta', 'delay_time', 'fast_scan', 'slow_scan'))
# This should be 0, otherwise the unstack will not work, which means you didn't put
print('number of duplicates = ', ds_us.im.indexes['lab_time'].duplicated().sum())
ds_us = ds_us.unstack(('lab_time'))
```

```
number of duplicates =  0
```

Extend the theta range

data were collected with theta varying over a half of 360° because the pattern has 2 fold rotational symmetry. So we can fairly add pi/2 to half of the data to extend the theta range

In [99]:
```
# Select data with odd slow_scan values
odd_slow_scan_data = ds_us.sel(slow_scan=ds_us.slow_scan % 2 == 1)

even_slow_scan_data = ds_us.sel(slow_scan=ds_us.slow_scan % 2 == 0)

# Modify theta and slow_scan for the selected data
odd_slow_scan_data = odd_slow_scan_data.assign_coords(
    theta=(odd_slow_scan_data.theta + 1) % 2,  # Ensure theta is between 0 and 2
    slow_scan=odd_slow_scan_data.slow_scan - 1
)

# Merge the modified data back into the original dataset
ds_us_2 = xr.concat([odd_slow_scan_data, even_slow_scan_data], dim='theta')
# Order the thetas
ds_us_2 = ds_us_2.sortby('theta')
ds_us_2
```

Out[99]: xarray.Dataset

► Dimensions: (**x**: 130, **y**: 130, **theta**: 16, **delay_time**: 2, **fast_scan**: 4, **slow_scan**: 6)

▼ Coordinates:

delay_time	(delay_time)	float64	-3.0 ...
fast_scan	(fast_scan)	float64	0.0 1....
x	(x)	int64	0 1 2 ...
y	(y)	int64	0 1 2 ...
theta	(theta)	float64	0.0 0....
slow_scan	(slow_scan)	float64	0.0 2....

▼ Data variables:

im_old	(x, y, theta, delay_time, fast_scan, slow_scan)	float64	0.0 0....
tot_counts	(theta, delay_time, fast_scan, slow_scan)	float64	2.132...
im	(x, y, theta, delay_time, fast_scan, slow_scan)	float64	0.0 0....

► Indexes: (6)

► Attributes: (0)

Summing over slow scan runs

In [100…

```
ds2 = ds_us_2.im.sum(('slow_scan')).to_dataset()
ds2
```

Out[100… xarray.Dataset

► Dimensions: (**delay_time**: 2, **fast_scan**: 4, **x**: 130, **y**: 130, **theta**: 16)

▼ Coordinates:

delay_time	(delay_time)	float64	-3.0 0.0
fast_scan	(fast_scan)	float64	0.0 1.0 2.0 3.0
x	(x)	int64	0 1 2 3 4 5 ... 12...
y	(y)	int64	0 1 2 3 4 5 ... 12...
theta	(theta)	float64	0.0 0.125 0.25 ... ...

▼ Data variables:

im	(x, y, theta, delay_time, fast_scan)	float64	0.0 0.0 0.0 0.0 ... ...

► Indexes: (5)

► Attributes: (0)

Convert pixels in momentum

from data in notebook "G:\Shared drives\LUMiNaD\Data_analysis\Si-grating_4pinem\20240131_C015_CW_analysis4calibration.ipynb"

In [101…
```
conversion_ratio = 1.8622526765
ds2['p_x'] = conversion_ratio*ds2.x
ds2['p_x'] = ds2.p_x - ds2.p_x.mean()
ds2['p_y'] = conversion_ratio*ds2.y
ds2['p_y'] = ds2.p_y - ds2.p_y.mean()

ds2.p_x.attrs['long_name'] = '$\overline{k}_x$ ($\mu$m$^{-1}$)'
ds2.p_y.attrs['long_name'] = '$\overline{k}_y$ ($\mu$m$^{-1}$)'
```

In [102…
```
# ds2.im.mean(('delay_time', 'scan'))
ds2.swap_dims({'x':'p_x', 'y':'p_y'}).im.mean(('theta','delay_time', 'fast_scan')).
```

Out[102… `<matplotlib.collections.QuadMesh at 0x2a92180c0a0>`

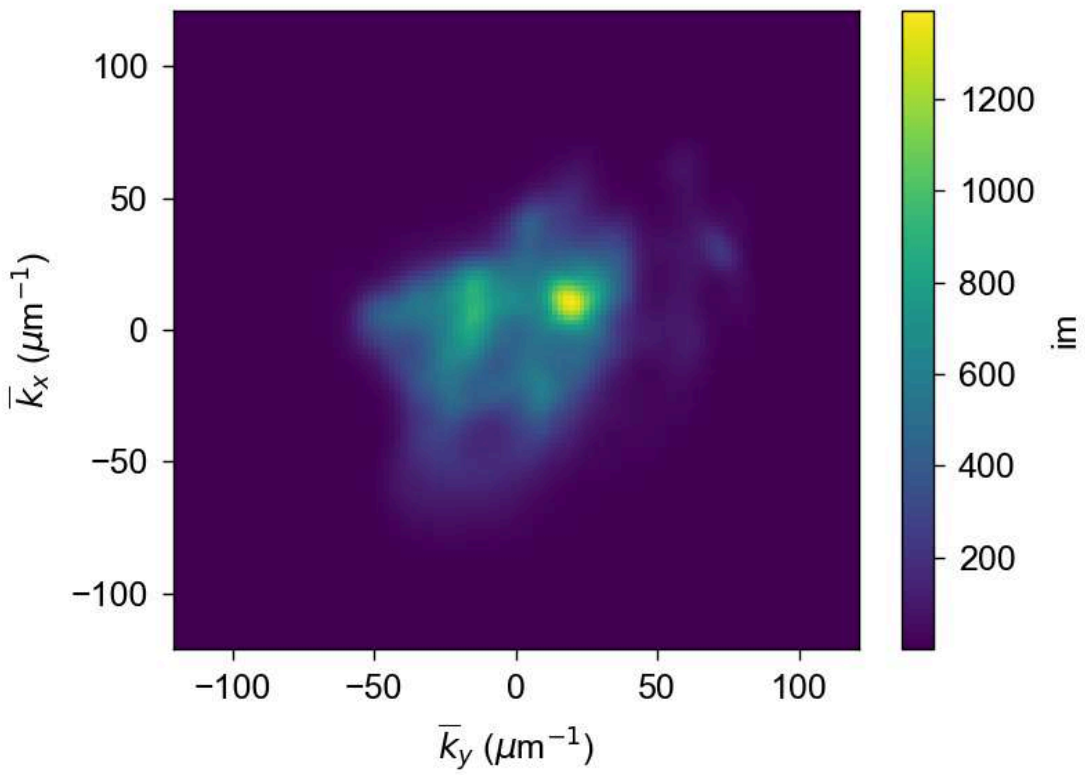

In [103…
```
#should be around
2*np.pi/1.030  #um^-1
```

Out[103… `6.100179909883093`

Some plots

In [104…

```
vmin = 0
vmax = 2700

ds2.im.sel(fast_scan=0).plot(col='theta', row='delay_time', vmin=vmin, vmax=vmax, c


for fast_scan_value in ds2.fast_scan.values:
    ds2.im.sel(fast_scan=fast_scan_value).plot(col='theta', row='delay_time', vmin=

    # Save plot
    fname = os.path.join(plot_folder, f'color_maps_fast_scan_{fast_scan_value}.png'
    plt.savefig(fname, dpi=300, bbox_inches='tight')
    plt.close()
```

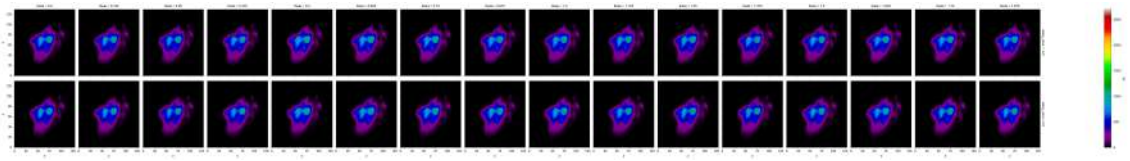

Profile manipulation

Select good area to integrate to get the profile

In [105…

```
ds2.im.mean(('theta', 'delay_time','fast_scan')).plot(cmap='nipy_spectral')

min_val = 69
max_val = 81
# plot ROI as vertical lines
plt.axvspan(min_val, max_val, color='lightblue', alpha=0.7)
plt.title('Mean image with ROI for profile extraction')

#save
plt.savefig(os.path.join(plot_folder, 'mean_image_with_ROI.png'), dpi=300, bbox_inc
```

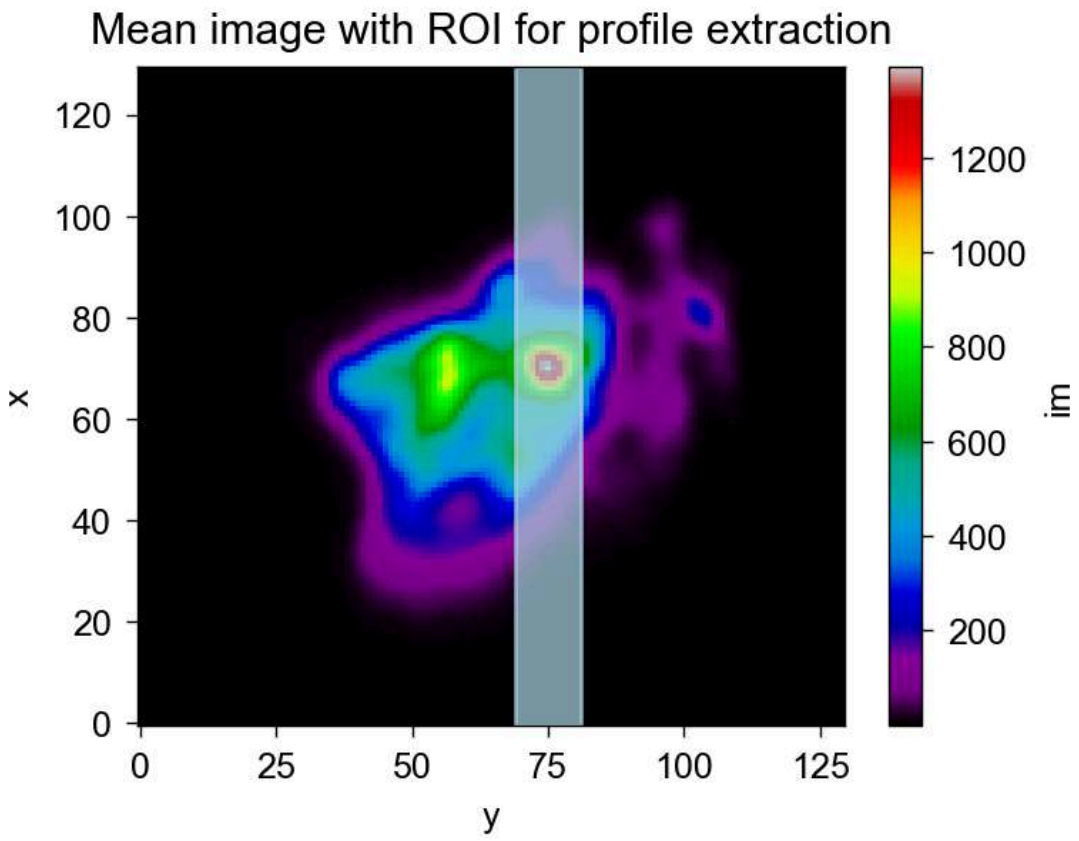

Normalization

I want the profiles to be normalized with respect to the maximum of the delay_time[0]

In [106…
```
no_norm_prof = ds2.im.sel(y=slice(min_val, max_val)).sum('y')

ds2['profile'] = no_norm_prof / no_norm_prof.isel(delay_time=0).max(('x')) # * no_n

ds2.profile.attrs['long_name'] = 'counts'
```

Summing along y axis, streaking is along x

In [107…
```
ds2.profile.isel(fast_scan=0).plot(hue='delay_time', col='theta', col_wrap=4)
```

Out[107…
```
<xarray.plot.facetgrid.FacetGrid at 0x2a921a93a30>
```

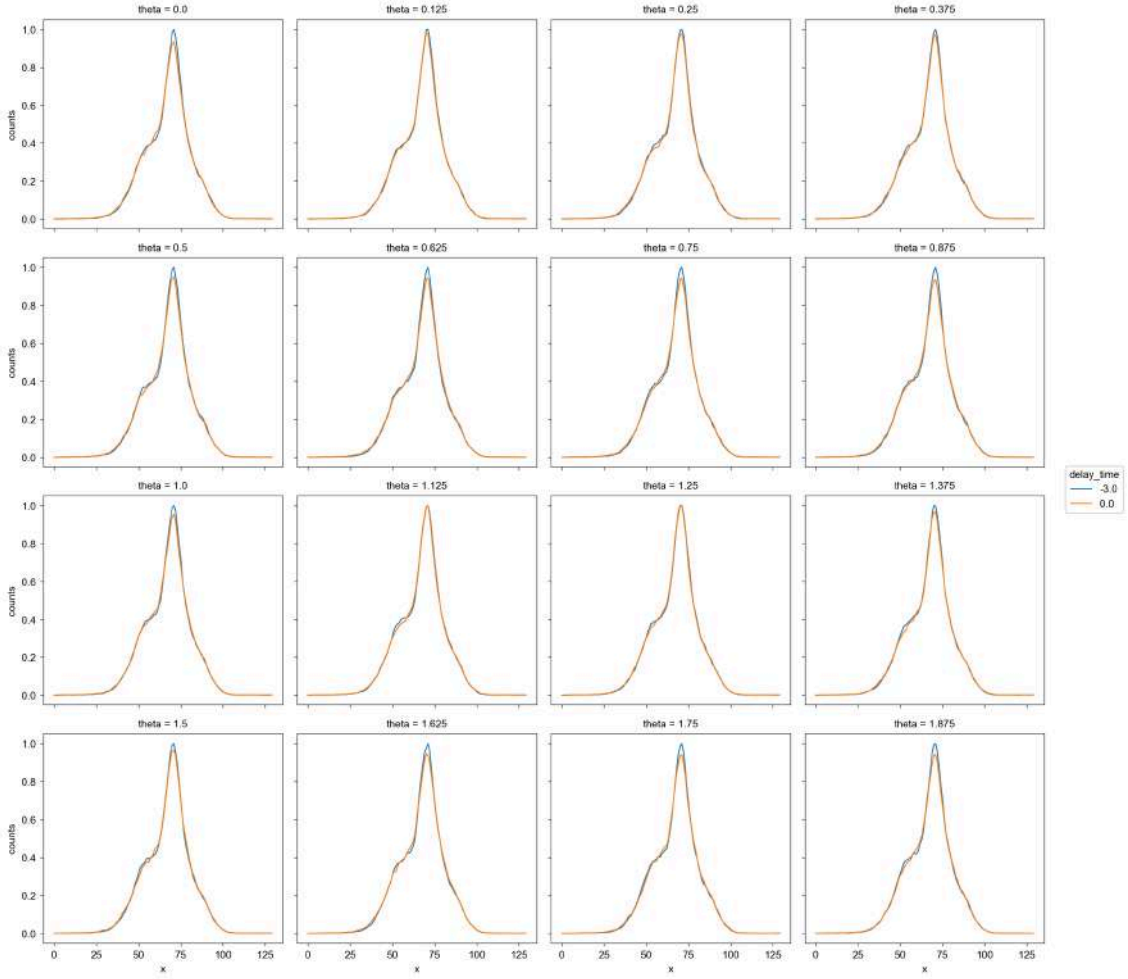

In [108…
```
#save plot for all fast scans
for fast_scan_value in ds2.fast_scan.values:
    ds2.profile.sel(fast_scan=fast_scan_value).plot(hue='delay_time', col='theta',

    # Save plot
    fname = os.path.join(plot_folder, f'profile_fast_scan_{fast_scan_value}.png')
    plt.savefig(fname, dpi=300, bbox_inches='tight')
    plt.close()
```

Profiles difference

In [109…
```
ds2['diff_profile'] = ds2.isel(delay_time=1).profile - ds2.isel(delay_time=0).profi
ds2.diff_profile.attrs['long_name'] = 'counts'
```

In [110…
```
import seaborn as sns
sns.set_palette('inferno', n_colors=len(ds2.theta))

spacing = [i*0.001 for i in range(len(ds2.theta))] + ds2.theta*0  #quick way to gen
(ds2.diff_profile + spacing).plot(hue='theta', col='fast_scan')
```



```
#Figure title of the entire grid
```

```
plt.suptitle('Profile difference for all fast scans', fontsize=16, y=1.03)

#save plot
plt.savefig(os.path.join(plot_folder, 'diff_profile.png'), dpi=300, bbox_inches='ti
```

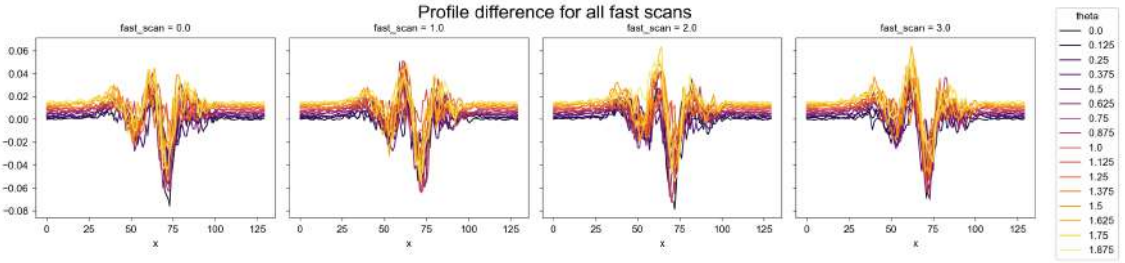

In [111…

```
spacing = [i*0.001 for i in range(len(ds2.theta))] + ds2.theta*0  #quick way to gen
(ds2.diff_profile.mean('fast_scan') + spacing).plot(hue='theta')

# Get the existing legend
legend = plt.gca().get_legend()
legend.set_bbox_to_anchor((1, 1))
legend.set_loc('upper right')

plt.ylabel('Profile difference Sum')
plt.grid(True)
plt.title('Profile difference for all fast scans for x ROI selection')


#ROI selection #######
# Calculate the average profile by summing over the relevant dimensions
average_profile = ds2.diff_profile.mean(dim=('theta', 'fast_scan'))

# Find the x value corresponding to the minimum of the average profile
# notice that slice will include both the starting AND the ending value, whih is go
roi_center = average_profile.x[average_profile.argmin()].item()
min_val = roi_center - 3
max_val = roi_center + 2

# Define the width of the ROI
plt.axvspan(min_val, max_val, color='lightblue', alpha=0.7, label='ROI')

# Save plot
plt.savefig(os.path.join(plot_folder, 'profile_with_ROI.png'), dpi=300, bbox_inches
```

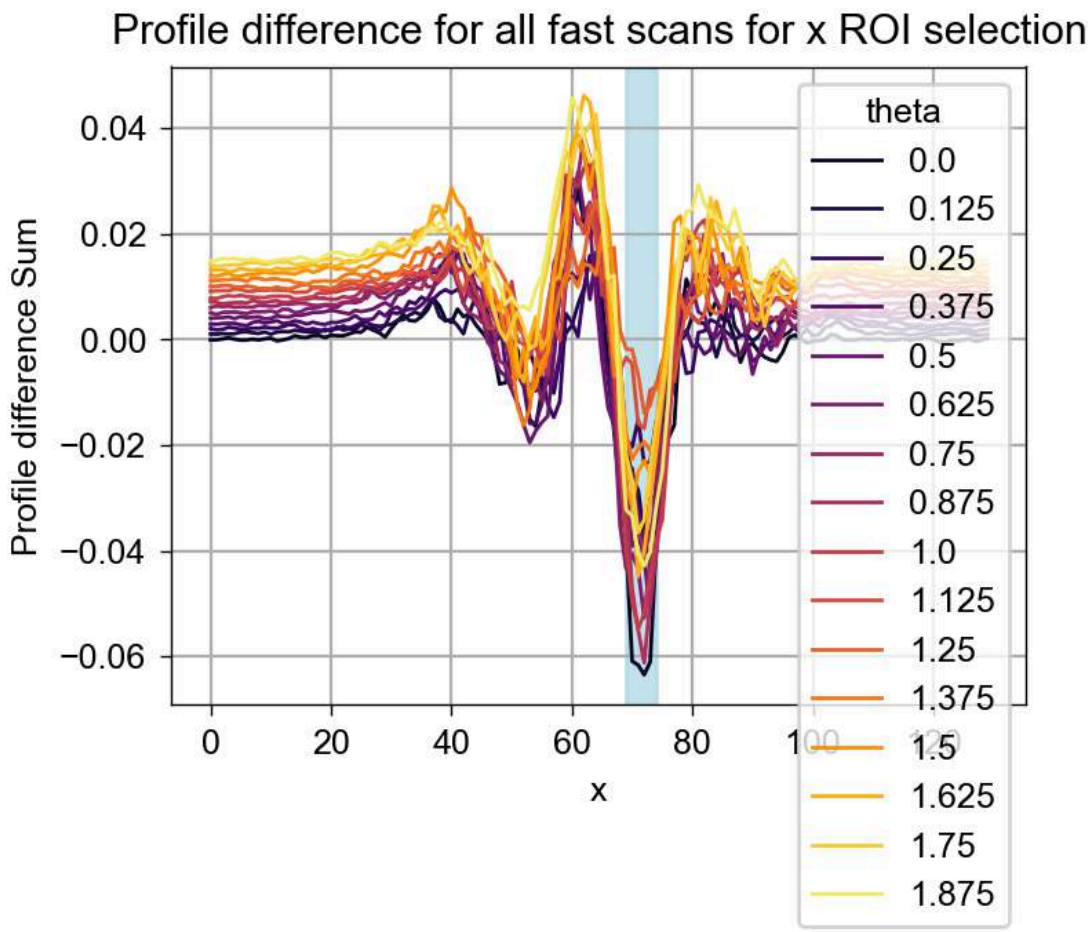

In [112…

```
# Add error bars and theory
# I define EPI signal as minus the sum of the counts in the roi
epi_signal_multi = -ds2.diff_profile.sel(x=slice(min_val, max_val)).sum('x')
epi_signal_multi['theta'] = epi_signal_multi.theta * np.pi

#plot
sns.set_palette('tab10')
epi_signal_multi.plot(marker='o', hue='fast_scan')

plt.xlabel('theta (rad)')
plt.ylabel('EPI signal ')
```

Out[112…

```
Text(0, 0.5, 'EPI signal ')
```

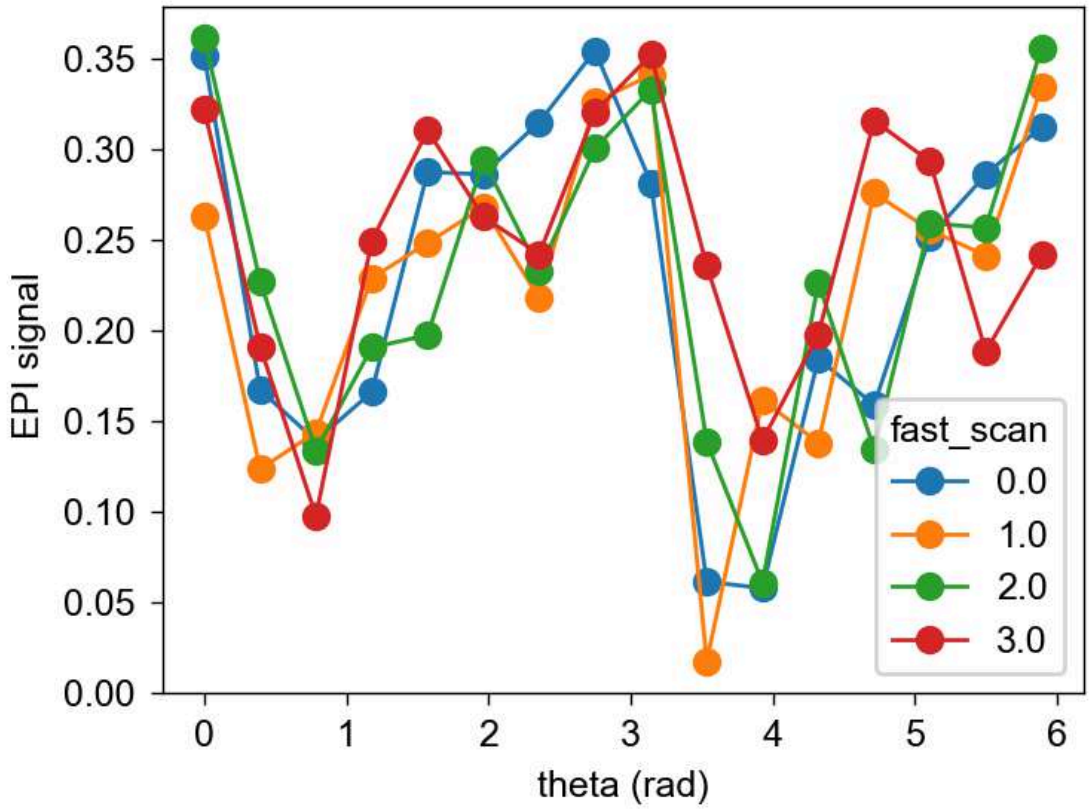

In [113…

```
epi_signal = epi_signal_multi.mean(dim='fast_scan')
epi_signal_sig = epi_signal_multi.std(dim='fast_scan')
epi_signal_err = epi_signal_sig / np.sqrt(len(ds2.fast_scan))

plt.errorbar(epi_signal.theta, epi_signal, yerr=epi_signal_err, fmt='o', label='EPI
plt.xlabel('theta (rad)')
plt.ylabel('EPI signal')
plt.title('EPI signal')

# #Save
# plt.savefig(os.path.join(plot_folder, 'epi_signal.png'), dpi=300, bbox_inches='ti
```

Out[113…

```
Text(0.5, 1.0, 'EPI signal')
```

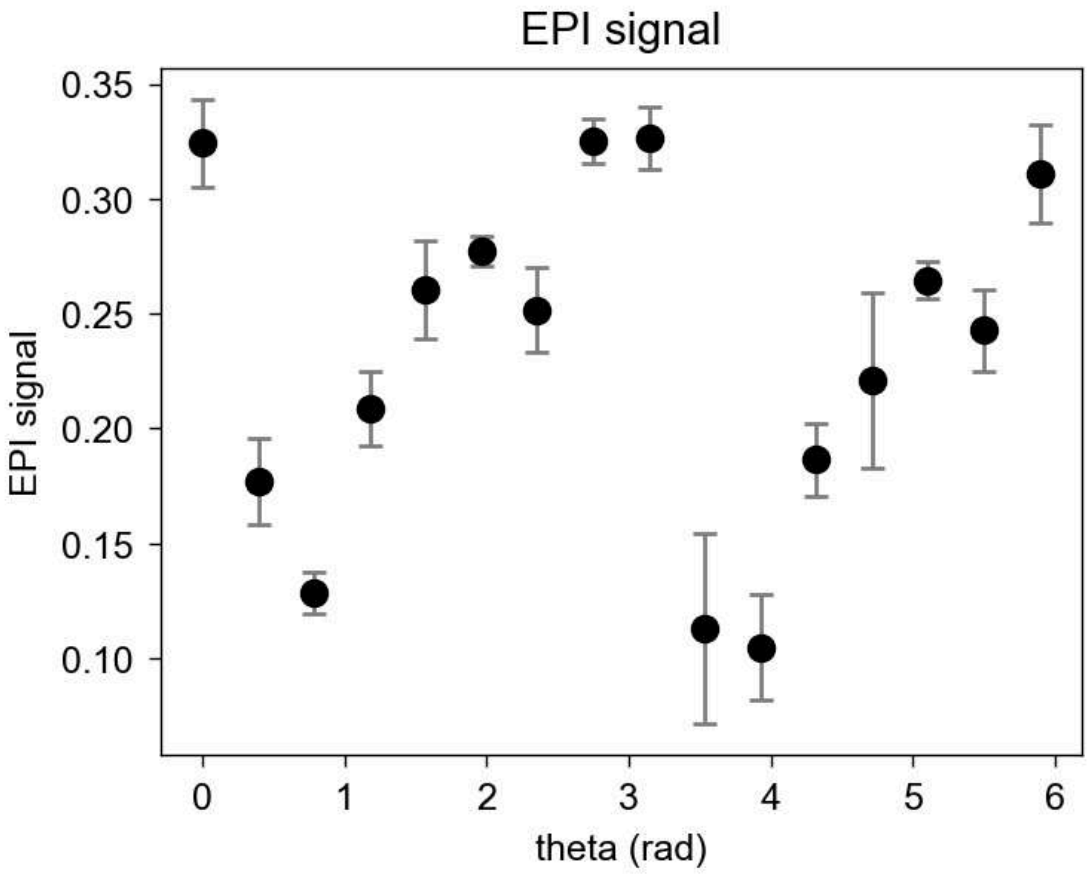

Fitting of the signal

The most basic way of reconstructing a signal is fitting with sinusoidal harmonics

In [114…
```
def harmonic_fit(theta, theta_0, c0, c1, c2, c3):
    return c0 + c1*np.sin(2*(theta - theta_0)) + c2*np.sin(4*(theta - theta_0)) + c
```

In [115…
```
# def harmonic_fit(theta, theta_0, c0, c1, c2, c3, c4):
#     return c0 + c1*np.sin(2*(theta - theta_0)) + c2*np.sin(4*(theta - theta_0)) +
```

In [116…
```
# Fit the EPI signal to a harmonic function
#   th0, c0, c1, c2, c3
p0 = (0, 0.2, -0.15, 0, 0)

# Plot the EPI signal with the fitted curve
plt.errorbar(epi_signal.theta, epi_signal, yerr=epi_signal_err, fmt='o', label='EPI
plt.xlabel('theta (rad)')
plt.ylabel('EPI signal')

# Plot the guessed curve
theta_fit = np.linspace(epi_signal.theta.min().values, epi_signal.theta.max().value
plt.plot(theta_fit, harmonic_fit(theta_fit, *p0), label='Guess', color='blue')

popt, pcov = curve_fit(harmonic_fit, epi_signal.theta, epi_signal, p0=p0, sigma=epi
```

```
#construct the fitted curve with finer theta values
epi_signal_fit = harmonic_fit(theta_fit, *popt)
```

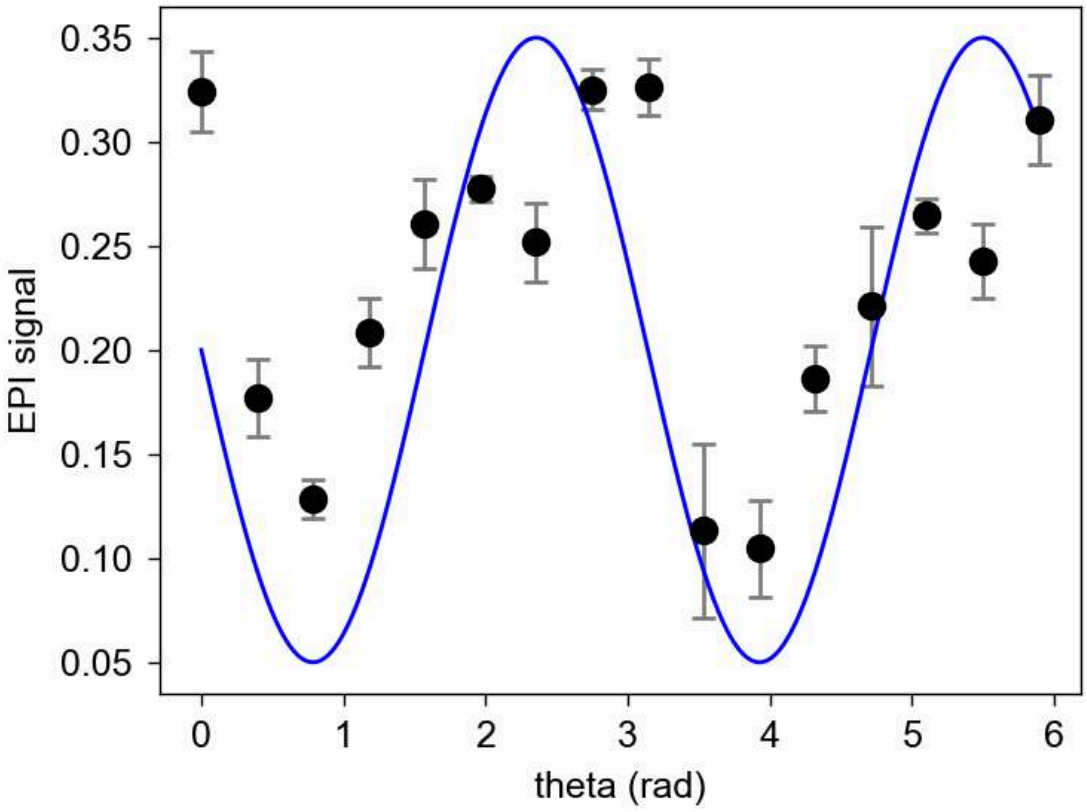

In [117…

```
# Convert theta to rad/π for plotting
theta_plot = epi_signal.theta / np.pi
theta_fit_plot = theta_fit / np.pi

# Plot the EPI signal
plt.errorbar(theta_plot, epi_signal, yerr=epi_signal_err, fmt='o', label='EPI signa
plt.xlabel('theta (rad/$\pi$)')
plt.ylabel('EPI signal')

#Fitted curve
plt.plot(theta_fit_plot, epi_signal_fit, label='Fitted curve', color='red')

# #Theoretial curve: c2 and c3 = 0
# theory_curve = harmonic_fit(theta_fit, *(popt[0], popt[1], popt[2], 0, 0))
# plt.plot(theta_fit_plot, theory_curve, label='Theory', color='blue', linestyle='-

plt.legend(loc='upper right')

# Print  the fit function with the fit result parameters
fit_eq = (r'Fit: {:.2f} + {:.2f} $\cdot \sin(2 \cdot (\theta - {:.2f})) {:.2f} \cdo
    popt[0], popt[1], popt[0], popt[2], popt[0], popt[3], popt[0], popt[4], popt[0]
# plt.text(0.05, 0.05, fit_eq, transform=plt.gca().transAxes, fontsize=10, vertical
#          bbox=dict(boxstyle='round,pad=0.3', edgecolor='black', facecolor='white'
plt.title(fit_eq)
```

```
# Save the plot with the fitted curve
plt.savefig(os.path.join(plot_folder, 'epi_signal_fit.png'), dpi=300, bbox_inches='
```

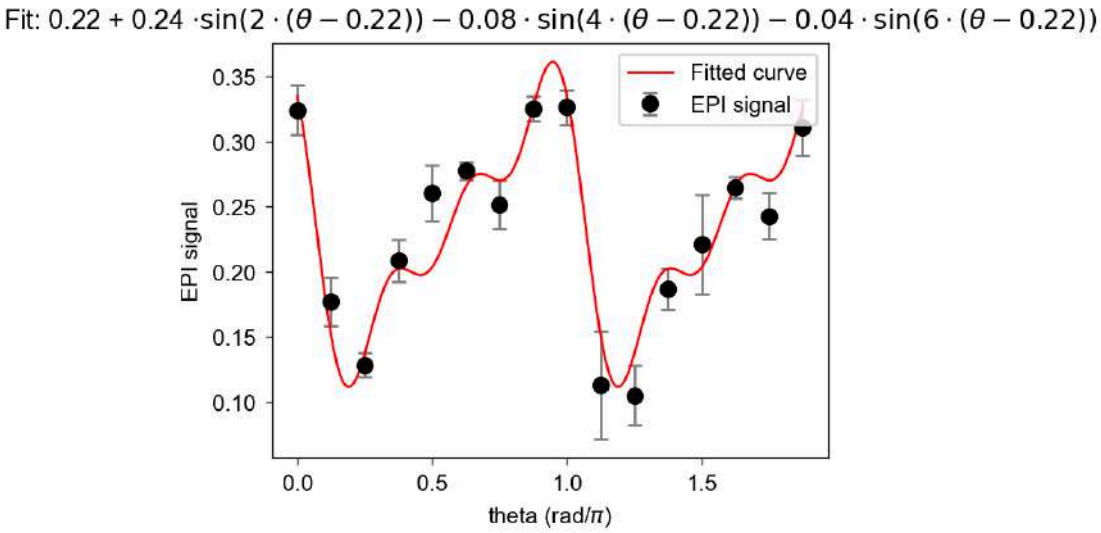

In [118…

```
# Convert theta to rad/π for plotting
theta_plot = epi_signal.theta / np.pi
theta_fit_plot = theta_fit / np.pi

# Plot the EPI signal
plt.figure(figsize=(4.2/2.54, 4.2/2.54))
plt.errorbar(theta_plot, epi_signal, yerr=epi_signal_err, fmt='o', label='EPI signa
plt.xlabel('θ (rad)', labelpad=-7)
plt.ylabel('EPI signal', labelpad=-11)

#set ticks
plt.xticks([0,2], ['0', '2π'])
plt.xlim(-0.1, 2.1)
plt.yticks([0.1,0.35], ['0.1', '0.35'])

#Fitted curve
plt.plot(theta_fit_plot, epi_signal_fit, label='Harmonic fit', color='red')

# Save the plot with the fitted curve
plt.savefig(os.path.join(plot_folder, 'epi_signal_fit.png'), dpi=300, bbox_inches='
# plt.savefig(os.path.join('G:\Shared drives\LUMiNaD\Group papers\ESPI\Figures\SI_S
#             dpi=300, bbox_inches='tight', format='svg', transparent=True)
```

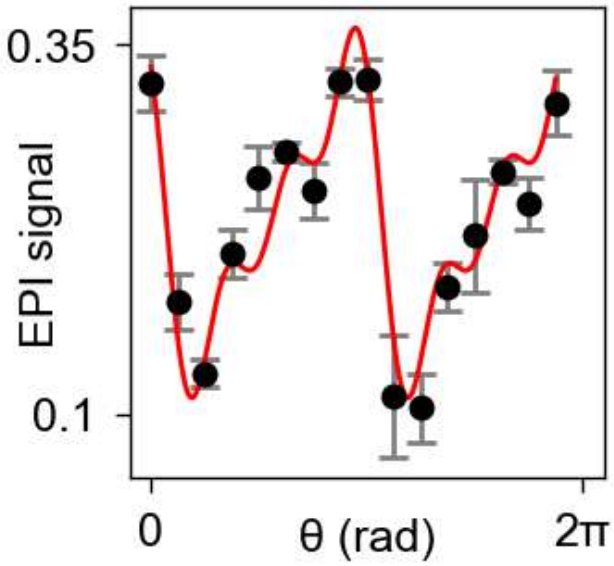

2D image reconstruction

I know that the sample has cylindrica (azimuythal) symmetry. So I can map this 1D function back into 2D

In [119…

```
radius = np.linspace(0, 1, 1000)  # radius values for the circle
theta_grid = np.linspace(0, 2*np.pi, 1000)

# Create a 2D grid in polar coordinates
R, Theta = np.meshgrid(radius, theta_grid)

# Convert polar coordinates to Cartesian coordinates
X = R * np.cos(Theta)
Y = R * np.sin(Theta)

# Compute the harmonic fit for each theta (same result for all radii)
theta_0 = np.pi/8
rec_im = harmonic_fit(Theta, theta_0, *popt[1:])  # set theta 0 as the phase offset

da_reconstruction = xr.DataArray(
    data=rec_im,
    dims=["theta", "r"],
    coords=dict(
        x=(["theta", "r"], X),
        y=(["theta", "r"], Y),
    ),
)
```

In [120…

```
fig = plt.figure(figsize=(5/2.54, 5/2.54))
ax = da_reconstruction.plot(x='x', y='y', cmap='Greys_r', add_colorbar=False, raste
ax.axes.set_axis_off()
ax.axes.set_aspect('equal')
plt.title('Reconstructed image')
```

```
# Add a horizontal colorbar in the bottom right
im = ax
cbar = plt.colorbar(im, ax=ax.axes, orientation='horizontal')
# Make the colorbar shorter
cbar.ax.set_position([0.7, 0.3, 0.15, 0.1])  # [left, bottom, width, height]
# cbar.set_label('EPI signal')
cbar.ax.xaxis.set_ticks_position('bottom')
cbar.ax.xaxis.set_label_position('bottom')
# Set custom colorbar ticks
cbar.set_ticks([0.1, 0.6])

plt.savefig(os.path.join(plot_folder, 'reconstructed_img.png'), dpi=300, bbox_inche
# plt.savefig(os.path.join('G:\Shared drives\LUMiNaD\Group papers\ESPI\Figures\SI_S
#             dpi=300, bbox_inches='tight', format='svg', transparent=True)
```

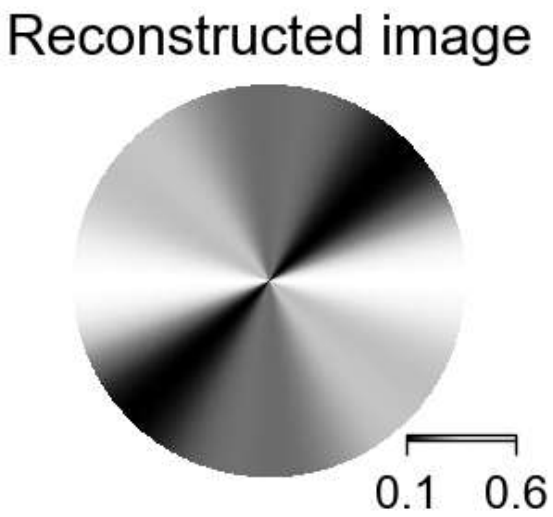

In [121…

```
da_reconstruction.isel(r=0).plot()
```

Out[121…

```
[<matplotlib.lines.Line2D at 0x2a9618ea410>]
```

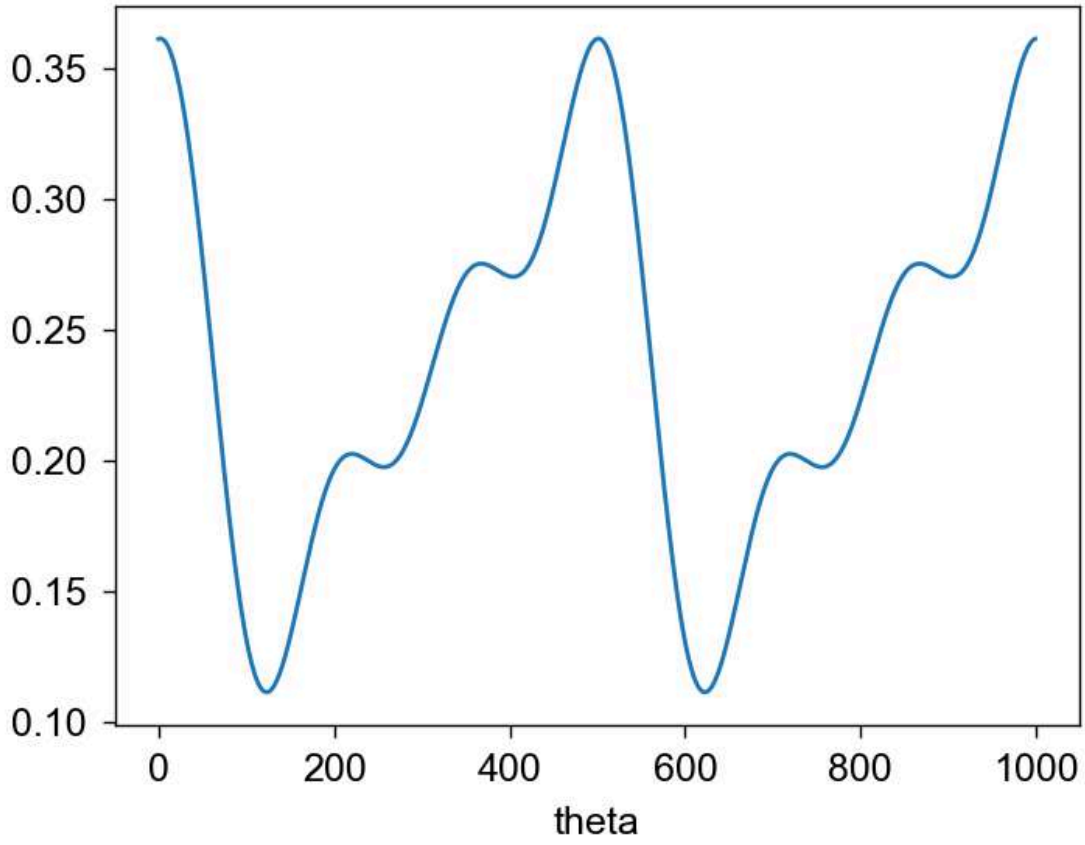

.teX generation

In [124…
```
!jupyter nbconvert --to latex 20240822_pinem_rotate_v2_copy4thesisApp.ipynb
```

```
[NbConvertApp] Converting notebook 20240822_pinem_rotate_v2_copy4thesisApp.ipynb to
latex
C:\Users\bea97\anaconda3\share\jupyter\nbconvert\templates\latex\display_priority.j
2:32: UserWarning: Your element with mimetype(s) dict_keys(['application/vnd.plotly.
v1+json']) is not able to be represented.
  ((*- endblock -*))
[NbConvertApp] Support files will be in 20240822_pinem_rotate_v2_copy4thesisApp_file
s\
[NbConvertApp] Making directory 20240822_pinem_rotate_v2_copy4thesisApp_files
[NbConvertApp] Writing 138101 bytes to 20240822_pinem_rotate_v2_copy4thesisApp.tex
```

In [ ]:
```
!jupyter nbconvert --to webpdf 20240822_pinem_rotate_v2_copy4thesisApp.ipynb
```

Acknowledgements

I first want to thank **Gianmaria** for being such an understanding supervisor. You have always been there whenever I asked for support. A big thank you to the most important mate in my PhD (and life) journey: **Irene**, you were always beside me for both fun and pain. We grew a lot together and I hope we will continue to do so. Thank you also to **Maria Giulia**. It was beautiful to see you develop from a Master's student into a PhD researcher. I'm so happy to have had someone to work with and our conferences together were amazing adventures. Thanks to **Cameron**: as a postdoc, you taught me how to work in the lab and always brought good energy to our lunch breaks. **Floriana**, even if we only overlapped for a short time, thank you for your support and tenacity.

Thanks to the **CNR-Nano** collegues and especially to **Paolo Rosi** for all his EBL, FIB, and calculation work and for patiently answering my "Can I ask you a question?" messages. I thank the **LUMES** group for hosting me—and for the parties!—with a special thanks to **Ivan**, who helped me stand up after a bad fall.

A great thank you to the **quasicrystal team** this project was the most exciting part of my PhD, and it wouldn't have been possible without each of you. Thanks to **Marc** for replying to the email of an unknown PhD student, for providing the crystal, for sharing your knowledge, and for putting me in contact with **Tsunetomo**, whom I also thank, for the diffuse scattering simulations. Thanks so much to **Jan** for running the COMSOL simulations and for the great scientific discussions we had. Thanks also to the **graphene-quasicrystal team** for providing the samples to a confused but enthusiastic PhD student. A special thanks to **Antonio Rossi** for the inspiring paper discussions we shared.

A great acknowledgment goes to **ChatGPT**, which accompanied me through this thesis as both an assistant and a coach. It helped me find papers, organize my mental chaos, point out missing connections, and turn my messy sentences into clear ones. It made the long writing process possible without completely burning out.

I also thank the wonderful crew of the **cookie office** for keeping my sugar levels in check and for all the great lunch breaks. I thank my friends. The Lausanne crew, with the amazing strong girls of **tuesday Beaulieu bouldering** and my other climbing friends. And the Italian **Arrampicose** and **swing dancing** communities. The adventures we

shared were the real fuel for my PhD. I thank my **parents** for their endless support. And last but not least, I thank my beloved **Kjeld**, who stood by my side during the latest and toughest period.

List of publications

- **Ferrari, B. M.**, Duncan, C. J. R., Yannai, M., Dahan, R., Rosi, P., Ostroman, I., ... & Vanacore, G. M. (2025). Realization of a pre-sample photonic-based free-electron modulator in ultrafast transmission electron microscopes. ACS Photonics (https://doi.org/10.1021/acsphotonics.5c00549)
- García de Abajo, F. J., Polman, A., ... **Ferrari, B. M.**, ... & Solà-Garcia, M. (2025). Roadmap for quantum nanophotonics with free electrons. ACS photonics, 12(9), 4760.
- Hajduček, J., Andrieux, A., Arregi, J. A., Tichý, M., Cattaneo, P., **Ferrari, B.**, ... & LaGrange, T. (2025). Dislocation-Driven Nucleation Type Switching Across Repeated Ultrafast Magnetostructural Phase Transition. arXiv preprint arXiv:2507.18364.
- Hu, J., Xiang, Y., **Ferrari, B. M.**, Scalise, E., & Vanacore, G. M. (2023). Indirect exciton–phonon dynamics in MoS2 revealed by ultrafast electron diffraction. Advanced Functional Materials, 33(19), 2206395.

Bibliography

[1] G. P. Thomson. "The Diffraction of Cathode Rays by Thin Films of Platinum". In: *Nature* 120.3031 (Dec. 1927), pp. 802–802. ISSN: 1476-4687. DOI: 10.1038/120802a0.

[2] C. Davisson and L. H. Germer. "Diffraction of Electrons by a Crystal of Nickel". In: *Physical Review* 30.6 (Dec. 1927), pp. 705–740. DOI: 10.1103/PhysRev.30.705.

[3] M. Knoll and E. Ruska. "Beitrag Zur Geometrischen Elektronenoptik. I". In: *Annalen der Physik* 404.5 (1932), pp. 607–640. ISSN: 1521-3889. DOI: 10.1002/andp.19324040506.

[4] David B. Williams and C. Barry Carter. "The Instrument". In: *Transmission Electron Microscopy: A Textbook for Materials Science*. Ed. by David B. Williams and C. Barry Carter. Boston, MA: Springer US, 2009, pp. 141–171. ISBN: 978-0-387-76501-3. DOI: 10.1007/978-0-387-76501-3_9.

[5] Rolf Erni et al. "Atomic-Resolution Imaging with a Sub-50-pm Electron Probe". In: *Physical Review Letters* 102.9 (Mar. 2009), p. 096101. DOI: 10.1103/PhysRevLett.102.096101.

[6] Ondrej L. Krivanek et al. "Atom-by-Atom Structural and Chemical Analysis by Annular Dark-Field Electron Microscopy". In: *Nature* 464.7288 (Mar. 2010), pp. 571–574. ISSN: 1476-4687. DOI: 10.1038/nature08879.

[7] Akira Tonomura. *Electron Holography*. Ed. by Helmut K. V. Lotsch. Vol. 70. Springer Series in Optical Sciences. Berlin, Heidelberg: Springer, 1999. ISBN: 978-3-642-08421-8 978-3-540-37204-2. DOI: 10.1007/978-3-540-37204-2.

[8] Colin Ophus. "Four-Dimensional Scanning Transmission Electron Microscopy (4D-STEM): From Scanning Nanodiffraction to Ptychography and Beyond". In: *Microscopy and Microanalysis* 25.3 (June 2019), pp. 563–582. ISSN: 1431-9276. DOI: 10.1017/S1431927619000497.

[9] S. Fernandez-Perez et al. "Characterization of a Hybrid Pixel Counting Detector Using a Silicon Sensor and the IBEX Readout ASIC for Electron Detection". In: *Journal of Instrumentation* 16.10 (Oct. 2021), P10034. ISSN: 1748-0221. DOI: 10.1088/1748-0221/16/10/P10034.

[10] Ferenc Krausz and Misha Ivanov. "Attosecond Physics". In: *Reviews of Modern Physics* 81.1 (Feb. 2009), pp. 163–234. DOI: 10.1103/RevModPhys.81.163.

[11] Judy S. Kim et al. "Imaging of Transient Structures Using Nanosecond in Situ TEM". In: *Science (New York, N.Y.)* 321.5895 (Sept. 2008), pp. 1472–1475. ISSN: 1095-9203. DOI: 10.1126/science.1161517.

[12] Ahmed H. Zewail. "Four-Dimensional Electron Microscopy". In: *Science* 328.5975 (Apr. 2010), pp. 187–193. ISSN: 0036-8075, 1095-9203. DOI: 10.1126/science.1166135.

[13] Jo Verbeeck et al. "Demonstration of a 2×2 Programmable Phase Plate for Electrons". In: *Ultramicroscopy* 190 (July 2018), pp. 58–65. ISSN: 0304-3991. DOI: 10.1016/j.ultramic.2018.03.017.

[14] Arnaud Arbouet, Giuseppe M. Caruso, and Florent Houdellier. "Chapter One - Ultrafast Transmission Electron Microscopy: Historical Development, Instrumentation, and Applications". In: *Advances in Imaging and Electron Physics*. Ed. by Peter W. Hawkes. Vol. 207. Advances in Imaging and Electron Physics. Elsevier, Jan. 2018, pp. 1–72. DOI: 10.1016/bs.aiep.2018.06.001.

[15] Brett Barwick, David J. Flannigan, and Ahmed H. Zewail. "Photon-Induced near-Field Electron Microscopy". In: *Nature* 462.7275 (Dec. 2009), pp. 902–906. ISSN: 0028-0836, 1476-4687. DOI: 10.1038/nature08662.

[16] Sang Tae Park, Milo Lin, and Ahmed H. Zewail. "Photon-Induced near-Field Electron Microscopy (PINEM): Theoretical and Experimental". In: *New Journal of Physics* 12.12 (Dec. 2010), p. 123028. ISSN: 1367-2630. DOI: 10.1088/1367-2630/12/12/123028.

[17] David Nabben et al. "Attosecond Electron Microscopy of Sub-Cycle Optical Dynamics". In: *Nature* 619.7968 (July 2023), pp. 63–67. ISSN: 1476-4687. DOI: 10.1038/s41586-023-06074-9.

[18] John H. Gaida et al. "Attosecond Electron Microscopy by Free-Electron Homodyne Detection". In: *Nature Photonics* 18.5 (May 2024), pp. 509–515. ISSN: 1749-4893. DOI: 10.1038/s41566-024-01380-8.

[19] Tomer Bucher et al. "Coherently Amplified Ultrafast Imaging Using a Free-Electron Interferometer". In: *Nature Photonics* 18.8 (Aug. 2024), pp. 809–815. ISSN: 1749-4885, 1749-4893. DOI: 10.1038/s41566-024-01451-w.

[20] G. M. Vanacore et al. "Ultrafast Generation and Control of an Electron Vortex Beam via Chiral Plasmonic near Fields". In: *Nature Materials* 18.6 (June 2019), pp. 573–579. ISSN: 1476-1122, 1476-4660. DOI: 10.1038/s41563-019-0336-1.

[21] Shai Tsesses et al. "Tunable Photon-Induced Spatial Modulation of Free Electrons". In: *Nature Materials* 22.3 (Mar. 2023), pp. 345–352. ISSN: 1476-4660. DOI: 10.1038/s41563-022-01449-1.

[22] Ivan Madan et al. "Ultrafast Transverse Modulation of Free Electrons by Interaction with Shaped Optical Fields". In: *ACS Photonics* 9.10 (Oct. 2022), pp. 3215–3224. ISSN: 2330-4022, 2330-4022. DOI: 10.1021/acsphotonics.2c00850.

[23] Giovanni Maria Vanacore, Ivan Madan, and Fabrizio Carbone. "Spatio-Temporal Shaping of a Free-Electron Wave Function via Coherent Light–Electron Interaction". In: *La Rivista del Nuovo Cimento* 43.11 (Nov. 2020), pp. 567–597. ISSN: 0393-697X, 1826-9850. DOI: 10.1007/s40766-020-00012-5.

[24] F. Javier García De Abajo et al. "Roadmap for Quantum Nanophotonics with Free Electrons". In: *ACS Photonics* 12.9 (Sept. 2025), pp. 4760–4817. ISSN: 2330-4022, 2330-4022. DOI: 10.1021/acsphotonics.5c00585.

[25] L. C. Steinhauer, R. D. Romea, and W. D. Kimura. "Inverse Transition Radiation". In: *The Seventh Workshop on Advanced Accelerator Concepts*. Lake Tahoe, California (USA): ASCE, 1997, pp. 673–686. ISBN: 978-1-56396-697-2. DOI: 10.1063/1.53031.

[26] Yiqi Fang et al. "Structured Electrons with Chiral Mass and Charge". In: *Science* 385.6705 (July 2024), pp. 183–187. DOI: 10.1126/science.adp9143.

[27] Maximilian Mattes, Mikhail Volkov, and Peter Baum. "Femtosecond Electron Beam Probe of Ultrafast Electronics". In: *Nature Communications* 15.1 (Feb. 2024), p. 1743. ISSN: 2041-1723. DOI: 10.1038/s41467-024-45744-8.

[28] Andrea Konečná et al. "Single-Pixel Imaging in Space and Time with Optically Modulated Free Electrons". In: *ACS Photonics* 10.5 (May 2023), pp. 1463–1472. ISSN: 2330-4022, 2330-4022. DOI: 10.1021/acsphotonics.3c00047.

[29] F. Javier García de Abajo and Andrea Konečná. "Optical Modulation of Electron Beams in Free Space". In: *Physical Review Letters* 126.12 (Mar. 2021), p. 123901. DOI: 10.1103/PhysRevLett.126.123901.

[30] G.M. Vanacore, A.W.P. Fitzpatrick, and A.H. Zewail. "Four-Dimensional Electron Microscopy: Ultrafast Imaging, Diffraction and Spectroscopy in Materials Science and Biology". In: *Nano Today* 11.2 (Apr. 2016), pp. 228–249. ISSN: 17480132. DOI: 10.1016/j.nantod.2016.04.009.

[31] Armin Feist et al. "Ultrafast Transmission Electron Microscopy Using a Laser-Driven Field Emitter: Femtosecond Resolution with a High Coherence Electron Beam". In: *Ultramicroscopy* 176 (May 2017), pp. 63–73. ISSN: 03043991. DOI: 10.1016/j.ultramic.2016.12.005.

[32] Brett Barwick and Ahmed H. Zewail. "Photonics and Plasmonics in 4D Ultrafast Electron Microscopy". In: *ACS Photonics* 2.10 (Oct. 2015), pp. 1391–1402. ISSN: 2330-4022, 2330-4022. DOI: 10.1021/acsphotonics.5b00427.

[33] Albert Polman, Mathieu Kociak, and F. Javier García de Abajo. "Electron-Beam Spectroscopy for Nanophotonics". In: *Nature Materials* 18.11 (Nov. 2019), pp. 1158–1171. ISSN: 1476-4660. DOI: 10.1038/s41563-019-0409-1.

[34] Charles Roques-Carmes et al. "Free-Electron–Light Interactions in Nanophotonics". In: *Applied Physics Reviews* 10.1 (Jan. 2023), p. 011303. ISSN: 1931-9401. DOI: 10.1063/5.0118096.

[35] David J. Flannigan, Brett Barwick, and Ahmed H. Zewail. "Biological Imaging with 4D Ultrafast Electron Microscopy". In: *Proceedings of the National Academy of Sciences* 107.22 (June 2010), pp. 9933–9937. DOI: 10.1073/pnas.1005653107.

[36] Jianbo Hu et al. "Transient Structures and Possible Limits of Data Recording in Phase-Change Materials". In: *ACS Nano* 9.7 (July 2015), pp. 6728–6737. ISSN: 1936-0851, 1936-086X. DOI: 10.1021/acsnano.5b01965.

[37] Peter Baum, Ding-Shyue Yang, and Ahmed H. Zewail. "4D Visualization of Transitional Structures in Phase Transformations by Electron Diffraction". In: *Science* 318.5851 (Nov. 2007), pp. 788–792. DOI: 10.1126/science.1147724.

[38] Fabrizio Carbone, Oh-Hoon Kwon, and Ahmed H. Zewail. "Dynamics of Chemical Bonding Mapped by Energy-Resolved 4D Electron Microscopy". In: *Science* 325.5937 (July 2009), pp. 181–184. DOI: 10.1126/science.1175005.

[39] L. Piazza et al. "Design and Implementation of a Fs-Resolved Transmission Electron Microscope Based on Thermionic Gun Technology". In: *Chemical Physics* 423 (Sept. 2013), pp. 79–84. ISSN: 03010104. DOI: 10.1016/j.chemphys.2013.06.026.

[40] Bradley J. Siwick et al. "An Atomic-Level View of Melting Using Femtosecond Electron Diffraction". In: *Science* (Nov. 2003). DOI: 10.1126/science.1090052.

[41] Peter Baum. "On the Physics of Ultrashort Single-Electron Pulses for Time-Resolved Microscopy and Diffraction". In: *Chemical Physics* 423 (Sept. 2013), pp. 55–61. ISSN: 0301-0104. DOI: 10.1016/j.chemphys.2013.06.012.

[42] Armin Feist et al. "Quantum Coherent Optical Phase Modulation in an Ultrafast Transmission Electron Microscope". In: *Nature* 521.7551 (May 2015), pp. 200–203. ISSN: 0028-0836, 1476-4687. DOI: 10.1038/nature14463.

[43] S. R. Tauchert et al. "Polarized Phonons Carry Angular Momentum in Ultrafast Demagnetization". In: *Nature* 602.7895 (Feb. 2022), pp. 73–77. ISSN: 1476-4687. DOI: 10.1038/s41586-021-04306-4.

[44] Armin Feist et al. "High-Purity Free-Electron Momentum States Prepared by Three-Dimensional Optical Phase Modulation". In: *Physical Review Research* 2.4 (Nov. 2020), p. 043227. ISSN: 2643-1564. DOI: 10.1103/PhysRevResearch.2.043227.

[45] Jianbo Hu et al. "Indirect Exciton–Phonon Dynamics in MoS_2 Revealed by Ultrafast Electron Diffraction". In: *Advanced Functional Materials* 33.19 (May 2023), p. 2206395. ISSN: 1616-301X, 1616-3028. DOI: 10.1002/adfm.202206395.

[46] Robert P. Chatelain et al. "Coherent and Incoherent Electron-Phonon Coupling in Graphite Observed with Radio-Frequency Compressed Ultrafast Electron Diffraction". In: *Physical Review Letters* 113.23 (Dec. 2014), p. 235502. DOI: 10.1103/PhysRevLett.113.235502.

[47] Daniel Kazenwadel et al. "Cooling Times in Femtosecond Pump-Probe Experiments of Phase Transitions with Latent Heat". In: *Physical Review Research* 5.4 (Oct. 2023), p. 043077. DOI: 10.1103/PhysRevResearch.5.043077.

[48] Francesco Barantani et al. "Ultrafast Momentum-Resolved Visualization of the Interplay between Phonon-Mediated Scattering and Plasmons in Graphite". In: *Science Advances* 11.14 (Apr. 2025), eadu1001. DOI: 10.1126/sciadv.adu1001.

[49] Enrico Pomarico et al. "meV Resolution in Laser-Assisted Energy-Filtered Transmission Electron Microscopy". In: *ACS Photonics* 5.3 (Mar. 2018), pp. 759–764. DOI: 10.1021/acsphotonics.7b01393.

[50] G. M. Vanacore et al. "Attosecond Coherent Control of Free-Electron Wave Functions Using Semi-Infinite Light Fields". In: *Nature Communications* 9.1 (July 2018), p. 2694. ISSN: 2041-1723. DOI: 10.1038/s41467-018-05021-x.

[51] M. Th. Hassan et al. "High-Temporal-Resolution Electron Microscopy for Imaging Ultrafast Electron Dynamics". In: *Nature Photonics* 11.7 (July 2017), pp. 425–430. ISSN: 1749-4885, 1749-4893. DOI: 10.1038/nphoton.2017.79.

[52] L. Piazza et al. "Simultaneous Observation of the Quantization and the Interference Pattern of a Plasmonic Near-Field". In: *Nature Communications* 6.1 (Mar. 2015), p. 6407. ISSN: 2041-1723. DOI: 10.1038/ncomms7407.

[53] S. Meuret et al. "Time-Resolved Cathodoluminescence in an Ultrafast Transmission Electron Microscope". In: *Applied Physics Letters* 119.6 (Aug. 2021), p. 062106. ISSN: 0003-6951. DOI: 10.1063/5.0057861.

[54] P. A. Čerenkov. "Visible Radiation Produced by Electrons Moving in a Medium with Velocities Exceeding That of Light". In: *Physical Review* 52.4 (1937), pp. 378–379. DOI: 10.1103/PhysRev.52.378.

[55] Vitaly L. Ginzburg and Il'ya M. Frank. "Radiation of a Uniformly Moving Electron Due to Its Transition from One Medium into Another". In: *Journal of Physics (ussr)* 9 (1945), pp. 353–362. ISSN: 0368-3400.

[56] S. J. Smith and E. M. Purcell. "Visible Light from Localized Surface Charges Moving across a Grating". In: *Physical Review* 92.4 (Nov. 1953), pp. 1069–1069. ISSN: 0031-899X. DOI: 10.1103/PhysRev.92.1069.

[57] W. D. Kimura. "Laser Acceleration of Relativistic Electrons Using the Inverse Cherenkov Effect". In: *Physical Review Letters* 74.4 (1995), pp. 546–549. DOI: 10.1103/PhysRevLett.74.546.

[58] K. Mizuno et al. "Experimental Evidence of the Inverse Smith–Purcell Effect". In: *Nature* 328.6125 (July 1987), pp. 45–47. ISSN: 1476-4687. DOI: 10.1038/328045a0.

[59] T. Plettner et al. "Visible-Laser Acceleration of Relativistic Electrons in a Semi-Infinite Vacuum". In: *Physical Review Letters* 95.13 (Sept. 2005), p. 134801. DOI: 10.1103/PhysRevLett.95.134801.

[60] Uwe Niedermayer et al. "Alternating-Phase Focusing for Dielectric-Laser Acceleration". In: *Physical Review Letters* 121.21 (Nov. 2018), p. 214801. ISSN: 0031-9007, 1079-7114. DOI: 10.1103/PhysRevLett.121.214801.

[61] F. Javier García De Abajo, Ana Asenjo-Garcia, and Mathieu Kociak. "Multiphoton Absorption and Emission by Interaction of Swift Electrons with Evanescent Light Fields". In: *Nano Letters* 10.5 (May 2010), pp. 1859–1863. ISSN: 1530-6984, 1530-6992. DOI: 10.1021/nl100613s.

[62] Osip Schwartz et al. "Laser Phase Plate for Transmission Electron Microscopy". In: *Nature Methods* 16.10 (Oct. 2019), pp. 1016–1020. ISSN: 1548-7105. DOI: 10.1038/s41592-019-0552-2.

[63] Marius Constantin Chirita Mihaila et al. "Transverse Electron-Beam Shaping with Light". In: *Physical Review X* 12.3 (Sept. 2022), p. 031043. ISSN: 2160-3308. DOI: 10.1103/PhysRevX.12.031043.

[64] M. Kozák et al. "Inelastic Ponderomotive Scattering of Electrons at a High-Intensity Optical Travelling Wave in Vacuum". In: *Nature Physics* 14.2 (Feb. 2018), pp. 121–125. ISSN: 1745-2481. DOI: 10.1038/nphys4282.

[65] M. Kozák, N. Schönenberger, and P. Hommelhoff. "Ponderomotive Generation and Detection of Attosecond Free-Electron Pulse Trains". In: *Physical Review Letters* 120.10 (Mar. 2018), p. 103203. DOI: 10.1103/PhysRevLett.120.103203.

[66] P. H. Bucksbaum. "High-Intensity Kapitza-Dirac Effect". In: *Physical Review Letters* 61.10 (1988), pp. 1182–1185. DOI: 10.1103/PhysRevLett.61.1182.

[67] A. Weingartshofer et al. "Direct Observation of Multiphoton Processes in Laser-Induced Free-Free Transitions". In: *Physical Review Letters* 39.5 (Aug. 1977), pp. 269–270. DOI: 10.1103/PhysRevLett.39.269.

[68] Valerio Di Giulio, Mathieu Kociak, and F. Javier García de Abajo. "Probing Quantum Optical Excitations with Fast Electrons". In: *Optica* 6.12 (Dec. 2019), pp. 1524–1534. ISSN: 2334-2536. DOI: 10.1364/OPTICA.6.001524.

[69] Roy J. Glauber and M. Lewenstein. "Quantum Optics of Dielectric Media". In: *Physical Review A* 43.1 (Jan. 1991), pp. 467–491. DOI: 10.1103/PhysRevA.43.467.

[70] Yuya Morimoto and Peter Baum. "Diffraction and Microscopy with Attosecond Electron Pulse Trains". In: *Nature Physics* 14.3 (Mar. 2018), pp. 252–256. ISSN: 1745-2481. DOI: 10.1038/s41567-017-0007-6.

[71] Wentao Wang et al. "Energy-Momentum Transfer in the Free-Electron–Photon Interaction Mediated by a Film". In: *Physical Review B* 109.13 (Apr. 2024), p. 134305. ISSN: 2469-9950, 2469-9969. DOI: 10.1103/PhysRevB.109.134305.

[72] F. Javier García de Abajo and Valerio Di Giulio. "Optical Excitations with Electron Beams: Challenges and Opportunities". In: *ACS Photonics* 8.4 (Apr. 2021), pp. 945–974. DOI: 10.1021/acsphotonics.0c01950.

[73] Omid Zandi et al. "Transient Lensing from a Photoemitted Electron Gas Imaged by Ultrafast Electron Microscopy". In: *Nature Communications* 11.1 (June 2020), p. 3001. ISSN: 2041-1723. DOI: 10.1038/s41467-020-16746-z.

[74] Ivan Madan et al. "Charge Dynamics Electron Microscopy: Nanoscale Imaging of Femtosecond Plasma Dynamics". In: *ACS Nano* 17.4 (Feb. 2023), pp. 3657–3665. ISSN: 1936-0851, 1936-086X. DOI: 10.1021/acsnano.2c10482.

[75] P. Musumeci. "Multiphoton Photoemission from a Copper Cathode Illuminated by Ultrashort Laser Pulses in an Rf Photoinjector". In: *Physical Review Letters* 104.8 (2010). DOI: 10.1103/PhysRevLett.104.084801.

[76] Sascha Schäfer, Wenxi Liang, and Ahmed H. Zewail. "Structural Dynamics and Transient Electric-Field Effects in Ultrafast Electron Diffraction from Surfaces". In: *Chemical Physics Letters* 493.1 (June 2010), pp. 11–18. ISSN: 0009-2614. DOI: 10.1016/j.cplett.2010.04.049.

[77] Cheyne M. Scoby, R. K. Li, and P. Musumeci. "Effect of an Ultrafast Laser Induced Plasma on a Relativistic Electron Beam to Determine Temporal Overlap in Pump–Probe Experiments". In: *Ultramicroscopy*. Frontiers of Electron Microscopy in Materials Science 127 (Apr. 2013), pp. 14–18. ISSN: 0304-3991. DOI: 10.1016/j.ultramic.2012.07.015.

[78] Beatrice Matilde Ferrari et al. "Realization of a Pre-Sample Photonic-Based Free-Electron Modulator in Ultrafast Transmission Electron Microscopes". In: *ACS Photonics* (Oct. 2025). DOI: 10.1021/acsphotonics.5c00549.

[79] Masaya Uchida and Akira Tonomura. "Generation of Electron Beams Carrying Orbital Angular Momentum". In: *Nature* 464.7289 (Apr. 2010), pp. 737–739. ISSN: 1476-4687. DOI: 10.1038/nature08904.

[80] J. Verbeeck, H. Tian, and P. Schattschneider. "Production and Application of Electron Vortex Beams". In: *Nature* 467.7313 (Sept. 2010), pp. 301–304. ISSN: 1476-4687. DOI: 10.1038/nature09366.

[81] S. M. Lloyd et al. "Electron Vortices: Beams with Orbital Angular Momentum". In: *Reviews of Modern Physics* 89.3 (Aug. 2017), p. 035004. DOI: 10.1103/RevModPhys.89.035004.

[82] Amir H. Tavabi et al. "Experimental Demonstration of an Electrostatic Orbital Angular Momentum Sorter for Electron Beams". In: *Physical Review Letters* 126.9 (Mar. 2021), p. 094802. DOI: 10.1103/PhysRevLett.126.094802.

[83] I. Madan et al. "The Quantum Future of Microscopy: Wave Function Engineering of Electrons, Ions, and Nuclei". In: *Applied Physics Letters* 116.23 (June 2020), p. 230502. ISSN: 0003-6951. DOI: 10.1063/1.5143008.

[84] Yuval Adiv et al. "Quantum Nature of Dielectric Laser Accelerators". In: *Physical Review X* 11.4 (Dec. 2021), p. 041042. ISSN: 2160-3308. DOI: 10.1103/PhysRevX.11.041042.

[85] Marius Constantin Chirita Mihaila et al. *Light-Based Electron Aberration Corrector*. Apr. 2025. DOI: 10.48550/arXiv.2504.18661. arXiv: 2504.18661 [physics].

[86] Leonardo Rossi. "Pixel Detectors Hybridisation". In: *Nuclear Instruments and Methods in Physics Research Section A: Accelerators, Spectrometers, Detectors and Associated Equipment* 501.1 (Mar. 2003), pp. 239–244. ISSN: 01689002. DOI: 10.1016/S0168-9002(02)02041-7.

[87] P Allé et al. "Comparison of CCD, CMOS and Hybrid Pixel x-Ray Detectors: Detection Principle and Data Quality". In: *Physica Scripta* 91.6 (June 2016), p. 063001. ISSN: 0031-8949, 1402-4896. DOI: 10.1088/0031-8949/91/6/063001.

[88] G. McMullan et al. "Detective Quantum Efficiency of Electron Area Detectors in Electron Microscopy". In: *Ultramicroscopy* 109.9 (Aug. 2009), pp. 1126–1143. ISSN: 03043991. DOI: 10.1016/j.ultramic.2009.04.002.

[89] Kirsty A. Paton et al. "Quantifying the Performance of a Hybrid Pixel Detector with GaAs:Cr Sensor for Transmission Electron Microscopy". In: *Ultramicroscopy* 227 (Aug. 2021), p. 113298. ISSN: 03043991. DOI: 10.1016/j.ultramic.2021.113298.

[90] Françoise Viallefont-Robinet et al. "Comparison of MTF Measurements Using Edge Method: Towards Reference Data Set". In: *Optics Express* 26.26 (Dec. 2018), pp. 33625–33648. ISSN: 1094-4087. DOI: 10.1364/OE.26.033625.

[91] Rdiger R. Meyer and Angus I. Kirkland. "Characterisation of the Signal and Noise Transfer of CCD Cameras for Electron Detection". In: *Microscopy Research and Technique* 49.3 (May 2000), pp. 269–280. ISSN: 1059-910X, 1097-0029. DOI: 10.1002/(SICI)1097-0029(20000501)49:3<269::AID-JEMT5>3.0.CO;2-B.

[92] Zhou Wang et al. "Image Quality Assessment: From Error Visibility to Structural Similarity". In: *IEEE Transactions on Image Processing* 13.4 (Apr. 2004), pp. 600–612. ISSN: 1941-0042. DOI: 10.1109/TIP.2003.819861.

[93] Yujia Yang et al. "Unifying Frequency Metrology across Microwave, Optical, and Free-Electron Domains". In: *Nature Communications* 16.1 (Sept. 2025), p. 8369. ISSN: 2041-1723. DOI: 10.1038/s41467-025-62808-5.

[94] Grant R. Fowles. *Introduction to Modern Optics*. 2. ed., corr. republication. New York: Dover Publications, 1989. ISBN: 978-0-486-65957-2.

[95] A. Janzen et al. "A Pulsed Electron Gun for Ultrafast Electron Diffraction at Surfaces". In: *Review of Scientific Instruments* 78.1 (2007). DOI: 10.1063/1.2431088.

[96] F. O. Kirchner et al. "Coherence of Femtosecond Single Electrons Exceeds Biomolecular Dimensions". In: *New Journal of Physics* 15.6 (June 2013), p. 063021. ISSN: 1367-2630. DOI: 10.1088/1367-2630/15/6/063021.

[97] Andreas Gahlmann, Sang Tae Park, and Ahmed H. Zewail. "Ultrashort Electron Pulses for Diffraction, Crystallography and Microscopy: Theoretical and Experimental Resolutions". In: *Physical Chemistry Chemical Physics* 10.20 (May 2008), pp. 2894–2909. ISSN: 1463-9084. DOI: 10.1039/B802136H.

[98] Marco F. Duarte et al. "Single-Pixel Imaging via Compressive Sampling". In: *IEEE Signal Processing Magazine* 25.2 (Mar. 2008), pp. 83–91. ISSN: 1053-5888. DOI: 10.1109/MSP.2007.914730.

[99] Matthew P. Edgar, Graham M. Gibson, and Miles J. Padgett. "Principles and Prospects for Single-Pixel Imaging". In: *Nature Photonics* 13.1 (Jan. 2019), pp. 13–20. ISSN: 1749-4893. DOI: 10.1038/s41566-018-0300-7.

[100] T. B. Pittman et al. "Optical Imaging by Means of Two-Photon Quantum Entanglement". In: *Physical Review. A, Atomic, Molecular, and Optical Physics* 52.5 (Nov. 1995), R3429–R3432. ISSN: 1050-2947. DOI: 10.1103/physreva.52.r3429.

[101] Jeffrey H. Shapiro. "Computational Ghost Imaging". In: *Physical Review A* 78.6 (Dec. 2008), p. 061802. DOI: 10.1103/PhysRevA.78.061802.

[102] L. Kovarik et al. "Implementing an Accurate and Rapid Sparse Sampling Approach for Low-Dose Atomic Resolution STEM Imaging". In: *Applied Physics Letters* 109.16 (Oct. 2016), p. 164102. ISSN: 0003-6951. DOI: 10.1063/1.4965720.

[103] D.L. Donoho. "Compressed Sensing". In: *IEEE Transactions on Information Theory* 52.4 (Apr. 2006), pp. 1289–1306. ISSN: 0018-9448. DOI: 10.1109/TIT.2006.871582.

[104] Kaikai Guo, Shaowei Jiang, and Guoan Zheng. "Multilayer Fluorescence Imaging on a Single-Pixel Detector". In: *Biomedical Optics Express* 7.7 (July 2016), pp. 2425–2431. ISSN: 2156-7085. DOI: 10.1364/BOE.7.002425.

[105] M R Hestenes and E Stiefel. "Methods of Conjugate Gradients for Solving Linear Systems". In: ().

[106] Liheng Bian et al. "Experimental Comparison of Single-Pixel Imaging Algorithms". In: *JOSA A* 35.1 (Jan. 2018), pp. 78–87. ISSN: 1520-8532. DOI: 10.1364/JOSAA.35.000078.

[107] Benoit Truc et al. "Light-Induced Metastable Hidden Skyrmion Phase in the Mott Insulator Cu2OSeO3". In: *Advanced Materials* 35.33 (2023), p. 2304197. ISSN: 1521-4095. DOI: 10.1002/adma.202304197.

[108] S. Seki et al. "Observation of Skyrmions in a Multiferroic Material". In: *Science* 336.6078 (Apr. 2012), pp. 198–201. DOI: 10.1126/science.1214143.

[109] Yoshinori Tokura and Naoya Kanazawa. "Magnetic Skyrmion Materials". In: *Chemical Reviews* 121.5 (Mar. 2021), pp. 2857–2897. ISSN: 0009-2665. DOI: 10.1021/acs.chemrev.0c00297.

[110] Jan Hajduček et al. *Dislocation-Driven Nucleation Type Switching Across Repeated Ultrafast Magnetostructural Phase Transition*. July 2025. DOI: 10.48550/arXiv.2507.18364. arXiv: 2507.18364 [cond-mat].

[111] Paul A. Midgley and Rafal E. Dunin-Borkowski. "Electron Tomography and Holography in Materials Science". In: *Nature Materials* 8.4 (Apr. 2009), pp. 271–280. ISSN: 1476-4660. DOI: 10.1038/nmat2406.

[112] Luca Bindi et al. "Natural Quasicrystals". In: *Science* 324.5932 (June 2009), pp. 1306–1309. DOI: 10.1126/science.1170827.

[113] D. Shechtman. "Metallic Phase with Long-Range Orientational Order and No Translational Symmetry". In: *Physical Review Letters* 53.20 (1984), pp. 1951–1953. DOI: 10.1103/PhysRevLett.53.1951.

[114] Dov Levine. "Quasicrystals: A New Class of Ordered Structures". In: *Physical Review Letters* 53.26 (1984), pp. 2477–2480. DOI: 10.1103/PhysRevLett.53.2477.

[115] Walter Steurer. "Quasicrystals: What Do We Know? What Do We Want to Know? What Can We Know?" In: ().

[116] John W. Cahn, Dan Shechtman, and Denis Gratias. "Indexing of Icosahedral Quasiperiodic Crystals". In: *Journal of Materials Research* 1.1 (Feb. 1986), pp. 13–26. ISSN: 0884-2914, 2044-5326. DOI: 10.1557/JMR.1986.0013.

[117] M. De Boissieu et al. "Reversible Transformation between an Icosahedral Al-Pd-Mn Phase and a Modulated Structure of Cubic Symmetry". In: *Philosophical Magazine A* 78.2 (Aug. 1998), pp. 305–326. ISSN: 0141-8610, 1460-6992. DOI: 10.1080/01418619808241906.

[118] Marc de Boissieu and Sonia Francoual. "Diffuse Scattering and Phason Modes in the I-AlPdMn Quasicrystalline Phase". In: ().

[119] M. De Boissieu. "Stability of Quasicrystals: Energy, Entropy and Phason Modes". In: *Philosophical Magazine* 86.6-8 (Feb. 2006), pp. 1115–1122. ISSN: 1478-6435, 1478-6443. DOI: 10.1080/14786430500419411.

[120] Vincent Fournee et al. "Electronic Structure of Al-Pd-Mn Crystalline and Quasicrystalline Alloys". In: *Journal of Physics: Condensed Matter* 14.1 (Jan. 2002), pp. 87–102. ISSN: 0953-8984, 1361-648X. DOI: 10.1088/0953-8984/14/1/308.

[121] V. Fournée et al. "Electronic Structure of Quasicrystalline Surfaces: Effects of Surface Preparation and Bulk Structure". In: *Physical Review B* 62.21 (Dec. 2000), pp. 14049–14060. ISSN: 0163-1829, 1095-3795. DOI: 10.1103/PhysRevB.62.14049.

[122] M. Krajčí and J. Hafner. "Structure, Stability, and Electronic Properties of the i -AlPdMn Quasicrystalline Surface". In: *Physical Review B* 71.5 (Feb. 2005), p. 054202. ISSN: 1098-0121, 1550-235X. DOI: 10.1103/PhysRevB.71.054202.

[123] Yuki Nagai et al. "High-Temperature Atomic Diffusion and Specific Heat in Quasicrystals". In: *Physical Review Letters* 132.19 (May 2024), p. 196301. ISSN: 0031-9007, 1079-7114. DOI: 10.1103/PhysRevLett.132.196301.

[124] M. Widom. "Discussion of Phasons in Quasicrystals and Their Dynamics". In: *Philosophical Magazine* 88.13-15 (May 2008), pp. 2339–2350. ISSN: 1478-6435, 1478-6443. DOI: 10.1080/14786430802247163.

[125] Kento Fukushima et al. "Comparative Study of High-Temperature Specific Heat for Al–Pd–Mn Icosahedral Quasicrystals and Crystal Approximants". In: *Journal of Physics Communications* 5.8 (Aug. 2021), p. 085002. ISSN: 2399-6528. DOI: 10.1088/2399-6528/ac1875.

[126] Marc De Boissieu. "Phonons and Phasons in Icosahedral Quasicrystals". In: *Israel Journal of Chemistry* 51.11-12 (Dec. 2011), pp. 1292–1303. ISSN: 0021-2148, 1869-5868. DOI: 10.1002/ijch.201100131.

[127] A. Letoublon et al. "Phason Elastic Constants of the Icosahedral Al-Pd-Mn Phase Derived from Diffuse Scattering Measurements". In: *Philosophical Magazine Letters* 81.4 (Apr. 2001), pp. 273–283. ISSN: 0950-0839, 1362-3036. DOI: 10.1080/09500830010029409.

[128] Y. Ishii. "Phason Softening and Structural Transitions in Icosahedral Quasicrystals". In: *Physical Review B* 45.10 (Mar. 1992), pp. 5228–5239. ISSN: 0163-1829, 1095-3795. DOI: 10.1103/PhysRevB.45.5228.

[129] Laurent P. René De Cotret et al. "Time- and Momentum-Resolved Phonon Population Dynamics with Ultrafast Electron Diffuse Scattering". In: *Physical Review B* 100.21 (Dec. 2019), p. 214115. ISSN: 2469-9950, 2469-9969. DOI: 10.1103/PhysRevB.100.214115.

[130] Fabio Caruso and Dino Novko. "Ultrafast Dynamics of Electrons and Phonons: From the Two-Temperature Model to the Time-Dependent Boltzmann Equation". In: *Advances in Physics: X* 7.1 (Dec. 2022), p. 2095925. ISSN: null. DOI: 10.1080/23746149.2022.2095925.

[131] C. Janot. *Quasicrystals: A Primer*. Second edition. Oxford Classic Texts in the Physical Sciences. Oxford: Oxford University Press, 2012. ISBN: 978-0-19-965740-7.

[132] Ted Janssen and Marc De Boissieu. "Dynamics of Quasicrystals". In: *Comptes Rendus. Physique* 15.1 (2014), pp. 58–69. ISSN: 1878-1535. DOI: 10.1016/j.crhy.2013.09.011.

[133] M de Boissieut et al. "Dynamics of the AlPdMn Icosahedral Phase". In: ().

[134] Marko V. Jarić and David R. Nelson. "Diffuse Scattering from Quasicrystals". In: *Physical Review B* 37.9 (Mar. 1988), pp. 4458–4472. ISSN: 0163-1829. DOI: 10.1103/PhysRevB.37.4458.

[135] Justus A. Kromer et al. "What Phasons Look Like: Particle Trajectories in a Quasicrystalline Potential". In: *Physical Review Letters* 108.21 (May 2012), p. 218301. ISSN: 0031-9007, 1079-7114. DOI: 10.1103/PhysRevLett.108.218301.

[136] S. E. Krasavin. *An Alternative Mechanism of Heat Transport in Icosahedral i-AlPdMn Quasicrystals*. Nov. 2004. DOI: 10.48550/arXiv.cond-mat/0411189. arXiv: cond-mat/0411189.

[137] K. Tanaka, Y. Mitara, and M. Koiwa. "Elastic Constants of Al-based Icosahedral Quasicrystals". In: *Philosophical Magazine A* 73.6 (June 1996), pp. 1715–1723. ISSN: 0141-8610, 1460-6992. DOI: 10.1080/01418619608243008.

[138] Sergio Pezzini et al. "30°-Twisted Bilayer Graphene Quasicrystals from Chemical Vapor Deposition". In: *Nano Letters* 20.5 (May 2020), pp. 3313–3319. ISSN: 1530-6984, 1530-6992. DOI: 10.1021/acs.nanolett.0c00172.

[139] Sung Joon Ahn et al. "Dirac Electrons in a Dodecagonal Graphene Quasicrystal". In: *Science* 361.6404 (Aug. 2018), pp. 782–786. ISSN: 0036-8075, 1095-9203. DOI: 10.1126/science.aar8412.

[140] Pilkyung Moon, Mikito Koshino, and Young-Woo Son. "Quasicrystalline Electronic States in 30 ∘ Rotated Twisted Bilayer Graphene". In: *Physical Review B* 99.16 (Apr. 2019), p. 165430. ISSN: 2469-9950, 2469-9969. DOI: 10.1103/PhysRevB.99.165430.

[141] Bing Deng et al. "Interlayer Decoupling in 30° Twisted Bilayer Graphene Quasicrystal". In: *ACS Nano* 14.2 (Feb. 2020), pp. 1656–1664. ISSN: 1936-0851, 1936-086X. DOI: 10.1021/acsnano.9b07091.

[142] Yung-Chang Lin et al. "Coupling and Decoupling of Bilayer Graphene Monitored by Electron Energy Loss Spectroscopy". In: *Nano Letters* 21.24 (Dec. 2021), pp. 10386–10391. ISSN: 1530-6984, 1530-6992. DOI: 10.1021/acs.nanolett.1c03689.

[143] Chao-Xing Liu et al. "Electron– K -Phonon Interaction in Twisted Bilayer Graphene". In: *Physical Review B* 110.4 (July 2024), p. 045133. ISSN: 2469-9950, 2469-9969. DOI: 10.1103/PhysRevB.110.045133.

[144] Shiyuan Gao et al. "First-Principles Electron-Phonon Interactions and Electronic Transport in Large-Angle Twisted Bilayer Graphene". In: *Physical Review Materials* 8.5 (May 2024), p. L051001. ISSN: 2475-9953. DOI: 10.1103/PhysRevMaterials.8.L051001.

[145] Florence J. Nelson et al. "Electronic Excitations in Graphene in the 1–50 eV Range: The π and $\pi + \sigma$ Peaks Are Not Plasmons". In: *Nano Letters* 14.7 (July 2014), pp. 3827–3831. ISSN: 1530-6984, 1530-6992. DOI: 10.1021/nl500969t.

[146] S. C. Liou et al. "π- Plasmon Dispersion in Free-Standing Graphene by Momentum-Resolved Electron Energy-Loss Spectroscopy". In: *Physical Review B* 91.4 (Jan. 2015), p. 045418. ISSN: 1098-0121, 1550-235X. DOI: 10.1103/PhysRevB.91.045418.

[147] William Hadley Richardson. "Bayesian-Based Iterative Method of Image Restoration∗". In: *J. Opt. Soc. Am.* 62.1 (Jan. 1972), pp. 55–59. DOI: 10.1364/JOSA.62.000055.

[148] L. B. Lucy. "An iterative technique for the rectification of observed distributions". In: 79 (June 1974), p. 745. DOI: 10.1086/111605.

[149] Jake Dudley Mehew et al. "Ultrafast Umklapp-assisted Electron-Phonon Cooling in Magic-Angle Twisted Bilayer Graphene". In: *Science Advances* 10.6 (Feb. 2024), eadj1361. ISSN: 2375-2548. DOI: 10.1126/sciadv.adj1361.

[150] W. Cochran and R.A. Cowley. "Dielectric Constants and Lattice Vibrations". In: *Journal of Physics and Chemistry of Solids* 23.5 (May 1962), pp. 447–450. ISSN: 00223697. DOI: 10.1016/0022-3697(62)90084-7.

[151] J.J. Quinn. "Bulk and Surface Plasmons in Solids". In: *Nuclear Instruments and Methods in Physics Research Section B: Beam Interactions with Materials and Atoms* 96.3-4 (May 1995), pp. 460–464. ISSN: 0168583X. DOI: 10.1016/0168-583X(95)00246-4.

[152] Georgios D. Evangelidis and Emmanouil Z. Psarakis. "Parametric Image Alignment Using Enhanced Correlation Coefficient Maximization". In: *IEEE Transactions on Pattern Analysis and Machine Intelligence* 30.10 (Oct. 2008), pp. 1858–1865. ISSN: 1939-3539. DOI: 10.1109/TPAMI.2008.113.